Novel methodology for assessing cement injection behaviour in cancellous bone

Antony Bou Francis

Submitted in accordance with the requirements for the degree of Doctor of Philosophy

The University of Leeds

Mechanical Engineering

May 2014

The candidate confirms that the work submitted is his/her own, except where work which has formed part of jointly authored publications has been included. The contribution of the candidate and the other authors to this work has been explicitly indicated below. The candidate confirms that appropriate credit has been given within the thesis where reference has been made to the work of others

Sections of work from chapters 2 to 5 were published as jointly authored conference and journal publications. The candidate was the lead author in all publications performing all laboratory work, analysis and final write-up. The cements tested were provided by Uppsala University, Sweden via Dr C. Persson and help with cement preparation and mixing was provided by Dr A. López. A collaboration was formed with the ETH, Zürich to cross-validate our experimental data with their computational code for simulating the displacement of bone marrow by bone cement in porous media. Prof N. Kapur and R.M. Hall had supervisory roles and contributed towards the final review of all work.

"And all knowledge is vain save when there is work, and all work is empty save when there is love; and when you work with love you bind yourself to yourself, and to one another, and to God."

— Kahlil Gibran, *The Prophet*

ACKNOWLEDGEMENTS

I would like to thank my two supervisors, Prof. Nik Kapur and Prof. Richard M. Hall for their continued support and guidance throughout this PhD. Thanks are extended to my colleagues within the School of Mechanical Engineering with a special attention to the Spine group members, particularly Nicola Brandolini for always being there to bounce ideas, offer technical insight and provide artistic inspiration on illustrations. Thanks are also extended to our clinical advisor Mr. Jake Timothy for his dedicated time and expertise providing a much valued clinical perspective.

This work was funded by the European Union within the project SPINEFX-ITN under the FP7 Marie Curie Action (grant agreement no. PITN-GA-2009-238690). I am grateful to my supervisors who initiated this funding giving me the opportunity to visit other laboratories and attend workshops hosted by our academic and industrial partners across Europe. I would like to acknowledge the collaboration formed with Prof. Stephen Ferguson and Dr. René P. Widmer from the ETH, Zürich to cross-validate our experimental data with their computational code for simulating the displacement of bone marrow by bone cement in cancellous bone. This collaboration has led to the submission of a manuscript for publication. A further collaboration was formed with Dr. Cecilia Persson and Dr. Alejandro López from Uppsala University, Sweden, which has led to the publication of a manuscript entitled "Assessing cement injection behaviour in cancellous bone: An in-vitro study using flow models" in the Journal of Biomaterials Applications.

Finally, I would like to thank my parents and my brother for their endless love and support. I am truly blessed to have a loving family and two grandmothers that keep me in their prayers. I dedicate this work to my late grandfathers, may you rest in peace.
Thank you.

ABSTRACT

Understanding the cement injection behaviour in cancellous bone and accurately predicting the cement placement within the vertebral body is extremely challenging. We propose a novel method using reproducible and pathologically representative 2D and 3D bone surrogates to help study the influence of cement properties on injection behaviour. Bespoke methodology was developed to control the injection volume and flow rate, measure the injection pressure, and allow visualization and quantitative analysis of the spreading distribution. Morphology analysis showed that the variability in the 2D and 3D bone surrogates was very low, indicating that the geometrical structure of the surrogates was constant. The overall pore size of the surrogates was very similar to that reported for human osteoporotic vertebral cancellous bone, indicating that the surrogates were pathologically representative. Injections performed into the 3D surrogates revealed that an increase in the fluid starting viscosity significantly increases the injection pressure in all surrogates, decreases the risk of leakage for osteoporosis surrogates only, decreases the mean spreading distance for multiple myeloma surrogates only and increases the sphericity causing a more uniform spreading pattern for the metastasis surrogates only. Injections performed into the 2D surrogates highlighted the influence of cement formulations and model structure on the injection behaviour and showed that (i) cements with similar composition/particle size have similar flow behaviour, (ii) cements with a high liquid-to-powder ratio cause irregular filling patterns and have a high risk of leakage, and (iii) the injection behaviour of certain cement formulations improves in the presence of lesion or fracture, suggesting the notion of pathology specific bone cements. The developed methodology provides a fast, robust tool for discerning subtle differences in bone cement formulations and allows comprehensive assessment of cement flow behaviour through controlling the surrogate morphology, controlling the injection parameters, measuring the injection pressure, and allowing the visualization and quantitative analysis of the spreading distribution. The advantage of this methodology is that it provides a clinically relevant representation of cement flow patterns and a tool for validating computational simulations.

TABLE OF CONTENTS

LIST OF TABLES

LIST OF FIGURES

NOMENCLATURE

$BaSO_4$	Barium Sulfate
BMD	Bone Mineral Density
BPO	Benzoyl peroxide
BV/TV	Bone Volume/Tissue Volume
CAD	Computer Aided Design
CaP	Calcium Phosphate
CaS	Calcium Sulphate
CCD	Charge-Coupled Device
ConnD	Connectivity Density
CT	Computed Tomography
DA	Degree of Anisotropy
DMPT	N,N-dimethyl-*p*-toluidine
DICOM	Digital Imaging and Communications in Medicine
DXA	Dual-energy X-ray Absorptiometry
EVVP	External Vertebral Venous Plexuses
FDA	Food and Drug Administration
FE	Finite Element
FSU	Functional Spinal Unit
HA	Hydroxyapatite
HU	Hounsfield Unit
IVVP	Internal Vertebral Venous Plexuses
QCT	Quantitative Computed Tomography
QUS	Quantitative Ultrasound
L/P	Liquid-to-Powder ratio
OC	Opacity+
OP	Osteopal V
PKP	Percutaneous Kyphoplasty
PL	Parallax
PMMA	Polymethyl Methacrylate
PVP	Percutaneous Vertebroplasty
MMA	Methyl Methacrylate
MRI	Magnetic Resonance Imaging
RP	Rapid Prototyping
SD	Standard Deviation
Si	Silicone Oil
SP	Simplex P
SLS	Selective Laser Sintering
SMI	Structure Model Index
STL	StereoLithography
Tb.N	Trabecular Number
Tb.Sp	Trabecular Separation
Tb.Th	Trabecular Thickness
VB	Vertebral Body
VF	Vertebral Fractures
WHO	World Health Organization
ZrO_2	Zirconium dioxide

GLOSSARY

Bone Mass	The amount of bone tissue as the total of protein and mineral in the whole skeleton or in a specific segment of bone.
Bone Mineral Density	BMD is the amount of mineral matter per cubic centimeter of bone and is generally used as an indicator for Osteoporosis (< 70 mg/cm^3) and Osteopenia (70 - 100 mg/cm^3).
Cancellous Bone	Referred to as trabecular or spongy bone is a type of osseous tissue composed of multiple trabeculae which form a three dimensional lattice-like structure.
Functional Spinal Unit	The smallest physiological motion unit of the spine to exhibit biomechanical characteristics similar to the entire spine. Mainly made up of the intervertebral disc, two vertebrae, and the interconnecting ligaments.
Morbidity	A diseased state, disability, or poor health due to any cause.
Multiple Myeloma	A cancer of plasma cells which accumulate in bones, where they cause small, multiple bone lytic lesions.
Percutaneous Vertebroplasty	This is a minimally invasive procedure performed under fluoroscopic image-guidance in which bone cement is injected into a fractured vertebra with the goal of relieving pain and restoring spinal stability.
Rapid Prototyping	A special class of machine technology that produces physical three-dimensional models using a layer-by-layer additive approach.
Spinal Metastases	Tumor cells that migrate from a primary site to the spine where they often cause a large bone lesion.
Stereology	The study of methods for obtaining estimators of geometric properties from samples of a structure. It provides practical techniques for extracting quantitative information about a three-dimensional material from measurements made on two-dimensional planar sections of the material.

CHAPTER 1 INTRODUCTION

Osteoporosis is a disease that weakens the bone mainly by reducing the bone mineral density (BMD) and deteriorating the bone microarchitecture. Known to affect postmenopausal women and elderly men, osteoporosis is increasingly becoming a major public health problem due to its impact on morbidity and social cost. The morbidity associated with osteoporosis arises principally from fractures. In the United States, the burden of osteoporosis for the year 2005 was estimated to be >2 million incident fractures resulting in a direct cost of $17 billion [1-4]. Vertebral fractures (VF) account for the majority (~30%) of these osteoporotic-induced factures [4, 5]. For the European Union (EU) countries, a prospective osteoporosis study showed that the annual incidence of VF was (approximately 440,000) 10.7/1000 in woman and 5.7/1000 in men [6]. The annual incidence of osteoporotic-induced fractures is on the rise and it is projected that this increase will reach 50% by the year 2025 [4]. Consequently, the procedures used to treat the chronic pain associated with VF, which are mainly caused by osteoporosis and other skeletal pathologies such as spinal metastasis or multiple myeloma, are also on the rise.

Percutaneous vertebroplasty (PVP) is a minimally invasive procedure in which bone cement is injected into a fractured vertebra with the goal of relieving pain and restoring mechanical stability [7, 8]. The number of PVP performed in the United States has increased by 72.4% between 2001 and 2010 [9-12]. Although the number of procedures is on the rise, several hurdles are currently preventing PVP from becoming the standard of care for the treatment of pain related to VF. The Food and Drug Administration (FDA) has issued a warning about possible complications following the injection of bone cement into a fractured vertebra [13]. The primary concern of the FDA is cement leakage into the surrounding structures which may cause serious clinical complications such as nerve root or spinal cord compression as well as pulmonary embolism. These complications may lead to paraplegia or, in severe cases, death [14-19]. This thesis is focused on the development of *in vitro* assessments and their subsequent usage to study cement injection behaviour in cancellous bone.

1.1 Spine Anatomy and Physiology

The spine is a flexible, multi-segmented anatomic structure that provides support and balance for an upright posture and allows motion in six degrees of freedom [20]. Despite the fact that the spine appears straight in the coronal plane, when viewed in the sagittal plane, the normal adult spine has four distinct curves: two in kyphosis and two in lordosis (Figure 1.1). Kyphosis is a curvature in the sagittal plane with a concavity towards the front (anterior concavity); whereas, lordosis is a curvature in the sagittal plane with a concavity towards the back (posterior concavity). Based on vertebral shape and sagittal plane curves, the spine is divided into four regions: cervical (lordosis), thoracic (kyphosis), lumbar (lordosis), and sacral (kyphosis).

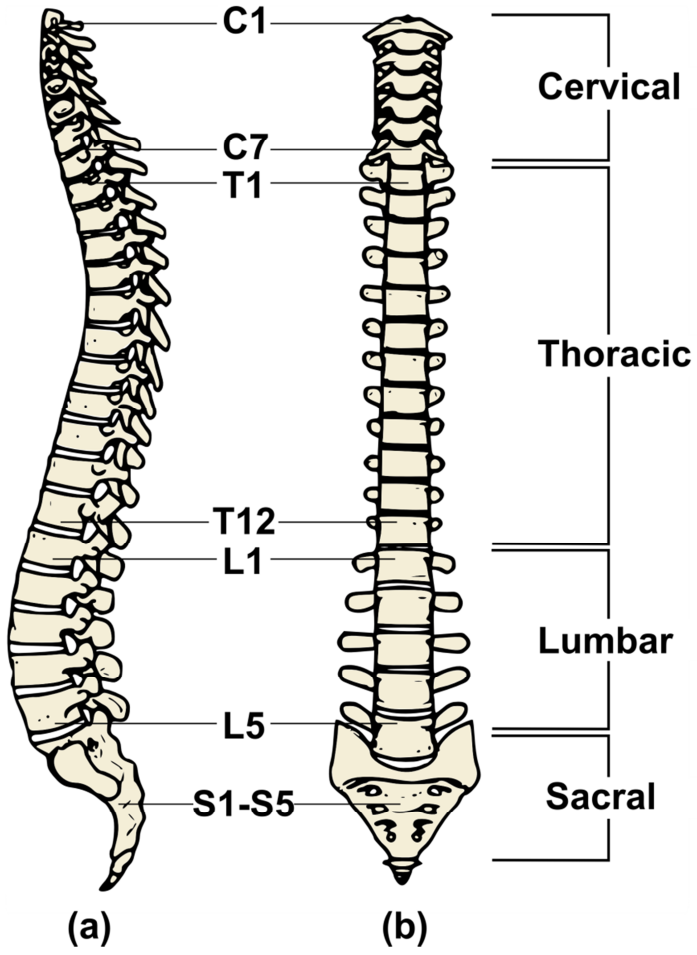

Figure 1. 1 Sagittal (a) and coronal (b) views of the normal adult spine. Adapted from [20].

The cervical spine supports the skull and is made up of seven vertebral segments: C1 to C7. The normal cervical spine has a lordosis ranging from 20° to 40°. Inferior to the cervical is the thoracic spine which consists of twelve vertebral segments: T1 to T12. The normal thoracic spine forms part of the rib cage and has a kyphosis ranging from 20° to 40°. Following the thoracic is the lumbar spine, consisting of five vertebral segments: L1 to L5. The normal lumbar spine has a lordosis ranging from 30° to 50°. The last region of the spine is the sacrococcygeal, which is made up of nine fused vertebrae. The first five vertebrae, S1 to S5, form the sacrum, and the remaining four vertebrae form the coccyx. The normal sacrococcygeal spine has a kyphosis with a wide range of concavities [20]. The size of the vertebrae increases from the cervical to the sacrum. However, the structure of each vertebral segment is similar in all regions of the spine (except in the cervical, where C1 and C2 have a distinct structure). The following reviews the basic structures common to all vertebrae. Each vertebral segment is divided into the vertebral body which is located on the anterior side and the vertebral arch which is located on the posterior side (Figure 1.2).

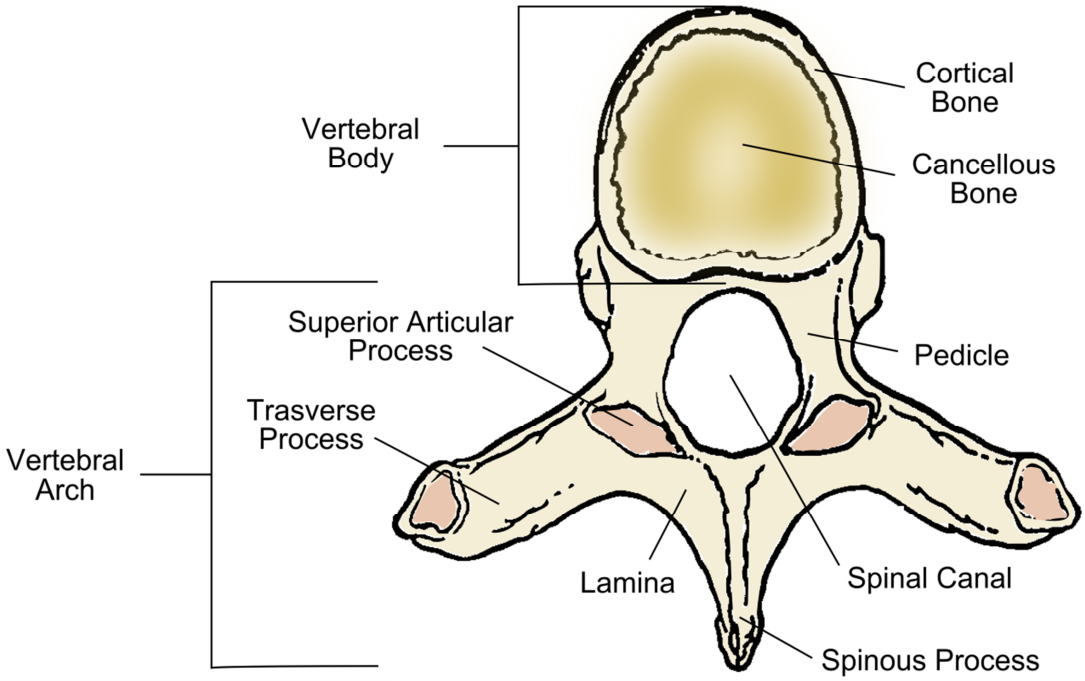

Figure 1. 2 Structures common to all vertebrae. Adapted from [21].

The vertebral body is a semi-cylindrical structure made of a thin layer of cortical bone encompassing cancellous bone. The vertebral arch is made up of two pedicles, two laminae, two transverse processes, one spinous process and four articular processes. The two pedicles are short, rounded structures that extend posteriorly from the lateral edges of the dorsal side of the vertebral body. The two laminae are flat structures that extend medially from the two pedicles. The spinous process extends posteriorly from the junction of the two laminae and serves as an attachment point for tendons and ligaments. The two transverse processes extend laterally from each pedicle and also serve as attachment points for tendons and ligaments. The four articular processes (two superior and two inferior) extend from the junction of the pedicles and the laminae. The two superior processes extend superiorly from each vertebra, and the two inferior processes extend inferiorly from each vertebra. The inferior processes of a vertebra join with the superior processes of an adjacent vertebra below to form the facet joints, which are synovial joints containing lubricating synovial fluid that allows the articular surfaces to glide over each other. The facet joints and the intervertebral discs, located between the articular surfaces of the vertebral body endplates, work in conjunction to regulate intervertebral segment motion [20].

The spine achieves its main functions by being both resistant and flexible. Resistance to axial loading forces, arising from both body weight and muscle action, is accomplished via: (1) the alternating lordosis and kyphosis curves in the four regions of the spine, and (2) the increase in the size of each vertebra from C1 to the sacrum, which compensates for the increase in load demand from C1 to the sacrum. Conversely, the flexibility of the spine is mainly due to intervertebral segment motion, which is accomplished by the facet joints and the intervertebral discs. This segment motion allows the spine to achieve a wide range of motion in six degrees of freedom [20]. Whilst the osteoligamentous spine is relatively unstable, muscles are the key feature of the stable spine, which provide the mechanism for upright posture and dynamic stability achieved during a range of daily activities.

1.2 CANCELLOUS BONE MICROARCHITECTURE

Cancellous bone, also referred to as trabecular or spongy bone, is a type of osseous tissue composed of multiple trabeculae which form a three dimensional lattice-like structure. The individual trabecula is mainly composed of hydroxyapatite and collagen. The scale of a trabecula can be as small as 20 μm and its shape can often be in the form of a plate or rod. The trabecular orientation and the degree of anisotropy drastically vary between anatomical sites. Some regions may be very dense with consistently coarse trabeculae, while others may be sparse with thin trabeculae. This trabecular arrangement or architecture is not random and forms the basis for the formulation of Wolf's law, which links the trabecular architecture to the load environment it is placed under by adaptation. However, the challenge in relating specific mechanical properties to the trabecular architecture lies mainly in the explicit definition of the architectural variables to be included [22, 23].

Three-dimensional morphometric indices (Table 1.1) have been used to describe the cancellous or trabecular bone microarchitecture [24-27]. These indices have been previously derived from two-dimensional images using stereological methods and assuming a fixed plate or rod model. However, with the advent of microcomputed tomography (microCT), it has been possible to assess these indices directly from the three-dimensional images. Such imaging techniques are independent of model type and therefore not biased by the deviations of the actual structures from the assumed models, although the resolution of the imaging system has been shown to greatly affect the measurement of the morphometric indices, particularly the trabecular thickness (Tb.Th). A high resolution (< 5μm) is required to obtain reliable measurements [28, 29]. Other challenges are mainly in the post-processing of the images. Selecting an appropriate image threshold to discriminate bone tissue (foreground) from the surrounding environment (background) is subjective and often difficult. Ridler T.W. and Calvard S. [30] have developed an objective method that automatically chooses a threshold value based on an iterative process, where successive iterations are performed to achieve increasingly reliable extractions of the foreground (bone tissue).

Table 1. 1 Three-dimensional morphometric indices used to describe the trabecular microarchitecture

Symbol	Parameter	Definition
BV/TV (%)	Bone Volume/Tissue Volume	Number of bone voxels divided by total number of voxels in the volume of interest
Tb.Th (μm)	Trabecular Thickness	Average length of continuous bone voxels along a surface. Provides a quantitative estimate of trabecular thinning
Tb.Sp (μm)	Trabecular Separation	Average length of gaps between bone voxels. Can be interpreted as the thickness of the marrow cavities
Tb.N (mm^{-1})	Trabecular Number	The number of trabeculae per unit length
ConnD (mm^{-3})	Connectivity Density	The number of trabecular elements that may be removed without separating the network. Provides an estimate of the number of trabecular connections/mm3
SMI	Structure Model Index	The estimate of plate-rod characteristics of the structure. SMI value is 0 for ideal parallel plate structure and 3 for ideal rod structure
DA	Degree of Anisotropy	The direction of the preferred orientation of trabeculae

Several studies have used microCT imaging to quantify vertebral trabecular bone morphology and have demonstrated significant variations in the 3D morphometric indices within various regions of the vertebral body and with age [25, 31-35]. Table 1.2 summarizes the specimens and techniques used in these five studies to quantify vertebral trabecular bone morphology. Figure 1.3 illustrates details of the specimens used in these five studies. The figure provides information on the location where the specimens were obtained within the vertebral body as well as the regions that were visualized using microCT and analyzed for three-dimensional morphometric indices. Hildebrand et al. [25] were the only group that did not provide detailed information on where their specimens were obtained and simply stated that their specimens were obtained from the center of the vertebral body. Table 1.3 compares the trabecular bone

morphometric indices across the five studies providing an indication for the range of values.

Table 1. 2 Specimens and techniques used to quantify vertebral trabecular bone morphology.

Study	Bone Condition	Specimen	Vertebral Levels	Quantification Method
Lochmuller et al., 2008 [31]	Osteoporosis and Osteopenia	Total: 118 Mean Age: 79.1	T10 and L2	- Direct 3D - µCT 20 Scanco Medical - Resolution 26 µm - Threshold 22% of max grey value - Software provided by manufacturer
Chen et al., 2008 [32]	Osteoporosis and Osteopenia	Total: 56 Mean Age: 77.5	L4	- Direct 3D - µCT, Hitachi Medical - Resolution 15 µm - Software TRI/3D-BON (Racto System Engineering Co. Ltd., Japan)
Hulme et al., 2007 [33]	Osteoporosis	Total: 40 Mean Age: 74.2	T9 to L5	- Direct 3D - XtremeCT, Scanco Medical - Resolution 82 µm - Threshold to preserve structure - Software provided by manufacturer
Gong et al., 2006 [34, 35]	No pathologies affecting structure	Total: 6 Mean Age: 65.7	L4	- Direct 3D - µCT 40 Scanco Medical - Resolution 20 µm - Threshold based on volume fractions - Software provided by manufacturer
Hildebrand et al., 1999 [25]	N/A	Total: 52 Mean Age: 67.3	L2 and L4	- Direct 3D and Traditional indirect - µCT 20 Scanco Medical - Resolution 28 µm - Software provided by manufacturer and stereological techniques

Chen et al. [32], Gong et al. [34, 35], and Hildebrand et al. [25] all analyzed lumbar trabecular structure, however Lochmuller et al. [31] and Hulme et al. [33] analyzed both thoracic and lumbar trabecular structure. Hildebrand et al. [25] were the only group that analyzed the trabecular structure using both direct 3D methods and traditional indirect methods which were derived from 2D images using stereological techniques and assuming a fixed plate model.

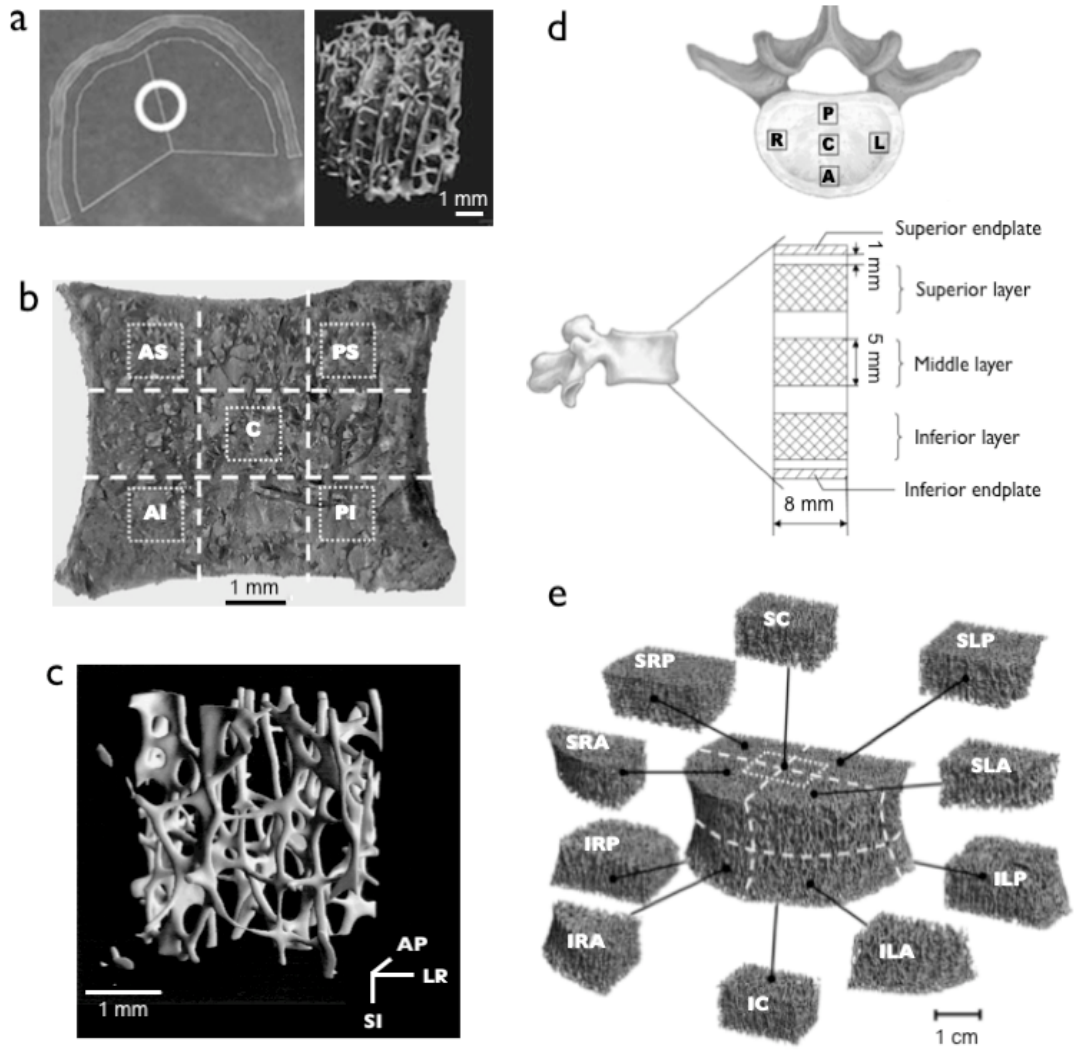

Figure 1. 3 Details of specimens used in studies quantifying vertebral trabecular bone morphology. ***a)*** **Lochmuller et al. [31] obtained a 8 mm full length cylinder in the superior-inferior direction at the middle along the transverse direction and the transition of the anterior third and posterior two thirds of the sagittal VB (left) then the center 6 mm was visualized / analyzed (right).** ***b)*** **Chen et al. [32] obtained a 8 mm thick sagittal section close to the midline of the VB then 5 cubes of 8 x 8 x 8 mm^3 were visualized / analyzed.** ***c)*** **Hildebrand et al. [25] visualized / analyzed specimens from the center of the VB.** ***d)*** **Gong et al. [34, 35] obtained and visualized 5 full length squared columns 8 x 8 mm^2 (top) which were divided into 3 layers (bottom) resulting in 15 regions of interest per specimen then 5 x 5 x 5 mm^3 in the center of each region were analyzed.** ***e)*** **Hulme et al. [33] visualized the VB then analyzed 10 regions.**
Abbreviations: vertebral body (VB), anterior (A), posterior (P), superior (S), inferior (I), left (L), right (R), and center (C).

They found that direct 3D methods systematically yielded higher indices compared to the traditional indirect methods. This is possibly due to the deviation of the trabecular structure form the ideal plate model. The indirect methods underestimated the derived

indices by 30%. They also found no statistically significant differences in morphometric indices between the two analyzed lumbar vertebral levels (L2 and L4). However, when compared to other anatomical sites, specifically the femoral head, the lumbar spine tended to have lower bone volume, thinner trabeculae and a more rod-like structure. Lochmuller et al. [31] also found no statistically significant differences in morphometric indices between the thoracic (T10) and the lumbar (L2) spine. They also compared the trabecular structure of 62 male specimens with a mean age of 78.3 years to 56 female specimens with a mean age of 79.9 years and found no statistically significant gender differences in morphometric indices at either of the two analyzed vertebral levels (T10 and L2).

Table 1. 3 Comparison of vertebral trabecular bone morphometric indices across five studies.

Parameter	Lochmuller et al., 2008 [31]	Chen et al., 2008 [32]	Hulme et al., 2007 [33]	Gong et al., 2006 [34, 35]	Hildebrand et al., 1999 [25]
BV/TV (%)	10.7 ± 3.90	13.5 ± 1.60	12.5 ± 2.40	8.26 ± 1.40	8.30 ± 2.40
Tb.Th (mm)	0.150 ± 0.02	0.112 ± 0.09	0.215 ± 0.02 [a]	0.116 ± 0.01	0.122 ± 0.02
Tb.Sp (mm)	0.96 ± 0.18	0.81 ± 0.08	1.11 ± 0.11	-	0.79 ± 0.13
Tb.N (mm^{-1})	1.03 ± 0.19	1.15 ± 1.17	0.89 ± 0.08	1.17 ± 0.20	1.28 ± 0.20
ConnD (mm^{-3})	2.50 ± 1.51	3.04 ± 0.25	1.32 ± 0.37	3.76 ± 1.44	-
SMI	1.75 ± 0.52	2.21 ± 0.23	2.42 ± 0.31	1.76 ± 0.40	2.13 ± 0.35
DA	1.51 ± 0.21	1.62 ± 0.19	1.36 ± 0.08	1.46 ± 0.15	1.42 ± 0.16

[a] Hulme at al. had a relatively low resolution of 82 μm (Table 1.2), hence the large value for Tb.Th.

Gong et al. [34, 35], Hulme et al. [33] and Chen et al. [32] all investigated the differences in morphometric indices between various regions of the vertebral body (VB). They all found that the posterior-inferior (posterior in general) regions of the VB had higher bone volume, higher number of trabeculae, higher connections and

lower trabecular separation compared to the central and anterior-superior regions (anterior in general). Furthermore, Hulme et al. [33] and Chen et al. [32] both found no statistically significant differences in trabecular thickness between any regions of the VB. However, Chen at al. [32] also found no statistically significant differences in the degree of anisotropy and the structural model index in any regions of the VB. Gong et al. [34, 35] and Chen et al. [32] also investigated the differences in morphometric indices with age and gender. They both found that bone volume tended to decrease (on average by 22%) with age for both men and women, however in the central regions it tended to remain the same. Furthermore, in all regions of the VB, the trabecular number and the connectivity density tended to decrease (on average by 17.5% and 40%, respectively), however the trabecular spacing and the structural model index tended to increase (on average by 19%) with age for both men and women. Gong et al. [34, 35] found that the trabecular thickness slightly decreased with age, whereas the degree of anisotropy increased with age in all regions of the VB. On the other hand, Chen et al. [32] found no statistically significant age-related changes in the degree of anisotropy and the trabecular thickness for both men and women though they report a 10% decrease in trabecular thickness from ages 62 to 92 years.

From the current literature review, it can be concluded that the vertebral trabecular bone morphology tends to remain constant between thoracolumbar vertebral levels and with gender. However, there are significant variations in the three-dimensional morphometric indices within various regions of the vertebral body and with age. With respect to regional variations within the VB, the differences in morphometric indices seem to decrease with age and are more pronounced in young, adult individuals. Furthermore, the posterior-inferior regions of the VB seem to have higher bone volume, higher number of trabeculae, higher connections and lower trabecular separation. A possible rationale for this regional variation is that the posterior-superior region of the VB is reinforced via the pedicles and therefore relies less on trabecular structure for strength. However, the posterior-inferior region of the VB relies more directly on trabecular structure for strength as there is no reinforcement via the posterior elements. The age-related changes in the vertebral trabecular bone morphology include:

- Decrease in bone volume, thickness, number and connectivity density
- Increase in trabecular spacing
- Shift from plate-like to rod-like structure

1.3 Vertebral Circulatory System

The vertebral circulatory system is mainly a large open venous network within and around the vertebral column. The volume of this venous network is around 20 times larger than that of the contributing arterial network. The vertebral venous network is not controlled by valves, thus blood flow can occur in either direction depending on changes in thoracic and abdominal pressure, such as coughing and straining. The vertebral venous network can be divided into three inter-communicating systems: (1) the internal vertebral venous plexuses (IVVP), (2) the basivertebral veins, and (3) the external vertebral venous plexuses (EVVP) [36, 37].

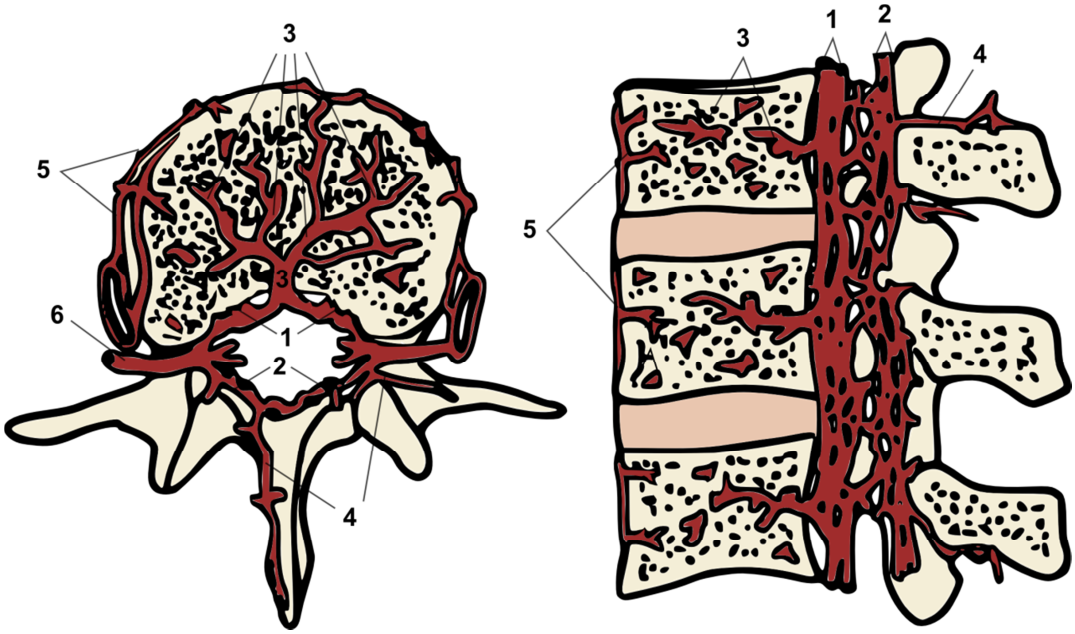

Figure 1. 4 Schematic of a thoracolumbar vertebral circulatory system showing the (1) anterior internal vertebral venous plexus, (2) posterior internal vertebral venous plexus , (3) basivertebral veins, (4) posterior external vertebral venous plexus, (5) anterior external vertebral venous plexus, and (6) intervertebral vein. Adapted from [36].

The IVVP consist of a network of veins that lie within the spinal canal surrounding the dura matter. They run mainly in the vertical direction and form four longitudinal veins, two anterior and two posterior (Figure 1.4). The anterior and posterior IVVP communicate freely with one another, however the anterior IVVP consist of larger veins located along the posterior surface of the vertebral bodies and connect to one another by transverse branches into which the basivertebral veins unite. The posterior IVVP are located in front of the vertebral arches and connect to the posterior EVVP via veins passing through the vertebral arches and the posterior vertebral processes [36, 38]. The basivertebral veins emerge horizontally from the anterior to the posterior surface of the vertebral body where they unite and drain directly into the anterior IVVP, often breaching the cortical wall as a single vein but sometimes as two separate branches. On the anterior surface of the vertebral body, they directly connect to the anterior EVVP through small openings that breach the cortical wall on the front and/or sides (Figure 1.4). The basivertebral veins are contained within the bony channels of the vertebral body and converge with the bone marrow which is also present within these bony channels. Consequently, the bone marrow can be considered as part of the vertebral venous network [36, 38, 39].

1.4 PATHOLOGY

The lifetime prevalence of low back pain is between 70 to 90% [40]. Although the specific causes of most back pain are unknown, a significant portion of the problem is of mechanical origin and related to clinical spinal instability. However, clinical spinal instability is controversial and not well understood. Some researchers define clinical spinal instability as the loss of the spine's ability under physiological conditions to maintain normal intervertebral segment motion so that there is no initial or additional neurologic deficit, no major deformity, and no incapacitating pain [41-44].

Mechanical spinal stability plays a crucial role in the basic biomechanical function of the spine allowing segment motion, load transfer as well as protection of the spinal cord and the nerve roots. Panjabi [45, 46] has conceptualized the overall mechanical spinal stability under physiological conditions as consisting of three main subsystems:

(i) the passive musculoskeletal subsystem which provides intrinsic stability and consists of the vertebrae, the intervertebral discs, the facet joints, the spinal ligaments as well as the passive muscle action, (ii) the active musculoskeletal subsystem which provides dynamic stability and consists of the muscles surrounding the spinal column, and (iii) the neural feedback control which evaluates the requirements for stability and coordinates the muscle's response accordingly. Under normal conditions, these three subsystems work in harmony providing the necessary mechanical stability in response to instantaneously varying demands due to changes in spinal posture as well as static and dynamic loads. A disruption in any of these three subsystems due to trauma, degradation and/or disease can lead to spinal instability which overtime is likely to cause chronic dysfunction and pain [45, 46]. This section focuses on the disruption of the passive stabilization of the spine via diseases, particularly osteoporosis and cancer, which disrupt the mechanical integrity of the vertebrae leading to vertebral compression fractures at the site of the weakened vertebrae.

1.4.1 Osteoporosis

Osteoporosis is increasingly becoming a major public health problem due to its impact on morbidity and social cost. The morbidity associated with osteoporosis arises principally from fractures. In the United States, the burden of osteoporosis for the year 2005 was estimated to be >2 million incident fractures resulting in a direct cost of $17 billion [1-4]. Osteoporosis is a skeletal disease which systematically weakens the bone via reducing the bone mass and deteriorating the bone tissue microarchitecture consequently increasing bone fragility and susceptibility to fracture [47]. Peak bone mass results from linear growth, which is generally completed at around 30 years of age. An equilibrium period is then followed where bone mass is maintained for a duration of 5 to 15 years, after which it starts to gradually decrease regardless of gender. However, peak bone mass is lower for women and the rate at which bone loss occurs is higher for a period after menopause due to increased osteoclast activity and turnover rates which are mainly caused by estrogen deficiency (Figure 1.5) [48, 49]. Thus, osteoporosis is more common in women with a lifetime fracture risk of up to

40% [50], however this also implicates a significant problem for men with a lifetime fracture risk of up to 25% [51, 52].

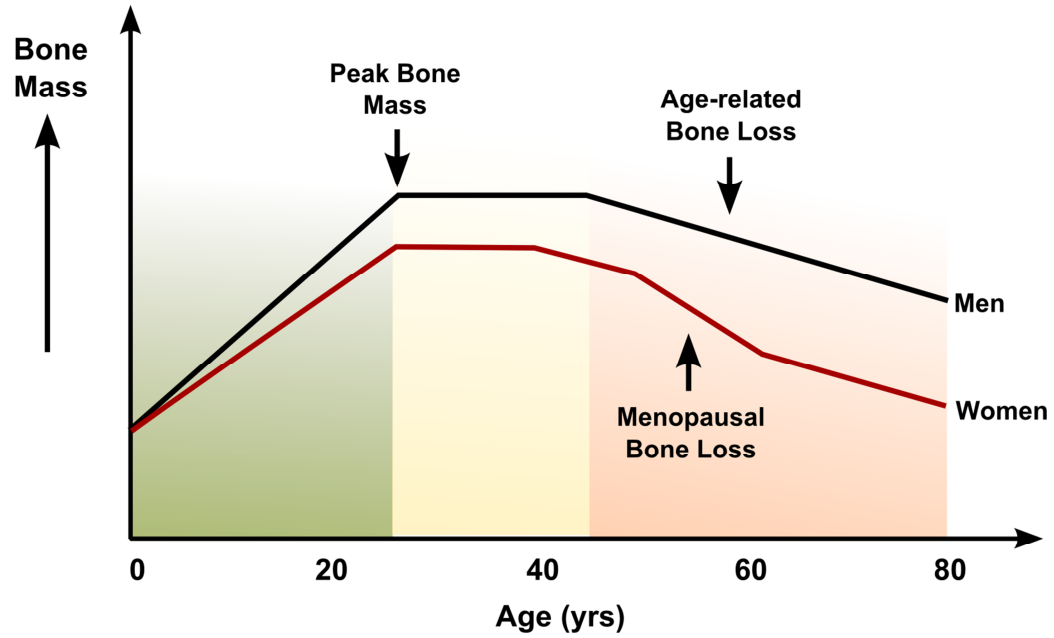

Figure 1. 5 Changes in bone mass throughout aging for both men (black) and women (red). Three distinct trends can be observed: 1) linear growth till the age of about 30 years (green), 2) maintenance of bone mass for about 10 years (yellow), and 3) gradual decrease in bone mass with age (pink). Adapted from [48].

Osteoporotic bone loss occurs due to an imbalance in the remodeling process which increases the osteoclast resorption activity, and inhibits sufficient formation of replacement bone tissue by osteoblasts. The central skeleton is mostly affected due to its higher remodeling activity compared to the peripheral skeleton, thus increasing fracture risk particularly in the vertebrae [53]. There are three mechanisms of remodeling that can influence net bone loss or gain. The first is metabolic remodeling which occurs continuously whereby old bone tissue is replaced by new bone tissue. The second is adaptive remodeling which occurs as a result of the mechanical loading conditions applied to the bone. This mechanism causes bone mass to increase in areas which are subject to high mechanical loads and decrease in unloaded or redundant areas. The third mechanism is microdamage remodeling which occurs preferentially in areas of high microdamage where osteoclasts are activated causing the resorption of damaged bone tissue which eventually gets replaced by new bone tissue [54-59]. It is

hypothesized that metabolic remodeling is the main cause for the deterioration of the bone tissue microarchitecture in age-related osteoporosis, however this bone loss is also modulated by adaptive and microdamage remodeling (Figure 1.6) [48, 60].

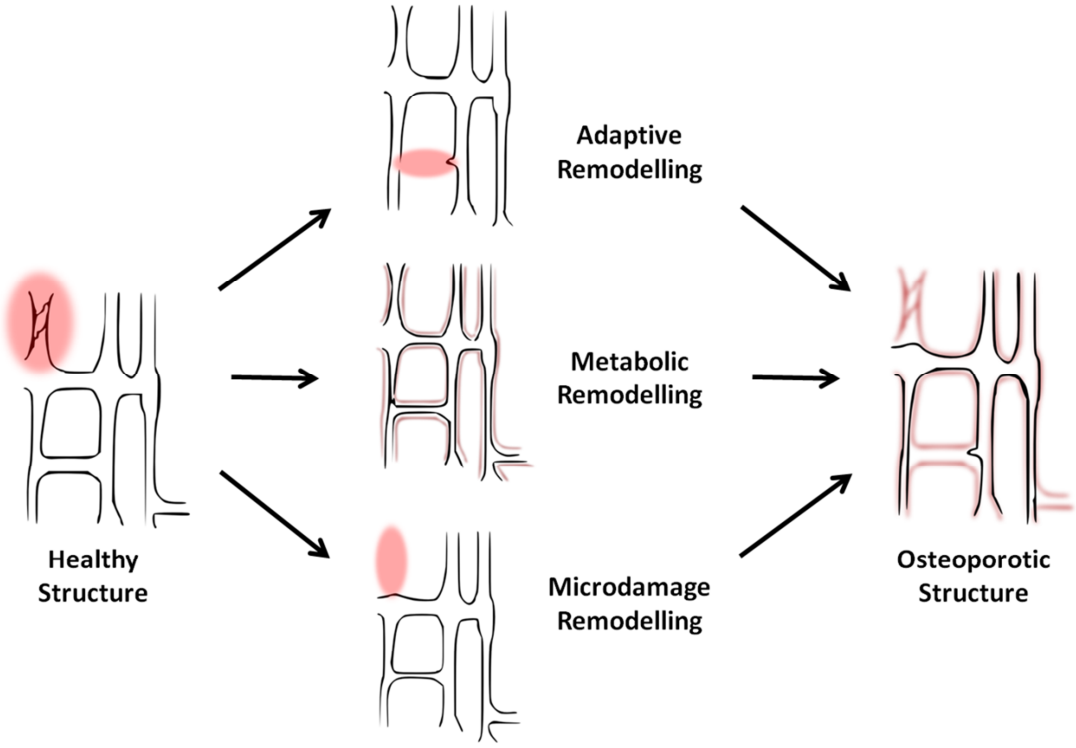

Figure 1. 6 Hypothesized remodeling for osteoporotic bone loss showing a healthy structure (left) with a microfracture which undergoes 1) preferential resorption of unloaded and maintenance of loaded trabeculae (adaptive remodeling), 2) uniform thinning and perforation of trabeculae (metabolic remodeling) and 3) preferential remodeling of damaged trabeculae (microdamage remodeling). This results in an osteoporotic structure (right) with vertical trabeculae maintaining thickness, horizontal trabeculae preferentially being resorbed and microdamged trabeculae undergoing remodeling. Adapted from [48].

The highest risk of fracture is at skeletal sites where cancellous bone is predominant, particularly the head of the femur and the vertebra. Low bone mass is not the only factor that increases bone susceptibility to fractures. Bone mass in this context refers to the amount of bone tissue as the total of protein and mineral in the whole skeleton or in a specific segment of bone. There are other aspects of bone quality such as microarchitecture, tissue properties and levels of microdamage which also contribute to the risk of fractures [61, 62]. However, the current standard diagnostic tool for predicting fracture risk focuses on the measurement of areal bone mineral density (BMD) which only provides information on the amount of bone

mineral per area [63, 64]. The most widely used BMD measurement technique is based on X-ray absorptiometry, particularly dual-energy X-ray absorptiometry (DXA), although other techniques are also available including quantitative ultrasound (QUS), quantitative computed tomography (QCT) and other radiographic techniques [65-68]. BMD values are typically expressed with respect to a reference population in standard deviation (SD) units. The diagnostic criteria for osteoporosis, as suggested by the World Health Organization (WHO), is a BMD value more than 2.5 SD below the young adult mean [1, 69]. As BMD measurements only reflect one aspect of bone quality, the quantity of bone mineral, novel imaging modalities and biomarkers, which are capable of assessing various components of bone quality, have the potential to improve the diagnosis of osteoporosis, the prediction of fractures as well as the monitoring of treatment response. A study by Wehrli et al. [70] showed that magnetic resonance imaging (MRI) of the calcaneus had superior diagnostic accuracy for discriminating vertebral fracture patients from control subjects compared to vertebral BMD measurements. In terms of biomarkers, Gamero [71] showed that currently available biochemical indices, particularly those of bone resorption, can predict fracture risk independently of BMD.

1.4.2 Spine Tumors

Primary spine tumors do not frequently occur (roughly 6 per 100,000 per year) [72], however the thoracolumbar spine is the most common site for bone metastasis which is a frequent complication of cancer occurring in up to 70% of terminal cancer patients [73]. These secondary or metastatic spine tumors originate from a wide range of tumor types including prostate (90%), breast (75%), lung (45%), and renal (30%) cancer [74]. Furthermore, multiple myeloma (MM) is a plasma cell neoplasm that also frequently involves the spine. In the United States alone, MM represents 10% of all hematological malignancies with an annual incidence of 16,000 mainly in patients who are older than 60 years of age [75]. The consequences of spinal metastasis and MM are often devastating causing severe pain, pathologic fractures due to poor bone quality as well as spinal cord compression and other neurological syndromes [76-78]. Furthermore, the prevalence of spinal metastases and MM is likely to increase due to

improved cancer treatments and prolonged survival rates [79]. Many factors account for the frequency of metastatic spine tumors and MM, however blood flow is the most common means of malignant tumor spread to the spine. This is in part related to the paravertebral venous plexus system (refer to section 1.3) which communicates with multiple other venous systems including the vena cava, azygous, intercostals, pulmonary and renal. As the blood flow changes direction depending on intrathoracic and intraabdominal pressures, tumors get deposited in the spine from multiple sites of the major body cavities [79, 80]. Spine metastases are generally classified according to their anatomical location. Tomita et al. [81] devised a classification system which grouped tumors into three categories and subdivided them into seven types. The three categories are based on whether the tumors are (i) contained within the vertebral bones (Intra-compartmental), (ii) extending into the paravertebral region and/or the epidural space (Extra-compartmental), and (iii) involving multiple vertebrae (Figure 1.7).

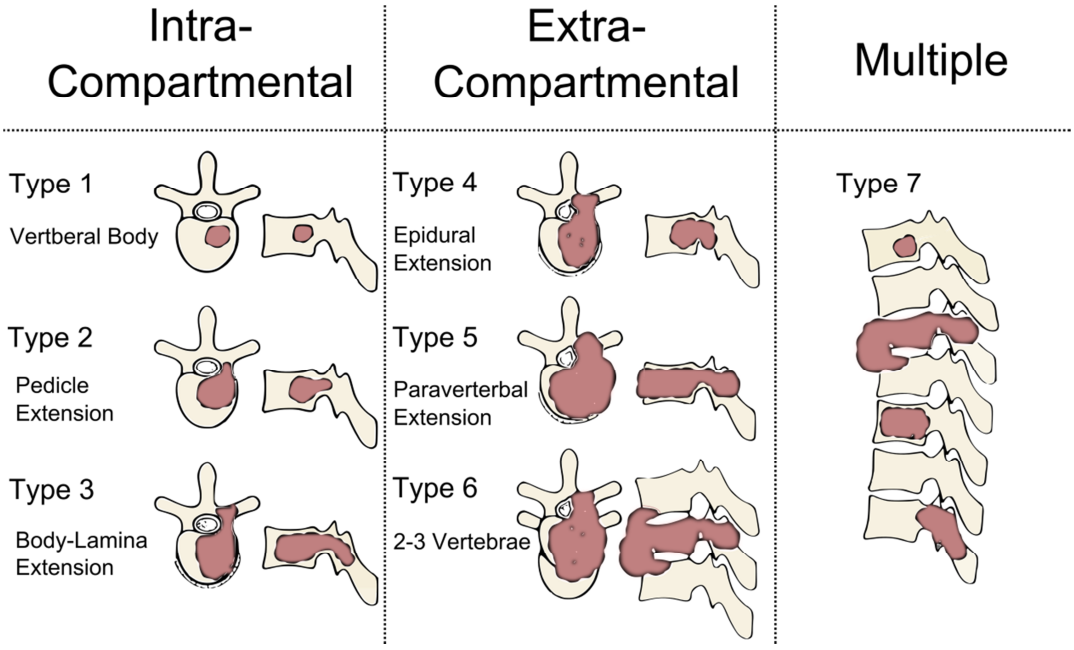

Figure 1. 7 Schematic showing the surgical classification of spine tumors. Adapted from [81].

Spine metastases can be either osteoblastic causing abnormal bone formation, osteolytic causing bone destruction, or a mix of both [82]. Osteoblastic lesions are generally observed in patients with metastatic prostate carcinoma. The mechanism of osteoblastic lesions and the factors involved are not well understood, however the

levels of Endothelin-1, which stimulates the formation of bone and the proliferation of osteoblasts in bone organ cultures, have been shown to increase in patients with osteoblastic metastasis from prostate cancer [83]. In osteolytic lesions, bone destruction is primarily mediated by osteoclasts rather than the tumor cells. Osteoclast stimulating factors, which vary depending on the tumor, play a significant role in the process of bone resoprtion [84, 85]. Most osteolytic lesions have been observed in patients with multiple myeloma and metastatic renal cell carcinoma. However, only in myeloma do pure lytic bone lesions occur due to the increase in bone resorption as well as the suppression of bone formation. Also, the osteoclasts in multiple myeloma accumulate at surfaces adjacent to the myeloma cells thus causing pure lytic lesions only in areas with tumor involvement (Figure 1.8) [86, 87]. A mixture of osteoblastic and osteolytic lesions are mainly observed in patients with metastatic breast carcinomas, although the lesions are predominantly osteolytic [78].

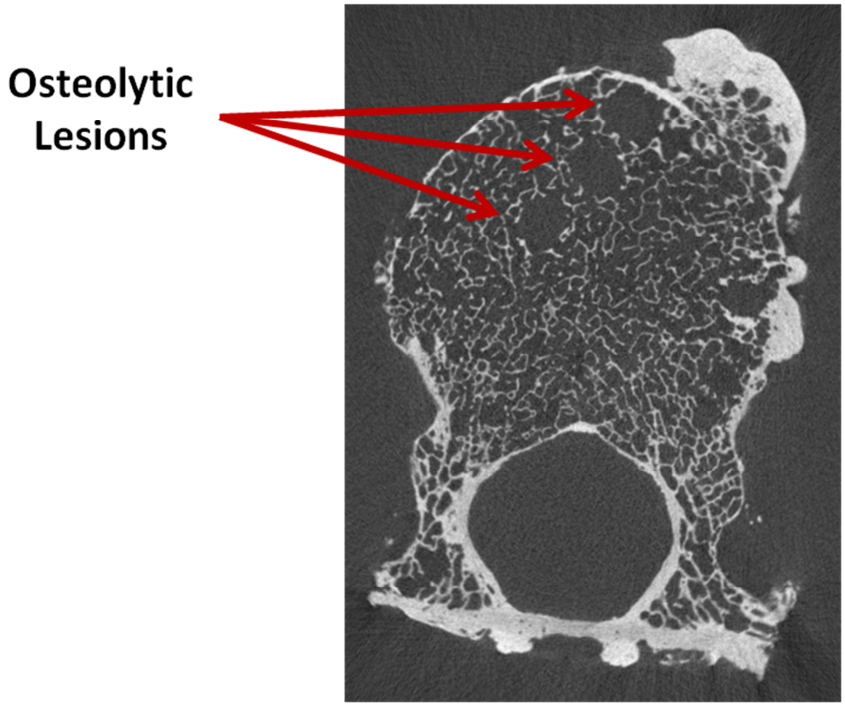

Figure 1. 8 In-house microCT scan showing lytic lesions in a human thoracic vertebra (T6) from a donor whose cause of death was multiple myeloma.

The biomechanical effect of spine tumors and the mechanisms of neoplastic vertebral fractures remain controversial; however, mechanical pain causes significant morbidity in this patient population. Tumor involvement of the cancellous bone within the vertebral body may not result in spinal instability, especially when the cortical wall is intact. Pathological compression fractures are more likely to occur when the tumor involves the posterior half of the vertebral body (the middle column) as extrusion of tumor, bone, or disc into the spinal canal may result in neurological compromise. There are no standardized methods for predicting the risk of pathological fractures even if the lesions have been well characterized by various imaging modalities such as CT scans and MRI. Some fractures can be prevented via radiotherapy which inhibits the growth of radiosensitive tumors and stops lytic destruction of the vertebra. If the tumors reach a critical size, fractures can only be prevented via prophylactic surgical stabilization such as vertebroplasty which reinforces and stabilizes the weakened vertebra. These surgical techniques also alleviate mechanical pain which is the presenting complaint in the majority of patients with spinal metastasis and multiple myeloma, thus improving the quality of life in these patients who often have limited life expectancy [88-91].

1.4.3 Vertebral Fractures

In the United States, of the 1.5 million fractures that occur annually due to osteoporosis, almost half (700,000) are attributed to vertebral fractures (VF) [5]. For the European Union countries, a prospective osteoporosis study showed that the annual incidence of VF was approximately 440,000 [6]. VF represent a catastrophic structural failure of bone which is initiated at the material level. The ability of any structure to carry load depends on the amount and distribution of matter which makes up the structure, the intrinsic properties of the matter itself, and the loading conditions applied. The key factors that influence the ability of bone to resist fracture include: (i) the overall composition of the bone tissue (mineral, collagen, water and matrix proteins), (ii) the physical and biochemical characteristics of these components, (iii) the bone morphology which includes the bone size, cortical cross-sectional geometry, porosity, as well as trabecular microarchitecture, and (iv) the amount of pre-existing

microdamage [61]. The loading conditions applied on the spine arise from daily living activities as well as trauma such as falls or motor vehicle accidents. The applied compressive forces are transferred from the intervertebral discs to the vertebral endplates then distributed over the trabecular microarchitecture. Osteoporosis and spine tumors compromise the structural integrity of the vertebra, thus increasing its fragility and susceptibility to fracture [61, 92, 93].

Osteoporotic vertebral compression fractures which result from structural failure can be classified into three groups: (i) wedge fractures which involve anterior collapse while the posterior height remains relatively the same, (ii) biconcave fractures which involve central compression and fracture of the endplate regions with relative maintenance of anterior and posterior heights, and (iii) crush fractures which involve compression of the vertebral body resulting in posterior collapse while the anterior height remains relatively unchanged (Figure 1.9). Different loading patterns, which are influenced by the local biomechanics of the spine level, can cause different deformities although most fractures have characteristics of more than one deformity. Wedge deformities are most frequent in the mid-thoracic region and occur due to loading in flexion. However, biconcave deformities more frequently occur in the lumbar spine due to the more posterior position of the center of gravity in this region [94, 95]. Genant et al. [96] devised a semi-quantitative method for assessing vertebral fractures. This method provides insight on the severity of the fracture regardless of the type of deformity present (wedge, biconcave or crush fractures). A vertebra receives a severity grade based upon the visual estimation of apparent vertebral height reduction and morphological change (Figure 1.9). Thoracolumbar vertebrae from T4 to L4 are graded as normal (grade 0), mildly deformed (grade 1: reduction of 20-25% in height and 10–20% in projected vertebral area), moderately deformed (grade 2: reduction of 25–40% in height and 20–40% in projected vertebral area), and severely deformed (grade 3: reduction of >40% in height and projected vertebral area). Furthermore, visual inspection of the endplate deformities, the lack of parallelism of the endplates and the general altered appearance compared with adjacent vertebrae provide a strong qualitative aspect to the assessment. The reproducibility of this semi-quantitative method for the diagnosis of prevalent and incident vertebral fractures is high, with

intra- and inter-observer agreement of 90-99%. The limitation of this method, which may also apply to other standardized visual approaches, is that the experience of the examiner has great influence on the ability to distinguish between normal variations and degenerative changes due to true fractures. In normal patients, the vertebrae in the mid thoracic spine (especially in women) and thoracolumbar junction (especially in men) are slightly more wedged than in other regions. Also, some degree of biconcavity is observed in the mid to lower lumbar spine. Based on the experience of the examiner, these normal variations in vertebral morphology can be misinterpreted as mild vertebral deformities [95-98].

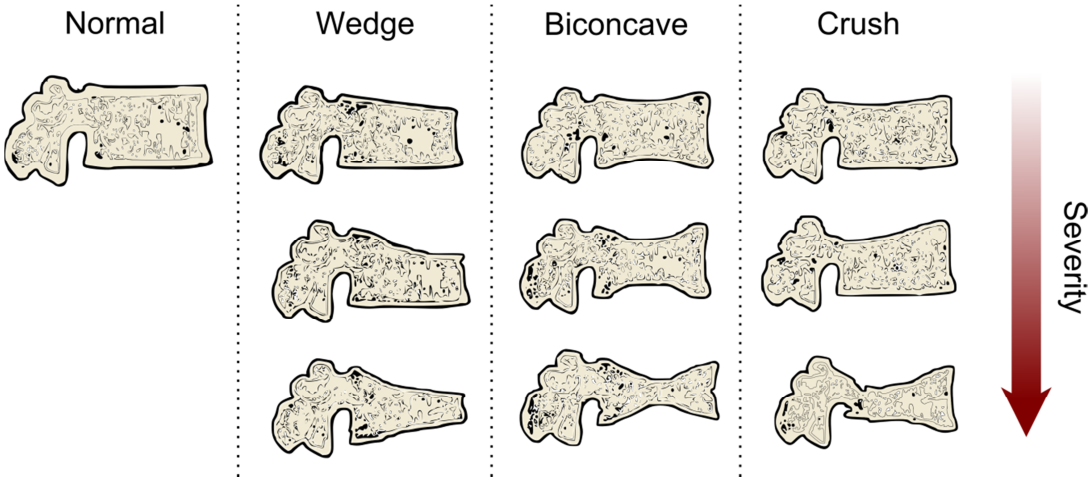

Figure 1. 9 Schematic showing various types vertebral fractures: wedge, biconcave and crush. The severity of the fracture increases from top to bottom and can be graded as normal (grade 0), mildly deformed (grade 1), moderately deformed (grade 2), and severely deformed (grade 3). Adapted from [96].

1.5 TREATMENT

Vertebral augmentation procedures are primarily used for the treatment of chronic pain resulting from vertebral fractures (VF) which are caused by osteoporosis and other skeletal pathology such as spinal metastasis or multiple myeloma. Patients typically present with axial back pain at the site of the fractured vertebra. This pain is exacerbated with weight-bearing and simple daily living activities such as rising from a chair or getting out of bed. In a physical assessment, palpation over the spinous process of the affected vertebra can reproduce the patient's pain. As augmentation procedures are only useful for treating pain related to fractures, it is essential to identify that the pain is due to the fracture itself and no other abnormalities such as spondylosis, disk disease or nerve compression. Clinical features which indicate symptomatic canal stenosis or nerve root compression are relative contraindications to these procedures as pressurization during the augmentation increases the risk of exacerbating the nerve compression. Furthermore, extreme vertebral collapse with a height loss greater than 70% is another contraindication as displaced fracture fragments can also compress the spinal cord or nerve roots. In some instances, augmentation procedures are the treatment of choice due to the patient's poor bone quality, which precludes successful implantation of screw-rod constructs and cages used for complex reconstruction [99-101]. This section focuses on two vertebral augmentation procedures: percutaneous vertebroplasty (PVP) and kyphoplasty (PKP).

1.5.1 Percutaneous Vertebroplasty

Percutaneous vertebroplasty (PVP) is a minimally invasive surgery performed under fluoroscopic image-guidance in which bone cement is injected into a fractured vertebra with the goal of relieving pain and restoring mechanical stability [7, 8]. Single-plane or biplane fluoroscopy is required for needle placement as well as direct visualization of the cement flow during injection. The cement injection is generally performed via a posterior approach through the pedicles into the vertebral body (VB) (Figure 1.10).

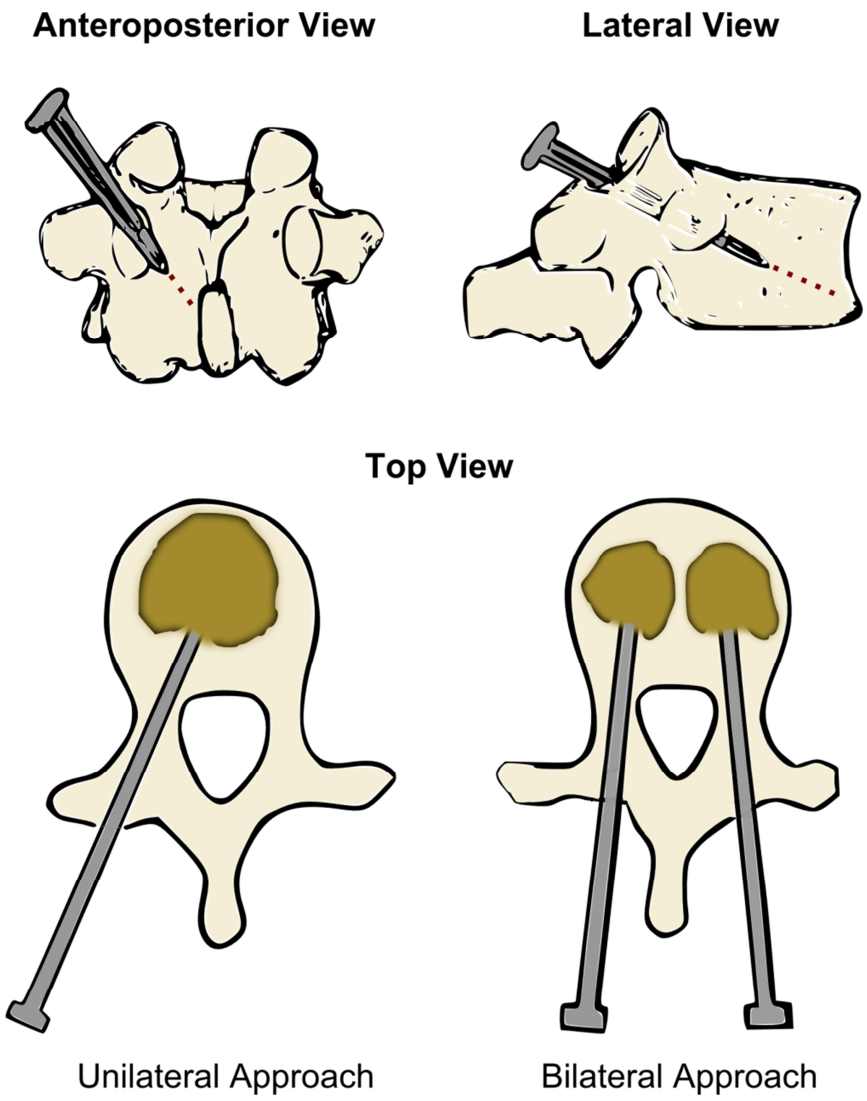

Figure 1. 10 Schematic of a PVP procedure. Anteroposterior and lateral views of a bone biopsy needle being inserted through the pedicles (top). Comparison of unilateral and bilateral transpedicular vertebral cement filling along the transverse plane (bottom). Adapted from [90] (top) and [13] (bottom).

The target site for cement deposition is the anterior third and center of the VB in the weight-bearing portion. Care must be taken in positioning the needle tip at the target site while minimizing complication risks by avoiding critical structures such as traversing nerve roots and local blood vessels. Unilateral transpedicular approaches are most commonly used in the mid to lower lumbar spine where the pedicles are large and oriented obliquely which often allows placement of the needle tip at the target site. In the thoracic and upper lumbar spine, the pedicles are smaller and oriented in a near

sagittal plane, thus midline positioning of the needle tip may be difficult from a unilateral transpedicular approach while using conventional straight needles. In these scenarios, a bilateral transpedicular approach or sometimes even an extra-pedicular approach may be required for optimum augmentation. Transpedicular needle placement is performed with the patient lying prone. The needle entry site is localized over the pedicle by positioning the fluoroscope obliquely to allow anteroposterior (AP) visualization along the pedicle. The needle is then advanced slowly until it breaches the cortex of the pedicle and remains relatively fixed. Subsequently, the fluoroscope is rotated to the orthogonal position allowing lateral visualization of the needle to ensure the plane of entry is parallel to the pedicle and the needle trajectory will not perforate the pedicle, especially medially into the spinal canal (Figure 1.11) [99].

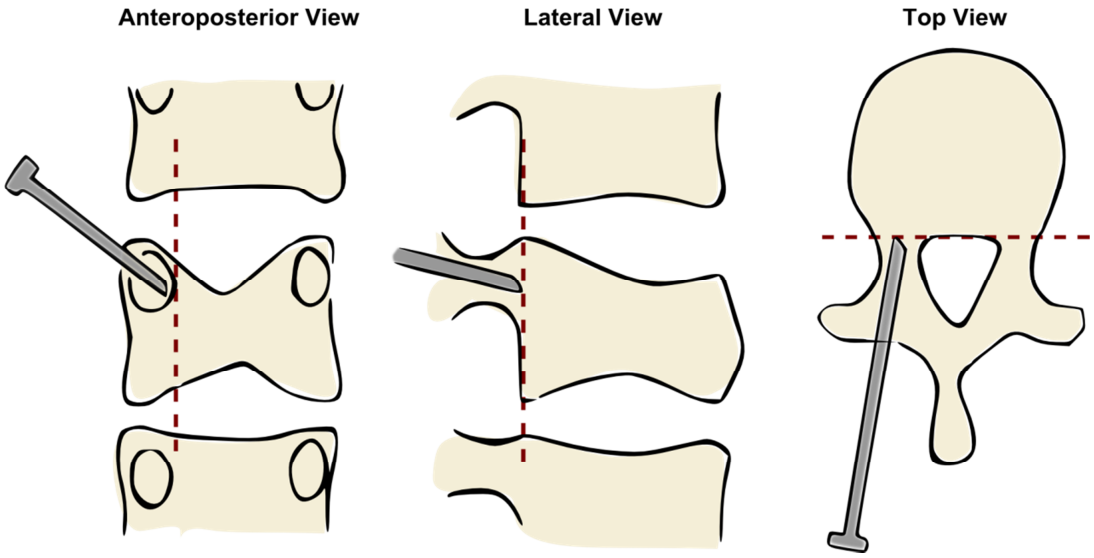

Figure 1. 11 Schematic showing that the needle tip should not cross the medial border of the pedicle on the AP view before it reached the posterior cortex of the VB on the lateral view. Adapted from [13].

The vertebral level being treated dictates the choice of needle being used. Typically 13-gauge needles are used in the upper thoracic spine, whereas 11-gauge needles are used in the lower thoracic and lumbar spine. Furthermore, some needles have a diamond tip which facilitates perforation of the cortex; while, others have a bevel tip which may assist in needle tip steering and redirection. The bone cement

most widely used in PVP is poly(methyl methacrylate) (PMMA). Many commercial PMMA cements are available on the market, however the ones typically used in PVP contain radio-opacifiers such as barium sulfate to allow visualization of the cement mixture under fluoroscopy. This is essential to ensure that the PMMA fills the VB and does not leak into the surrounding vasculature, through the endplates into the disks, or into the posterior aspect of the VB near the spinal canal. The injection is typically performed under lateral visualization however intermittent AP projections are performed to ensure the PMMA does not leak lateral of the VB. The injection is terminated if the cement leaks from the VB, the cement extends into the posterior third of the VB in the direction of the basivertebral vein, the filling is considered adequate, or the mixture becomes too viscous to inject [99].

1.5.2 Percutaneous Kyphoplasty

Percutaneous kyphoplasty (PKP) is an extension of PVP that uses an inflatable bone tamp (IBT) to create a cavity within the VB into which the bone cement is injected (Figure 1.12). Needles are inserted through the pedicles similar to PVP, however the target site for the needle tip is within the posterior third of the VB. Once the needle placement is achieved, the uninflated IBT is inserted through the access needle under intermittent fluoroscopy. The needle can then be retracted to its ready for injection position at the base of the pedicle. Fluoroscopy visualization along the AP and lateral directions is perfomed to help position the IBT within the vertebral body at least 1-2 mm beyond the tip of the access needle. The IBT is a high-pressure balloon which upon inflation aims to restore the VB height by creating a cavity into which the PMMA is injected. Balloon inflation is performed under lateral fluoroscopy and is stopped if the fracture is reduced, the balloon comes into close contact with any cortical surface, or the maximum inflation pressure is attained. IBT’s are typically selected based on the AP diameter of the VB. They are available in various sizes with a maximum volume of 6 ml [90, 99].

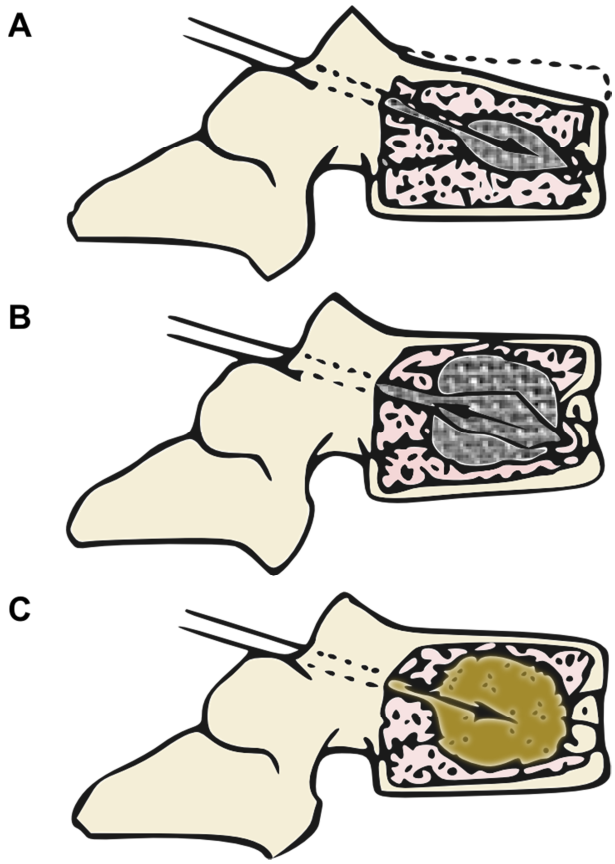

Figure 1. 12 Schematic of a PKP procedure using a transpedicular approach. The inflatable bone tamp is inserted through the access needle (A) then inflated creating a cavity (B) into which the PMMA cement is injected (C). Adapted from [101].

1.5.3 Safety and Efficacy

PVP first became popular in the early 1980s when Galibert et al. injected PMMA bone cement into a partially destroyed cervical vertebra (C2) and successfully relieved the patient's long-term pain [102, 103]. This initiated the use of PVP for the treatment of chronic pain resulting from VF. Subsequent adaptations of the procedure, expansion of indications, and development of novel injectable biomaterials have led to an increase in the number of vertebral augmentations performed. For instance, the number of PVP performed in the United States has increased by 72.4% between 2001 and 2010 [9-12]. Although the number of procedures is on the rise, several hurdles are currently preventing PVP and PKP from becoming the standard of care for the treatment of chronic pain related to VF. The Food and Drug Administration (FDA) has issued a warning about possible complications following the injection of PMMA into

a fractured vertebra [13]. The primary concern of the FDA was cement leakage into the surrounding structures which may cause clinical complications such as nerve root or spinal cord compression as well as pulmonary embolism. These complications may lead to paraplegia or, in severe cases, death [14-19].

The incidence of cement leakage is high, particularly in PVP. It has been reported to occur in 30% [104] to 65% [105, 106] of patients with osteoporotic-induced VF, and in 38% [107] to 72.5% [108] of patients with malignant-induced VF. Although cement leakage is tolerated in the majority of patients, it is the root cause for clinical complications. The cement may leak into various anatomical structures including the needle track, the paravertebral soft tissue (52.5% [108]), the surrounding vasculature (5% [108] to 16.5% [109]), the spinal canal (37.5% [108]) and the intervertebral discs (25% [110]). Leakage into the paravertebral soft tissue is generally asymptomatic with the exception of two studies which have reported clinical complications [108, 109]. This type of leakage usually occurs due to anterior cortical breach, either pre-existing or resulting from wrong needle placement (Figure 1.13).

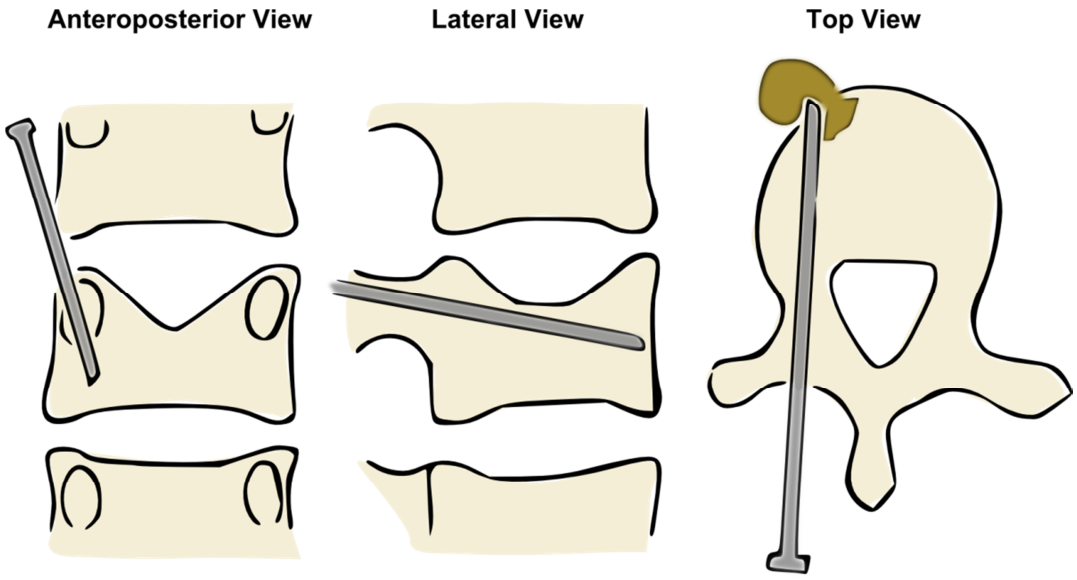

Figure 1. 13 Schematic showing an example of a wrong needle placement. Although the needle tip appears to be within the VB on both the AP and lateral views, it is actually partly in the prevertebral space due to the round shape of the vertebral body. Adapted from [13].

Leakage into the surrounding vasculature may cause pulmonary embolisms especially when venous migration of cement is not recognized early in the procedure [16, 19, 111]. Leakage into the spinal canal and the foramen may also cause serious complications such as spinal cord and nerve root compression. However, leakage into the spinal canal may be more tolerated, especially in cases where there is enough residual space for the thecal sac. Cotton et al. [108] reported no complications following spinal canal leakage in all 15 patients while 2 out of 8 patients with foraminal cement leakage presented with nerve root compression which required surgery 1 month later. Although this type of leakage is most frequent when a breach in the posterior cortex of the VB is present, leakage may also be due to medial or inferior perforation of the pedicles during needle placement (Figure 1.14). Leakage into the intervertabral discs is generally asymptomatic, however long-term mechanical consequences on adjacent vertebrae (i.e. adjacent fractures) may occur. This type of leakages is most frequent in severe VF where the cement has a tendency to leak through cortical osteolysis or fractures in the endplates [112, 113].

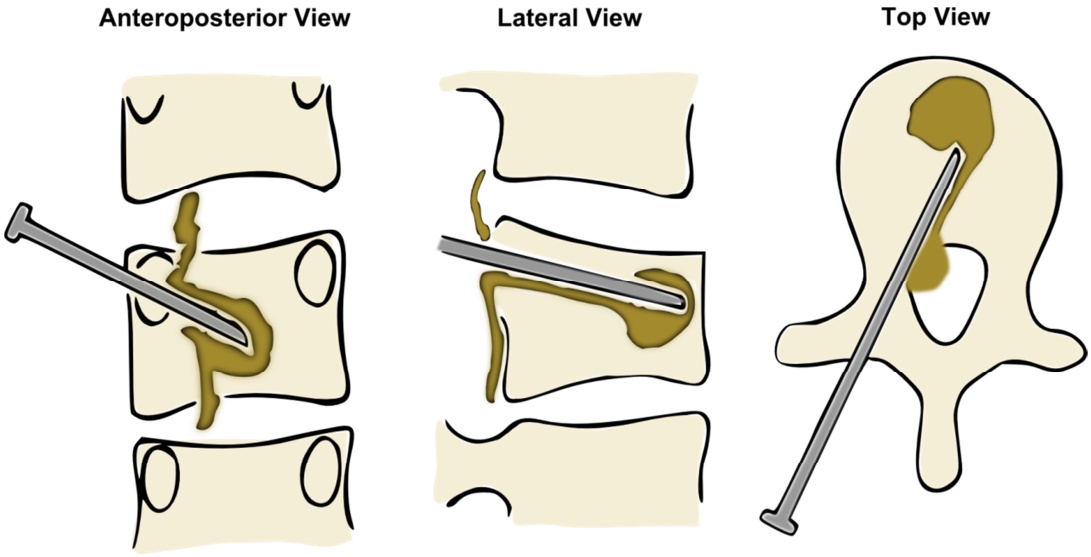

Figure 1. 14 Schematic showing an example of a breach in the medial cortex of the pedicle during needle placement creating a risk of cement leakage into the spinal canal. Adapted from [13].

There has been many studies in the literature that point to the suitability of PVP in reducing both short and long term pain in patients with osteoporotic vertebral

compression fractures [114-118]. However, two recent studies [119, 120] have caused controversy over the efficacy of PVP. These studies performed a multicenter clinical trial to determine the short-term efficacy of PVP for improving pain and pain-related disability in patients with osteoporotic VF up to a year old. Patients were randomly assigned to undergo PVP or a sham procedure without cement injection (control group). Kallmes et al. [120] and Buchbinder et al. [119] found no significant benefit of PVP over a sham procedure during their 1 month and 6 months follow-up, respectively. However, both studies were criticized mainly about their patient selection and other methodological issues which hampered their clinical interpretation [121]. In a more recent study, Klazen et al. [122] aimed to clarify whether PVP has additional value compared to conservative treatment in patients with acute VF and persistent pain. Their results showed immediate pain relief after PVP which was sustained for a least a year and was significantly greater than that achieved with conservative treatment.

Although augmentation procedures have been limited largely for treating osteoporotic-induced VF, they are increasingly being used to treat malignant induced VF. Fourney et al. [90] devised a treatment algorithm for painful thoracolumbar VF in cancer patients (Figure 1.15). PVP and PKP procedures were considered when disabling pain was present and conservative therapy which consisted of analgesic medication, bed rest, and in some cases external bracing had failed. Contraindications for both procedures include epidural compression, failure to localize symptomatic level(s), pain that was predominantly radicular in nature and local infection at the planned injection site. The choice for performing PVP or PKP at a given symptomatic level depended on several factors. PKP was favoured in the presence of i) kyphosis (>20º) which was deemed to be a significant contributor to morbidity, ii) destruction of the posterior vertebral cortex, and iii) significant vertebral collapse where height restoration was desired. On the other hand, PVP was the procedure of choice when the vertebral collapse did not permit insertion of the inflatable bone tamps and the patients could not tolerate general anesthesia or the relatively longer procedure time required for PKP.

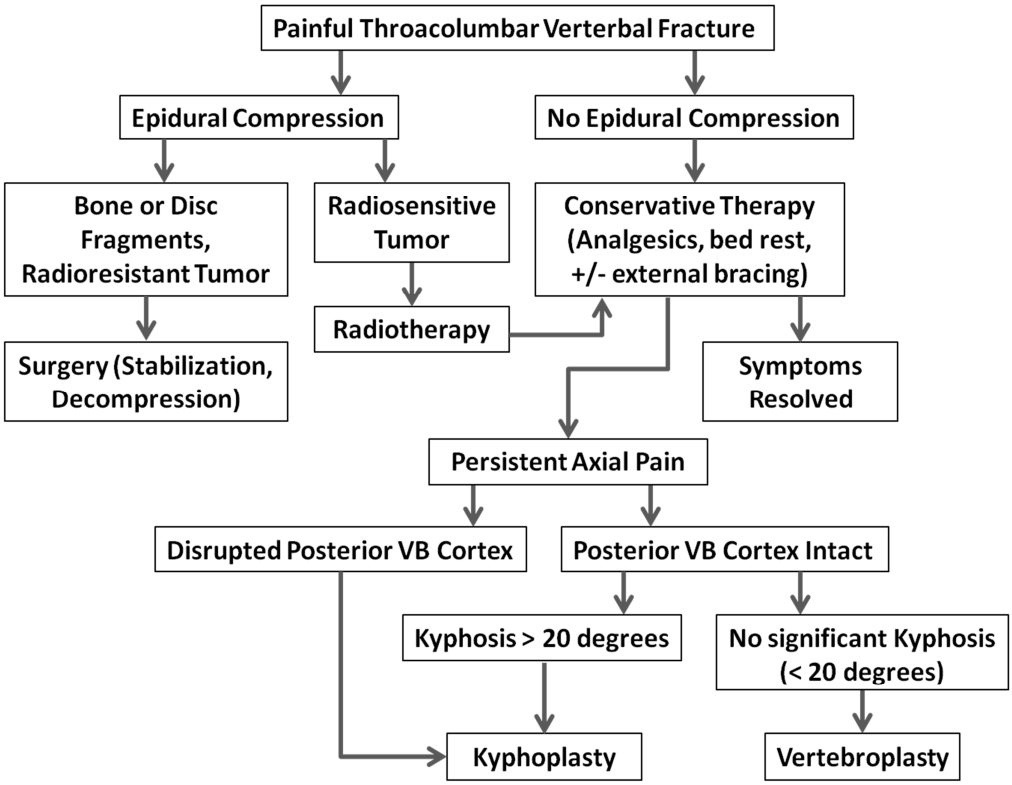

Figure 1. 15 Flow chart showing the treatment algorithm for painful thoracolumbar vertebral fractures in cancer patients. Adapted from [90].

Several prospective studies have reported on the safety and efficacy of PVP [108, 123-126] and PKP [127-132] for the treatment of malignant-induced VF (Table 1.4). In the five PVP studies, 96 patients were treated for VF due to spinal metastases (76%) and multiple myeloma (24%). PKP was used in six studies to treat 204 patients with VF due to spinal metastases (45%) and multiple myeloma (55%). In terms of safety, cement leakage using PVP was almost five times higher compared to PKP and caused neurological complications in four patients (4.1%). The symptoms of one patient resolved in a couple of days, however the remaining three patients required surgical decompression [108, 124]. In all the studies which included 300 patients, only one experienced an adverse medical condition. Khanna et al [129] reported one myocardial infarction which occurred in the post-anaesthesia care unit following PKP. Furthermore, adjacent fractures were only reported following PKP and occurred in 6 of the 204 patients with 3 of the patients requiring subsequent PKP stabilization [131, 132]. In terms of efficacy, all studies reported significant improvement in pain which

was assessed via various methods including the Visual Analog Scale [123, 126, 128, 131], the Verbal Rating Scale [124], the McGill and Melzack classification [108], the Site Specific Pain Score [125], and the Short-Form 36 Bodily Pain sub-score [127, 129]. All studies also reported successful improvement in function which was assessed by various methods including the Eastern Cooperative Oncology Group Performance Scale [124, 126], the Townsend Functional Assessment Scale [7], the Oswestry Disability Index [11, 37, 40], and the Short Form 36 Physical Function [112, 123].

Table 1. 4 Summary of prospective studies using PVP and PKP in cancer patients.

Prospective Studies		Verterboplasty	Kyphoplasty
No. studies		5	6
No. patients		96	204
Tumor Types	Metastases	73 (76%)	91 (44.6%)
	Multiple Myeloma	23 (24%)	113 (55.4%)
Leakage	Total per level	59/101 (58.4%)	12/239 (12.1%)
	Symptomatic Patients	3 (3.1%)	0
Complications	Medical	0	1 (0.5%)
	Neurological	4 (4.1%)	0
	Corrective Surgery	3 (3.1%)	0
Adjacent Fracture	Total Adjacent Fractures	0	6 (2.9%)
	Corrective Surgery	0	3 (1.5%)

Some correction in sagittal alignment was reported following PKP, however only two studies by Pflugmacher et al. [131, 132] included reliable long-term data. In the first study [131], 20 patients were treated for VF due to multiple myeloma. Post-operative improvement in vertebral height by a mean of 4.3 mm ($P < 0.05$) was observed in 64.5% of fractures, whereas kyphotic deformity correction by a mean of 6.3° ($P <$

0.05) was observed in 78.5% of patients. This statistical significance in height improvement and kyphotic correction was lost at the 1-year follow-up. In the second study [132], 41 of the 65 patients treated for VF caused by metastases were followed for two years. Although significant post-operative improvement in height and kyphotic deformity was observed, both improvements returned to preoperative levels at the 2-year follow-up.

1.6 Fluid Flow in Cancellous Bone

During vertebral augmentation procedures, bone cement is injected through a cannula into the cancellous bone of the vertebral body. The cements used, such as PMMA, are chemically complex, multi-component and significantly non-Newtonian with their viscosity having differing degrees of time and shear-rate dependency. These cements also interact with other fluids present within the porous media and with the porous structures through which they flow [133]. When two or more fluids are present within a porous media, the displacement of these fluids can be characterized as miscible or immiscible. Miscible flow occurs when the fluids are completely soluble in one another with no distinct fluid-fluid interface due to a zero surface tension between the fluids, where surface tension is a measure of the force or energy required to deform the fluid-fluid interface per area. However, immiscible flow is the simultaneous displacement of the fluids or phases in the porous media due to the nonzero surface tension between the fluids, resulting in a distinct fluid-fluid interface which separates the fluids within each pore. In vertebral augmentation, the biomaterial used (PMMA cement) is generally assumed insoluble in any biofluid (bone marrow) it comes into contact with, thus the cement-marrow displacement is characterized as a two-phase immiscible flow in porous media. A rationale for this assumption is that the PMMA cement is hydrophobic and does not dissolve into the red bone marrow which is hydrophilic [134, 135].

Vertebral cancellous bone has highly complex geometrical structures and displays architectural inhomogeneities over a range of length scales (refer to section 1.2). Thus, the pore-scale cement viscosity varies due to its non-linear dependency on

deformation rates which are affected by variations in the local tissue morphology. Small pores (< 0.8 mm) in the cancellous bone reduce the void volume available for cement flow, thus the cement's interstitial velocity increases in order to preserve the continuity with the entering superficial flow. This leads to an increase in the deformation rate, which causes a decrease in the viscosity as the cements are known to exhibit shear-thinning behaviour. Furthermore, the vertebral cancellous bone microarchitecture varies among the patients being treated, thus making the scientific understanding of the cement flow behaviour difficult in clinical or cadaveric studies. It is also extremely difficult to measure the patient's local tissue morphology due to x-ray dosage limitations and geometrical constraints, which inhibit the use of micro-computed tomography to scan patients prior to the treatment [136, 137].

1.7 RHEOLOGY

Most techniques that are used to measure the rheological properties of a fluid apply a kind of shear flow referred to as viscometric flow. Figure 1.16 represents a fluid confined between two plates of area A and separated by a distance D.

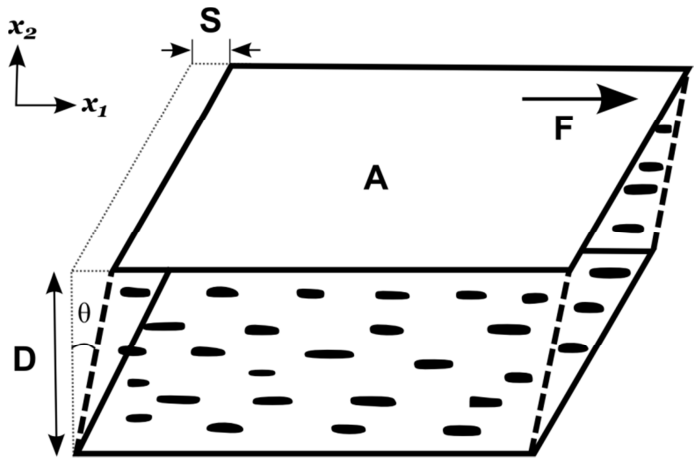

Figure 1. 16 Viscometric flow of a fluid confined between two plates. Adapted from [138].

In a viscometric flow, the fluid motion is along one coordinate direction (x_1) while the fluid velocity varies along the orthogonal direction (x_2). When the upper plate is

moved along the x_1 direction relative to the lower plate, the fluid is subjected to an amount of shear strain (γ) defined as:

$$\gamma = tan\,\theta = \frac{\text{Amount of shear displacement, S}}{\text{Distance between shearing surfaces, D}} \quad (1)$$

the rate of shear strain, also referred to as the shear rate, can be computed as:

$$\dot{\gamma} = \frac{\text{Relative velocity}}{\text{D}} \quad (2)$$

The constant force (F) required to move the top plate at a constant velocity with respect to the bottom plate is referred to as the shear force. Dividing the shear force (F) by the plate area (A) gives rise to the shear stress (τ) [138]. Under steady flow conditions, the viscosity (η) of a fluid may be defined as the ratio of the shear stress (τ) to the shear rate ($\dot{\gamma}$). Based on this relationship, the fluid can be classified as Newtonian or non-Newtonian. For Newtonian fluids, the shear stress is a linear function of the shear rate, thus the viscosity is a constant independent of the shear rate. Conversely, for non-Newtonian fluids, the shear stress is a non-linear function of the shear rate (Figure 1.17). The power law is commonly used in polymer engineering to describe the relationship between the shear stress and the shear rate for various types of fluid behaviour, although other mathematical relationships are available including Cross, Williamson and Sisko [139]. The power law states that shear stress is proportional to shear rate raised to the power n:

$$\tau = C\left(\dot{\gamma}\right)^n \quad (3)$$

where C and n are constants used to describe the fluid flow behaviour. C is referred to as the consistency index and n is referred to as the power index. Taking the logarithm of both sides of the equality results in the equation of a straight line on the log-log graph:

$$\log\tau = \log C + n\log\left(\dot{\gamma}\right) \quad (4)$$

where n is equal to the slope and C is equal to the intercept with the ordinate axis (shear stress) when log of the shear rate is zero. Since viscosity relates shear stress to shear rate, it can also be expressed as a power relationship by substituting equation (1) in the expression for viscosity in terms of the ratio of the shear stress to the shear rate:

$$\eta = \frac{\tau}{\dot{\gamma}} = \frac{C(\dot{\gamma})^n}{\dot{\gamma}} = C(\dot{\gamma})^{n-1} \qquad (5)$$

The power index (n) is a measure of the non-Newtonian behaviour of the fluid. Newtonian fluids have a power index (n) which equals to one. However, many fluids exhibit a form of non-Newtonian behaviour. Some fluids exhibit increasing viscosity with increasing shear rate, a behaviour known as shear-thickening or dilatant (n > 1). Other fluids exhibit decreasing viscosity with increasing shear rate, a behaviour known as shear-thinning or pseudoplastic (n < 1). A further type of fluid behaviour is that of Bingham plastic fluids which behave similar to Newtonian fluids, however a minimum shear stress, known as the yield stress, must be applied before the material will start to flow [140, 141]. This section focuses on the rheological properties of two fluids: bone cement and bone marrow.

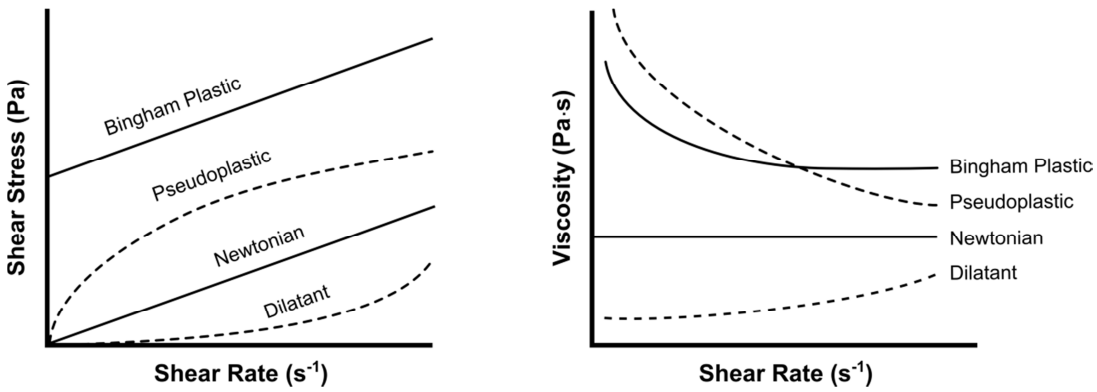

Figure 1. 17 Forms of viscous flow showing shear stress – shear rate relationship and viscosity – shear rate relationship between Newtonian (solid) and non-Newtonian fluids (dashed).

1.6.1 Bone Cement

Acrylic bone cements are most commonly used for vertebral augmentation, however other cements such as calcium phosphates, calcium sulphates and composite cements are currently in development. Acrylic cements are typically prepared directly before injection via mixing methyl methacrylate (MMA) liquid monomer with poly(methyl methacrylate) (PMMA) powder. An x-ray contrast agent, such as barium sulfate ($BaSO_4$), is generally added to the powder to increase the radiopacity of the cement [140, 142]. The PMMA cement is a self-curing polymer which polymerizes by a free radical exothermic reaction causing the cement to change over a short period of time (10-15 minutes) from a viscous liquid to an elastic solid. There are many factors that influence the curing process of PMMA bone cements, some of these include:

- Temperature [143, 144]
- Humidity [145]
- Sterilization [146]
- Handling [147-149]
- Mixing ratio and technique [141]
- Size of powder particles [150]

PMMA bone cements exhibit two flow characteristics: rheopectic (increasing viscosity with time) and pseudoplastic (decreasing viscosity with increasing shear rate). The ISO and ASTM standards state that the rheological properties of bone cements used as injectable biomaterials can be determined via the capillary extrusion method [140]. In this method, the test fluid (PMMA) is forced from a reservoir through a capillary under pressure from some kind of piston (Figure 1.18).

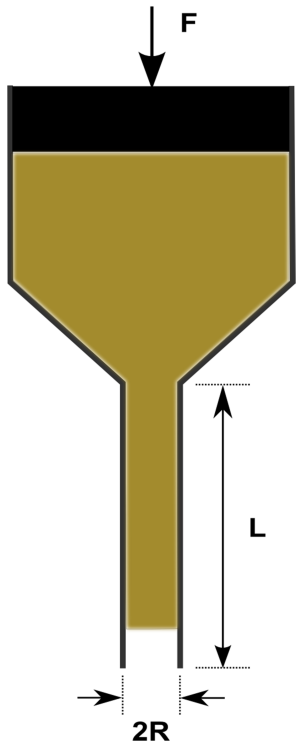

Figure 1. 18 Schematic of the capillary extrusion rheometer. Adapted from [142].

The basic requirements for the capillary extrusion method include a large narrow tube or capillary, means of determining the pressure drop along the capillary and means of measuring the volumetric flow rate (Q) through the capillary. Under steady state flow, isothermal conditions and assuming the PMMA to be incompressible, the viscous resistance to the motion in the capillary is equal to the force acting from the reservoir. Thus, the shear stress at the capillary wall can be calculated as:

$$\tau_w = \frac{R\Delta P}{2L} \tag{6}$$

where R is the radius of the capillary, ΔP is the pressure drop along the capillary, and L is the length of the capillary. For a Newtonian fluid the shear rate at the capillary wall is given as:

$$\dot{\gamma}_w = \frac{4Q}{\pi R^3} \tag{7}$$

For non-Newtonian fluids such as PMMA, correction factors must be applied to obtain the true shear stress and the true shear rate [142]. The Bagley correction (e) is used to correct the shear stress at the capillary wall. Equation (6) then becomes:

$$\tau_w = \frac{R\,\Delta P}{2(L + eR)} = \frac{\Delta P}{2(L/R + e)} \tag{8}$$

The Rabinowitsch equation is used to correct the shear rate at the capillary wall. Equation (7) then becomes:

$$\dot{\gamma}_w = \left(\frac{4Q}{\pi R^3}\right)\left(\frac{3n+1}{4n}\right) \tag{9}$$

where n is the power index value. In some instances, these correction factors are either not applicable or their values may not be derived at the time of computation. Thus, the expressions used to compute the shear stress and shear rate for Newtonian fluids are used to compute those for non-Newtonian fluids. In this case, the shear stress and the shear rate are referred to as the false apparent shear stress and the false apparent shear rate. Then, the derived viscosity is designated the false apparent viscosity which is expressed by combining equations (6) and (7) as:

$$\eta = \frac{\tau}{\dot{\gamma}} = \frac{\pi\,\Delta P\,R^4}{8QL} \tag{10}$$

The advantage of using a capillary rheometer is that the flow and the shear rate are similar to those used in current cement injection systems. The disadvantages include the varying shear across the radius of the capillary and the necessity to apply corrections factors in order to measure more accurate viscosity values [138, 142, 150]. Other traditional techniques for measuring PMMA viscosity include the rotational rheometer (cone-plate or plate-plate). Depending on the geometry used, the test fluid (PMMA) is contained within the annular space of the cone-plate or the plate-plate. In the cone-plate arrangement, the cone is rotated at a constant speed while the resisting torque (T) of the fluid is measured on the bottom plate. By knowing the angular

rotation of the cone (ω), the cone angle (α), and the radius of the plate (R), the viscosity can be derived as [138]:

$$\eta = \frac{\tau}{\dot{\gamma}} = \frac{3T\alpha}{2\pi R^3 \omega} \tag{11}$$

The major limitation for using either capillary or rotational rheometers when measuring PMMA viscosity is that such methods assume the cement to be a viscous material. Although this is a safe assumption at the early stages of mixing, as the cement cures it behaves more like an elastic solid and this assumption fails to be true. For this reason, it is more reasonable to treat PMMA cement as a viscoelastic material, for which it is convenient to use an oscillatory rheometer to measure viscosity [140, 141]. The set-up is very similar to a rotational rheometer in terms of the fluid being contained within the annular space of the cone-plate or the plate-plate. However, in this method the fluid is subjected to an oscillatory displacement which is typically sinusoidal in nature. Either a compressive (ε) or shear strain (γ) can be applied. These are in the form:

$$\varepsilon = \varepsilon_0 \sin\omega t \tag{12a}$$

or

$$\gamma = \gamma_0 \sin\omega t \tag{12b}$$

where ε_0 and γ_0 are the amplitude or maximum strain, ω is the frequency of oscillation and t is the time. The resulting compressive (σ) or shear (τ) stress oscillates with the same frequency but is shifted by a phase angle ϕ:

$$\sigma = \sigma_0 \sin(\omega t + \phi) \tag{13a}$$

or

$$\tau = \tau_0 \sin(\omega t + \phi) \tag{13b}$$

The equations for stress can be expanded to give:

$$\sigma = \sigma_0 \sin\omega t \cos\phi + \sigma_0 \cos\omega t \sin\phi \quad (13c)$$

or

$$\tau = \tau_0 \sin\omega t \cos\phi + \tau_0 \cos\omega t \sin\phi \quad (13d)$$

This indicates that the stress has two components, one which is in phase with the strain while another which is $\pi/2$ out of phase with the strain. Therefore, the complex modulus (compressive E^* or G^* shear) also has two components: the real component (or elastic), which is referred to as the storage modulus (E' or G'), is in-phase with the strain and the imaginary component (or viscous), which is referred to as the loss modulus (E'' or G''), is $\pi/2$ out of phase with the strain. These can be expressed as:

$$E^* = E' + iE'' = \frac{\sigma_0}{\gamma_0}(\cos\phi + i\sin\phi) \quad (14a)$$

or

$$G^* = G' + iG'' = \frac{\tau_0}{\gamma_0}(\cos\phi + i\sin\phi) \quad (14b)$$

Similarly, the true or complex viscosity (η^*) has two components and is expressed as:

$$\eta^* = \eta' + i\eta'' \quad (15)$$

where η' is referred to as the dynamic viscosity and is related to the loss modulus via:

$$\eta' = \frac{E''}{\omega} \quad \text{or} \quad \eta' = \frac{G''}{\omega} \quad (16)$$

η'' does not have a special name and is related to the storage modulus via:

$$\eta'' = \frac{E'}{\omega} \quad \text{or} \quad \eta'' = \frac{G'}{\omega} \quad (17)$$

The loss angle (ϕ) can also be calculated via:

$$\tan\phi = \frac{E''}{E'} \quad \text{or} \quad \tan\phi = \frac{G''}{G'} \tag{18}$$

The advantage of using the cone-plate geometry is that the shear rate is nearly constant throughout the system which is crucial when testing fluids that are very sensitive to shear rate, such as the case with PMMA. This allows reducing variability and obtaining more reliable measurements of viscosity. However, problems can occur with the cone-plate geometry particularly when the testing fluid, such as PMMA, is a suspension containing particles. These problems may be resolved by increasing the shear gap in the rheometer so that the gap becomes significantly (at least 5 times) greater than the size of the particles. As the particles in PMMA cements are typically on the order of 100 μm, the shear gap must be at least 500 μm. With the cone-plate geometry, this condition may be more difficult to achieve compared to a plate-plate geometry [140].

Farrar and Rose [140] studied the rheological properties of the following acrylic bone cements: Palacos R (Merck Biomaterial, Darmstadt, Germany), Simplex P (Howmedica International Ltd., London, UK), Zimmer low viscosity cement (Zimmer, Indiana, USA), Zimmer regular (Zimmer, Indiana, USA), Osteobond (Zimmer, Indiana, USA) and CMW 3 (Wright Medical Technology Inc., Tennessee, USA). The viscosity measurements were performed using a CarriMed CSL500 rheometer (TA Instruments Ltd., Leatherhead, Surrey, UK) in dynamic oscillation mode with a parallel plate configuration. The radius of the upper plate was 20 mm, the gap between the plates was 2 mm, and the frequency of oscillation was set to 5 Hz. The rheometer was used in ‘constant strain mode’ thus the applied stress was varied to achieve constant strain amplitude of 5×10^{-4} rad. This mode was selected, rather than constant stress, to maintain the applied strain throughout the curing of the cements. The dynamic viscosity as a function of time is presented in Figure 1.19.

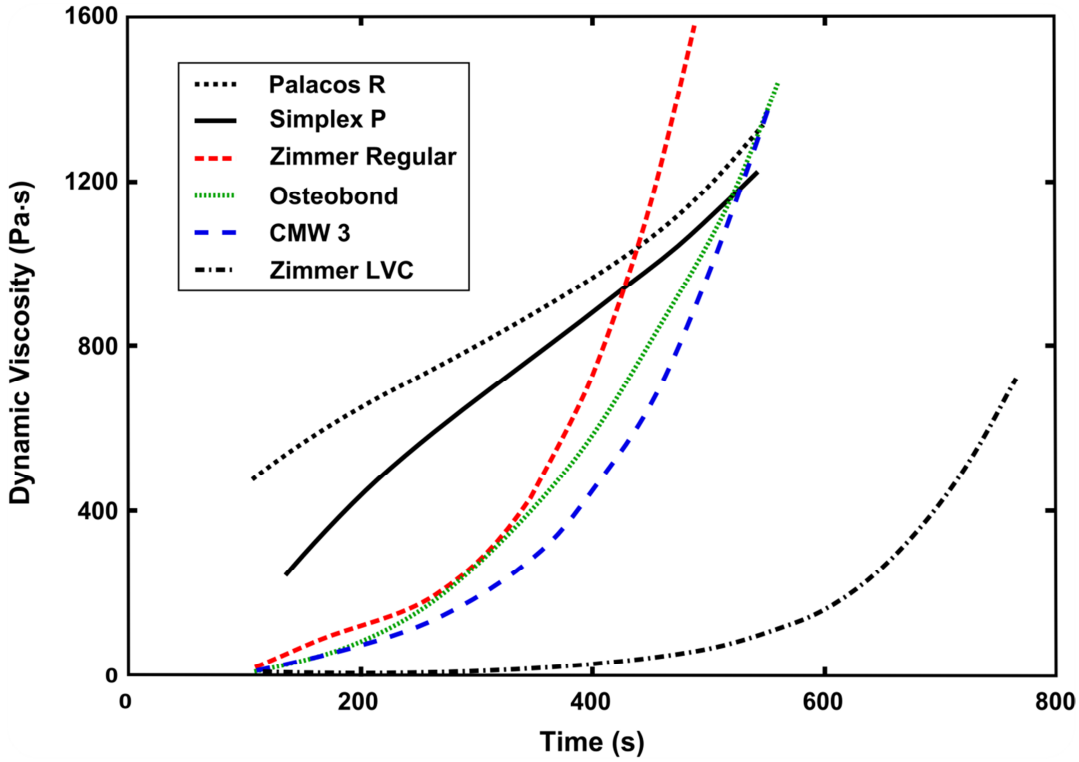

Figure 1. 19 Dynamic viscosity as a function of time for commercial acrylic bone cements. The shear rate at the rim of the plate was 50 s^{-1}. All measurements were performed at 23ºC. Adapted from [140].

The data shows that the cements have different initial viscosities as well as marked differences in their viscosity-time curves. These differences reflect the way the cements are intended to be used. For instance, Zimmer LVC is intend to be injected using a cement gun, thus the cement has a low initial viscosity which is maintained for some time before it starts to rise. On the other hand, Palacos R has a high initial viscosity as this cement is generally used for prosthesis fixation. There are two processes which contribute to the rise in viscosity as a function of time: 1) swelling of the PMMA polymer particles in the MMA monomer and 2) polymerisation of the monomer itself. This implies that the rate of viscosity rise is affected by various factors including particle size/shape/distribution, composition of the polymer particles, and molecular weight distribution of the polymer component [140]. There have been two categories of formulations for acrylic bone cements that are used as injectable biomaterials for vertebral augmentation. The first comprises the same commercially available brands that are used in cemented arthroplasties with an extra amount of

radiopacifier added by the surgeon to bring the concentration to 20–30 wt/wt % of the PMMA powder. The most common brand used is Simplex P with the addition of $BaSO_4$ to increase its radiopacity. The second category comprises commercially available brands that are specifically formulated with a high radiopacifier concentration, such as Osteopal V (Heraeus Medical GmbH, Hanau, Germany) for example [151]. One of the main concerns for using acrylic bone cements is related to the exothermal polymerization of the cement which generates a temperature elevation (reaching 100°C) high enough for causing thermal necrosis of the soft tissues at the peri-augmentation site. Based on post-mortem histological examination of a vertebra 6 month post-augmentation, San Millan et al. [152] showed that acrylic bone cements can cause necrosis of tumor tissue within and around the augmentation site. Other disadvantages for using acrylic bone cements include the non-biologic potential to remodel or integrate into the surrounding bone, the excessive inherent stiffness, and the potential for residual liquid monomer to cause toxicity and chemical necrosis of the surrounding tissue.

Ceramic bone cements such as calcium phosphate (CaP) and calcium sulphate (CaS) have also been used as injectable biomaterials for vertebral augmentation. Ceramic cements have been extensively investigated as bone substitutes due to their chemical characteristics and bioactive properties. They have the advantage of resorbing over time and allowing new bone to form, thereby restoring the vertebral body mass. Another key advantage is that these cements cure through a slow exothermic reaction which prevents the attainment of high curing temperatures and avoids any potential thermal effects within and around the augmentation site. When CaP cements are mixed in an aqueous solution, the setting is generally initiated by an acid-base reaction, where a relatively acidic CaP reacts with a relatively basic CaP to produce a neutral CaP. Based on the degradation rate, CaP cements can be classified as apatite or brushite. The degradation of apatite cements (although faster than hydroxylapatite) is considered slow *in vivo* and some formulations (such as tetracalcium phosphates) experience increase in strength with time. Brushite cements, on the other hand, have a faster degradation rate compared to apatite cements and

suffer a rapid decrease in strength *in vivo*. CaS cements, more commonly known as plaster of Paris or gypsum, have a long clinical history for use as a bone substitutes in various skeletal sites. When these cements are mixed in an aqueous solution, the powder is converted to calcium sulfate dihydrate producing a paste with a solid or partial solid structure. CaS cements resorb *in vivo* mainly by dissolution within about 2 months depending on the volume and location. The primary concern regarding ceramic cements is their rapid rate of resorption *in vivo* before the bone tissue has had time to grow into the defect which limits the mechanical support for spinal stability. Another major drawback for using ceramic cement as injectable biomaterials is that during injection the liquid and solid components of the suspension may separate. Once pressure is applied for injection, the suspension separates and only the liquid medium passes through the cannula while the particles accumulate at the tip and cannot infiltrate through the interstices of the bone. This separation effect is referred to as filter-pressing and can be detrimental to the patient. Other limitations for ceramic cements include their high cost, low viscosity and handling characteristics which differ to PMMA [151, 153, 154].

1.6.2 Bone Marrow

In vertebral augmentation procedures, bone marrow has been shown to affect the cement flow behaviour. Bohner et al. [136] have demonstrated that an increase in bone marrow viscosity significantly increases the tendency of cement leakage. Furthermore, bone marrow plays a crucial role in modulating the shear stress experienced by the cancellous bone in the vertebral body when subject to vibratory loads [155]. However, the rheological properties of bone marrow in various sites of the human body as well as the changes in these properties due to osteoporosis and other bone pathology are largely unknown. The only studies which have reported on the rheological properties of bone marrow are summarized in Table 1.5 [156-159].

Table 1. 5 Viscosity measurements reported in the literature for bone marrow and blood.

	Study	Specimen	Location	Temperature (°C)	Viscosity (mPa·s)
Bone Marrow	Bryant et al., 1983 [156]	Bovine	Proximal radius	35	400
			Distal radius	35	44
	Gurkan and Akkus, 2007 [158]	Bovine	Femur	37	123
	Davis and Praveen, 2006 [157]	Human	Calcaneus	36	38
	Zhong and Akkus, 2011 [159]	Human	Femur	37	44 - 142
Blood	Eguchi and Karino, 2008 [160]	Human	-	36	66

Bryant et al. [156] were the first to show that the viscosity of bovine bone marrow was dependent on temperature and varied across anatomical sites. The samples tested in their study were taken from proximal and distal ends of five radii. Newtonian fluid characteristics (viscosity independence to both shear rate and temperature) was reported in measurements performed at temperatures above 37°C for samples from the distal site and above 42°C for samples from the proximal site. All viscosity measurements performed above these temperatures reached a lower limit of 0.04 Pa·s and below these temperatures the measured viscosity of the proximal samples (0.4 Pa·s at 35°C) were about ten times higher compared to the distal samples (0.04 Pa·s at 35°C). This variation in viscosity can be associated with compositional variations of the marrow along the bone. The proximal site contains red marrow whereas the distal site contains yellow (fatty) marrow [161, 162]. This suggests that the increased fat content in the marrow may reduce its viscosity. Furthermore, the proximal marrow solidified at temperatures below 30°C, whereas the distal marrow remained liquid up till temperatures below 20°C. Bryant et al. also showed that removing blood cells and

other granular matter from the bovine marrow via centrifuging decreased the dependency of its viscosity on temperature. In a more recent study, Gurkan and Akkus [158] reported viscosity values of 0.123 Pa·s for bovine bone marrow taken from the femur.

Two studies [157, 159] have reported on the rheological properties of human bone marrow. The first study [157] was performed on specimens taken from the calcaneus of nine freshly amputated human legs within approximately 30 minutes of above- or below-knee amputation. This bone marrow, which is mainly yellow or fatty, exhibited Newtonian fluid characteristics (viscosity independence to shear rate) and had a viscosity value around 0.038 Pa·s at a temperature of 36°C. However, bone marrow samples containing red components or high blood cell concentration exhibited non-Newtonian behaviour. This result is not very surprising especially when human blood is known to exhibit non-Newtonian behaviour [160]. The second study [159] examined the effects of age on the rheological properties of human yellow bone marrow. Their samples were harvested from the femurs of male donors ranging between 22 to 82 years of age (N = 19). Their results showed that age did not have a significant effect on the viscosity of the marrow which decreased with increasing shear rates, ranging from 0.142 to 0.044 Pa·s at shear rates of 0.5 and 10 s^{-1}, respectively. However, at shear rates above 10 s^{-1}, the marrow behaved as a Newtonian fluid with its viscosity remaining constant.

The answer to this variation in bone marrow composition along the bones and at various sites in the human body remains unknown. One explanation is the temperature dependency of bone marrow which may affect its composition. Huggins et al. [163, 164] have demonstrated that the fat content of bone marrow in the limb bones (such as the femur or the radius) is higher compared to the bones in the central parts of the body (such as the vertebrae or the ribs) which may be associated with the greater body temperature in the central bones.

1.8 Two-Phase Flow in Porous Media

The rheological properties play a crucial role in the cement flow behaviour during injection and within a porous structure such as cancellous bone. Many factors influence the injection biomechanics and the tendency of cement leakage, however the cement viscosity has been identified as a key determinant of the cement flow patterns and therefore the risk of cement leakage [136, 165, 166]. Furthermore, cement placement has been identified as a critical parameter in the biomechanical behaviour of the construct post-augmentation [167, 168]. This section focuses on the theoretical and experimental approaches used to describe and characterize the non-Newtonian cement flow behaviour in cancellous bone during vertebral augmentation procedures.

1.8.1 Theoretical Models

The classic examples of two-phase flow in porous media are associated with oil recovery processes (oil-gas, -water, -polymers and/or -surfactants) and ground water flow (water-air) [169]. Predictive theories started with Darcy who investigated the flow of water in vertical homogenous sand filters and concluded that the rate of flow Q is: a) proportional to the cross-sectional area of the sand filter, b) proportional to the hydraulic head difference measured between the top and bottom of the sand filter and c) inversely proportional to the length of the filter [135, 170]. This gave rise to the Darcy formula:

$$Q = KA \left| \frac{h_1 - h_2}{L} \right| \qquad (19)$$

where K is a constant of proportionality and is referred to as the hydraulic conductivity which is a characteristic of the sand filter but does not provide any information about the degree of homogeneity in the sand filter. The hydraulic conductivity is a measure of the resistance to fluid flow through the porous media and can be separated into two parts: the first is related to the morphological properties of the porous matrix, expressed as the intrinsic permeability k^s and the second is related

to the dynamic viscosity of the injected fluid [135, 171]. The hydraulic conductivity is given as:

$$\mathrm{K} = \frac{k^s}{\eta} \tag{20}$$

Thus, high resistance occurs when the injected fluid has a high viscosity and the porous media through which the fluid flows has a low permeability, where zero permeability would give rise to infinite resistance. Baroud et al. [172, 173] described the intrinsic permeability of cancellous bone as a function of bone porosity (β) by introducing a constitutive law in the form:

$$k^s_{\xi\zeta} = \Gamma_{\xi\zeta}\,\frac{\beta}{1-\beta} \tag{21}$$

where $\Gamma_{\xi\zeta}$ is the intrinsic permeability fitting coefficient and $k^s_{\xi\zeta}$ is the intrinsic permeability in the $\xi\rightarrow\zeta$ direction. Their results showed that the fitting coefficient in the superoinferior direction (SI) and the anteroposterior (AP) direction were $\Gamma_{\mathrm{SI}} = 0.394\times10^{-8}$ (R^2=0.66) and $\Gamma_{\mathrm{AP}} = 0.347\times10^{-8}$ (R^2=0.82), respectively. Although their results showed no significant difference in porosity, the permeability in the AP direction was lower compared to the SI direction. This suggested that other morphological parameters, such as trabecular separation, may contribute to bone permeability. However, their model properly predicts the limits of the permeability (*k*) as a function of porosity (β), where *k* approaches zero as β approaches zero, and *k* approaches infinity as β approaches one. Furthermore, Teo et al. [174] performed experiments to estimate the local bone porosity via linear mapping and found a strong correlation (R=0.83) with Hounsfield unit (HU) values from calibrated computed tomography (CT) images. Their results led to the following relationship with respect to the position in space $\underline{\mathrm{x}}$:

$$\beta(\underline{\mathrm{x}}) = -340\times10^{-6}\cdot\mathrm{HU}(\underline{\mathrm{x}}) + 952.5\times10^{-3} \tag{22}$$

To describe fluid flow through complex porous structures such as cancellous bone, Darcy's law can be expressed more generally in the form of a differential equation:

$$\underline{q}^{\alpha} = -\frac{\underline{\underline{k}}^{s\alpha}}{\eta^{\alpha}} \nabla p^{\alpha} \qquad (23)$$

where α is the specific fluid phase, $\underline{q}$ is the apparent fluid velocity vector, $\underline{\underline{k}}^{s}$ is the intrinsic permeability second-order tensor and ∇p is the pressure gradient. These parameters are most often a function of position in space $\underline{x}$ and time t [133]. However, a major limitation for Darcy's law is that its validity applies only when the fluid is Newtonian and the flow is dominated by viscous forces, where the ratio of inertial to viscous forces is considerably smaller than one. Therefore, Darcy' law must be extended to cover fluids with non-Newtonian rheological behaviour, such as PMMA. Most mathematical and numerical models used to quantify cement flow through cancellous bone assume that the definitions and intrinsic properties of the cement velocity, the cement pressure and the permeability of the cancellous bone are not altered by the rheological properties of the fluid. Thus, all non-Newtonian effects are taken into account via a suitable definition of viscosity at the continuum length scale. Consequently, this apparent or Darcy viscosity is determined from the pressure drop due to steady state and is a function of the fluid rheological properties, the apparent fluid flow and the morphology of the porous media [133, 137].

Baroud and Yahia [175] introduced the time-dependency factor into the power law (Eq. 5) in order to capture the non-Newtonian rheopectic and shear-thinning behaviour of PMMA cement. The extended form of the power law is expressed as:

$$\eta(t,\dot{\gamma}) = \left(a\frac{t}{t_s} + b\right) \cdot \left(\frac{\dot{\gamma}}{\dot{\gamma}_s}\right)^{c(t/t_s)+d} \qquad (24)$$

where a, b, c and d are the viscosity material constants which are derived experimentally from empirical rheological tests. t_s and $\dot{\gamma}_s$ are the characteristic

values for time and shearing rate, typically 60 s and 1.0 s^{-1}, respectively. $a(t/t_s)+b$ is the new term for the consistency index (C) which captures the time-dependent average viscosity of the cement and $c\left(t/t_s\right)+d$ is the new term of the power index (n) which captures the time-dependent deviation of the cement from Newtonian behaviour. Their results showed that the revised from of the power law (Eq. 24) provides an accurate fit to previously derived experimental data [138] and the viscosity material constants for Simplex (Stryker Corporation, Michigan, USA) were determined to be $a=590.0$, $b=-1048.8$, $c=-0.026$, and $d=-0.290$. However, their study was limited to the characterization of cement flow through a cannula and provides little description of the cement infiltration process through cancellous bone. Lian at al. [176] extended the rheological model proposed by Baroud and Yahia [175] to simulate the flow of PMMA cement through cancellous bone by approximating it geometrically as branching-pipe network. Due to the varying permeability and structure of cancellous bone, their geometrical model consisted of channels with continuously varying diameters. Thus, they chose a conical pipe to represent the elementary segment for each branch in their network and assumed that the PMMA flow is steady, incompressible and Newtonian in order for the Hagen–Poiseuille law (Eq. 10) to be applicable and the wall shear-rate to be calculated using Eq. 7. These equations were then modified to estimate the pressure drop and shear-rate across each elementary segment. Consequently, for a general branch segment that is filled and represented via a conical pipe with radii R_1 and R_2 at its ends, the overall pressure drop becomes:

$$-\Delta P=\frac{8\eta LQ}{\pi}\left[\frac{1}{3}\left(\frac{1}{R_1R_2^3}+\frac{1}{R_1^2R_2^2}+\frac{1}{R_1^3R_2}\right)\right] \tag{25}$$

and the effective shear-rate at the wall becomes:

$$\left|\dot{\gamma}\right|_{wall}=\frac{4Q}{\pi\left(\sqrt{R_1R_2}\right)^3} \tag{26}$$

To account for the non-Newtonian behaviour of PMMA, the viscosity was updated prior to the pressure drop computation based on the computed shear-rate, the elapsed

time from cement mixing and the extended form of the power law (Eq. 24) proposed by Baroud and Yahia [175]. Their methods improved the characterization of PMMA flow through cancellous bone and provided an estimation of the overall injection pressure, hence the reaction force required during manual injection. Teo at al. [177] presented a more clinically relevant model for PMMA flow through cancellous bone. They used patients CT datasets to compute the permeability of cancellous bone in the superior-inferior (SI) direction as a function of bone porosity and found good correlation (R^2=0.69). The permeability was expressed as:

$$k_{SI} = 4\times10^{-9}(1-\beta)^{-1.038} \qquad (27)$$

They also characterized the cement viscosity using the extended form of the power law (Eq. 24) with the viscosity material constants derived by Baroud and Yahia [175] for Simplex bone cement. The cement flow through the cancellous bone was determined via Darcy's law (Eq. 23). Several user inputs, which reflect the decisions made by surgeons during vertebral augmentation, were required for their computational model. These included needle position, needle gauge, flow rate and injected volume. Their main findings revealed that the injection pressure increases as the volume of the cement increases and as the distribution of the cement is in close proximity to the cortical walls.

Bohner et al. [136] were the first to present a theoretical model of cement spreading in cancellous bone with a special focus on the characterization of cement leakage. However, their models assumed spherical spreading patterns and Newtonian fluid properties. They considered that the cement leakage occurs along a path of least resistance, thus they assumed that leakage path is cylindrical with a diameter D_e and length L_e. For given cement and marrow viscosities (η_c and η_m, respectively), the pressure (ΔP_e) required to inject the cement through the leakage path is the sum of two pressures: 1) the pressure required to inject the cement into the path and 2) the pressure required to extrude the marrow outside the path. The extravasation pressure ΔP_e is given by:

$$\Delta P_e = \frac{128 Q_c}{\pi {D_e}^4}\left[\eta_c L_c + \eta_m\left(L_e - \frac{4Q_c}{\pi {D_e}^2}t\right)\right] \tag{28}$$

where Q_c is the cement flow rate and L_c is the length of the path which is filled with cement. Furthermore, they considered that the total pressure required to augment bone with cement (ΔP_a) is also a function of two pressures: 1) $\Delta P_{a,c}$ the pressure required to inject the cement into the bone and 2) $\Delta P_{a,m}$ the pressure required to push the marrow out of the bone. These pressures are given by:

$$\Delta P_{a,c} = -\frac{Q_c \eta_c}{4\pi k}\left(\frac{1}{R_o} - \frac{1}{r_c}\right) \tag{29}$$

and

$$\Delta P_{a,m} = -\frac{Q_m \eta_m}{4\pi k}\left(\frac{1}{r_c} - \frac{1}{R_v}\right) \tag{30}$$

These equations are then combined to calculate the total augmentation pressure ΔP_a:

$$\Delta P_a = -\frac{Q_c}{4\pi k}\left[\eta_c\left(\frac{1}{R_o} - \frac{1}{r_c}\right) + \eta_m\left(\frac{1}{r_c} - \frac{1}{R_v}\right)\right] \tag{31}$$

where R_o is the radius of the cavity at the injection point, r_c is the radius of the spherical cement bolus, and R_v is the radius of the bone sphere into which the cement is injected. The cement spreading can be represented in terms of time, flow rate and matrix porosity (β) via:

$$r_c = \left({R_o}^3 + \frac{3Q_c}{4\pi\beta}t\right)^{1/2} \tag{32}$$

The ratio between the augmentation pressure and the extravasation pressure determines the risk of cement leakage λ, which is given by:

$$\lambda = \frac{\Delta P_a}{\Delta P_e} = \frac{{D_e}^4}{512\beta k} f\left(\eta_c, \eta_m, t, R_o, L_e\right) \tag{33}$$

Their theoretical model predicts that cement leakage increases with a decrease in the matrix porosity (β), a decrease in permeability (*k*) and an increase in the diameter of the leakage path D_e. The radius at injection point R_o has a significant effect on the augmentation pressure only. Based on this model, an increase in R_o decreases the augmentation pressure, thus decreasing the risk of cement leakage.

Widmer et al. [135] improved previous models by introducing methods to describe and simulate the displacement of bone marrow by bone cement in cancellous bone. They devised a strategy to efficiently incorporate the fluid-fluid boundary information into the local properties in order to govern the Darcy flow. They consider the cement-marrow boundary as a one-dimensional, arbitrarily oriented column of length *l*, referred to as the finite element Ω^e. Then, instead of treating the cement and marrow as separate entities, they treat them as one continuum and represent the apparent cement-marrow property as the homogenization or mixture of both fluid properties according to the element factor δ^e. Thus, the pressure drop ΔP^i occurring along each fluid portion δ_i^e (i=1, 2) is replaced with the total pressure drop ΔP^e occurring along the column Ω^e. Darcy's Law is now expressed as:

$$q = K^e \frac{\left|\Delta p^e\right|}{l} \tag{34}$$

where K^e is the overall hydraulic conductivity of the element Ω^e and is expressed as:

$$K^e = \frac{k^s}{\delta^e \eta_c + \left(1-\delta^e\right)\eta_m} \tag{35}$$

The expression of K^e provides a linear interpolation between the fluid properties η_c and η_m with δ^e as the weighting factor of the interpolation. Furthermore, they hypothesize that the relation in Eq. 35 remains valid if the scalar intrinsic property (k^s) is replaced by its second-order tensor counterpart $\underline{\underline{k^s}}$ and assume that the fluids are incompressible so the principles of mass conservation may be replaced by the

principles of volume or flux conservation. Subsequently, they replaced $\underline{q}^{\alpha}(\underline{\underline{K}}^{\alpha})$ with $\underline{q}^{e}(\underline{\underline{K}}^{e})$ to express Darcy's law in the form of one single constitutive equation in terms of the mixed boundary representation rather than two separate fluid phase properties. They also characterized the cement viscosity using the extended form of the power law (Eq. 24) and recovered the shearing rate magnitude from the specific discharge of the fluid interface which is represented by the flux vector field $\underline{q}^{e}$:

$$\underline{\underline{\dot{\gamma}}} = \underline{\underline{\nabla q^{e}}} + \left(\underline{\underline{\nabla q^{e}}}\right)^{T} \tag{36}$$

In a more recent study, Widmer at al. [137] introduced a multi-scale approach to the characterization of the cement flow through cancellous bone. They proposed that the Reynolds number $\overline{\mathrm{Re}}$ can be used to relate the pore and continuum length-scale rheological properties and showed a strong correlation between the viscosity and $\overline{\mathrm{Re}}$. Their results also showed that a viscosity change of the order of one magnitude was observed on the pore length scale, whereas the shear-thinning properties caused a viscosity change of the order of only 10% on the continuum length scale. Their findings highlight the importance of incorporating the non-Newtonian cement properties at the appropriate length scale.

1.8.2 Experimental Studies

Due to the high frequency of cement leakage and the potential cause for serious clinical complications, *in vitro* studies have been designed to better understand the fundamental mechanisms underlying cement leakage [136, 166, 178-180]. However, this is just one part of a wider requirement to understand how the cement flows within the bone and accurately predict the cement placement, which has been identified as a critical parameter in the biomechanical behaviour of the construct post-augmentation [167, 168]. All *in vitro* studies on cement leakage have generally differed in terms of

experimental setups and protocols, cements used, means of cement mixing and cement injection (Table 1.6).

Table 1. 6 Comparison of cements used, means of cement mixing and cement injection between experimental studies on cement leakage.

Study	Bohner et al., 2003	Loeffel et al., 2008	Baroud et al., 2006	Mohamed et al., 2010
Cement Used	Palacos LV-40 (Essex Chemie AG, Luzern, Switzerland)	Vertecem (Synthes Inc, Bettlach, Switzerland)	DP-Pour (DenPlus Inc, Montreal, Quebec)	DP-Pour (DenPlus Inc, Montreal, Quebec)
Means of Cement Mixing	10.45 g of powder with 4.7 ml of monomer in a 20 ml syringe using a spatula for 40 s	7 g of powder with 3.07 g of monomer in a 10 ml syringe using a steel rod for 60 s	liquid-to-powder ratio recommended by manufacturer then oscillatory mixer for 90 s at 400 rpm	liquid-to-powder ratio recommended by manufacturer mixed with a spatula for 30 s then an oscillatory mixer for 80 s
Means of Cement Injection	50 ml syringe with two needle diameters 7 and 11- gauge	6 ml syringe with 9-gauge needle and a computer-assisted injection device	20 ml syringe with 8-guage needle	10 ml syringe and novel aspiration needle with double concentric tubing
Injection Parameter	constant flow rates of 13.6 and 27.1 mL/min	cement volume of 4 mL injected at flow rates of 3 and 9 mL/min	cement volume of 5 mL injected at a rate of 7 mL/min	cement volume of 5 mL injected at a rate of 4 mL/min

Bohner et al. [136] aimed to determine the effects of various parameters on the tendency of cement leakage. Their experiments were performed according to a factorial design and aimed at testing the following parameters: (1) with and without bone marrow substitute, (2) elapsed time after cement mixing of 1.5 min and 3 min, and (3) leakage hole diameter of 2 mm and 4 mm. Their results showed that the risk of cement leakage significantly increased in the presence of marrow substitute and when the leakage hole diameter was 4 mm ($p < 0.0001$). Among these factors, the only parameter that did not depend on the bone structure was cement viscosity. Hence, their findings suggested that the simplest means of reducing cement leakage was via increasing cement viscosity. However, increasing the cement viscosity would drastically increase the injection pressure which might not be suitable for a clinical setting as the force that a human hand can apply limits the injection pressure.

Subsequently, Baroud et al. [166] performed a study to test the hypothesis that high viscosity cement spreads more uniformly compared to low viscosity cement which follows the path of least resistance. They performed injection tests over a range of 5 to 11.5 minutes after cement mixing in 30-seconds increments. Their results showed that cement viscosity significantly affected all the recorded parameters and recommended that surgeons must inject the cement as late as possible in order to reduce cement leakage and increase the safety of the vertebral augmentation procedure. They also emphasize that the point in time at which the cement becomes manually non-injectable depends on the syringe diameter and the needle gauge used. Loeffel et al. [180] aimed to characterize cement distribution and quantify the effects of cement viscosity, bone porosity and injection speed on cement spreading. They tested four different cement viscosities (50, 100, 200 and 400 Pa·s) and used two indicators, circularity and mean cement spreading distance, to quantitatively describe the differences in the resulting cement distribution patterns. Similar to Baroud et al., their results showed that an increase in cement starting viscosity had a significant impact on both indicators and produced a more predictable flow pattern. Their results also suggested that an increase in porosity negatively affected the compactness of the cement cloud and was more likely to cause irregular flow patterns especially with low viscosity cements. On the other hand, Mohamed et al. [178] aimed to test the hypothesis that a novel hybrid approach for cement injection via aspirating the bone marrow and imposing a pressure gradient to direct cement flow would improve the uniformity of cement filling, consequently minimizing cement leakage. Their experiments had two factors: (1) Elapsed time of 4 minutes and 8 minutes corresponding to low and high cement viscosity, respectively. (2) Aspiration with four levels: (i) valve closed, (ii) valve open, (iii) simultaneous aspiration and injection, and (iv) suction 1 minute before and continued during injection. Their results supported their hypothesis and showed that cement leakage significantly decreased with simultaneous aspiration and injection, especially with the low cement viscosity. However, establishing suction before delivering the cement did not have a significant effect on cement leakage. Furthermore, aspiration had no significant effect on the force required to perform the cement injection.

All the bone surrogates that have been used in these experimental studies on cement leakage have been made of open-porous aluminum foam. Generally, aluminum foam has been selected due to its well-controlled porosity. However, the surrogates have differed in terms of shape, size, manufacturer used, porosity, vertebral shell mimic, bone marrow mimic and the generated cement leakage paths (Table 1.7). Bohner et al. [136] and Loeffel et al. [180] both used off-the-shelf surrogates with an overall porosity of 90%, conversely Baroud et al. [166] used surrogates with 91% porosity and Mohamed et al. [178] used surrogates with 95% porosity. To mimic the vertebral shell, Loeffel et al. [180] used PMMA enclosure of outer dimensions 60×60×32 mm, while Baroud et al. [166] and Mohamed et al. [178] coated their surrogates with a 1 mm layer of PMMA cement. On the other hand, Bohner et al. [136] did not include any enclosure in their surrogates. To mimic bone marrow, Bohner et al. [136] and Loeffel et al. [180] both used melted cow butter, whereas Baroud et al. [166] and Mohamed et al. [178] both used a water/gelatin solution. To generate a cement leakage path, Bohner et al. [136], Baroud et al. [166] and Mohamed et al. [178] all drilled a cylindrical channel through the main plane of their surrogates, however Loeffel et al. [180] drilled vent holes through each of the four sides of their reusable PMMA enclosure.

The bone surrogates that have been used in these cement leakage experiments have several limitations that our future work will endeavour to overcome. An important limitation is that although the porosity was controlled among a group of respective surrogates, the geometrical structure within these surrogates was irregular and uncontrolled. Thus, the surrogates were inherently unique. Achieving a bone surrogate with constant porosity as well as structural geometry is crucial to reduce the variability, render the experiments reproducible and shift the focus onto understanding the cement flow behaviour. Another important limitation is that the surrogates did not provide a true representation of the leakage phenomenon. It is essential to simulate the vertebral boundary, particularly the blood vessels that breach the cortex to supply blood in and out of the vertebral body as well as other breaches in the cortex due to skeletal pathology or vertebral fractures. This is crucial as such breaches create paths of least resistance providing means for cement leakage outside the vertebral body.

Further limitation of previous surrogates is the true representation of bone marrow as such properties significantly affect the cement flow behaviour [136].

Table 1. 7 Comparison of bone surrogates used in experimental studies on cement leakage following percutaneous vertebroplasty.

Study	Bohner et al., 2003	Loeffel et al., 2008	Baroud et al., 2006	Mohamed et al., 2010
Shape	Cubic	Rectangular	Cylindrical	Cylindrical
Size	50x50x50 mm	45x45x12 mm	Diameter 38.1 Height 25.4 mm	Diameter 38.1 Height 25.4 mm
Manufacturer	Filter plates Sivex; Pyrotek SA, Sierre, Switzerland	m-Pore GmbH, Dresden, Germany	ERC Aluminum and Aerospace, CA	ERC Aluminum and Aerospace, CA
Porosity	90%	90%	91.1±0.6%	95%
Cortical Mimic	None	PMMA enclosure 60x60x32 mm	1 mm layer of PMMA cement	1 mm layer of PMMA cement
Marrow Mimic	Melted cow butter	Melted cow butter	Water/gelatin	Water/gelatin
Cement Leakage Path	Cylindrical channel 2 and 4 mm in diameter	4 mm hole in each of the 4 sides of PMMA enclosure	Cylindrical channel 3 mm in diameter	Cylindrical channel 3 mm in diameter

1.9 THESIS AIMS AND OBJECTIVES

From the assessment of the current literature, it is evident that the cement leakage during vertebral augmentation is an important cause for serious clinical complications. The high frequency of cement leakage is a major hurdle preventing augmentation procedures from becoming the standard of care for the treatment of chronic pain related to vertebral fractures, which are caused by osteoporosis and other skeletal pathology such as metastasis or multiple myeloma. Although many factors influence the injection biomechanics and the tendency of cement leakage, the rheological properties play a crucial role in the cement flow behaviour during injection and within a porous structure such as cancellous bone. Furthermore, cement placement has been identified as a critical parameter in the biomechanical performance of the construct post-augmentation. We hypothesize that a novel method using reproducible and pathologically representative bone surrogates can be developed to comparatively assess the injection behaviour of different cement formulations and help study cement-fluid interaction.

1.9.1 Study Aim

To develop novel methodology for assessing cement injection behaviour using reproducible and pathologically representative bone surrogates. The goal is to better understand how the cement flows within cancellous bone and address issues of cement placement following vertebral augmentation.

1.9.2 Objectives

Objective 1: Development and manufacturing of reproducible and pathologically representative 2D and 3D bone surrogates

Objective 2: Assessment of bone surrogate morphology and surface properties.

Objective 3: Development of methods for allowing controlled injections into the 2D and 3D bone surrogates.

Objective 4: Comprehensive assessment of bone cements via *in vitro* experiments.

CHAPTER 2 MATERIALS AND METHODS

This chapter outlines the materials and methods used in this thesis for the *in vitro* assessment of cement injection into vertebral cancellous bone. The first step was to develop reproducible and pathologically representative bone surrogates to mimic the vertebral body with different skeletal conditions including osteoporosis, spinal metastasis and multiple myeloma. This required comprehensive understanding of the morphology of the cancellous bone microarchitecture and the vertebral body anatomy with its rheological environment to establish key requirements for these bone surrogates. Then, a suitable manufacturing technique had to be identified to ensure accurate and precise reproduction of the surrogates. The next step was to develop and validate methods that allow fluid injection into the bone surrogates under a controlled environment, through measuring the injection pressure and flow rate as well as monitoring the cement flow distribution. Two experimental testing rigs were developed to allow the injections to be performed under a constant flow rate. The first system uses a syringe pump, while the other uses a material testing machine to control the displacement of the syringe plunger and achieve a constant injection flow rate. The final step was to utilize this developed methodology for assessing the flow behaviour of different bone cement formulations through the visualization and quantitative analysis of the cement spreading at various time intervals during the injection.

2.1 BONE SURROGATE REQUIREMENTS

There are several key requirements for bone surrogates used in experimental studies on cement leakage following vertebral augmentation (Table 2.1). In addition, the surrogates must be manufactured using a technique that allows their accurate and precise reproduction. Achieving a constant surrogate is crucial to reduce the variability, render the experiments reproducible and shift the focus onto understanding the cement flow behaviour.

Table 2. 1 Key requirements for bone surrogates used in experimental studies on cement flow during percutaneous vertebroplasty.

Parameter	Requirement	Reference
Trabecular Bone Morphology	Normal: Tb.Th (vertical/horizontal) = 0.2 mm Tb.Sp (vertical/horizontal) = 0.5 mm Osteoporotic: Tb.Th (horizontal) = 0.15 mm Tb.Th (vertical) = 0.25 mm Tb.Sp (horizontal) = 1.0 mm Tb.Sp (vertical) = 0.8 mm	[181]
	Metastasis: normal or osteoporotic morphology with one large lesion (11% vertebral body volume)	[182, 183]
	Myeloma: osteoporotic morphology with multiple small lesions (> 1.7 mm in diameter)	[184]
	Porosity: Normal 75% Osteoporotic 90%	[166]
Vertebral Shell	Solid thin layer surrounding the surrogates	[185]
Boundary	Blood vessels that breach the vertebral shell to exchange blood in and out of vertebral body: - Posterior: 1 or 2 holes through the cortex midway along the craniocaudal and lateral directions, with a 3 mm overall diameter - Anterior: front and/or side holes through the cortex one-third below the superior endplate in the craniocaudal direction, with 2 mm height and 1 mm width	[36]
Rheological Environment	Surface properties must match those of trabecular bone A true representation of the rheological properties of red bone marrow must be included	[136]
Shape / Size	Semi-cylindrical to match the vertebral body with dimensions of 40 x 30 x 30 (Width x Depth x Height) to match the size of thoracolumbar vertebrae	[186]
Manufacturing	Reproducible, accurate and cost effective	

The surrogates must also simulate the trabecular bone morphology, particularly the trabecular separation (TbSp) and trabecular thickness (Tb.Th). Three-dimensional morphometric indices are used to describe the trabecular microarchitecture (refer to section 1.2). Several studies have demonstrated significant variations in the three-dimensional morphometric indices with age amongst other variables [25, 31-35].

Thus, it is important that the bone surrogates provide a representation of the trabecular bone morphology that reflects the underlying pathology or age. Furthermore, the surrogates must also mimic the vertebral shell which confines the flow and controls the intravertebral pressure, significantly affecting the filling pattern [185]. Another important requirement is simulating blood vessels that breach the cortex to supply blood in and out of the vertebral body. This is crucial as these breaches create paths of least resistance providing means for leakage outside the vertebral body. Finally, it is essential to simulate the rheological environment within the vertebral body. The surface properties of the surrogates must match those of trabecular bone. This is crucial as surface properties (particularly the surface wettability) may influence the cement flow. The surrogates must also include a true representation of the rheological properties of red bone marrow. This is extremely important as such properties significantly affect the cement flow behaviour [136]. Although there has been data in the literature that describes the rheological properties of human yellow bone marrow [157, 159], there is still a need to test the rheological properties of human red bone marrow (contains stem cells and may have different viscosity) which is found within the trabecular bone of the vertebral body.

2.2 Three-Dimensional Bone Surrogates

The three-dimensional (3D) bone surrogates were achieved by first developing computer aided design (CAD) models then manufacturing the physical models through a suitable rapid prototyping (RP) technique. To mimic prescribed vertebral trabecular bone, CAD models were developed in SolidWorks (Dassault Systèmes, Vélizy, France). The models were based on square beams and an open-cell geometry with a lattice structure [187]. Data from Mosekilde [181] was used to adjust the dimensions of the geometry and mimic osteoporotic bone. Mosekilde studied age related morphometric changes in human vertebral trabecular bone and described the geometrical changes in terms of trabecular thickness and spacing, which were measured in both horizontal and vertical directions [181]. Figure 2.1 (a) shows the unit cell of the 3D surrogates and the dimensions associated with normal and osteoporotic bone conditions. Figure 2.1 (b) illustrates cubic samples of the 3D bone surrogates

with their respective porosities. It is important to note that a uniform structure was chosen and the loss of connectivity typically observed in osteoporotic bone was not simulated to simplify the representation of the bone morphology and facilitate the manufacturing process.

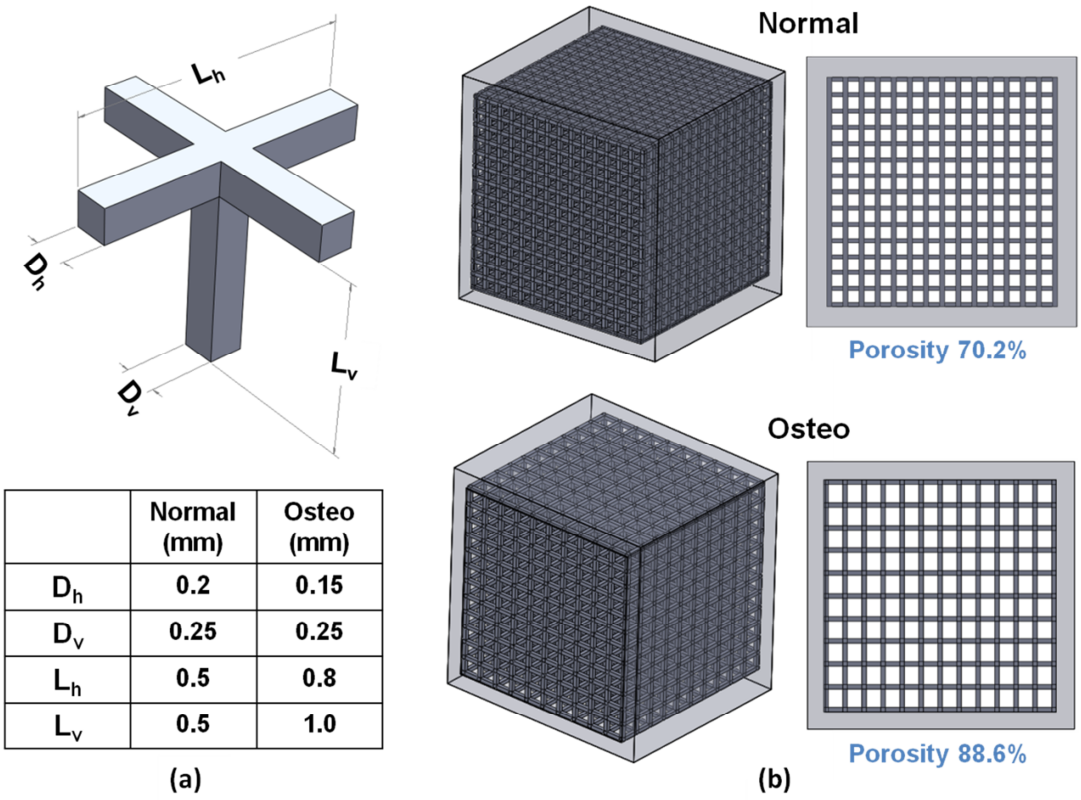

	Normal (mm)	Osteo (mm)
D_h	0.2	0.15
D_v	0.25	0.25
L_h	0.5	0.8
L_v	0.5	1.0

Figure 2. 1 (a) The unit cell and the dimensions associated with normal and osteoporotic bone conditions. (b) cubic models with their respective porosities.

The external shape of the 3D bone surrogates was semi-cylindrical (refer to Figure 2.2) with outer dimensions of 40 x 30 x 30 mm (width x depth x height) to better mimic the overall shape of the vertebral body [21, 186, 188]. The boundary of the surrogates was 1 mm thick to mimic the cortex of the vertebral body. Openings in the boundary were applied to mimic blood vessels that breach the vertebral shell and exchange blood in and out of the vertebral body. Furthermore, 11-gauge insertion channels were incorporated to allow consistent needle placement during injection. This was essential to minimize error and ensure that the flow inlet (i.e. needle tip) was in the same location for all the injections. The needle entry site on the posterior boundary was 6.0 mm below the superior surface in the craniocaudal direction and

16.5 mm from the midline along the left and right transverse directions. The inclination of the insertion channels was 20.0 and 6.0° in the sagittal and transverse planes, respectively. The location and inclination of the needle insertion channels were chosen to mimic those of human thoracolumbar pedicles [21, 188].

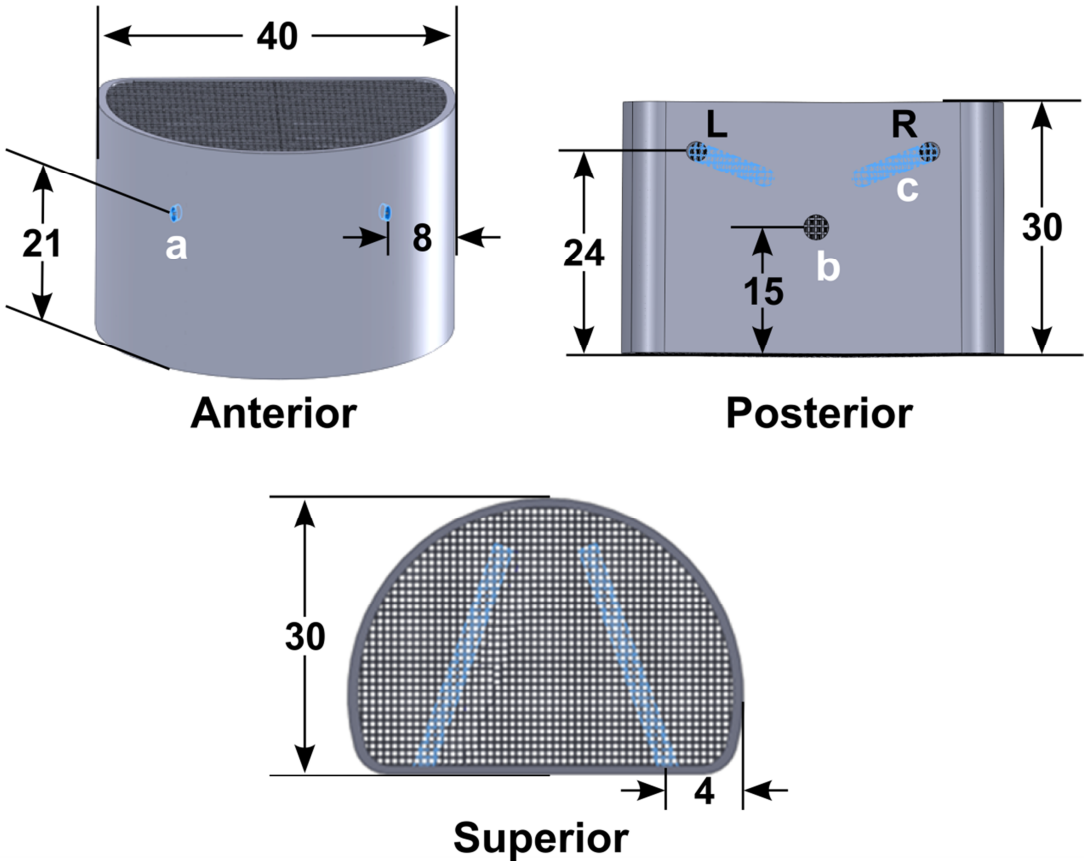

Figure 2. 2 The boundary of the 3D bone surrogates showing: (a) two identical and symmetrical elliptical openings 2 mm in height and 1 mm in width applied to mimic breaches due to anterior blood vessels, (b) one circular opening 3 mm in diameter applied to mimic breaches due to posterior blood vessels, and (c) the insertion channels that were incorporated to allow consistent needle placement during injection. The superior and inferior surfaces of the surrogates were kept open due to manufacturing restrictions. All dimensions are in millimeters.

The size and location of the breaches in the cortex of the vertebral body due to blood vessels were determined based on in-house microCT scans of five human thoracic vertebrae. The DICOM stack of each scan was imported into imageJ [189] and visually inspected slice by slice until a breach (anterior or posterior) in the cortex of the vertebral body was detected. The number of slices that spanned the breach in the craniocaudal direction was recorded. The width of the breach was measured on the

middle slice and the height (h) of the breach was determined through multiplying the number of slices by the scan resolution. The location of the breach in the craniocaudal direction was determined based on the total number of slices and the range of slices that spanned the breach. Table 2.2 summarizes the measurements performed on the five human thoracic vertebrae to determine the size and location of the breaches and Figure 2.3 shows the measurements performed on a T6 vertebra to determine the width of the breaches.

Table 2. 2 Summary of measurements performed on five human thoracic vertebrae to determine the size and location of breaches in the cortex due to blood vessels. Slice increments are in the craniocaudal direction.

Vertebral Level	Scan Resolution (μm)	Total Number of Slices	Anterior Blood Vessels			Posterior Blood Vessels		
			Slice Range	h (mm)	w (mm)	Slice Range	h (mm)	w (mm)
T1	74	233	65-95	2.2	1.1	100-140	3.0	2.5*
T2	74	232	60-90	2.2	1.4	95-135	3.0	3.4*
T3	74	219	60-85	1.85	1.1	70-120	3.7	2.8
T6	74	253	70-100	2.2	1.3	90-135	3.3	3.2
T8	74	285	90-120	2.2	1.2	120-170	3.7	3.3

* The blood vessel breached the cortex as two separate branches. The value presented is the sum of the two widths.

The analysis of the data revealed that the blood vessels consistently breached the posterior cortex of the vertebral body approximately midway along the craniocaudal and lateral directions, generally as a single vessel but sometimes as two separate branches. The average height and width of the posterior breaches were 3.3 ± 0.4 and 3.0 ± 0.4 mm, respectively. In the 3D bone surrogates, the posterior breach was therefore chosen to be circular with a 3 mm diameter, and the location was chosen to be on the posterior wall midway along the craniocaudal and lateral directions. Breaches due to the anterior blood vessels were not consistent. Single or multiple breaches were along the anterior cortex of the vertebral body in the front and/or sides.

In the craniocaudal direction, the breaches were consistently located approximately one-third below the superior endplate. The average height and width of the anterior breaches were 2.1 ± 0.2 and 1.2 ± 0.1 mm, respectively. Two elliptical openings, 2 mm in height and 1 mm in width, were therefore applied to the boundary of the 3D bone surrogates to simulate beaches due to the anterior blood vessels. The two openings were located on the anterior boundary one-third below the superior surface in the craniocaudal direction and one-fifth from the left and right edges along the transverse direction, respectively.

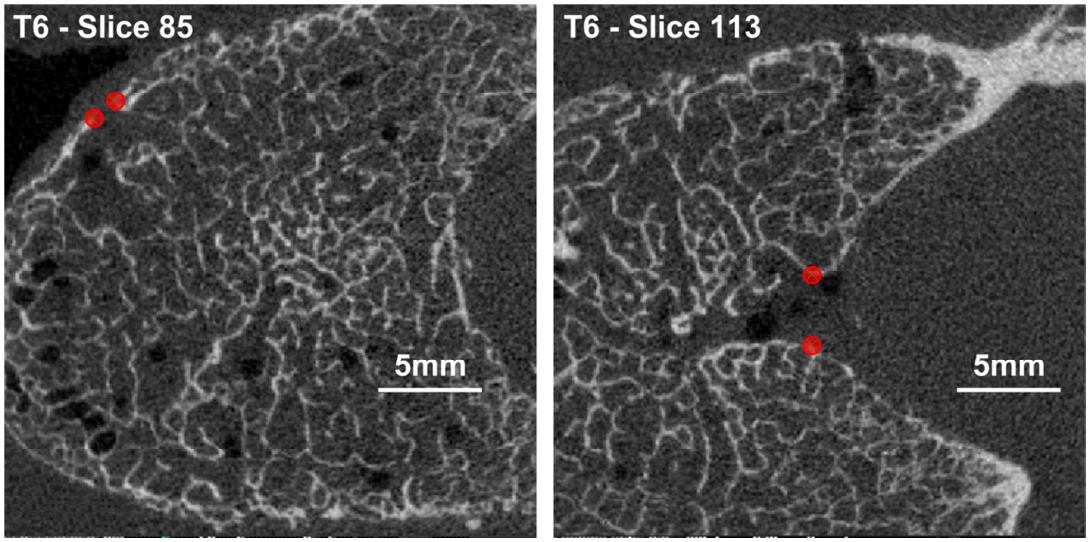

Figure 2. 3 MicroCT slices of a human thoracic vertebra (T6) showing the measurements performed to determine the width of the anterior (left) and posterior (right) breaches in the cortex due to blood vessels. Slice increments are in the craniocaudal direction.

The boundary including the openings and the needle insertion channels (Figure 2.2) were kept constant for all the 3D bone surrogates. However, the structure of the surrogates was tailored to mimic three skeletal pathologies: osteoporosis (Osteo), spinal metastasis (Lesion) and multiple myeloma (MM). To achieve the Lesion and MM surrogates, voids were incorporated into the Osteo structure (refer to Figure 2.1) to mimic the presence of lytic lesions. One large spherical void, 19.0 mm in diameter, was incorporated into the Lesion structure and occupied 11% of the total volume of the surrogate. The size of the void was based on data reported by Ahn et al. [183] and the location was chosen, breaching the posterior wall, to simulate a worst case scenario. The size and location of the voids in the MM structure were based on in-

house microCT scans of six human vertebrae from three donors whose cause of death was multiple myeloma. The DICOM stack of each scan was imported into imageJ [189] and visually inspected slice by slice until a structural void was detected within the vertebral body. The number of slices that spanned the void in the craniocaudal direction was recorded. The width (w) of the void was measured on the middle slice along the anteroposteior and lateral directions. The height (h) of the void was determined through multiplying the number of slices by the scan resolution. Table 2.3 summarizes the measurements performed on the six human thoracolumbar vertebrae to determine the size and location of lytic lesions within the vertebral body.

Table 2. 3 Summary of measurements performed on human thoracolumbar vertebrae to determine the size and location of lytic lesions within the vertebral body due to multiple myeloma. Slice increments are in the craniocaudal direction.

Donor	Level	Scan Resolution (μm)	Total Number of Slices	Lesion Size			Lesion	
				Slice Range	h (mm)	w* (mm)	Location	% vertebra volume
1	T6	74	192	28-75**	3.5	4.5	S, A and C	3.7
	L4	74	280	34-87	3.9	7.1	S, P and C	1.9
				38-69	2.3	4.2	S, P and L	
2	T6	74	182	74-128	4.0	7.3	S, P and L	9.5
				88-153	4.8	5.3	S, P and R	
	L4	74	247	45-174	9.5	15.0	S and C	20.8
3	T6	74	182	86-142	4.1	6.5	I, A and L	3.3
	L4	74	455	347-402	4.1	4.2	I, P and C	1.6
				393-451	4.1	5.0	I, P and L	

* Width (w) presented as the average of measurements along the anteroposteior and lateral directions.
** Three identical, collinear lesions were present (refer to Figure 2.4).
S = Superior, I = Inferior, A = Anterior, P = Posterior, L = Left, R = Right and C = Central

Figure 2.4 shows microCT scans of human thoracolumbar vertebrae with lytic lesions present within the vertebral body. There was no clear trend in the size and location of the lytic lesions among the analyzed microCT scans of the thoracolumbar (T6 and L4) vertebrae from the three donors.

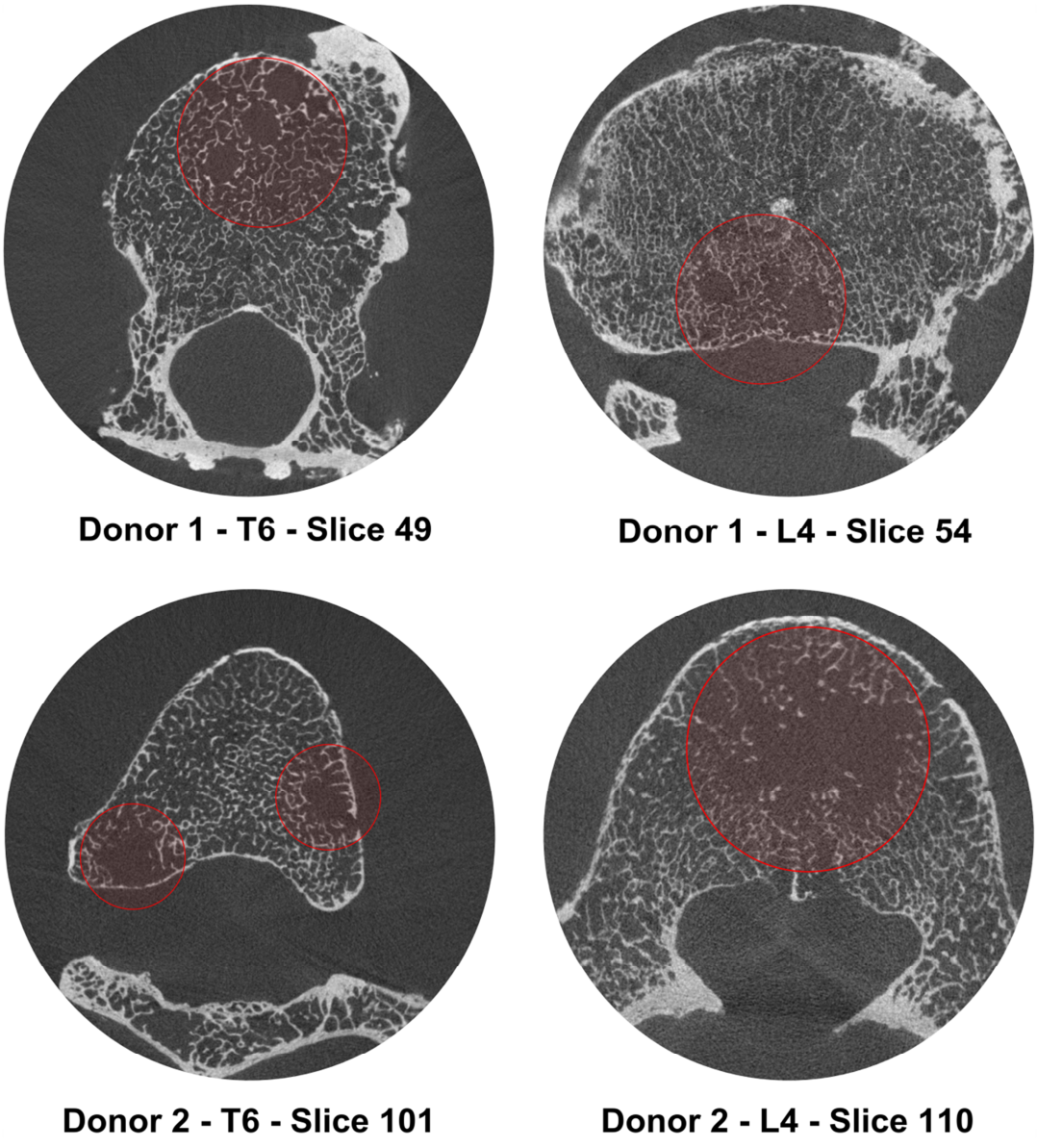

Figure 2. 4 Examples of lytic lesions that have been detected in microCT scans of human thoracolumbar vertebrae (T6 and L4) from two donors whose cause of death was multiple myeloma.

Most vertebrae had multiple small lesions, on average 4.1 ± 0.9 mm in height and 5.4 ± 1.3 mm in width. The L4 vertebra from donor 2 was the only case having one large lesion 9.5 mm in height and 15.0 mm in width. Three spherical voids, 6.0 mm in diameter each, were therefore incorporated into the MM structure and occupied 9% of the total volume of the surrogate. The voids were located 8.0 mm below the superior surface and were collinear along the anteroposterior direction with one of the voids breaching the posterior cortex to simulate a worst case scenario.

Figure 2.5 illustrates the developed Osteo, Lesion and MM bone surrogates with a section-view (left) showing the internal structure of each surrogate and a craniocaudal view (right) showing the elements incorporated into each surrogate. Table 2.4 describes the elements that were incorporated into each bone surrogate.

Table 2. 4 Details of the location and size of all the elements incorporated into the 3D bone surrogates. All coordinates are measured with respect to the centre of each element.

Surrogate	Element	Coordinate			Description
		x	y	z	
Osteo, Lesion and MM	1	0.0	0.0	0.0	Reference point
	2	20.0	0.0	15.3	Outlet, circular Ø 3.0 mm
	3	13.5	-20.6	8.0	Inlet, circular Ø 2.1 mm
	4	8.2	-26.1	9.3	Outlet, elliptical width 1.0 and height 2.0 mm
	5	31.8	-26.1	9.3	Outlet, elliptical width 1.0 and height 2.0 mm
Lesion	6	14.3	0.0	10.0	Outlet, circular Ø 2.7 mm
	7	14.3	-8.9	10.0	Spherical void Ø 19.0 mm
MM	6	14.3	0.0	8.0	Outlet, circular Ø 2.6 mm
	7	14.3	-2.2	8.0	Spherical void Ø 6.0 mm
	8	14.3	-14.9	8.0	Spherical void Ø 6.0 mm
	9	14.3	-23.4	8.0	Spherical void Ø 6.0 mm

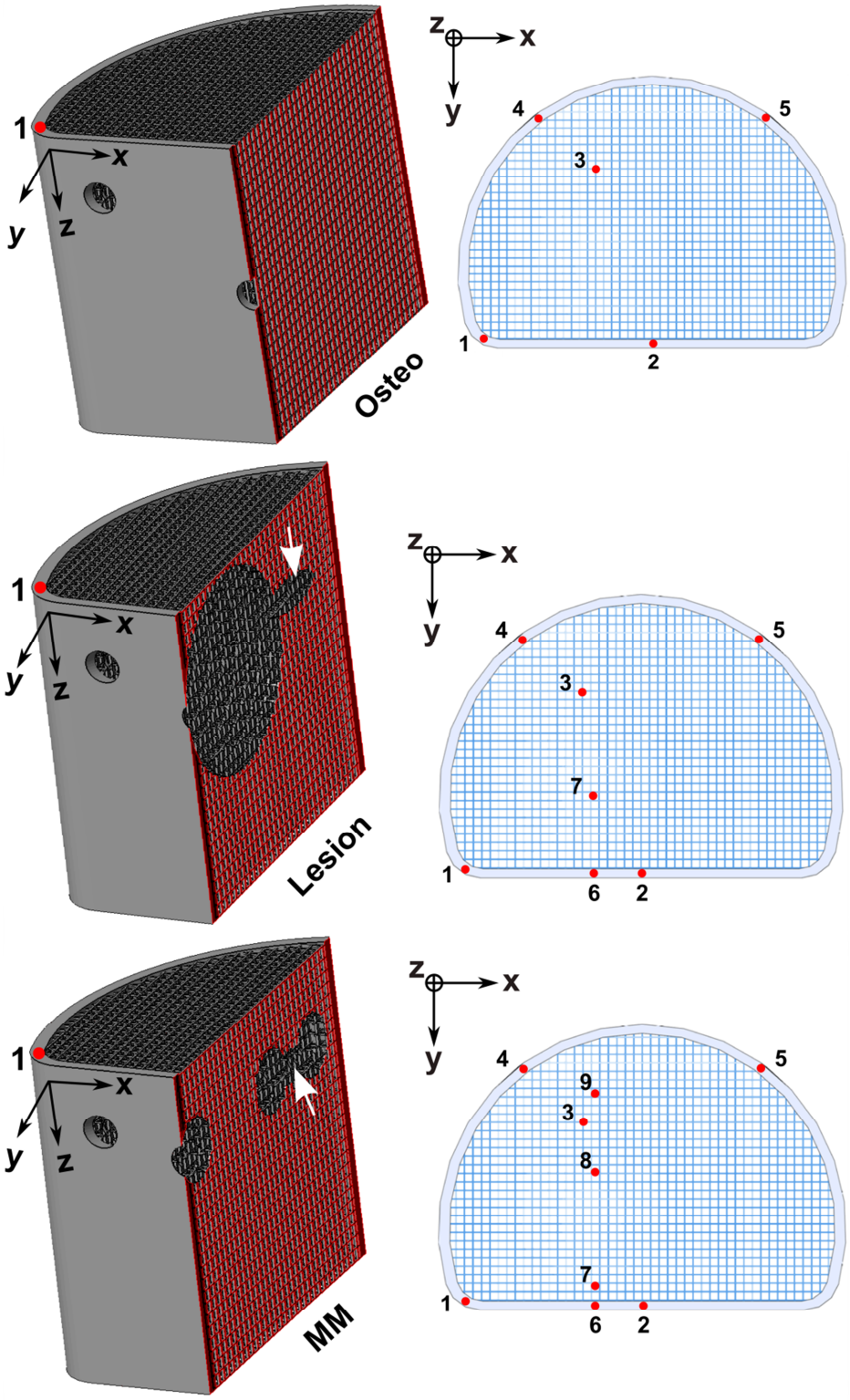

Figure 2. 5 The developed 3D bone surrogates. (Left) Section-view of the Osteo, Lesion and MM surrogates. The white arrows show the needle insertion channels with respect to the lesions. (Right) Craniocaudal view showing the location of all elements incorporated into each surrogate (refer to Table 2.4).

2.2.1 Benchmarking and Manufacturing

Once the models were developed in SolidWorks, they were converted to a special file format known as stereolithography (STL), which is the de facto standard for the RP industry. RP is a special class of machine technology that produces physical 3D models using a layer-by-layer additive approach. RP techniques are most widely classified according to the initial form of raw material used. Liquid based systems begin with the build material in the liquid state, which is then converted to a solid state via a curing process. Powder based systems begin with the build material in granular form, then an energy source is used to increase the temperature and soften the powder particles which results in layer-by-layer particle bonding forming a solid. The RP techniques that have been selected as potential means for manufacturing the proposed models are summarized in Table 2.5.

Table 2. 5 List of selected RP techniques for manufacturing the 3D bone surrogates.

RP Technique	Company	Headquarters
HP DesignJet 3D Printer	Hewlett-Packard	California, USA
Projet HD 3000 3D Printer	3D Systems	South Carolina, USA
Vanguard HS HiQ Selective Laser Sintering	3D Systems	South Carolina, USA
EnvisionTEC Prefatory	EnvisionTEC GmbH	Gladbeck, Germany

The EnvisionTEC Perfactory is a liquid based technique which builds 3D objects using a projector to cure the liquid resin. Sequential voxel planes are projected into the liquid resin with each voxel having dimensions as small as 16 × 16 × 15 µm in the lateral (x), anteroposteior(y) and craniocaudal (z) directions, respectively. Although this technique has a high manufacturing resolution, the main disadvantages are the limited material choice (photopolymer), the inherent distortion of the manufactured object due to the phase change of the liquid resin, and the small build envelope of 80 × 80 × 120 mm in the x, y and z directions, respectively. The selective laser sintering (SLS) machine and the 3D printers are powder based techniques. The SLS machine

uses a laser to heat the powder particles and cause the layer-by-layer particle bonding which forms the solid. The laser spot size (Ø = 0.7 mm) generally limits the manufacturing resolution of such techniques. However, the SLS machine has a large build envelope of 370 × 320 × 445 mm in the x, y and z directions, respectively. The 3D printers, on the other hand, use a binder material (similar to ink-jet printing technology) to selectively join the powder particles. The resolution of such techniques is mainly dictated by the material used and the machine's mechanical components (screw driven systems tend to have a higher resolution in the x-y plane compared to belt and pulley systems). When a thermal RP process is employed, such as in the powder based techniques, the main disadvantage is material shrinkage, which does not always occur uniformly as areas at high temperatures tend to shrink more than those at a lower temperatures [190, 191].

Figure 2.6 illustrates the benchmark part developed to obtain an objective view on the performance of the selected RP techniques and choose the most suitable for manufacturing the 3D bone surrogates. Table 2.6 summarizes the geometrical features included in the benchmark part and their purpose.

Table 2. 6 The geometrical features included in the benchmark part and their purpose.

Label	Feature	Purpose	Number and Size
A	Square Base	Form (base for other features)	Size: 30 x 30 x 5 mm Likely to fit build size of all machines
-	Walls	Linear accuracy and thin wall build	x-direction: 5 and y-direction: 10 width: 1, 0.3, 0.2, 0.1 and 0.05 mm z-direction: height 4, 3 and 2 mm
B	Slots	Linear accuracy and repeatability	x and y-directions: 9 width: 0.4, 0.3, 0.2, 0.1 and 0.05 mm spacing : 0.5, 0.4, 0.3, 0.2 and 0.1 mm
C	Solid Beams	Linear accuracy and repeatability	x-direction: 12 and y-direction: 9 square base: 0.06, 0.1, 0.12 and 0.17 mm z-direction : 12 square base: 0.15, 0.18, 0.2 and 0.25 mm
D	Solid Cylinders	Comparison with solid beams	Same as Solid Beams but with cylinders
E	Circular Holes	Build capability	x, y and z-directions: 5 diameter: 0.5, 0.4, 0.3, 0.2 and 0.1 mm

The benchmark part was developed in SolidWorks and adapted to include geometrical features that were related to our own work [192]. The aim of the benchmark part was to comparatively test the selected RP techniques in terms of geometrical accuracy and repeatability in the x, y and z-directions, respectively. A detailed drawing of the benchmark part is presented in Appendix A.

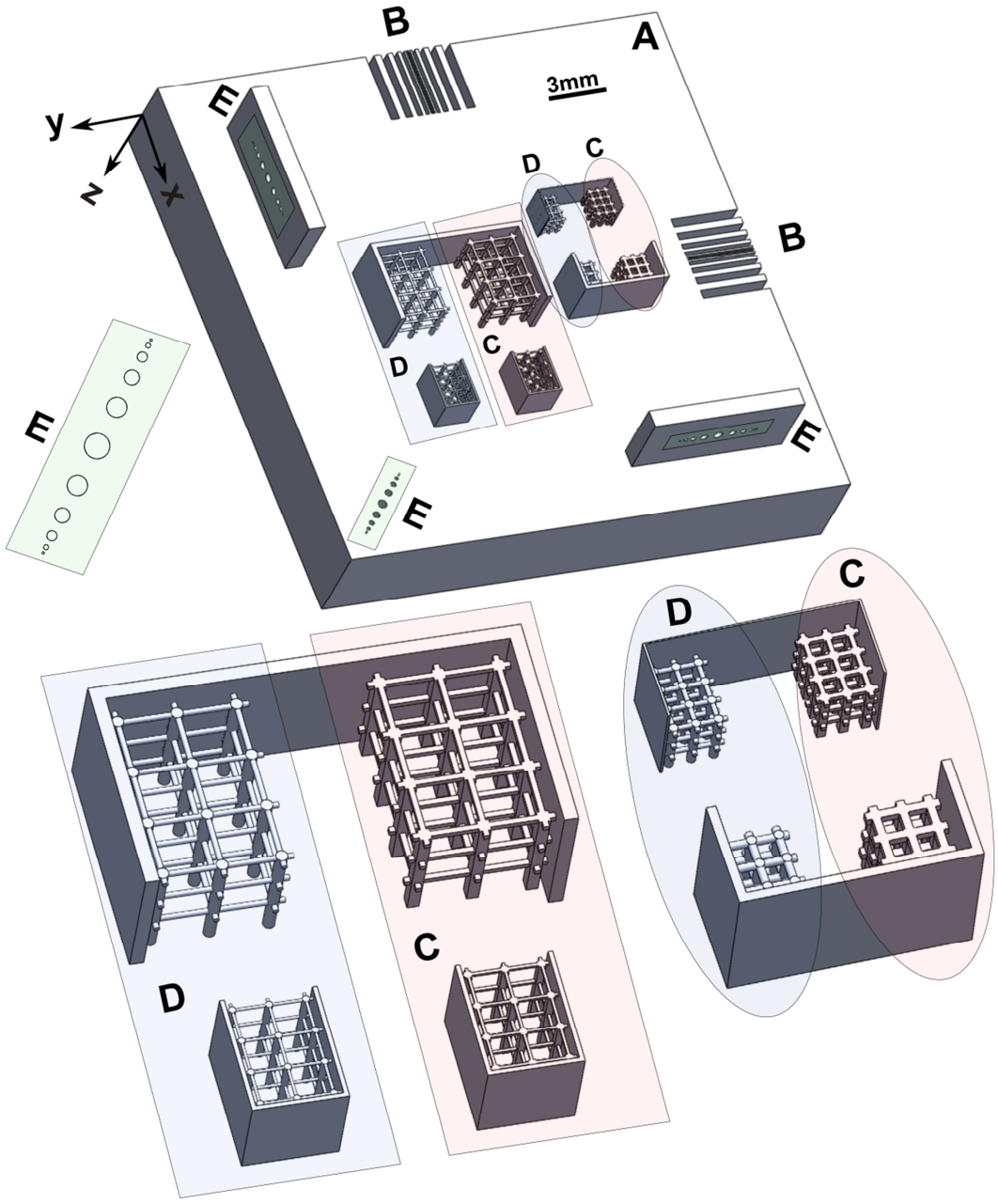

Figure 2. 6 The benchmark that was used to comparatively test the geometrical accuracy of the selected RP techniques.

Qualitative and quantitative assessments were performed once the benchmark part was manufactured. Visual inspection was used to identify the benchmark part with the best quality and form. The dimensions of the various benchmark features were quantified using a profile projector (Model V-16D, Nikon Corporation, Tokyo, Japan) to determine the RP technique with the highest geometrical accuracy and repeatability (i.e. build resolution). The benchmark part was placed on the x-y table of the profile projector (Figure 2.7).

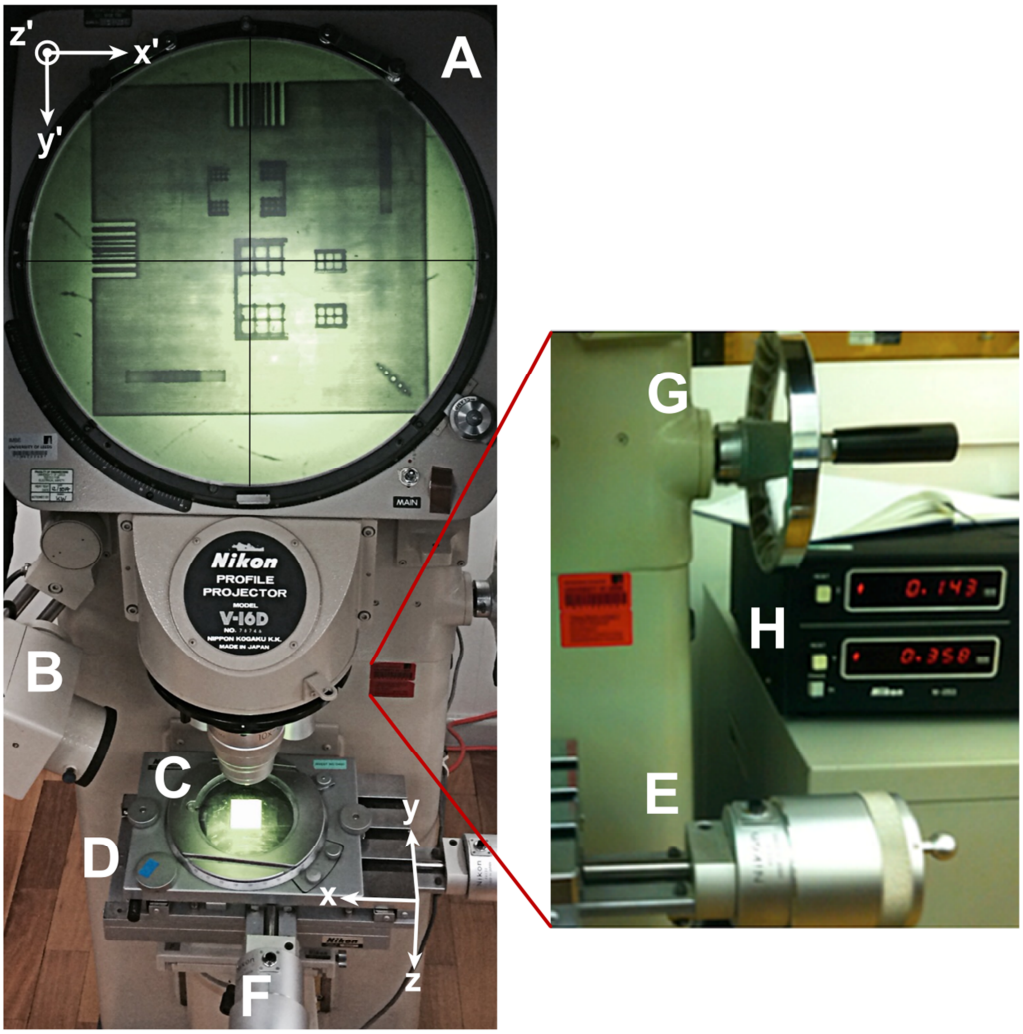

Figure 2. 7 The profile projector used to quantify the dimensions of the benchmark features. (A) is the 400 mm projection screen with reference lines along the x and y-axes showing the Projet HD benchmark using a '×10' magnification. (B) is the light source. (C) is the 230 × 170 mm x-y table where the benchmark part is placed. (D) is the dial that controls the rotation of the table about the z-axis. The two knobs (E and F) and the wheel (G) control the movement of the table along the x, y and z-axes, respectively. (H) is the 0.001 mm precision display for movements along the x and y-axes.

The height of the table was adjusted using the wheel (G) to ensure that the edges of the desired features are in focus. The dial (D) was used to adjust the rotation of the table and ensure that the square base of the benchmark was aligned with the x and y-axes. The knobs (E and F) were used to move the x-y table and target a particular feature (i.e. walls, slots, beams, etc.). Once the reference lines on the screen (A) were aligned with the edge of a feature, the precision display was zeroed and the knobs were used to move the table until one of the reference lines (along the x or y-axis) reached the opposite edge of that feature. The value of the precision display was recorded. This process was repeated for each visible geometrical feature. Three independent measurements were obtained and the results were presented in terms of the average of the three measurements and the range of the measurement error. The overall linear dimensional accuracy of each RP technique was calculated by taking the total average difference between the measured geometrical dimensions and their respective actual, true dimensions in SolidWorks.

The benchmark surface finish was assessed using a non-contact profiling system (Wyko® NT3300™, Veeco, Plainview, New York, USA) to compare the surface characteristics to that of cortical bone from a dry human femur. The surface texture analysis was performed on the same 0.9 × 1.9 mm area of each benchmark part (Figure 2.6 adjacent to label A) using white light interferometry to produce the surface topographical image of each area. In this technique (Figure 2.8), light from a single source (i.e. laser or LED) is split into two beams: one goes to an internal reference mirror and the other goes to the sample. The two beams are then reflected and recombined inside the interferometer. This causes the beams to undergo constructive and destructive interference producing patterns of light fringes that represent the surface topography of the area being tested. The fringes result from the difference in optical path lengths that the beams travel in the reference and test arms. This process allows the measurement of a number of different parameters including the ISO 25178 height parameters, which were compared between all the benchmark parts. The height parameters included in the comparison were: S_a which is the average roughness evaluated over the complete three-dimensional surface as well as S_p and S_v which are

evaluated from the absolute highest and lowest points found on the surface. S_p is the height of the highest point and is referred to as the maximum peak height. S_v is the depth of the lowest point and is referred to as the maximum valley depth, which is expressed as a negative number [193, 194].

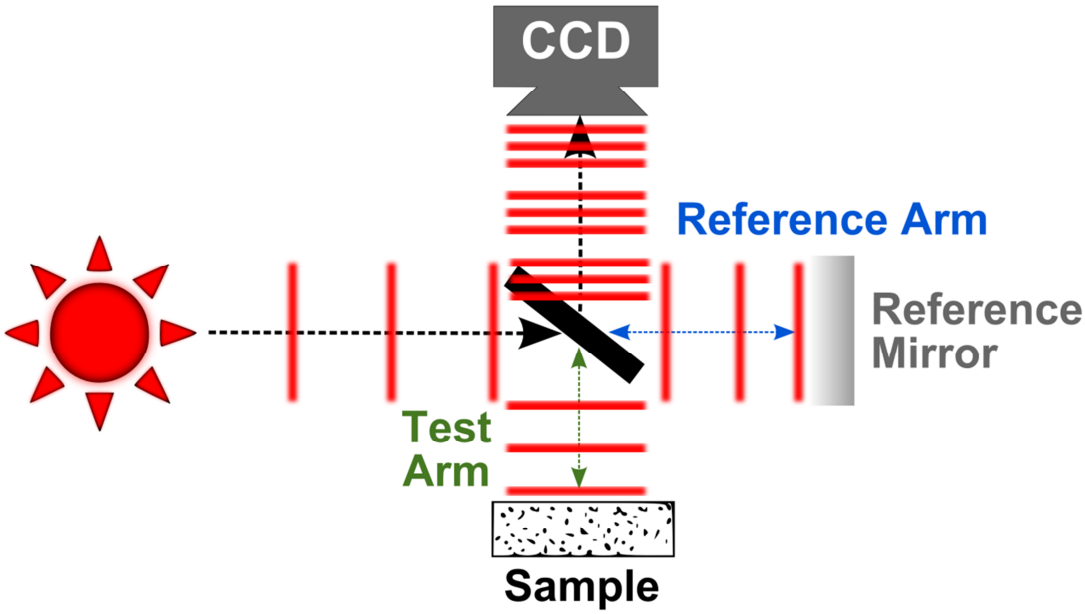

Figure 2. 8 Mechanism of white light interferometry. Light is divided by a beamsplitter (solid black rectangle) into two beams: one is reflected from the reference mirror and the other from the sample. These two beams are then recombined by the beamsplitter and the difference in optical path lengths that the beams travel in the reference and test arms is captured on the CCD camera. Adapted from [194].

2.2.2 Morphology Characterization

From the analysis of the manufacturing methods described in section 2.2.1, the bone surrogates presented in Figure 2.5 were manufactured. MicroCT (µCT 100, Scanco Medical, Switzerland) was used to assess the variability in the morphology. Eight osteoporotic type (Osteo) 3D bone surrogates were scanned at a 24.6 µm spatial resolution (isotropic voxel size) with an integration time of 300 ms, a tube voltage of 70 kV, a tube current of 114 µA and a 0.1 mm aluminum filter. Then, a cylindrical volume of interest 15 mm in diameter and 15 mm in length was consistently defined at the center of each specimen. Within this volume of interest, three-dimensional structural parameters were determined using the following settings: Sigma 1.2, Support 2.0, Threshold -120 HA mg/ccm (based on Ridler's method [30]), and the

software provided by the manufacturer. Only the bone volume fraction (BV/TV) in %, trabecular thickness (Tb.Th) in mm, and trabecular separation (Tb.Sp) in mm were compared.

Porosity

The porosity of the Osteo surrogates was obtained from the microCT data (100 - BV/TV) and cross-validated using Archimedes' suspension method of measuring volume [195] which was performed using six cubes ($2 \times 2 \times 2$ cm^3) with the same structure as the Osteo surrogates. Based on this method (Figure 2.9), a container filled with purified water was weighed using an electronic balance with an accuracy of ± 0.01 g. Each cube was suspended below the surface of the water and a slight vacuum was applied for five minutes to ensure all air bubbles were removed.

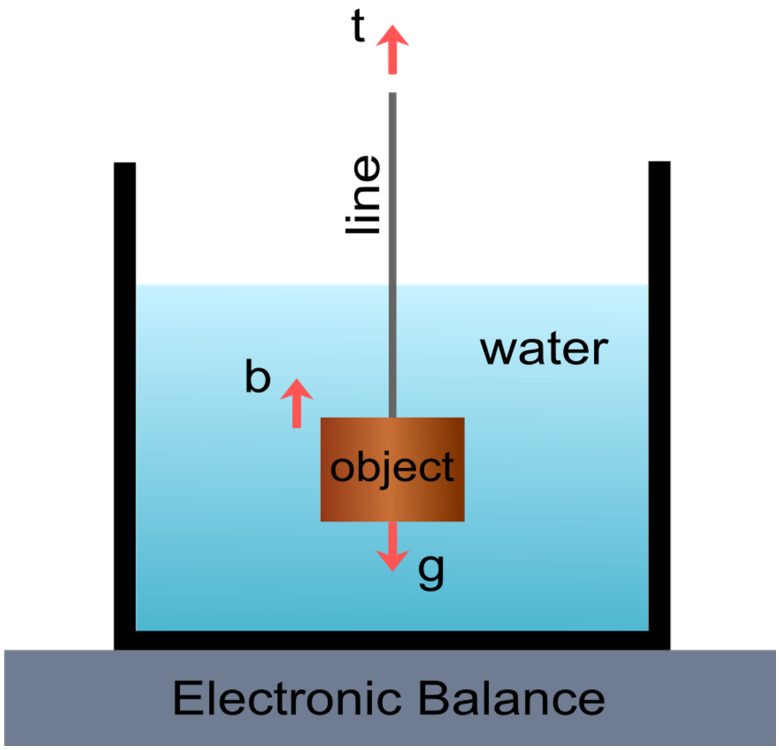

Figure 2. 9 Schematic representation of Archimedes' suspension method of measuring volume. An object is suspended below the surface of the water in a container placed on an electronic balance. Since the object is stationary, the sum of the forces acting on it is zero. Thus, the downward force due to gravity (g) is balanced by the upward buoyancy (b) and line tension (t). Consequently, the immersed object is equivalent to a 'virtual' volume of water of exactly the same size and shape. Adapted from [195].

The container (with the suspended cube) was weighed again using the electronic balance and the change in weight was recorded. The volume of each cube was calculated using $V = \Delta w/\rho$, where Δw is the change in weight recorded by the balance and ρ is the density of the water. This allowed measuring the material volume (V_m) of each cube. A caliper was used to measure the outer dimensions, thus calculate the total volume (V_t) of each cube. The porosity or void fraction was therefore calculated using $\varphi = 1 - V_m/V_t$.

Permeability

One of the six cubes ($2 \times 2 \times 2$ cm^3) that were used for measuring the porosity was also used to experimentally derive the permeability of the Osteo surrogates using Darcy's law [172, 196]. The cube with the same structure as the Osteo surrogates was fixed at the end of a long (1.0 m) clear rigid tube held vertically (Figure 2.10). A silicone sealant was used to seal the perimeter of the cube. A valve was used to continuously fill water into the top end of the tube. The valve flow rate was controlled to achieve a constant column of water at various heights. Once this was achieved, the height was recorded and a container was used to collect the water filtering through the sample. A stopwatch was started as the container was placed under the sample and stopped as it was removed. The time was recorded and the container was weighed using an electronic balance with an accuracy of ± 0.01 g. A temperature probe was used to measure the temperature of the water. This process was repeated three times for each constant column of water. The time and the weight (i.e. volume) allowed calculating the flow rate of the water passing though the Osteo structure. The height of the water column allowed calculating the pressure using the hydrostatic pressure equation ($p = \rho \cdot g \cdot h$). The flow rate was then plotted against the pressure and the permeability was computed using Equations 19 and 20.

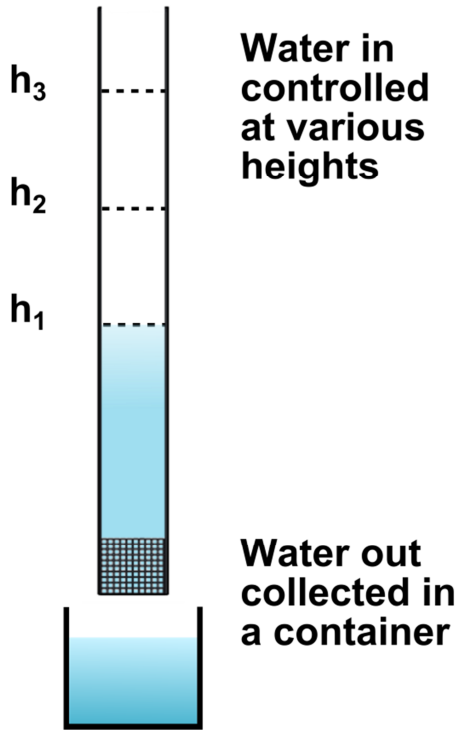

Figure 2. 10 Schematic of the experimental set-up designed to measure the permeability of the Osteo structure.

Contact Angle

Contact angle measurements were performed on the material used to manufacture the 3D bone surrogates to compare the surface wettability to that of cortical bone from a dry human femur and a fresh ovine vertebra. Static contact angle analysis (FTA 4000, First Ten Angstroms, Virginia, USA) was performed on each sample in six locations. For the 3D bone surrogates, samples were obtained from four different manufacturing time points (total of 24 measurements). Each sample was placed on a round stage, approximately 100 mm in diameter, and rotated under a dispense tip. A drop of water was dispensed onto the surface of the samples. An analytical microscope with a horizontal field of view ranging from 2 mm down to 200 µm was used to allow lateral visualization of the water droplet on the surface of the samples (Figure 2.11). As the water droplet touched the surface, the image was captured and analyzed using proprietary software (FTA32, First Ten Angstroms, Virginia, USA). The results were assessed using Kruskal-Wallis one-way analysis of variance by ranks ($\alpha = 0.05$).

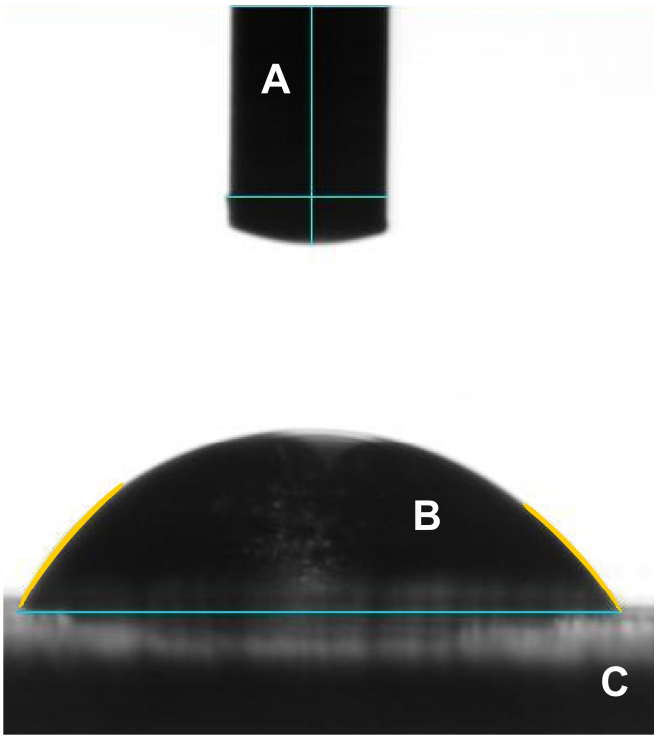

Figure 2. 11 Contact angle measurement performed on the surface of the material used to manufacture the 3D bone surrogates showing the dispense tip (A) through which the water drop (B) is dispensed onto the surface of the material (C).

2.3 2D Flow Models

Flow models represent an alternative simulated environment to quickly and effectively study the flow behaviour of different bone cement formulations. Although they only allow fluid flow in one plane, the flow models have a key advantage over 3D bone surrogates in terms of monitoring the cement flow during the injection, which is performed using a camera instead of a fluoroscope. This simplifies the experimental set-up and avoids exposure to x-rays.

Flow models were developed to represent a cross-section of the vertebral body. Each model was placed in a specimen holder (Removable Cage Plate, Thorlabs, New Jersey, USA) with its pattern facing up. A circular glass window (Ø= 50 mm) was placed on top of the model and a threaded ring was used to press the window against the model creating a tight seal (Figure 2.12). The trabeculae were represented as a series of solid columns (Ø= 0.25 mm; h= 0.5 mm) with a 1 mm intercolumnar spacing

to simulate the trabecular separation that has been reported for human vertebral osteoporotic bone [31, 33]. The injection inlet (Ø= 2.4 mm) was chosen to simulate the inner diameter of 11-gauge needles. The external shape was circular with a solid boundary to mimic the vertebral shell. A single flow exit point (Ø= 2.5 mm) was applied at the outer boundary to simulate a breach through the cortex due to a fracture or a blood vessel exchanging blood in and out of the vertebral body.

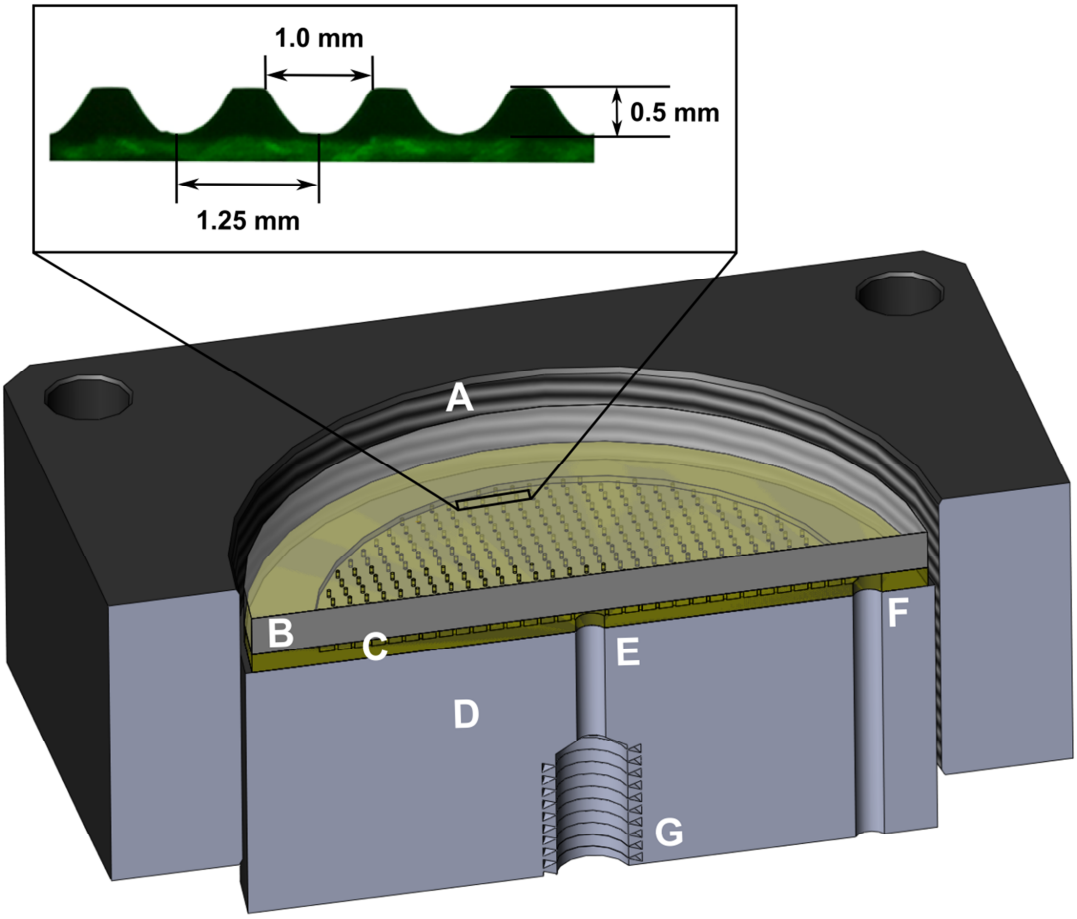

Figure 2. 12 Section-view of the specimen holder showing the threadeding (A) into which an aluminum ring is screwed to press the glass window (B) against the flow model (C) which is placed on the surface of an aluminum cylinder (D) with its pattern facing up. (E) shows the injection inlet and (F) shows the flow exit point. Fluid injections are performed using a luer-lok syringe which is attached to the threaded hole (G) via a female luer to 1/4-28 UNF adapter. The call-out shows a lateral view of the actual structure as visualized using a profile projector.

The structure of the flow models (Figure 2.13) was tailored to mimic three different skeletal conditions: osteoporosis (Osteo), spinal metastasis (Lesion) and vertebral fracture (Fracture). For the Osteo models, the solid columns representing the

trabeculae were uniformly distributed in a grid pattern. The thickness and spacing of the columns were chosen to yield a nominal porosity of 95.1%. To achieve the Lesion and Fracture models, voids were incorporated into the Osteo structure. The Lesion model included one large circular void, 19.0 mm in diameter, breaching the outer boundary at the flow exit point. The size and position of the void were chosen to simulate a cross-section of the developed 3D Lesion surrogates (Figure 2.5). Conversely, the fracture model included a horizontal cylindrical void, 2.5 mm wide, along the flow exit point. The void in this model was chosen to study and highlight the effect of a fracture plane (breaching the cortex) on the flow behaviour.

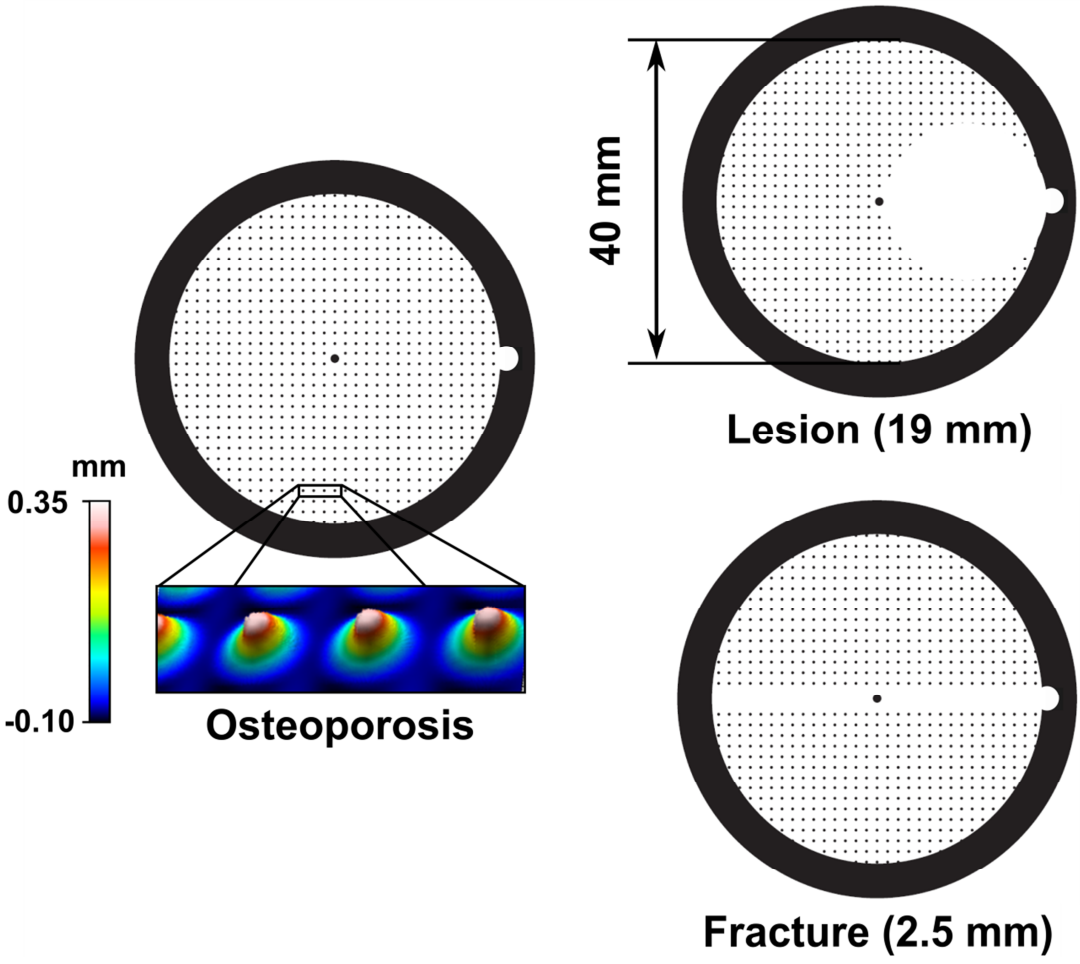

Figure 2. 13 The developed 2D flow models with 1 mm channel spacing, 0.25 mm column thickness, 50 mm outer diameter and a solid boundary representing the vertebral shell.

The 2D flow models were first designed in a graphic suite (CorelDRAW, Corel Corporation, Ontario, Canada) then manufactured via flexography (AFP-SH/DSH,

Asahi Photoproducts Europe, Brussels, Belgium), a technology used extensively within the print industry where a high degree of reproducibility is required. Once the models were manufactured, inter- and intra-variability in the model geometry was assessed. Left and right cuts were consistently performed through the sagittal plane close to the centre of three osteoporosis type models. A profile projector (Model V-16D, Nikon Corporation, Tokyo, Japan) was used to visualize the cuts from a lateral perspective and test the geometrical variations in terms of valley-to-valley (D_{vv}) and edge-to-edge (D_{ee}) distances as well as the total height (h) of the profiles (Figure 2.14). The profile projector was also used to measure the porosity of the flow models. Furthermore, static contact angle analysis (FTA 4000, First Ten Angstroms, Virginia, USA) was performed on two samples obtained from different manufacturing time points, each in six locations (12 measurements), to compare the surface wettability to that of cortical bone from a dry human femur and a fresh ovine vertebra.

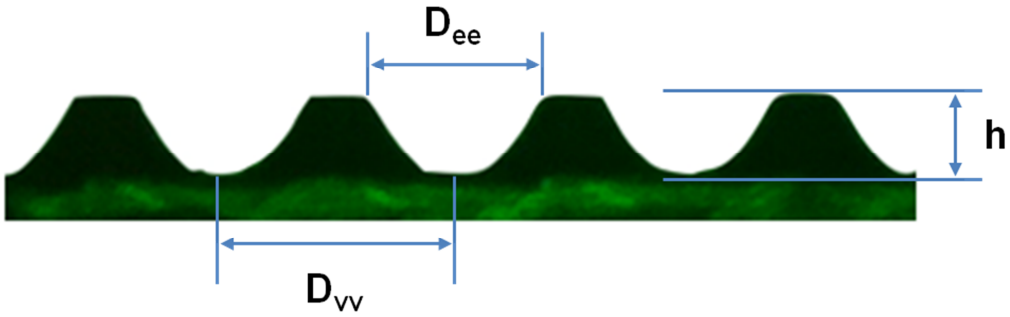

Figure 2. 14 Lateral profile of a cut through the sagittal plane of a flow model showing the measurements performed to test the geometrical variations in terms of the valley-to-valley (D_{vv}) and edged-to-edge (D_{ee}) distances as well as the total height (h).

2.4 Bone Marrow Substitute

The developed bone surrogates were filled with bone marrow substitute to simulate the rheological environment of the vertebral body in terms of bone marrow present within the bony channels. An aqueous solution of carboxymethyl cellulose (M_w ~250,000 - Sodium carboxymethyl cellulose, Sigma-Aldrich, MO, USA) 2.5% w/w was used as the bone marrow substitute with a nominal viscosity of 0.4 Pa·s which has been reported for red bovine marrow [156]. An additional formulation for the marrow substitute was also tested to assess its effect on the injection behaviour. This marrow

substitute formulation was prepared using an aqueous solution of carboxymethyl cellulose 1.25% w/w to reach a nominal viscosity of 0.06 Pa·s which has been reported for human blood [160]. The viscosity of the marrow substitutes was verified using a rheometer (Section 2.8).

2.5 Cement Preparation

Four brands of commercially available acrylic bone cements were comparatively tested (Table 2.7): Opacity+ (OC, Teknimed S.A.S, Bigorre, France), Osteopal V (OP, Heraeus Medical GmbH, Hanau, Germany), Parallax (PL, ArthroCare Corporation, Austin, TX, USA), and Simplex P (SP, Stryker Corporation, Kalamazoo, MI, USA).

Table 2. 7 Bone cement compositions and liquid/powder (L/P) ratios. A modified formulation was used for Simplex P and two L/P ratios were tested for comparison (SP1:2 and SP1:1).

	Composition	Opacity+	Osteopal V	Parallax	Simplex P (Regular)	Simplex P (Modified)
Liquid (v/v %)	Methyl methacrylate	99.0	92.0	99.0	97.5	97.5
	N,N-dimethyl-*p*-toluidine (DMPT)	1.00	2.00	1.00	2.50	2.50
	Other additives [a]	-	6.00	-	-	-
Powder (w/w %)	Poly(methyl methacrylate)	49.5	-	-	15.0	13.5
	Poly(methyl acrylate-*co*-methyl methacrylate)	-	54.6	-	-	-
	Poly(methyl methacrylate-*co*-styrene)	-	-	69.9	73.7	66.4
	Zirconium dioxide (ZrO_2)	45.0	45.0	-	-	-
	Barium sulphate ($BaSO_4$)	-	-	29.4	10.0	19.0
	Hydroxyapatite (HA)	5.00	-	-	-	-
	Benzoyl peroxide (BPO)	0.50	0.40	0.70	1.30	1.10
	L/P	1/2.7	1/2.6	1/2.4	-	1/2 [b] 1/1 [c]

[a] Usually hydroquinone is added as monomer stabilizer in concentrations on the order of ppm.
[b] SP1:2 prepared using 10 g of the modified Simplex P powder + 5 mL of liquid
[c] SP1:1 prepared using 10 g of the modified Simplex P powder + 10 mL of liquid

All the selected cements, except for Simplex P, are specifically formulated with a high radiopacifier concentration for use in PVP. However, commercially available brands

used in cemented arthroplasties (mainly Simplex P) have been used in PVP with an extra amount of radiopacifier added by the surgeon to bring the concentration to 20–30% w/w of the powder and increase the radiopacity of the cement [90, 151]. For this reason, a modified formulation for Simplex P was also used in this study. Each batch of cement was prepared according to the liquid-to-powder (L/P) ratio recommended by the manufacturer. For Simplex P, an additional L/P ratio (SP1:1) was also tested to assess its effect on the injection behaviour [122]. All powders were weighed in vials with an accuracy of ± 0.01 g and all liquids were measured using micropipettes with an accuracy of ± 2 μL. The timer on a stopwatch was started as the liquid monomer was added to the powder. Subsequently, the vial was capped and vigorously shaken for 30 s to uniformly distribute the liquid monomer throughout the powder. A metal spatula was then used to further mix the components for another 30 s ensuring no dry powder areas were visible in the vial. The times for which the cements were mixed and handled are summarized in Table 2.8. A standard protocol was adopted in all the experiments and involved mixing the cement for 1 min (shaking and stirring) then allowing the mixing vial to rest on its side for 1.5 min before the cement was transferred into a luer-lok syringe.

Table 2. 8 Procedure times from the addition of the liquid to the powder.

Brand	Notation	Mixing time (min)		Waiting time (min) [b]		Maximum application time (min)	
		Protocol A	Protocol B	Protocol A	Protocol B	Protocol A	Protocol B
Opacity +	OC	1.0	1.0	4.0	3.0	8.0	12.5
Osteopal V	OP	1.0	0.5	4.0	2.5	8.0	8.0
Parallax	PL	1.0	1.0	4.0	3.0	8.0	12.0
Simplex P	SP1:2	1.0	1.0 [a]	4.0	-	8.0	10.0
	SP1:1	1.0	1.0 [a]	4.0	-	8.0	10.0

Protocol A was standardized for all the materials.
Protocol B is recommended by the manufacturer for a temperature of 20°C and is included for comparison.
[a] Mixing time is recommended as a range between 1 and 2.5 minutes.
[b] Waiting time is the total time after mixing prior to cement application, including the time the cement is in the syringe.

Due to its known contribution to the flow behaviour [140], the morphology of the powder components was assessed through Scanning Electron Microscopy (SEM). The specimens were sputter-coated with palladium prior to image acquisition. The images were acquired on a LEO 1550/EVO MA15 (Carl Zeiss AG, Oberkochen, Germany) microscope, operated at an acceleration voltage of 2 kV with a secondary electron detector to achieve topographic contrast.

2.6 Silicone Oil

As acrylic bone cements are chemically complex, multi-component and significantly non-Newtonian with their viscosity having differing degrees of time and shear-rate dependency, Newtonian fluids 10 and 60 Pa·s silicone oil (200® Fluid, Dow Corning Corp, Michigan, USA) were tested to compare their effect on the injection behaviour. The silicone oils were mixed with 20% v/v Lipiodol (Guerbet, Villepinte, France), which is an oil-soluble radiopacifier, to allow their visualization under fluoroscopy. A high concentration was chosen to ensure that the oil was saturated with the Lipiodol. The viscosity of the silicone oil was verified using rheology to ensure Newtonian fluid behaviour after the addition of the Lipiodol (Section 2.8).

2.7 Testing Protocol

This section details the methods that were developed to allow fluid injections into the bone surrogates under a controlled environment through measuring the injection pressure and flow rate as well as monitoring the flow distribution. Two experimental testing rigs were developed to allow the injections to be performed under displacement control achieving a constant flow rate. One system uses a syringe pump, while the other uses a materials testing machine to control the displacement of the syringe plunger and achieve a constant injection flow rate. For the 3D bone surrogates, a fluoroscope was used to monitor the flow distribution. However, the 2D flow models have a key advantage over the currently developed and previously used 3D bone surrogates in terms of monitoring the flow distribution during the injection, which is

performed using a camera instead of a fluoroscope. This simplifies the experimental set-up and avoids exposure to x-rays.

2.7.1 3D Bone Surrogate Injections

This section details the methods that were designed to allow injections into the 3D bone surrogates under a controlled environment. The schematic of the experimental set-up is presented in Figure 2.15.

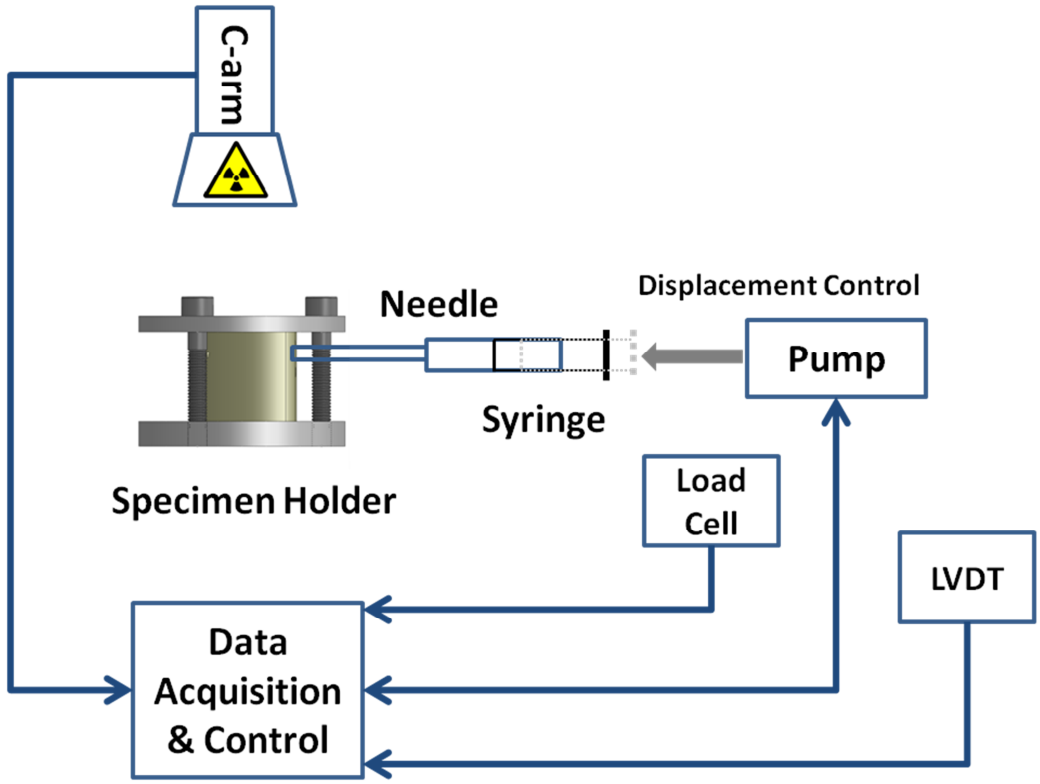

Figure 2. 15 Schematic of the experimental set-up designed for use with the developed 3D bone surrogates. The main components include a syringe pump, a load cell, an LVDT, a 10mL luer-lok syringe, a gauge 12 needle, a specimen holder, and a fluoroscope. A personal computer running LabVIEW software was used to allow data acquisition.

The syringe pump (Nexus 6000, Chemyx, Texas, USA) was used to control the displacement of the syringe plunger and achieve a constant injection flow rate. This is a high pressure, screw-driven syringe pump with a 0.05 µm step resolution and is capable of delivering up to 2.2 KN of linear force. The LVDT (LDC2000A, RDP Electronics Ltd, Wolverhampton, UK) was used to determine the displacement of the

syringe plunger and obtain a second, independent measure of flow rate. The displacement measurements were calculated based on previously determined calibration curves (Appendix B). The load cell (Model 31, Honeywell-Sensotec, Minneapolis, USA) was used to measure the force (N) applied on the syringe plunger, thus calculate the pressure (MPa) in the system. The force measurements were also calculated based on previously determined calibration curves (Appendix B). A photograph of the actual set-up (without the fluoroscope) is presented in Figure 2.16.

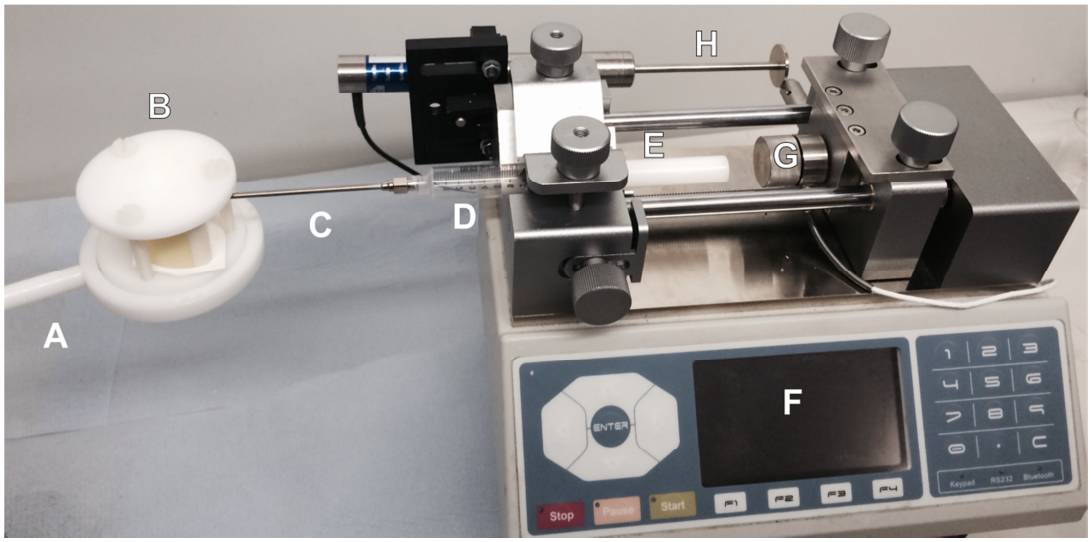

Figure 2. 16 Photograph of the experimental set-up designed for use with the developed 3D bone surrogates showing: (A) the specimen holder with (B) the 3D bone surrogate, (C) the 12 gauge needle, (D) the 10 mL luer-lok syringe with (E) a custom built plastic plunger (Delrin®, DuPont, Delaware, USA), (F) the syringe pump, (G) the load cell and (H) the LVDT.

A fluoroscope (BV-25, Philips, Eindhoven, Netherlands) was used to radiographically monitor the injection, while a specimen holder attached to a tripod was designed to keep the 3D bone surrogates at the same height with respect to the fluoroscope and ensure that the top plane of the surrogates was parallel to the plane of the fluoroscope (Figure 2.17). The video data from the fluoroscope was captured using Debut software (NCH Software, Canberra, Australia). All data was acquired at a sampling frequency of 25 Hz.

LabVIEW software (2010 SP1, National Instruments, Texas, USA) was used control the syringe pump through serial communication. A custom LabVIEW code

(refer to Appendix C) was developed to allow starting and stopping the pump as well as setting the injected volume and flow rate. LabVIEW software was also used to acquire the load cell and LVDT data. The signals from both transducers were pre-conditioned using appropriate amplifiers (RDP Electronics Ltd, Wolverhampton) then acquired using a data acquisition system (cRIO-9074 chassis, National Instruments, Newbury, UK).

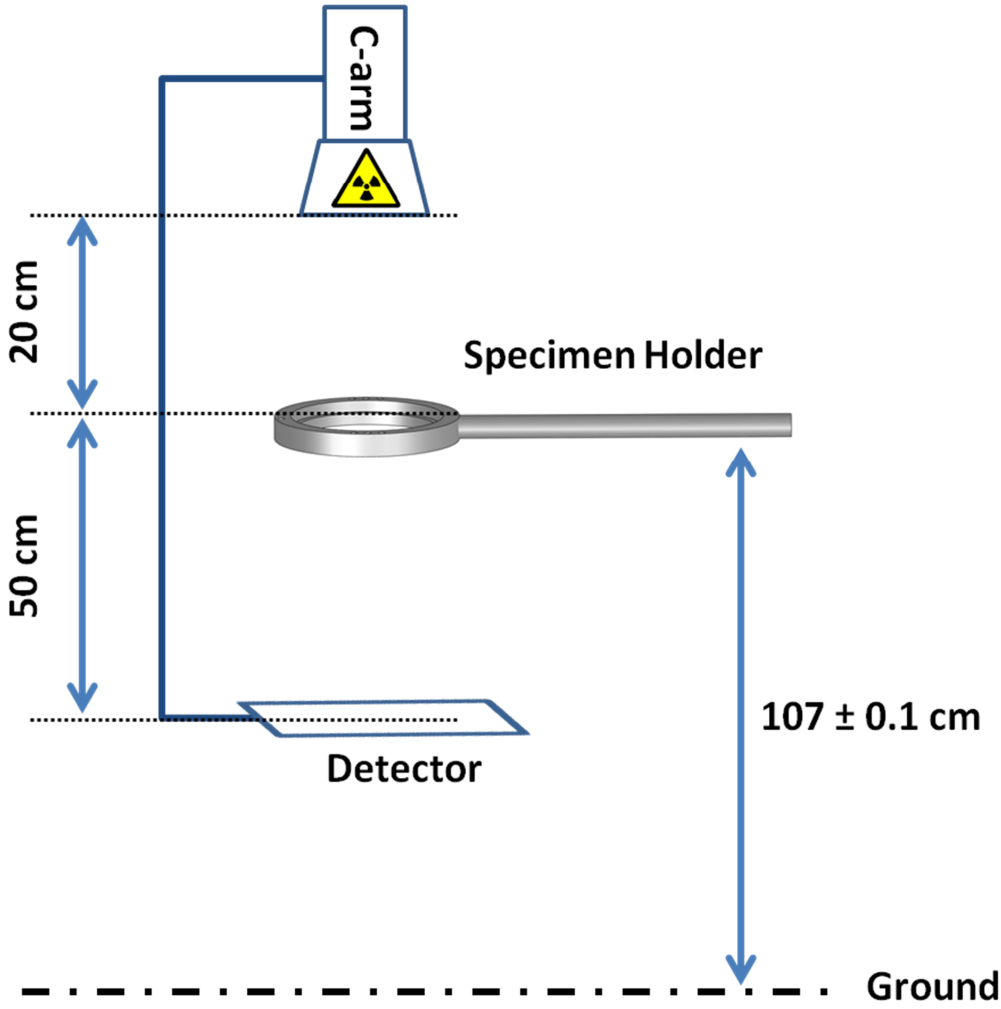

Figure 2. 17 Schematic showing the height of the specimen holder that was standardized for all injections performed using the 3D bone surrogates.

A custom LabVIEW code (refer to Appendix C) was developed to allow real-time reading of the signals at a pre-defined sampling frequency (25 Hz) and logging of the data into a spread sheet. The architecture of the program was based on the

Producer/Consumer design. In this design, the signal is acquired in the producer loop then streamed using a data queue to the consumer loop, where it is handled based on the state machine algorithm. The state machine divides the handling algorithm into simple tasks (i.e. data plotting, calibration, logging, etc.), which execute depending on the pre-determined conditions. The data acquisition was tested and validated to ensure that the LVDT and load cell data were synchronized and simultaneously saved into a spread sheet.

Fluid Injection

As the superior and inferior surfaces of the 3D bone surrogates were kept open due to manufacturing restrictions, silicone rubber sheets were placed on these surfaces, then superior and inferior plates (Delrin®, DuPont, Delaware, USA) were used to push the rubber sheets against the surrogates creating a tight seal (Figure 2.18).

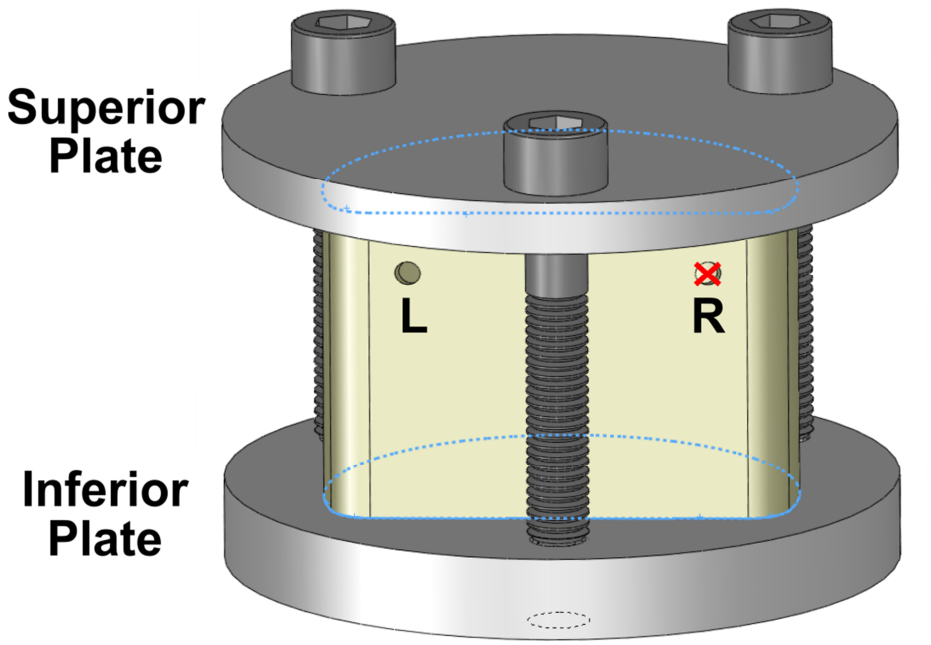

Figure 2. 18 3D surrogate ready for injection with the plates used to push the silicone rubber sheets against the superior and inferior surfaces (blue lines) of the surrogates creating a tight seal. The injections were consistently performed through the left insertion channel (L), while the entry point of the right insertion channel (R) was closed off on the outer surface of the boundary.

A standardized protocol was used to fill the surrogates with the bone marrow substitute. A high strength adhesive tape was used to seal all openings incorporated

into the boundary of the surrogates (Figure 2.2). The surrogates were then placed on top of the inferior plate and submerged in a container filled with the marrow substitute. The container was vacuumed for five minutes to ensure all air bubbles were removed. While the surrogates were still in the container, the superior plate was placed on top of the surrogates and nylon screws (Nylon 6.6 M6×50, Premier Farnell plc, London, United Kingdom) were used to fasten the superior and inferior plates pushing the silicone rubber sheets against the surrogates, thus creating a tight seal and confining the marrow substitute within the surrogates

Following this, the adhesive tape was removed from all openings except the one used to seal the entry point of the right needle insertion channel. The surrogates were then placed into the experimental set-up (Figures 2.15 and 2.17) and 5 mL of Newtonian fluid 10 and 60 Pa·s silicone oil as well as Simplex P (SP1:1, Table 2.7) bone cement were separately injected into each bone surrogate (Osteo, Lesion and MM) at a constant flow rate of 3 mL/min. This process was repeated three times. The injections were performed using a 10 mL luer-lok syringe (Becton Dickinson, New Jersey, USA) with a 12-gauge needle (Blunt SS 12-gauge × 4 inch, W. W. Grainger Inc, Illinois, USA). For the Simplex P bone cement, two injection time points (4 and 8 min from the addition of the liquid to the powder) were tested to assess the effect on the flow behaviour. The same syringe, needle and cement were used to perform the two injection time points into separate surrogates. All the injections were performed at room temperature (21.5±0.1ºC) using a unilateral approach. The needles were consistently placed through the left insertion channel, while the entry point on the outside of the right insertion channel (i.e. outer surface of the surrogate boundary) remained closed off to prevent any fluid from escaping through the cortex. The error in the needle placement within the 3D bone surrogates was quantified through measuring the needle length (d) from the posterior wall and the needle angle (α) relative to the posterior wall (Figure 2.19).

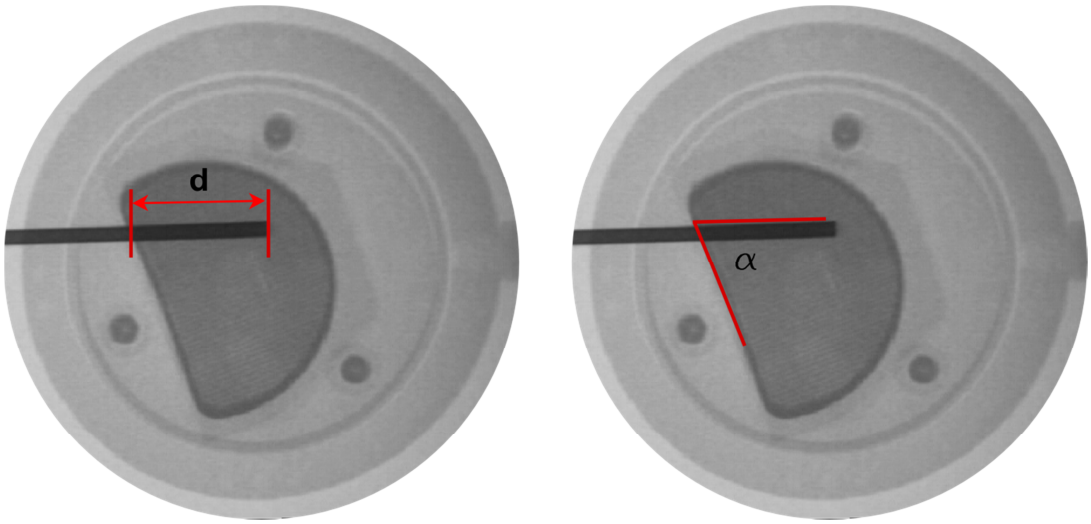

Figure 2. 19 Measurements performed to quantify the error in the needle placement within the 3D surrogates.

Data Analysis

The data acquired from the LVDT and the load cell was analyzed for the duration of the injection. The LVDT data was used to confirm that the injection flow rate was constant at 3 mL/min. The displacement of the syringe plunger was plotted against time and the slope (mm/s) was multiplied by the cross-sectional area of the syringe (mm^2) to determine the injection flow rate. The load cell data was used to calculate the pressure drop in the system with respect to time. The measured force (N) applied on the syringe plunger was divided by the cross-sectional area of the syringe (mm^2) to determine the pressure drop in the system (MPa). As the load cell was used to measure the force applied on the syringe plunger, the calculated pressure drop was the sum of two pressures: 1) ΔP_n, the pressure required to inject the fluid through the needle and 2) ΔP_s, the pressure required to inject the fluid into the structure of the bone surrogates. For this reason, injections were also performed without the surrogates to determine the pressure drop across the needle (ΔP_n). This was then subtracted from the calculated pressure drop in the system to determine the pressure drop (ΔP_s) at the inlet, which is required to inject the fluid into the structure of the bone surrogates.

To quantitatively describe the resulting flow patterns, the video data from the fluoroscope was analyzed in Matlab (R2009b, MathWorks, Massachusetts, USA). A

custom Matlab script (refer to Appendix D) was developed to allow automated segmentation of the flow distribution by subtracting the first frame of the video sequence, which shows the surrogates with no fluid injected, from the remaining frames. Two parameters were measured: (1) the time and type of leakage (i.e. anterior or posterior) which was obtained directly from the captured video sequences, and (2) the mean spreading distance (MSD) in the filled region of the surrogates measured on the superior view of the fluoroscopy projection. The segmented image of the flow distribution was imported into imageJ [189] and the 'Analyze Particles' function was used to calculate the maximum and minimum Feret diameters, which are the longest and shortest distances, respectively, along the geometric center of the flow contour, also referred to as the caliper diameters. MSD in pixels was then calculated by taking the mean of the two distances and converted to millimeters using a conversion factor (refer to Fluoroscopy Error Quantification and Correction).

The cement injections were microCT scanned post-augmentation at a spatial resolution of 73.6 µm (isotropic voxel size) with an integration time of 300 ms, a tube voltage of 70 kV, a tube current of 114 µA and a 0.5 mm aluminum filter. The DICOM stack of each scan was processed in imageJ [189] to obtain the final shape of the cement bolus and measure its sphericity (Eq. 37), which is defined as the surface area of a sphere enclosing the same volume (V) as the 3D object, divided by the surface area (A) of the 3D object. A perfect sphere has a sphericity of one and the value is below one for non-spherical objects [197].

$$\text{Sphericity} = \frac{\sqrt[3]{36\pi V^2}}{A} \tag{37}$$

Two functions within the BoneJ plug-in for imageJ were used to calculate the sphericity: (1) the 'Volume Fraction' function, which was used to obtain the volume of the cement bolus, and (2) the 'Isosurface' function, which was used to obtain the surface area of the cement bolus. These functions were validated on a sphere (Figure 2.20) that was designed in SolidWorks then converted using a Matlab script into a DICOM stack with a spatial resolution of 70 µm (isotropic voxel size) to match that of

the microCT scans of the cements post-augmentation. The DICOM stack was then processed in imageJ to obtain the sphericity.

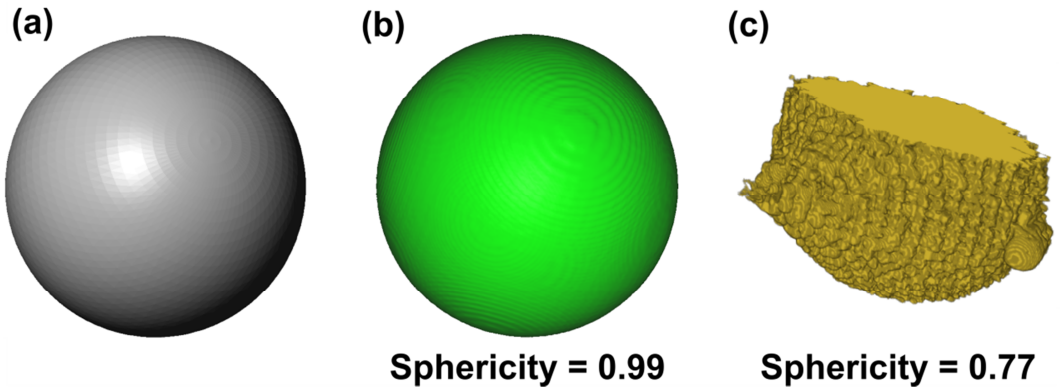

Figure 2. 20 (a) The sphere designed in SolidWorks then (b) processed in imageJ to obtain its sphericity. (c) The processed image of a cement bolus post-injection included for comparison.

Statistical Analysis

All data were presented as mean ± standard deviation. The influence of the viscosity and the structure on the measured parameters was evaluated using the Mann–Whitney U and the Kruskal-Wallis one-way analysis of variance with a significance level set at $\alpha = 0.05$. All statistical analyses were performed in SPSS version 21 (SPSS Inc, Illinois, USA).

Experimental/Computational Cross-validation

The work described in this section was completed by R. P. Widmer as part of the collaboration that was formed with the ETH, Zürich to cross-validate our experimental data with their computational code for simulating the displacement of bone marrow by bone cement in porous media [135, 198]. The developed CAD model of each bone surrogate was converted into a continuum scale finite element (FE) model. The computer simulation was set up with the same boundary conditions as in the experiments. Then, the flow behaviour of 60 Pa·s silicone oil as well as Simplex P bone cement was simulated in each bone surrogate for an injected volume of 5 mL at a flow rate of 3 mL/min. The marrow substitute (aqueous solution of carboxymethyl cellulose 2.5% w/w) and the silicone oil formulation (oil + 20% v/v Lipiodol) that

were used in the experiments were modeled in the simulation based on viscosity measurements performed in this thesis (Section 2.8). The Simplex P formulation (SP1:1, Table 2.7) was modeled in the simulation for injections performed at 4 min after cement mixing (i.e. from the addition of the liquid to the powder), while the viscosity was modeled based on previously published rheological tests [198]. A flowchart of the cross-validation study is presented in Figure 2.24.

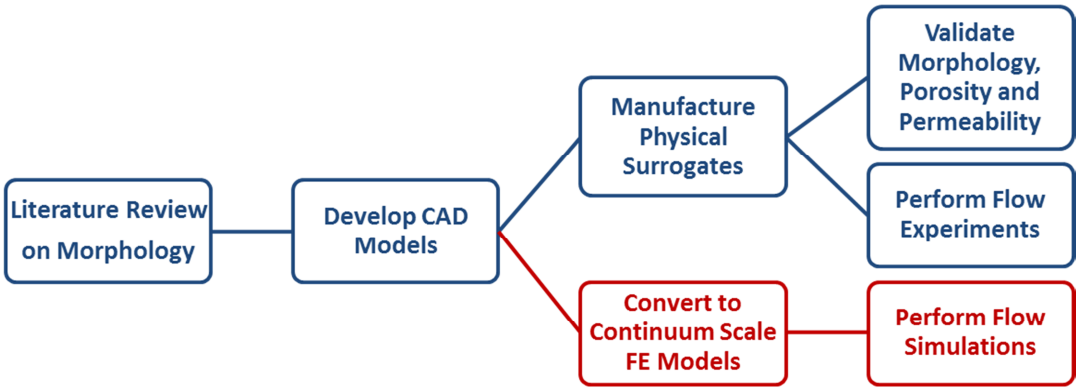

Figure 2. 21 Flow chart of the experimental / computational cross-validation study. The work completed in this thesis is shown in blue while that completed by R. P. Widmer is presented in red.

Fluoroscopy Error Quantification and Correction

Five glass beads, 2.5 mm in diameter, were inserted into each of the superior and inferior plates of the 3D bone surrogates (Figure 2.21). Prior to insertion, the bead diameters were measured using a caliper (Table 2.9). In the plane closest to the top surface of the 3D surrogates, one bead was inserted at the centre of the superior plate and four beads, labelled 1 to 4, were inserted at the vertices of a 1 cm square, which was concentric with the plate. In the plane closest to the bottom surface of the 3D surrogates, one bead was inserted at the centre of the inferior plate and four beads, labelled 6 to 9, were inserted at the vertices of a 2 cm square, which was also concentric with the plate. To ensure that the beads inserted in both plates were concentric and formed a prism, the sides made up of beads 1 – 3 and 6 – 8 were centered with respect to screw A (Figure 2.21).

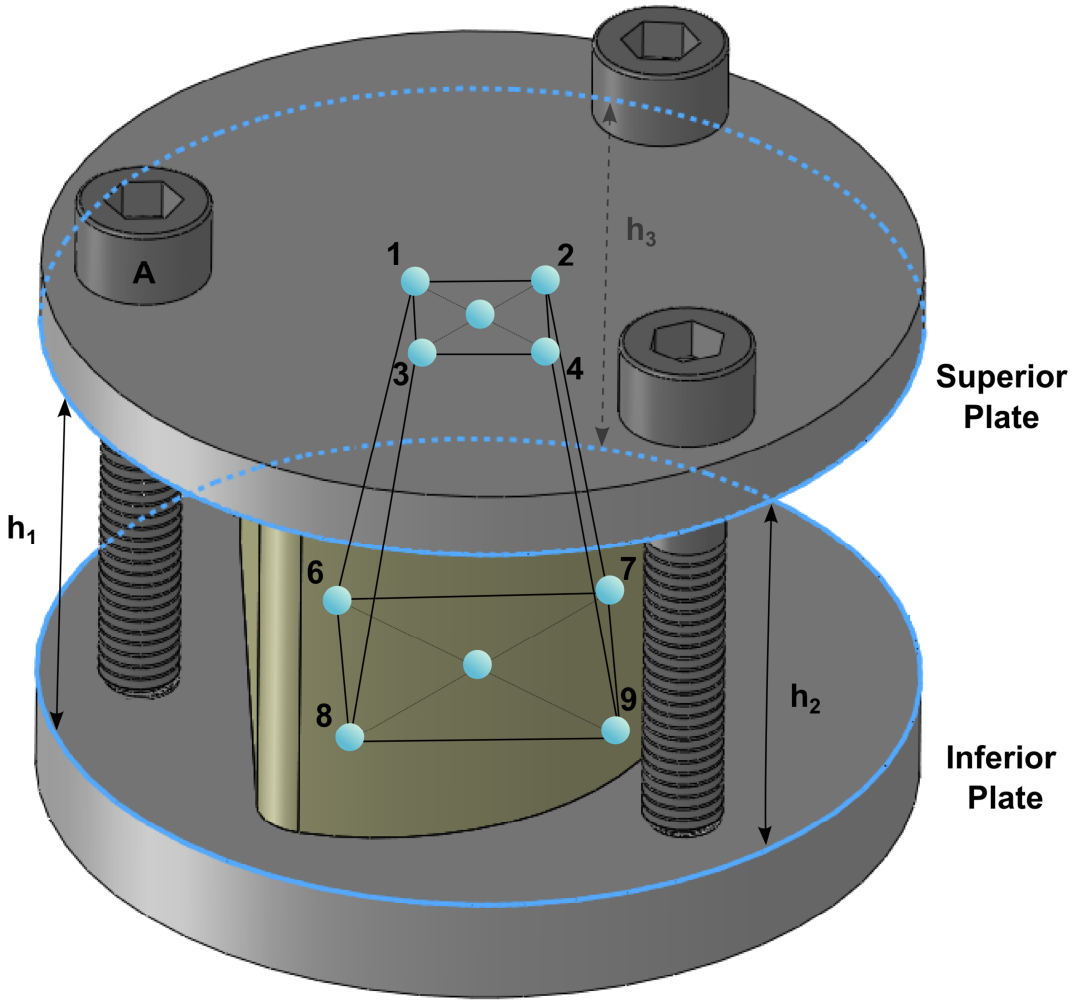

Figure 2. 22 The beads inserted into the superior and inferior plates of the 3D bone surrogates.

Once the beads were inserted into each plate, a profile projector (Nikon Profile Projector, Nikon Corporation, Tokyo, Japan) was used to measure the perpendicular distances between adjacent beads within a plate. This included the distances between beads 1 – 2, 2 – 4, 3 – 4, and 1 – 3 within the superior plate and the distances between beads 6 – 7, 7 – 9, 8 – 9, and 6 – 8 within the inferior plate (Table 2.10).

Table 2. 9 The bead diameters measured using a caliper and the corresponding diameters of the bead projections with their associated scaling factors.

Plate	Bead	Caliper Diameter (mm)	Projection Diameter (px)	Scaling Factor (mm/px)
Top	1	2.49	10.77	0.231
	2	2.60	11.18	0.233
	3	2.48	10.77	0.230
	4	2.61	11.705	0.223
Bottom	6	2.58	12.083	0.214
	7	2.49	11.705	0.213
	8	2.88	14.318	0.201
	9	2.58	12.649	0.204

Table 2. 10 The nominal and projected distances between adjacent beads within a plate and the error associated with the measured distances.

Plate	Beads	Nominal Distance (mm)	Projected Distance		% Error
			(px)	(mm)	
Top	1 – 2	9.955	44.851	9.802	1.54
	2 – 4	9.680	46.533	10.170	5.06
	3 – 4	9.797	45.641	9.975	1.81
	1 – 3	10.019	45.982	10.049	0.30
Bottom	6 – 7	19.819	95.090	20.782	4.86
	7 – 9	20.347	101.557	21.647	10.48
	8 – 9	19.898	95.067	22.195	9.08
	6 – 8	19.594	99.049	20.777	4.42

The fixed height (h) between the superior and inferior planes in which the beads were inserted was measured using a caliper. Three measurements (h_1 to h_3) were performed to obtain the average height (h), which was 32.32 ± 0.23 mm. Subsequently, the

nominal angle (α) was analytically calculated (Figure 2.22) on each of the four surfaces of the prism: the sides consisting of beads 3 – 4 and 8 – 9 were used to calculate α_1, the sides consisting of beads 1 – 2 and 6 – 7 were used to calculate α_2, the sides consisting of beads 1 – 3 and 6 – 8 were used to calculate α_3, and the sides consisting of beads 2 – 4 and 7 – 9 were used to calculate α_4. The average nominal angle was $\alpha = 81.2 \pm 0.4^{o}$.

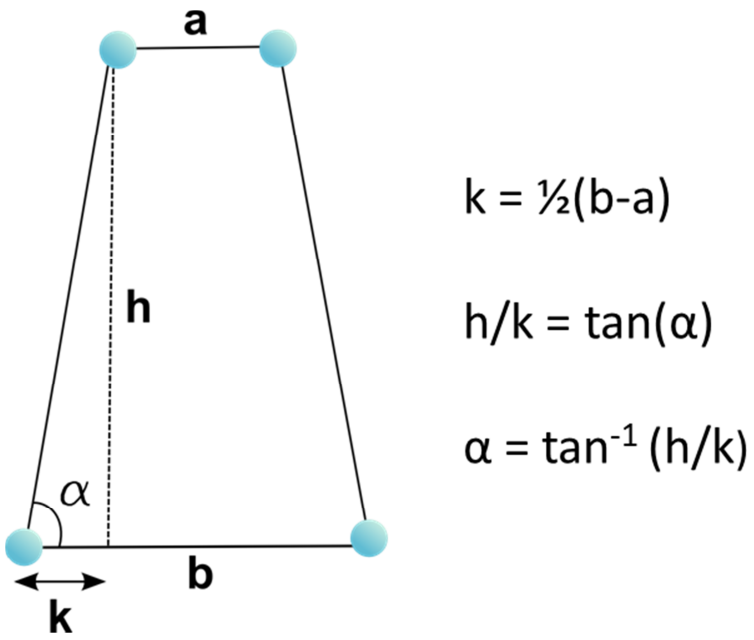

Figure 2. 23 Analytical calculation of angle α.

The specimen was then placed into the experimental set-up (Figure 2.17) and an x-ray was taken to obtain a projection of the beads (Figure 2.23). Image processing was performed using a custom Matlab script (Appendix D), which was developed to correct the inherent pincushion distortion and export the binary image of the beads. This image of the beads was imported into ImageJ [189] to measure the bead centroids and diameters using the 'Analyze Particles' function. The bead centroids were used to measure the perpendicular distances (in pixels) between adjacent beads within the fluoroscopy projection (Table 2.10). The bead diameters (Table 2.9) were used to obtain the corresponding scaling factors which allow converting the distances from pixels (px) to millimeters (mm). An average scaling factor of 0.219 mm/px was applied to convert the distances within the fluoroscopy projection to millimeters and

calculate the error associated with the measured distances by comparing the nominal distances between adjacent beads within a plate to their corresponding distances within the fluoroscopy projection (Table 2.10). The overall average error between the nominal and projected distances was 4.7 ± 3.6 %.

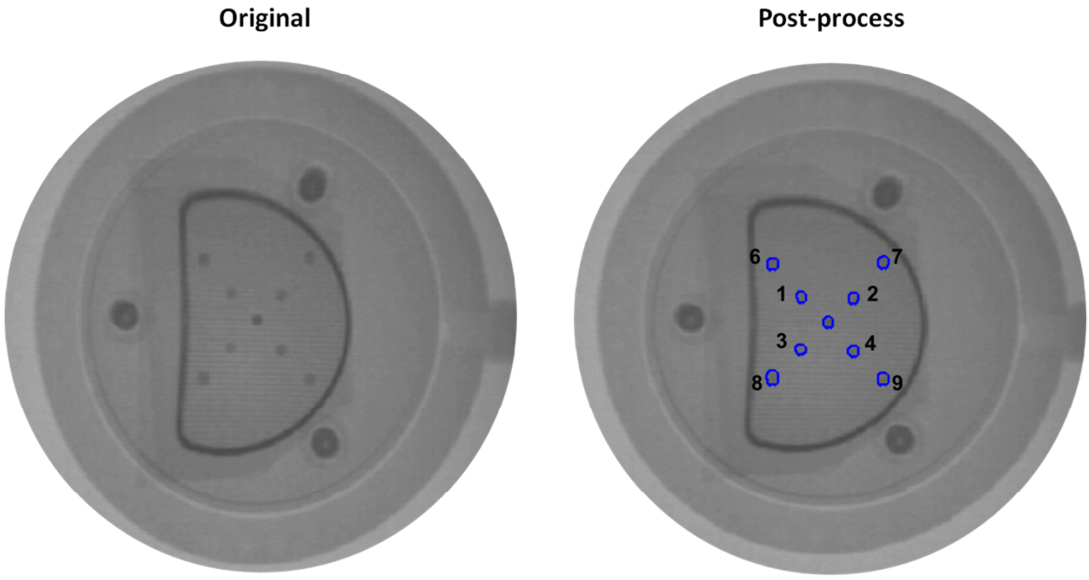

Figure 2. 24 Original and post-processed images showing the projection of the beads inserted into each of the superior and inferior plates of the 3D bone surrogates.

Considering that the height (h) between the superior and inferior planes in which the beads were inserted was fixed at 32.32 mm and knowing the perpendicular distances (in mm) between adjacent beads within the fluoroscopy projection, the analytical calculations of the angles were repeated. The average projected angle was $\alpha' = 81.4 \pm 0.5^{o}$. This shows that the nominal and projected angles are very similar with an average difference of 0.21^{o}.

2.7.2 2D Flow Model Injections

This section details the methods that were designed to allow injections into the 2D flow models under a controlled environment. The experimental set-up is presented in Figure 2.25.

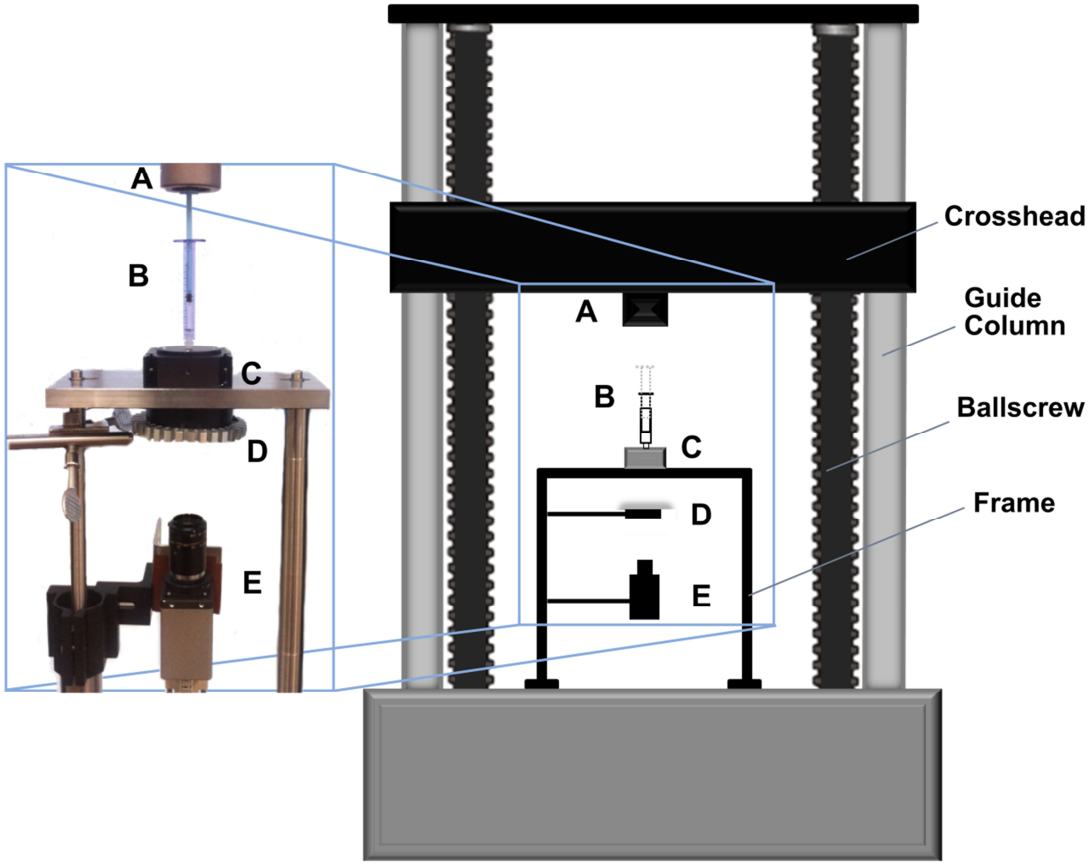

Figure 2. 25 Schematic drawing of the experimental set-up designed for use with the developed 2D flow models. The call-out shows the main components which include: (A) a load cell attached to the crosshead of a material testing machine, (B) a 3 mL syringe, (C) a specimen holder placed on the top plate of the frame, (D) an LED light source, and (E) a camera with a high resolution lens. A personal computer running LabVIEW software was used to allow data acquisition.

The material testing machine (Instron 3369, Instron Corp, Massachusetts, USA) was used to control the displacement of the syringe plunger and achieve a constant flow rate by keeping the testing machine's crosshead speed constant. The loading profile was customized to maintain a constant displacement of the syringe plunger and output the displacement of the crosshead, which allowed measuring the flow rate. The load cell (Model 31, Honeywell-Sensotec, Minneapolis, USA) was instrumented into the

crosshead to measure the force (N) applied on the syringe plunger, thus calculate the pressure (MPa) in the system. The frame was designed to keep the specimen holder above the camera and parallel to the crosshead actuator, while allowing the syringe plunger to be centered with respect to the load cell to ensure a uni-axial load was applied along the plunger. A custom-built stainless steel syringe plunger was used to withstand the loads applied on it without bending or breaking. A syringe adapter (Figure 2.26) was used to reinforce the syringe and prevent it from bending or failing at its attachment with the specimen holder through the threaded hole (G) using a female luer to 1/4-28 UNF connector.

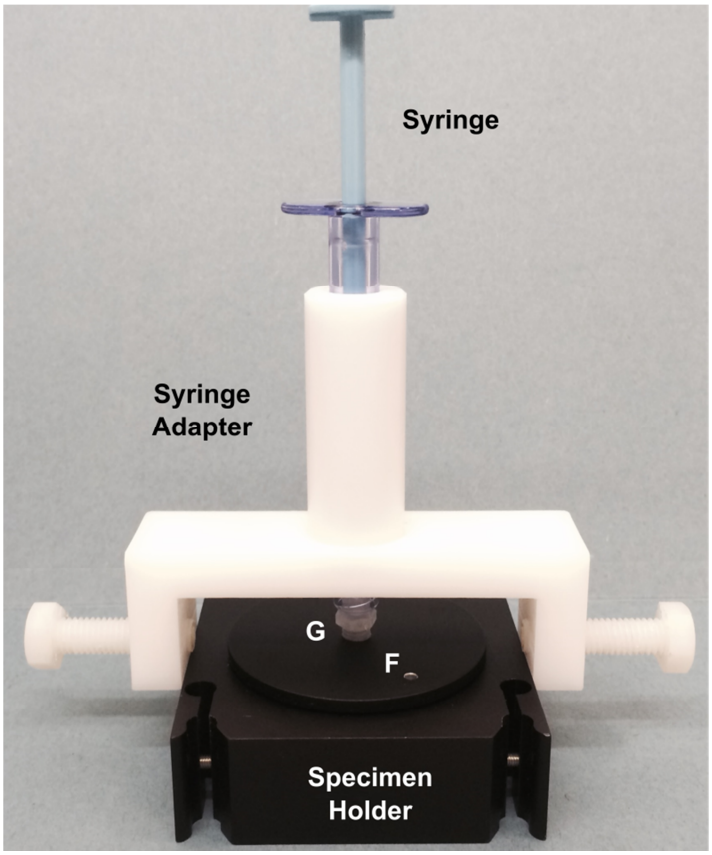

Figure 2. 26 The syringe adapter used to reinforce the syringe and prevent it from bending or failing at its attachment with the specimen holder through the threaded hole (G) using a female luer to 1/4-28 UNF connector. (F) shows the flow exit point.

The camera (1000m Series, Adimec, Eindhoven, the Netherlands) together with a high resolution fixed focal length lens (25mm FL, Edmond Optics Ltd, York, UK) and an LED light source (White LED Ring Light, Edmond Optics Ltd, York, UK) were used

to monitor the flow distribution during the injection. LabVIEW software was used to acquire the video and load cell data. A custom LabVIEW code (Appendix C) was developed to allow real-time reading of the signals at a pre-defined sampling frequency of 10 Hz and simultaneous logging of the data into two separate files. The data acquisition was tested and validated to ensure that the load cell and video data were synchronized and saved simultaneously such that the number of load cell data points corresponds to the number of video frames.

Specimen Preparation

Each flow model (Osteo, Lesion and Fracture) was placed in the specimen holder (Figure 2.27).

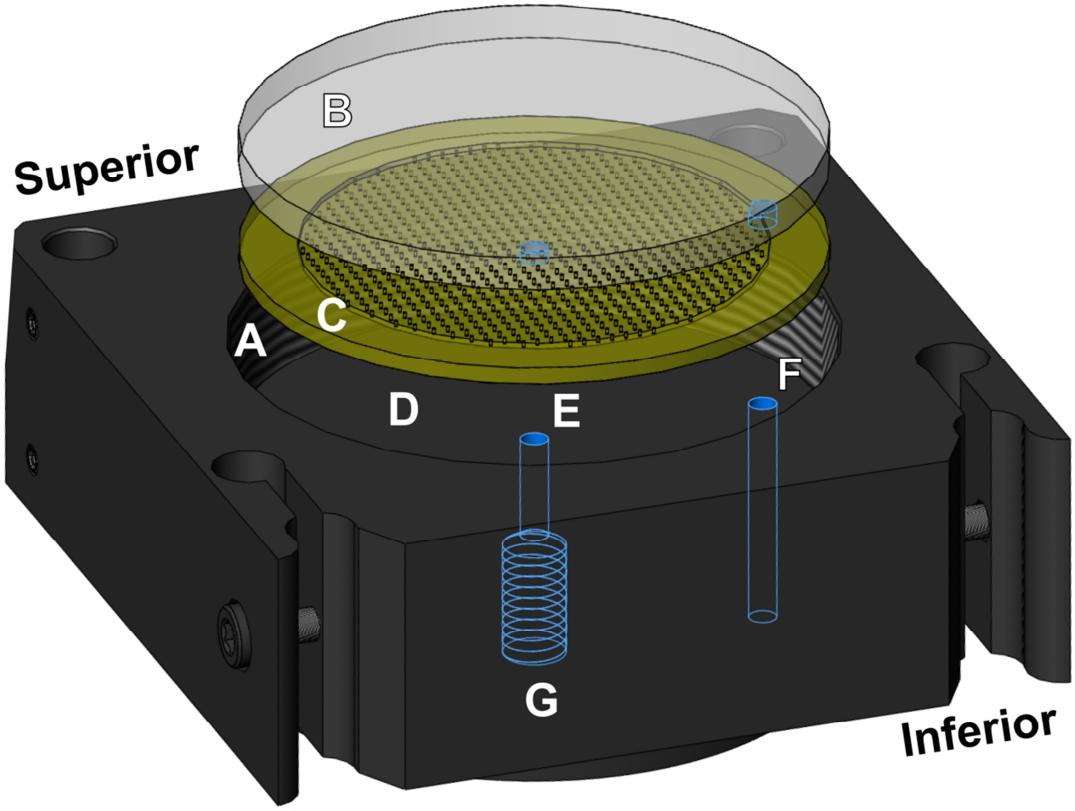

Figure 2. 27 The specimen holder showing (A) the threadeding into which an aluminum ring is screwed to press (B) the glass window against (C) the flow model which is placed on the surface of (D) an aluminum cylinder with its pattern facing up. (E) is the injection inlet and (F) is the flow exit point. Fluid injections are performed using a luer-lok syringe attached to the threaded hole (G) via a female luer to 1/4-28 UNF connector.

A syringe containing the marrow substitute was screwed into the corresponding threaded hole of the specimen holder (G) and manually injected until the entire flow model was filled. This simulates the rheological environment of the vertebral body in terms of bone marrow present within the bony channels. Once the marrow substitute was injected, the syringe was removed and the threaded hole (G) was further filled with the marrow substitute to prevent air bubbles within the flow system. Following this, a 3mL syringe (Becton Dickinson, New Jersey, USA) containing the injection fluid (bone cement or silicone oil) was screwed into the same threaded hole (G) and both the syringe and the specimen holder were placed into the experimental set-up (Figure 2.25) on the top plate of the frame, ensuring that the superior surface of the specimen holder was in direct contact with the superior surface of the plate (Figure 2.28).

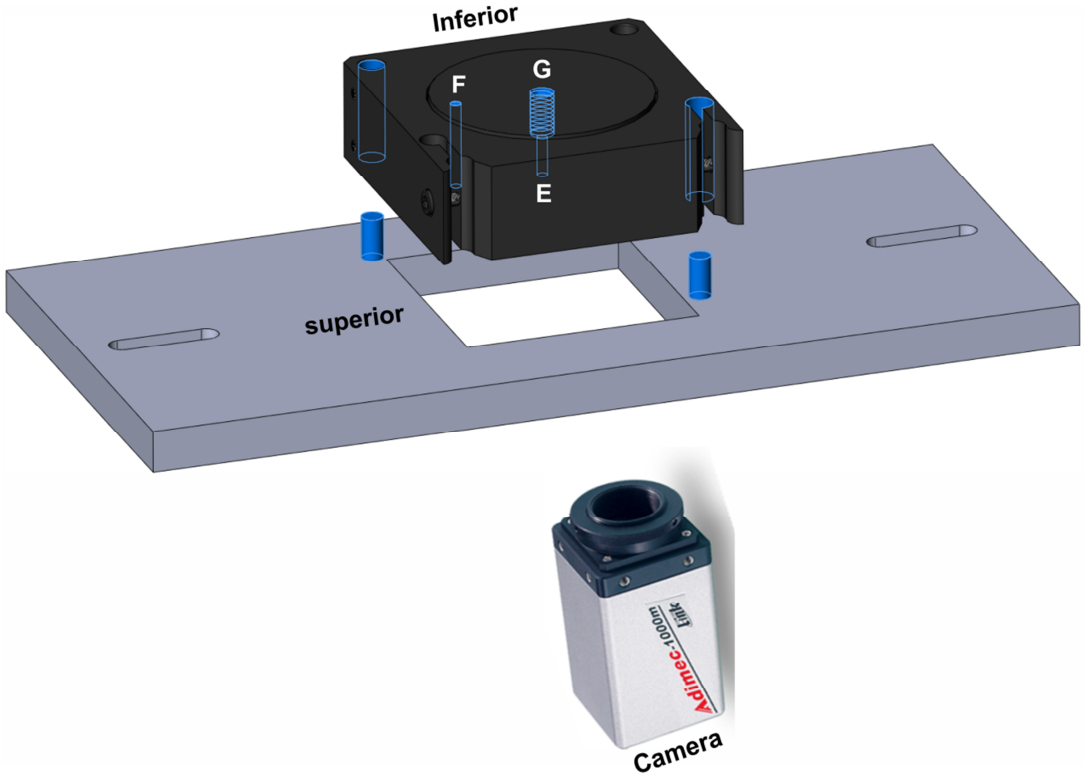

Figure 2. 28 The top plate of the frame used to keep the specimen holder of the 2D flow models locked in the same position above the camera and parallel to the ground. (E) shows the injection inlet and (F) shows the flow exit point. Fluid injections are performed using a luer-lok syringe which is attached to the threaded hole (G) via a female luer to 1/4-28 UNF connector.

The pins (solid blue cylinder) on the superior surface of the plate were used to ensure that the specimen holder was consistently locked in the same position with respect to the camera.

Oil Injections

Newtonian fluid 10 and 60 Pa·s silicone oil (Si 10Pas and Si 60Pas, respectively) were comparatively tested. The flow models were filled with 0.4 Pa·s marrow substitute (M0.4) formulated using an aqueous solution of carboxymethyl cellulose 2.5% w/w. Subsequently, a maximum volume of 1 mL of oil was injected into each model under two constant flow rates, 1 and 3 mL/min, to assess the effect on the injection behaviour. The injections were stopped when the oil had reached the boundary of the models. Furthermore, to assess the effect of marrow viscosity on the injection behaviour, the flow models were filled with 0.06 Pa·s marrow substitute (M0.06) formulated using an aqueous solution of carboxymethyl cellulose 1.25% w/w, and 10 Pa·s silicone oil was injected into each flow model under a constant flow rate of 1 mL/min. All injections were performed at room temperature (19.0 ± 1.4ºC) into separate models. This process was repeated three times.

Cement Injections

All the cement formulations (OC, OP, PL, SP1:1 and SP1:2) in Table 2.7 were comparatively tested. The flow models were filled with 0.4 Pa·s marrow substitute formulated using an aqueous solution of carboxymethyl cellulose 2.5% w/w. Subsequently, a maximum volume of 1 mL of cement was injected into each model. The injections were performed at a constant flow rate of 3 mL/min and stopped when the cement had reached the boundary of the models. The same 3 mL syringe was used to test the effect of three different injection time points (4, 6, and 8 min from the addition of the liquid to the powder) on the flow behaviour. All injections were performed at room temperature (19.0 ± 1.4ºC) into separate models. This process was repeated three times.

Data Analysis

The displacement of the testing machine's crosshead was plotted against time and the slope (mm/s) was multiplied by the cross-sectional area of the syringe (mm^2) to determine the injection flow rate. The load cell and video data were analyzed for the duration of the injection. The load cell data was used to calculate the pressure drop in the system with respect to time. The measured force (N) applied on the syringe plunger was divided by the cross-sectional area of the syringe (mm^2) to determine the pressure drop in the system (MPa). In order to quantitatively describe the resulting flow patterns, the video data was analyzed in Matlab. A custom Matlab script (Appendix D) was developed to allow automated segmentation of the flow distribution by subtracting the first frame of the video sequence, which shows the flow models with no fluid injected, from the remaining frames. The following parameters were calculated when the injection fluid (bone cement or silicone oil) had reached the boundary of the flow models: i) the time to reach the boundary, which is determined directly from the video sequences, ii) the filled area, which is a measure of the number of pixels in the segmented region converted to squared-millimeters (mm^2) using a conversion factor then presented as a percent of the total area on the basis of a flow model with an inner diameter of 40 mm, and (iii) the roundness (Eq. 38), which is a shape descriptor most sensitive to elongation, calculated by comparing the area A_s of a shape S to the maximum caliper diameter L_s of that shape measured for all orientations [199]. A perfect circular pattern has a roundness of one, whereas the value approaches zero for increasingly elongated contours.

$$\text{roundness} = \frac{4A_S}{\pi {L_S}^2} \tag{38}$$

Statistical Analysis

All data were presented as mean ± standard deviation. The influence of the model structure (Osteo, Lesion and Fracture), the cement formulation (OC, OP, PL, SP1:2 and SP1:1), and the injection time point (4, 6 and 8 min) on the peak pressure, the time to reach the boundary, the filled area, and the roundness was evaluated using a

multivariate general linear model (GLM) with a significance level set at $\alpha = 0.05$. The influence of the model structure (Osteo, Lesion and Fracture), the oil-marrow combination (Si10-M0.4, Si60-M0.4 and Si10-M0.06), and the injection flow rate (1 and 3 mL/min) on the peak pressure, the time to reach the boundary, the filled area, and the roundness was also evaluated using a multivariate general linear model (GLM) with a significance level set at $\alpha = 0.05$. All statistical analyses were performed in SPSS version 21 (SPSS Inc, Illinois, USA).

2.8 Viscosity Measurement

Rheological characteristics of the marrow substitute and the silicone oil formulations as a function of shear rate were measured using a Malvern Kinexus rheometer (Malvern Instruments Ltd, Malvern, UK) in rotation mode with a cone on plate configuration (Figure 2.29).

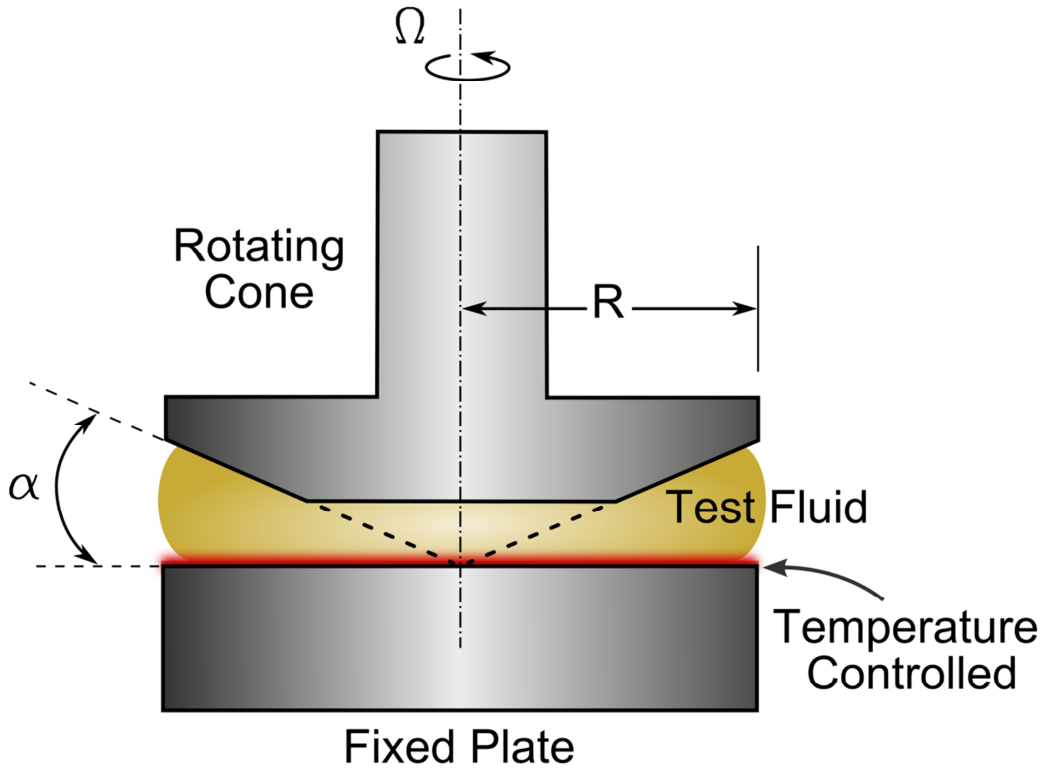

Figure 2. 29 Schematic of the rotational rheometer with the cone-plate configuration that was used to measure the viscosity of the marrow substitute and the oil formulations as a function of shear rate. Adapted from [138].

The cone used had a radius R = 25 mm and an angle α = 1º. The test fluid was contained within the annular space of the cone-plate and the temperature was set to 21ºC. The angular speed of the cone (Ω) was ramped to achieve varying shear rates from 0 to 100 s-1 (ramp time of 5 min) and 10 samples per decade were recorded. Knowing the instantaneous angular rotation of the cone (Ω) and measuring the resisting torque (T) of the fluid on the bottom plate allowed measuring the dynamic viscosity of the test fluid as a function of shear rate using proprietary software (rSpace for Kinexus, Malvern Instruments Ltd, Malvern, UK).

CHAPTER 3 Results

This chapter details the results of the work completed throughout the duration of this project. All materials and methods outlined in the previous chapter were carried out in full to satisfy the aims and objectives of this study. The first section summarizes the benchmark analysis performed to identify a suitable rapid prototyping technique that ensured accurate and reproducible manufacture of the 3D surrogates. The second section presents the morphology analysis performed to assess the geometrical variations within the bone surrogates. The third section summarizes the contact angle analysis performed on the bone surrogate material to compare the surface wettability to that of cortical bone. The fourth section presents the results of the rheological tests performed on the bone marrow substitute and the silicone oil formulations. The fifth section shows the imaging analysis of the bone cement powder composition. The final section details the results of the injections performed to comparatively test the flow behaviour of silicone oil as well as various bone cement formulations through the visualization and quantitative analysis of fluid spreading at various time intervals.

3.1 BENCHMARK ANALYSIS

Figure 3.1 shows the benchmark parts that were manufactured via the selected RP techniques (Table 2.2). Through part observation and visual inspection, the quality of the Projet HD benchmark was the best as all the geometrical features appear to have been built. The EnvisionTEC benchmark was comparable in terms of build capability, however its form was the worst as evident in the square base feature which does not appear straight or flat (Figure 3.2). Also, the top surface of the EnvisionTEC benchmark had layer lines and the bottom surface had a distinct grid pattern. Conversely, the SLS and HP benchmarks were not comparable in terms of build capability. The lattice structures located in the center of their benchmarks did not build properly due to the limited resolution of both techniques. The surface of the SLS benchmark could be described as granular and rough, whereas the HP benchmark had a distinct textured pattern on the top and bottom surfaces as well as obvious layer lines along the vertical surfaces.

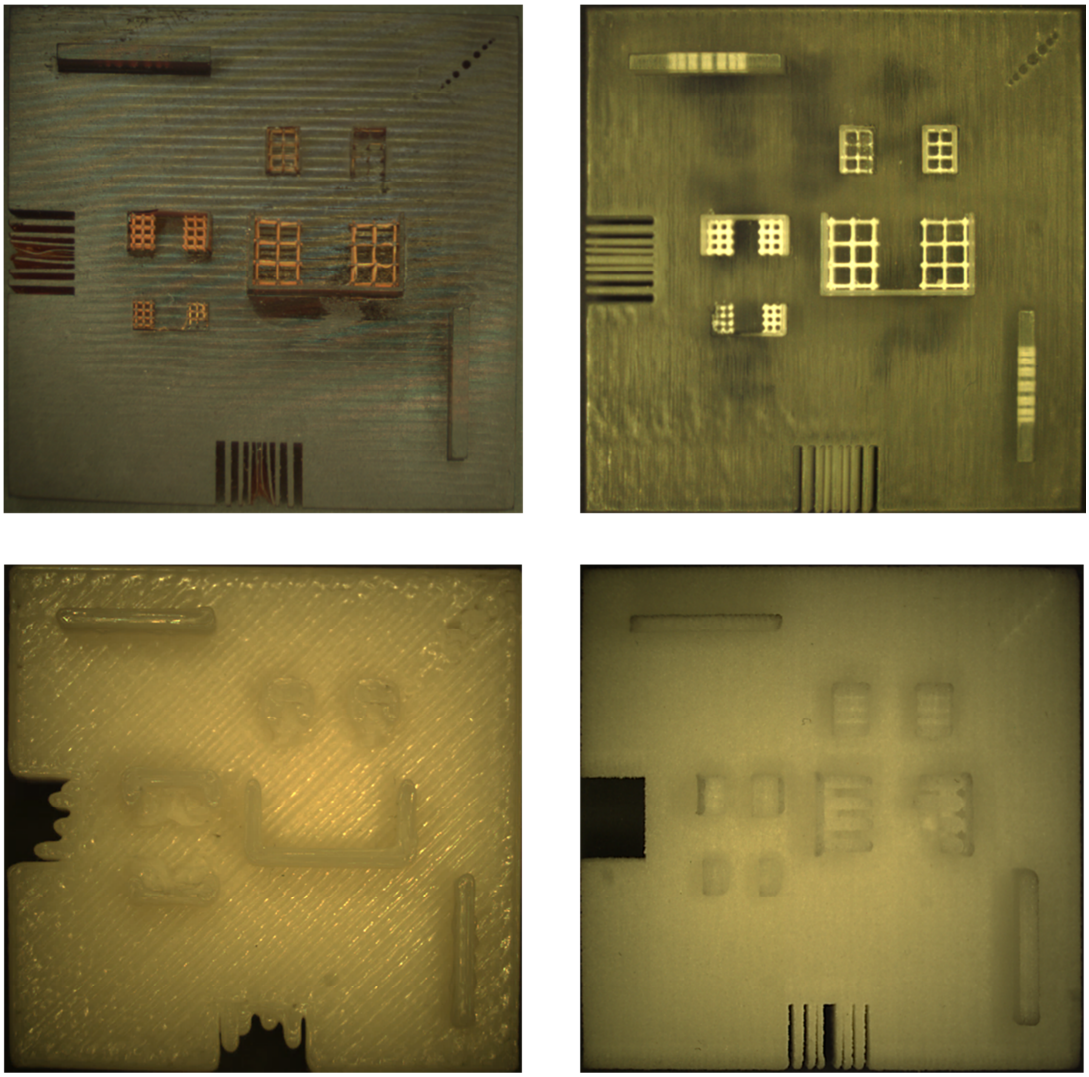

Figure 3. 1 Top views of the benchmark parts manufactured by the selected RP techniques: EnvisionTEC (top left), Projet HD (top right), HP (bottom left) and SLS (bottom right).

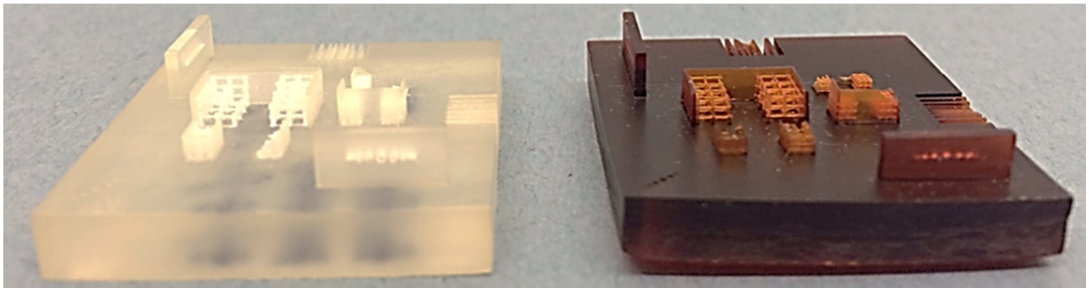

Figure 3. 2 The EnvisionTEC benchmark (right) with a distorted square base due to curing of the liquid resin and the Projet HD benchmark (left) for comparison.

Figure 3.3 shows the mean measurement and the range of measurement error across all the benchmarks for 3 mm wall height and 1 mm wall width. It is evident that the Projet HD and the EnvisionTEC benchmarks were the best in terms of dimensional accuracy. The EnvisionTEC benchmark had a lower range of measurement error due to the layer lines on its surface and its dark color allowing reliable edge detection of its features using the profile projector. The Projet HD benchmark was clear and its surface was smooth making the visualization and edge detection of its features more difficult.

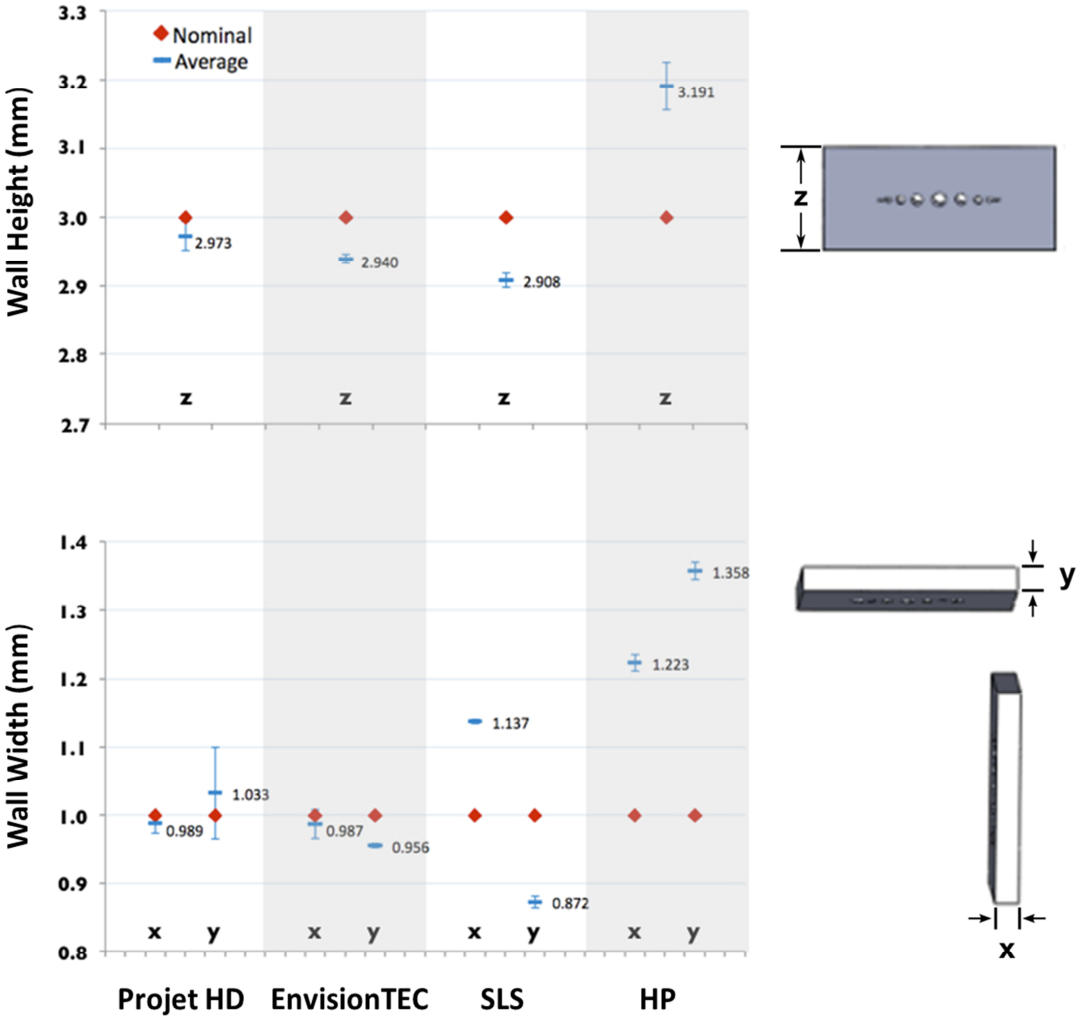

Figure 3. 3 Comparison of the measured wall dimensions across all the RP techniques for a nominal height of 3 mm and a nominal width of 1 mm.

Furthermore, the dimensional accuracy of the SLS benchmark was more comparable relative to that of the Projet HD and the EnvisionTEC, while the HP benchmark was evidently the worst. Figure 3.4 compares the mean measurement and the range of measurement error between the Projet HD and the EnvisionTEC benchmarks for 0.12 mm solid beam width as well as 0.68 and 1.13 mm solid beam spacing. The results for the SLS and HP benchmarks were not included, as measurements could not be obtained for features at this dimensional level due to the limited resolution of both techniques. The analysis of the results showed that the Projet HD and the EnvisionTEC techniques were generally comparable in terms of geometrical accuracy and repeatability.

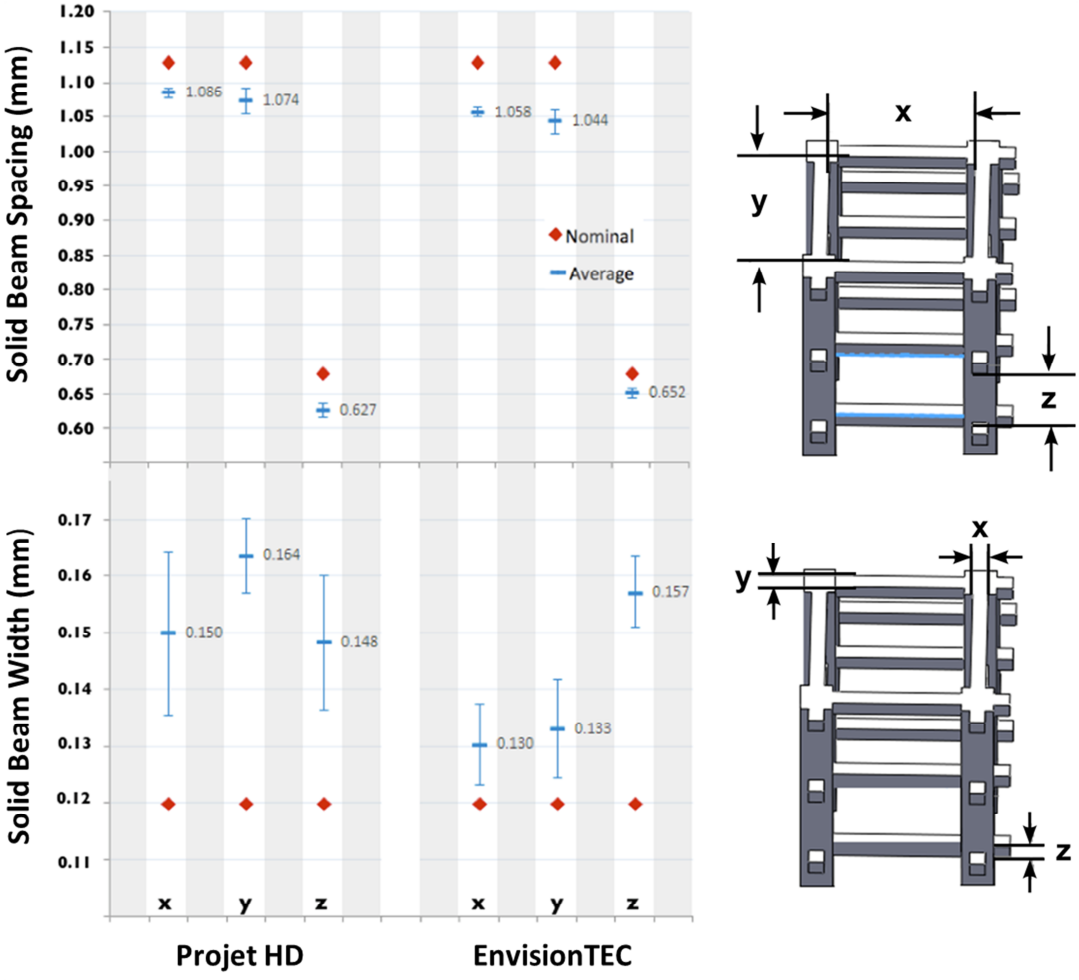

Figure 3. 4 Comparison of the measured solid beam dimensions between Projet and EnvisionTEC for a nominal spacing of 1.13 and 0.68 mm and a nominal width of 0.12 mm.

The data presented in Figure 3.4 is the mean of three independent measurements performed on three solid beams. The higher variability in the Projet HD is mainly due to the higher measurement error within each solid beam. For both techniques, the mean inter-variability in the measured width and spacing of the three solid beams was 3 and 2 µm, respectively, in all cardinal directions (x, y and z). Table 3.1 summarizes the overall linear dimensional accuracy of each RP technique based on the total mean difference between measurements obtained for all visible linear geometrical features and their respective actual, true dimensions in SolidWorks. The data is presented as the mean ± standard deviation of all measurements.

Table 3. 1 Overall linear dimensional accuracy of each RP technique.

RP Technique	Features Included		Accuracy		
	Geometry	Size(mm)	x (mm)	y (mm)	z (mm)
Projet HD	Walls, Slots, Beams	0.06 – 4.0	0.027 ± 0.02	0.029 ± 0.02	0.032 ± 0.02
EnvisionTEC	Walls, Slots, Beams	0.06 – 4.0	0.027 ± 0.02	0.028 ± 0.03	0.044 ± 0.02
SLS	Walls, Beams	0.2 – 4.0	0.404 ± 0.14	0.487 ± 0.16	0.122 ± 0.07
HP	Walls	0.3 – 4.0	0.574 ± 0.31	0.532 ± 0.25	0.127 ± 0.07

Figure 3.5 shows the surface texture analysis performed on the four benchmark parts and the human femur, and Table 3.2 summarizes the measured three-dimensional height parameters.

Table 3. 2 ISO 25178 height parameters measured using non-contact light interferometer.

Height Parameter	S_a (µm)	S_p (µm)	S_v (µm)
Projet HD	1.72	13.62	-11.49
EnvisionTEC	2.77	16.44	-27.38
HP	6.30	37.63	-40.94
SLS	18.85	94.67	-74.18
Human Femur	19.76	88.55	-106.25

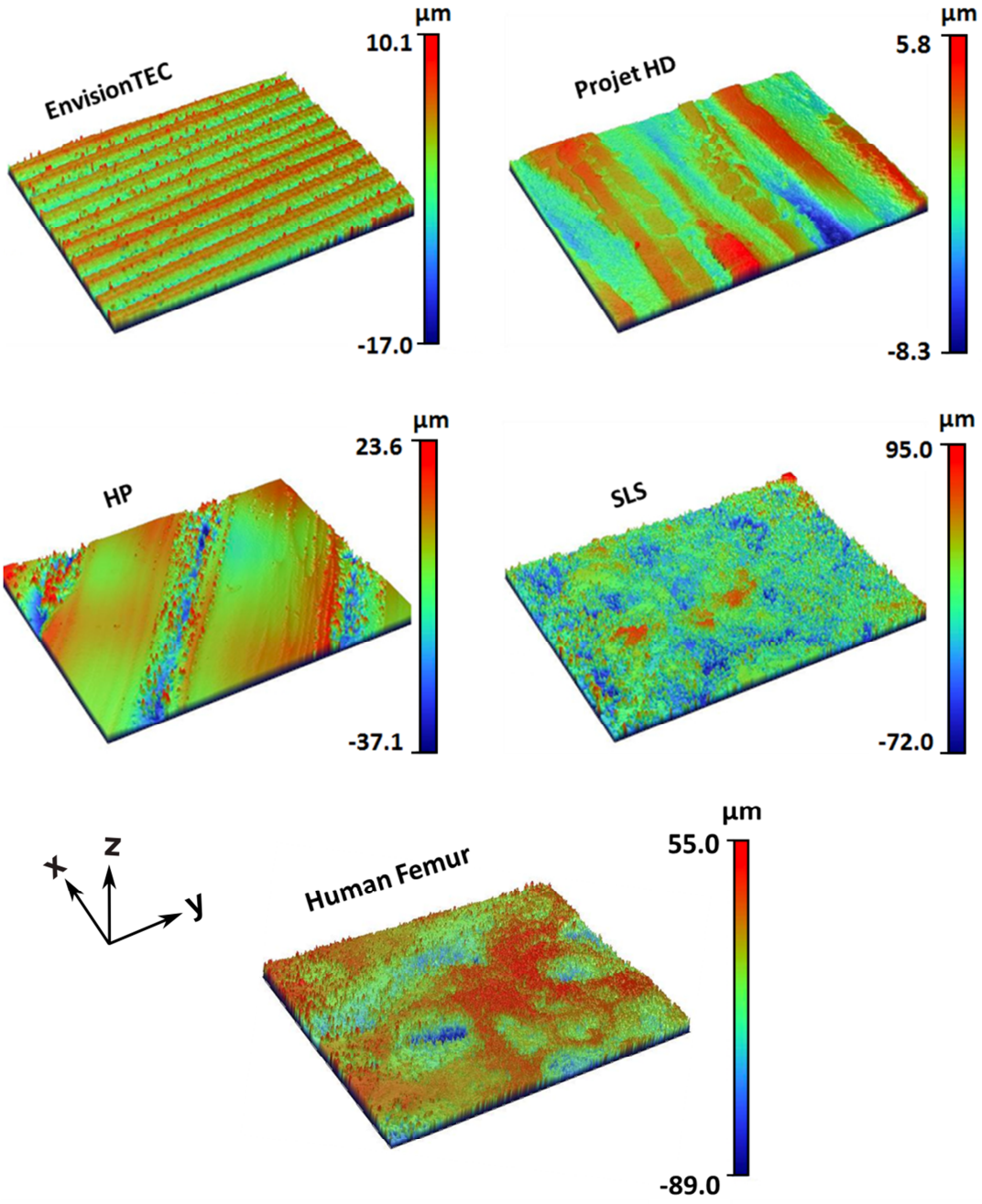

Figure 3. 5 Three-dimensional views of the surface texture analysis performed on the manufactured benchmark parts and a dry human femur.

The data revealed that the surface roughness was lowest for the Projet HD and highest for the human femur as evident in the measured S_a (average roughness), S_p (maximum peak height) and S_v (maximum valley depth) which were generally lowest for the

Projet HD benchmark and highest for the human femur. Although the surface roughness was similar between the SLS benchmark and the human femur, the results showed that the build resolution of the SLS technique is not suitable for manufacturing the proposed 3D bone surrogates. The overall analysis of the results revealed that only the Projet HD and the EnvisionTEC techniques have high geometrical accuracy and repeatability suitable to manufacture features at the dimensional level proposed in the 3D bone surrogates. However, the quality of the Projet HD benchmark was the best relative to the EnvisionTEC benchmark which had the worst form with a distorted square base. Thus, the Projet HD technique was chosen for manufacturing the proposed three-dimensional bone surrogates. Figure 3.6 shows an osteoporosis type bone surrogate manufactured via the Projet HD technique to simulate osteoporotic trabecular bone with a nominal strut thickness and spacing of 0.2 and 0.9 mm, respectively.

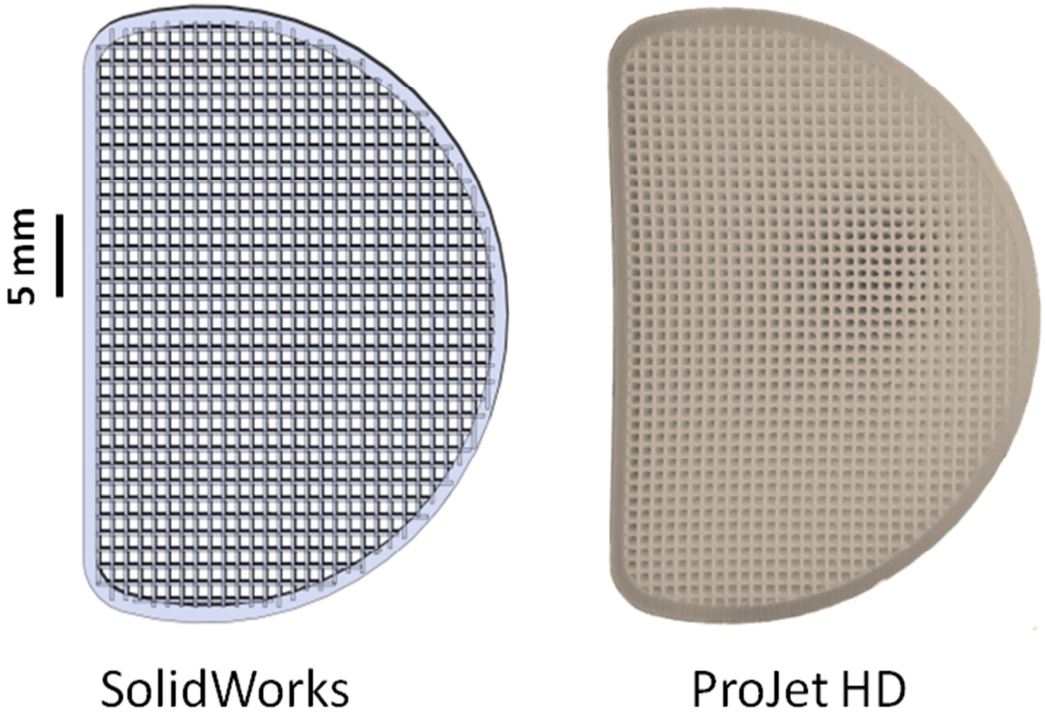

Figure 3. 6 Top views of the CAD model developed in SolidWorks (left) and the physical bone surrogate manufactured via Projet HD 3D printer (right).

3.2 Morphology Analysis

3.2.1 3D Bone Surrogate Morphology

MicroCT was used to assess the variability in the morphology of eight osteoporosis type (Osteo) 3D bone surrogates. Figure 3.7 shows an example of the cylindrical volume of interest (15 mm in diameter and 15 mm in length) that was consistently defined at the centre of each 3D Osteo surrogate and used to obtain the bone volume fraction (BV/TV) in %, trabecular thickness (Tb.Th) in mm, and trabecular separation (Tb.Sp) in mm (refer to Section 2.2.2). Figure 3.8 shows the histograms associated with the respective thickness and spacing maps.

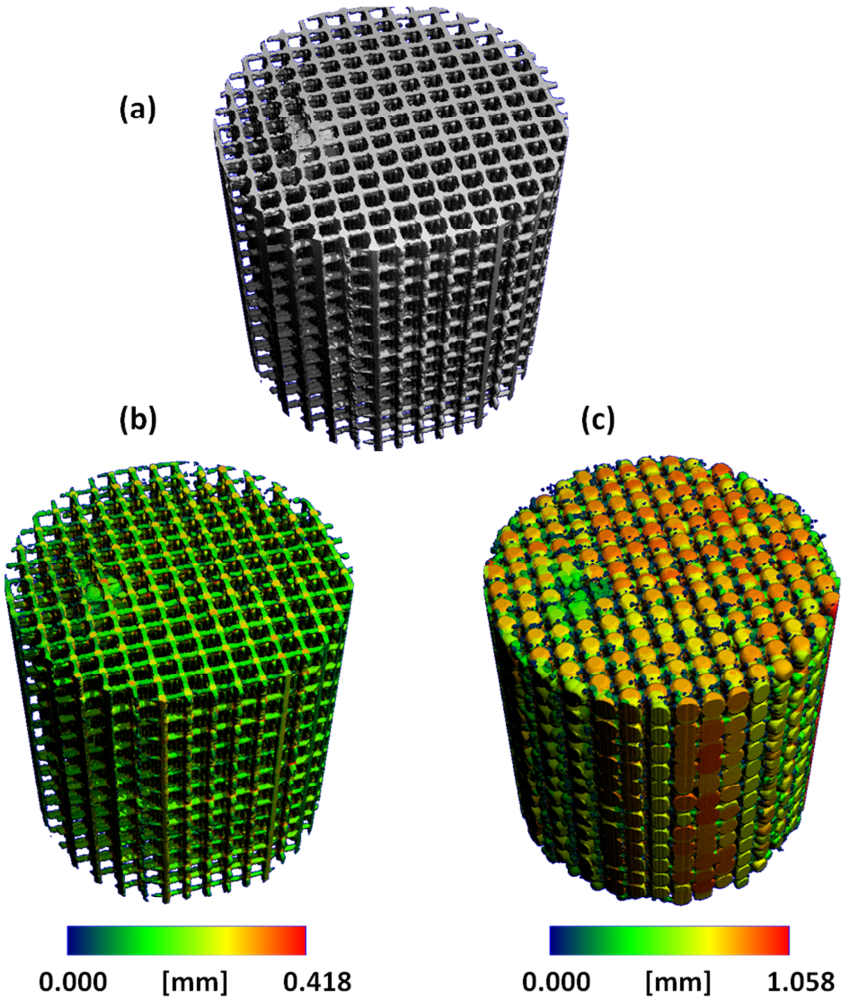

Figure 3. 7 (a) Cylindrical volume of interest defined at the centre of the osteoporotic type 3D bone surrogates with its associated thickness map (b) and spacing map (c).

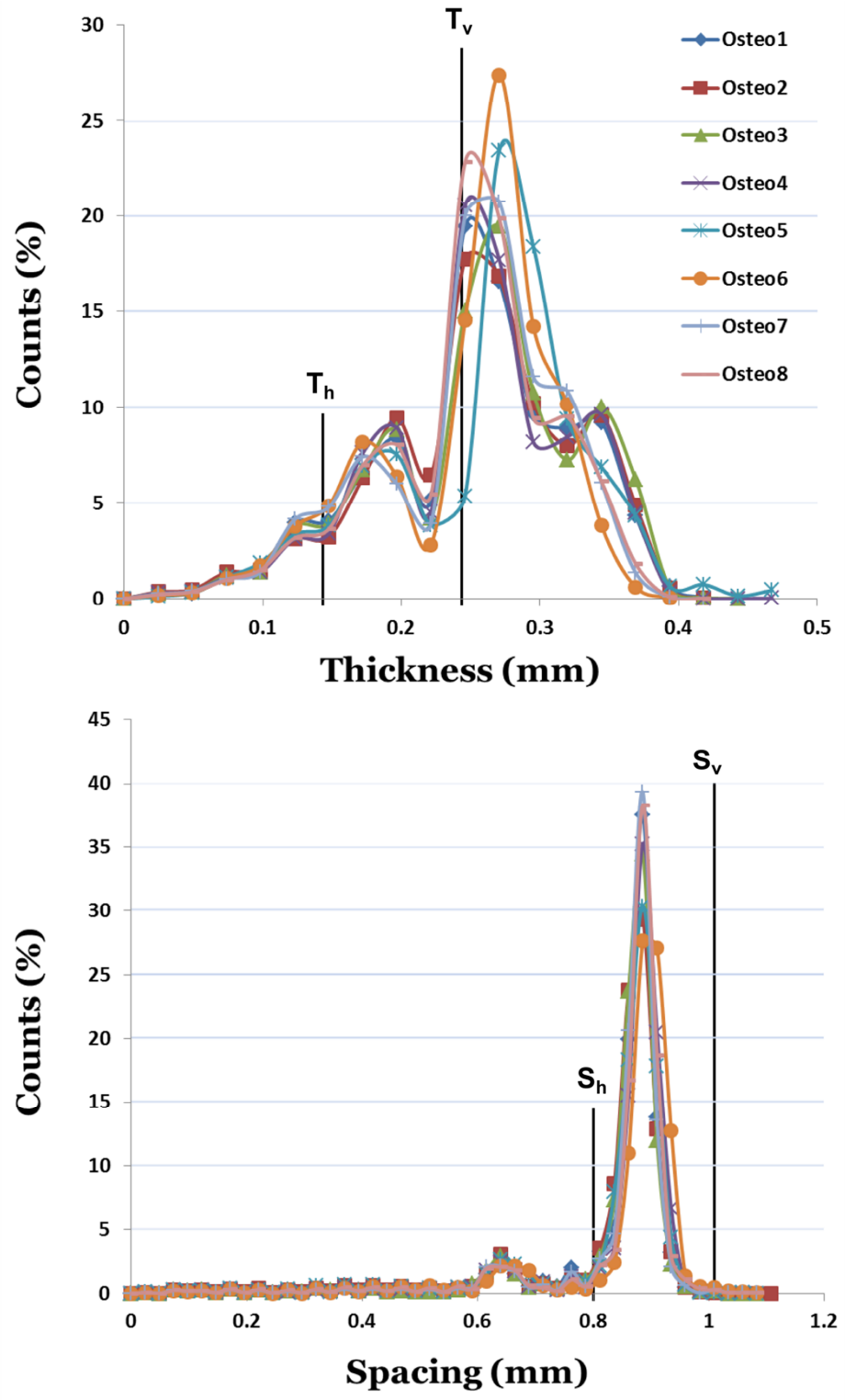

Figure 3. 8 Histograms of the trabecular thickness (top) and trabecular separation (bottom) obtained from the CT data of eight osteoporotic type (Osteo) 3D bone surrogates. The black lines represent the nominal horizontal and vertical thickness (T_h and T_v) and spacing (S_h and S_v), respectively.

The histogram of the thickness map revealed three distinct peaks at approximately 0.18, 0.27 and 0.34 mm. The first two peaks were associated with the horizontal and vertical struts of the 3D bone surrogates, which had a nominal thickness of 0.15 and 0.25 mm, respectively. The third peak could be related to manufacturing artifacts associated with residual support material within the structure. On the other hand, the histogram of the spacing map revealed one distinct peak at approximately 0.89 mm, which corresponded to the nominal spacings in the horizontal (i.e. between vertical struts) and vertical (i.e. between horizontal struts) planes of the 3D surrogates which were 0.8 and 1.0 mm, respectively. The variability in the morphology of the osteoporosis 3D bone surrogates was very low with an overall strut thickness (Tb.Th) of 0.25 ± 0.04 mm and an overall pore spacing (Tb.Sp) of 0.89 ± 0.03 mm. The average porosity which was obtained from the microCT data (100 - BV/TV) and validated using Archimedes' principle was 82.6 ± 1.1 %.

Figure 3.9 presents the flow rate and the pressure that were measured to experimentally derive the permeability of a cube ($2 \times 2 \times 2$ cm^3) with structure similar to an osteoporosis type 3D bone surrogate. The computed permeability based on Darcy's law (Equations 19 and 20) was $43.1 \pm 6.0 \times 10^{-10}$ m^2.

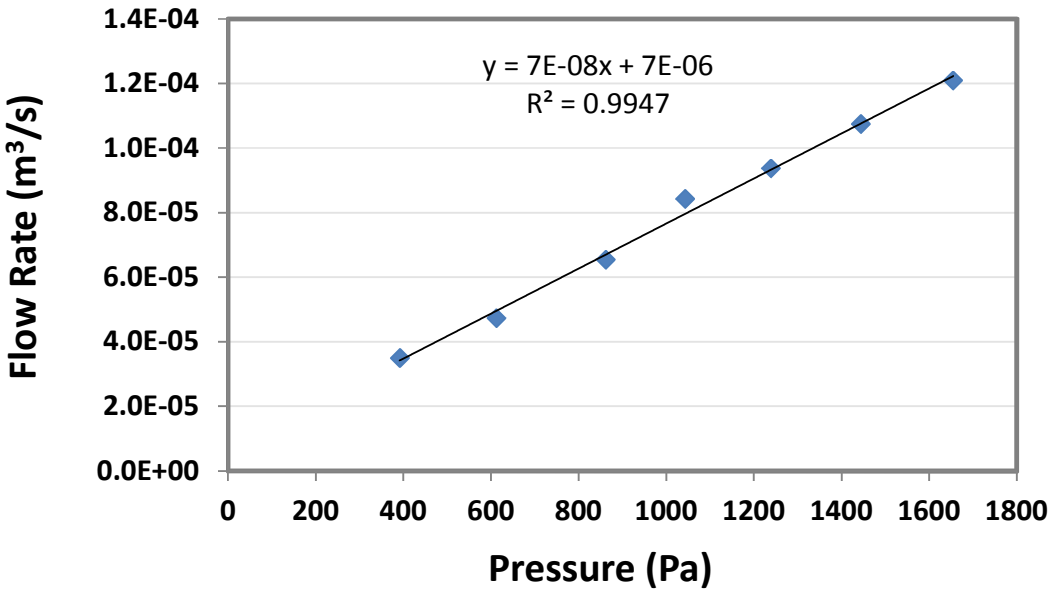

Figure 3. 9 The flow rate plotted against the pressure to compute the permeability of the osteoporosis type 3D bone surrogates.

3.2.2 2D Flow Model Morphology

This section presents the geometrical variations in the structure of the 2D flow models. Lateral visualization of the osteoporosis flow models revealed that the structure was conical rather than cylindrical in shape (see Figure 2.14). The overall edge-to-edge (D_{ee}) and valley-to-valley (D_{vv}) distances were 934 ± 3.2 and 1251 ± 0.5 µm, respectively. The average height (h) of the profiles was 433 ± 4.4 µm. The measured porosity of the osteoporosis flow models was 87.9 ± 2.0 %. Figures 3.10 to 3.12 present the results of the measurements performed on the lateral profiles of the left and right cuts through the sagittal plane of three osteoporosis flow models. It is evident that the geometrical variations between and within the flow models was very low.

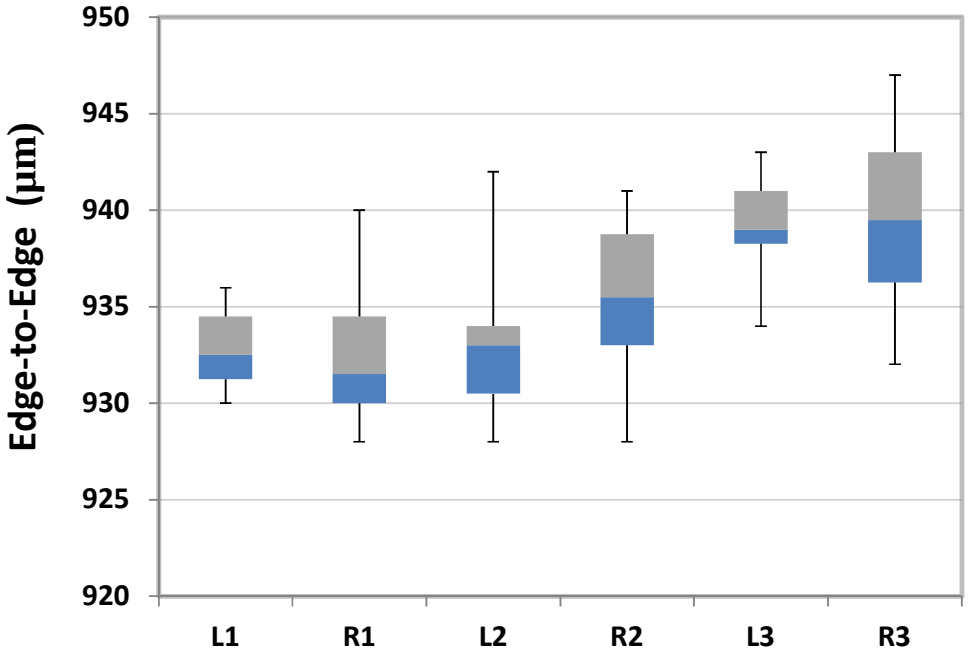

Figure 3. 10 The edge-to-edge distances (D_{ee}) measured on the lateral profiles of the left (L) and right (R) cuts performed through the sagittal plane of three osteoporosis type flow models.

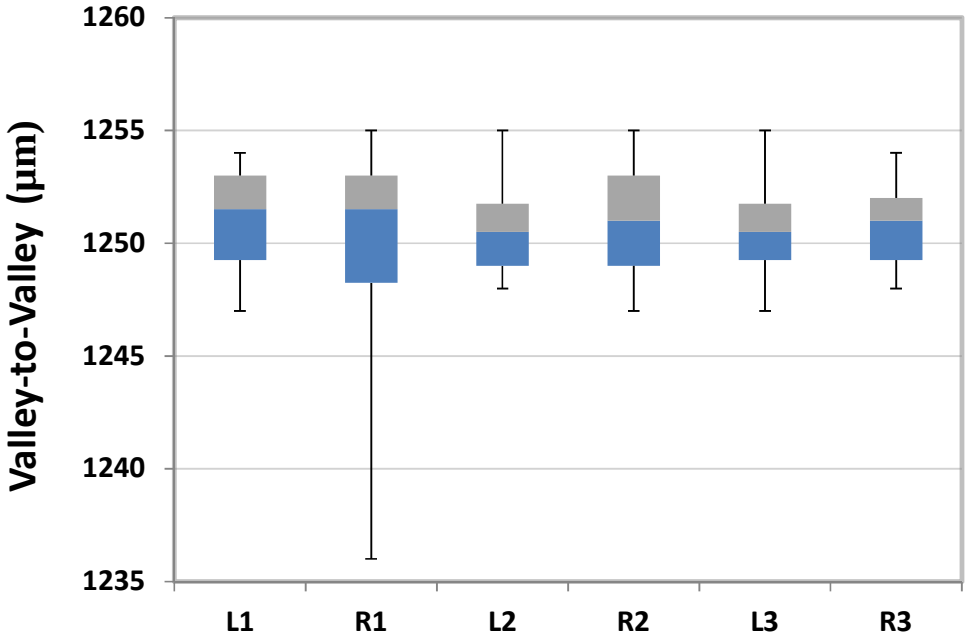

Figure 3. 11 The valley-to-valley distances (D_{vv}) measured on the lateral profiles of the left (L) and right (R) cuts performed through the sagittal plane of three osteoporosis type flow models.

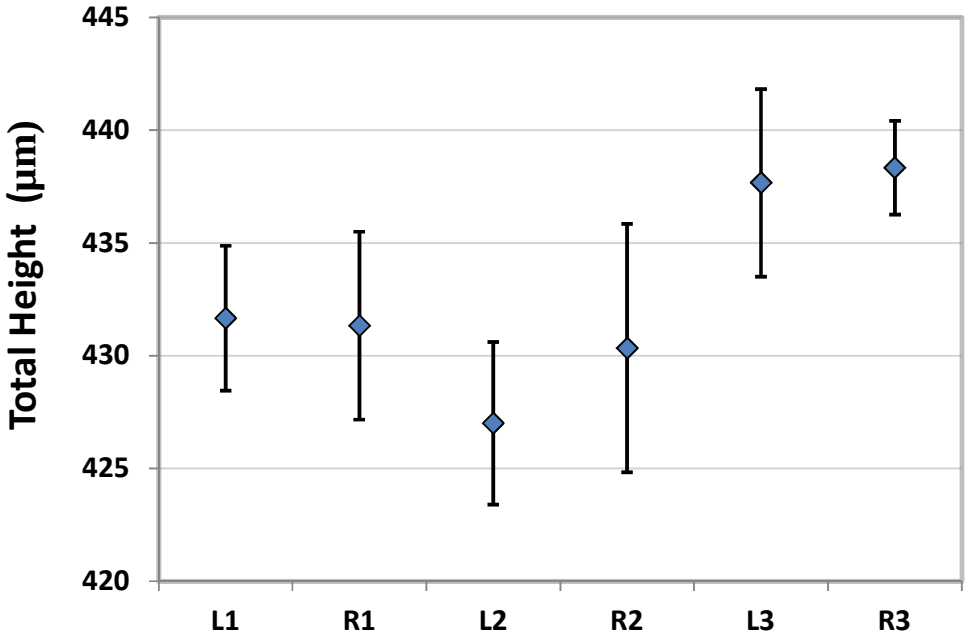

Figure 3. 12 The total heights (h) measured on the lateral profiles of the left (L) and right (R) cuts performed through the sagittal plane of three osteoporosis type flow models.

3.3 CONTACT ANGLE ANALYSIS

Figure 3.13 presents a representative sample of the static contact angle analysis performed on the material used to manufacture the 3D bone surrogates and the 2D flow models as well as cortical bone from a human femur and an ovine vertebra. Figure 3.14 compares the contact angle measurements performed on each material. No significant difference ($p = 0.21$) was found in the surface wettability of all materials. The range of contact angle measurements was 49 to 77º for the Projet material used to manufacture the 3D bone surrogates, 60 to 74º for the photopolymer used to manufacture the 2D flow models, 60 to 75º for bone form a human femur, and 58 to 69º for bone from an ovine vertebra. The Projet material had the highest range of contact angle measurements, however the measurements were obtained from material manufactured at four different time points. The mean difference in contact angle measurements performed on Projet material manufactured in one time point was 14º.

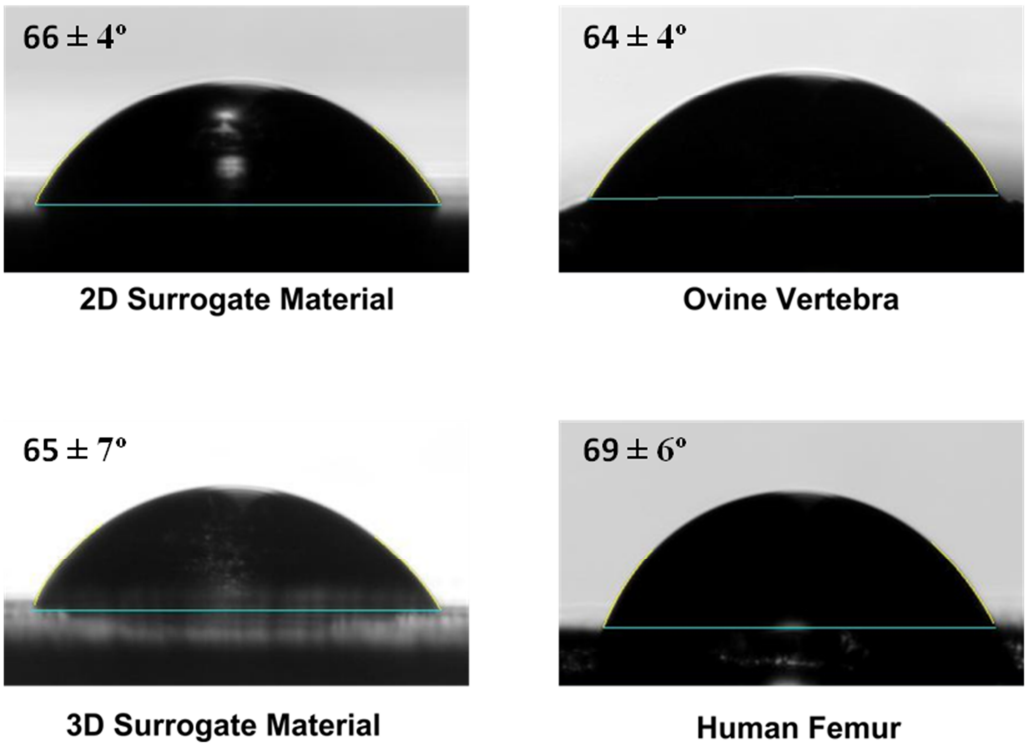

Figure 3. 13 A representative sample of the static contact angle analysis performed on the materials used to manufacture the 3D bone surrogates and the 2D flow models as well as cortical bone from a human femur and an ovine vertebra.

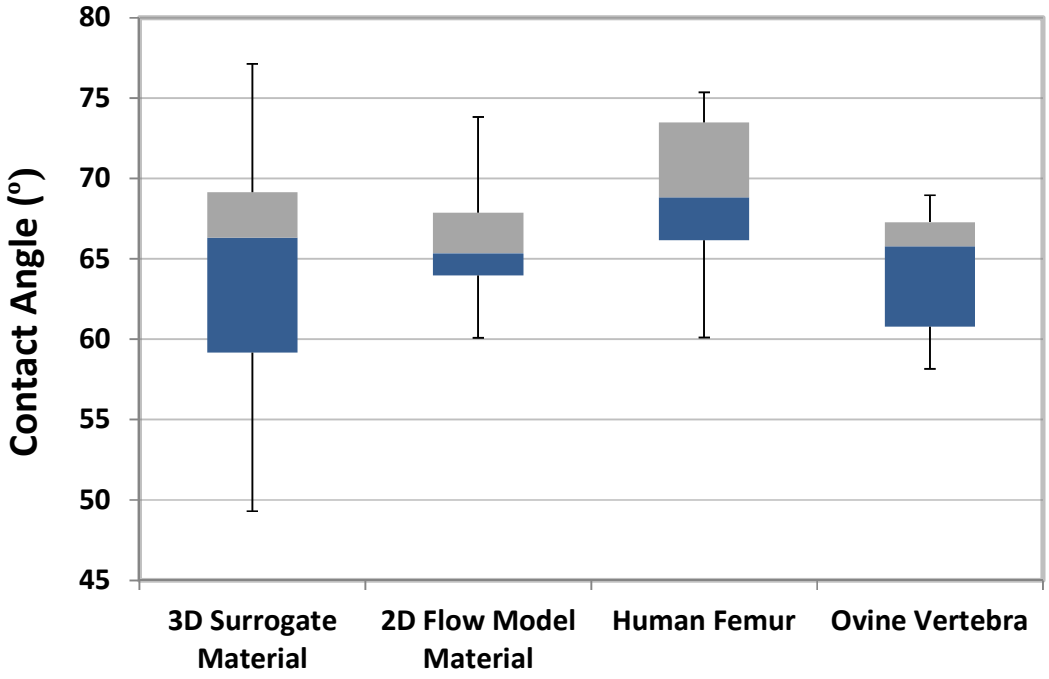

Figure 3. 14 The range of contact angle measurements performed on the materials used to manufacture the 3D bone surrogates and the 2D flow models as well as cortical bone from a human femur and an ovine vertebra.

3.4 Rheological Testing

Figure 3.15 presents the dynamic viscosity of the bone marrow substitutes as a function of shear rate. The marrow substitute, prepared using an aqueous solution of carboxymethyl cellulose 1.25% w/w, maintained an average viscosity of 0.063 ± 0.002 Pa·s at shear rates ranging from 1 to 100 s^{-1}. However, the one prepared using an aqueous solution of carboxymethyl cellulose 2.5% w/w had an average viscosity of 0.392 ± 0.034 Pa·s at similar shear rates. The results revealed that both marrow substitutes exhibited Newtonian fluid characteristics (viscosity independence to shear rate) at a temperature of 21 °C. The decrease in the viscosity of the 2.5% w/w carboxymethyl cellulose solution at shear rates above 40 s^{-1} indicates the state of shear thinning behaviour following a low shear plateau where the viscosity is relatively constant. At higher shear rates, the molecules start to unfold causing the viscosity to decrease. This effect is negligible in the 1.25% w/w carboxymethyl cellulose solution mainly due to the higher concentration of water.

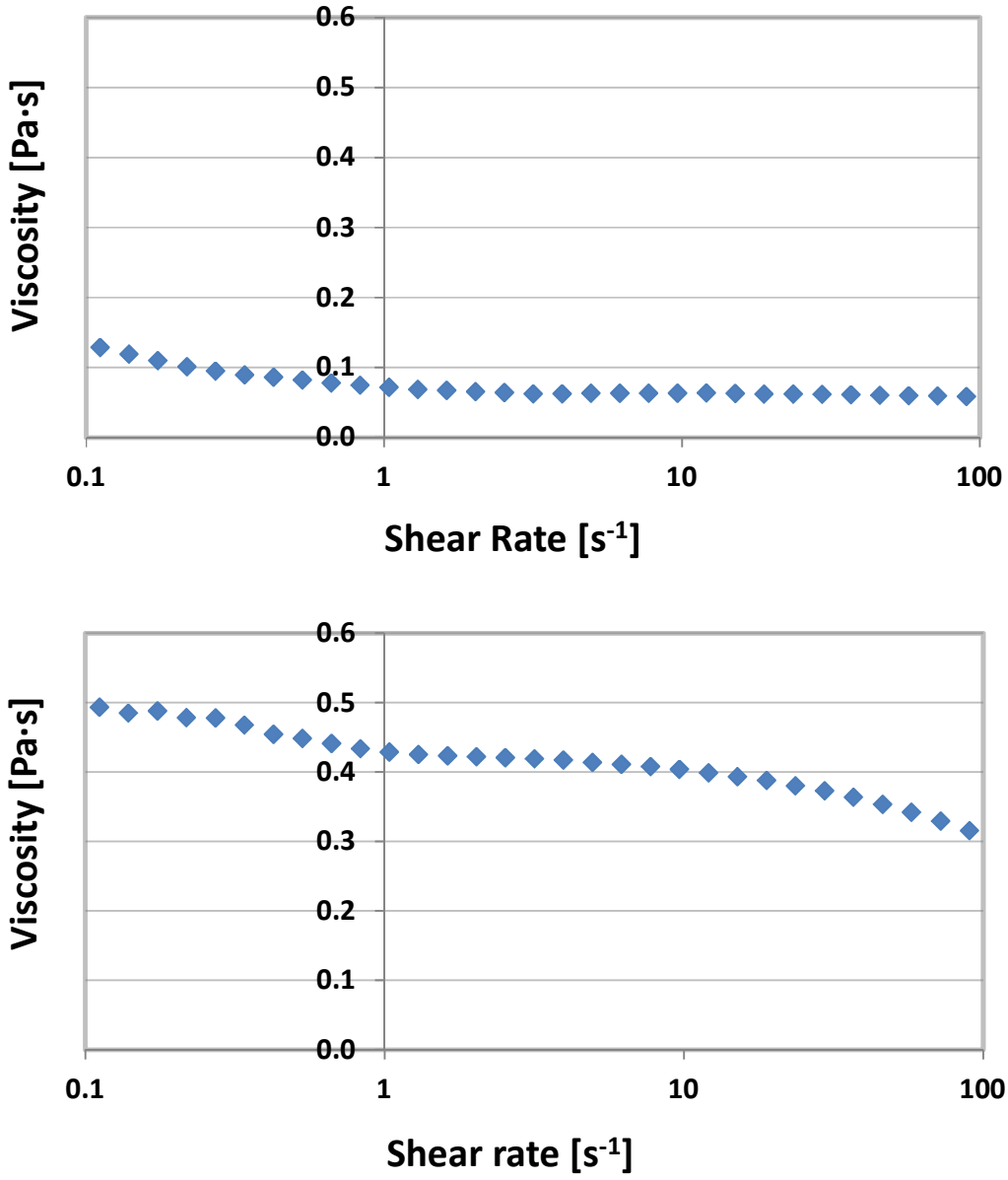

Figure 3. 15 Dynamic viscosity as a function of shear rate for the bone marrow substitute prepared using an aqueous solution of carboxymethyl cellulose 1.25% w/w (top) and 2.5% w/w (bottom). All measurements were performed at 21ºC.

Figure 3.16 presents the dynamic viscosity as a function of shear rate for 60 Pa·s silicone oil with and without the addition of 20% v/v Lipiodol. The viscosity measurements were performed at a temperature of 21 ºC. When no Lipiodol was present, the average viscosity of the silicone oil was maintained at 52.8 ± 2.4 Pa·s for shear rates below 40 s^{-1} then decreased to 41.1 ± 1.7 Pa·s for shear rates ranging from 40 to 100 s^{-1}. With the addition of Lipiodol, the silicone oil formulation had an

average viscosity of 48.0 ± 1.5 Pa·s at shear rates below 40 s^{-1}. The average viscosity decreased to 39.9 ± 2.4 Pa·s at shear rates ranging from 40 to 100 s^{-1}.

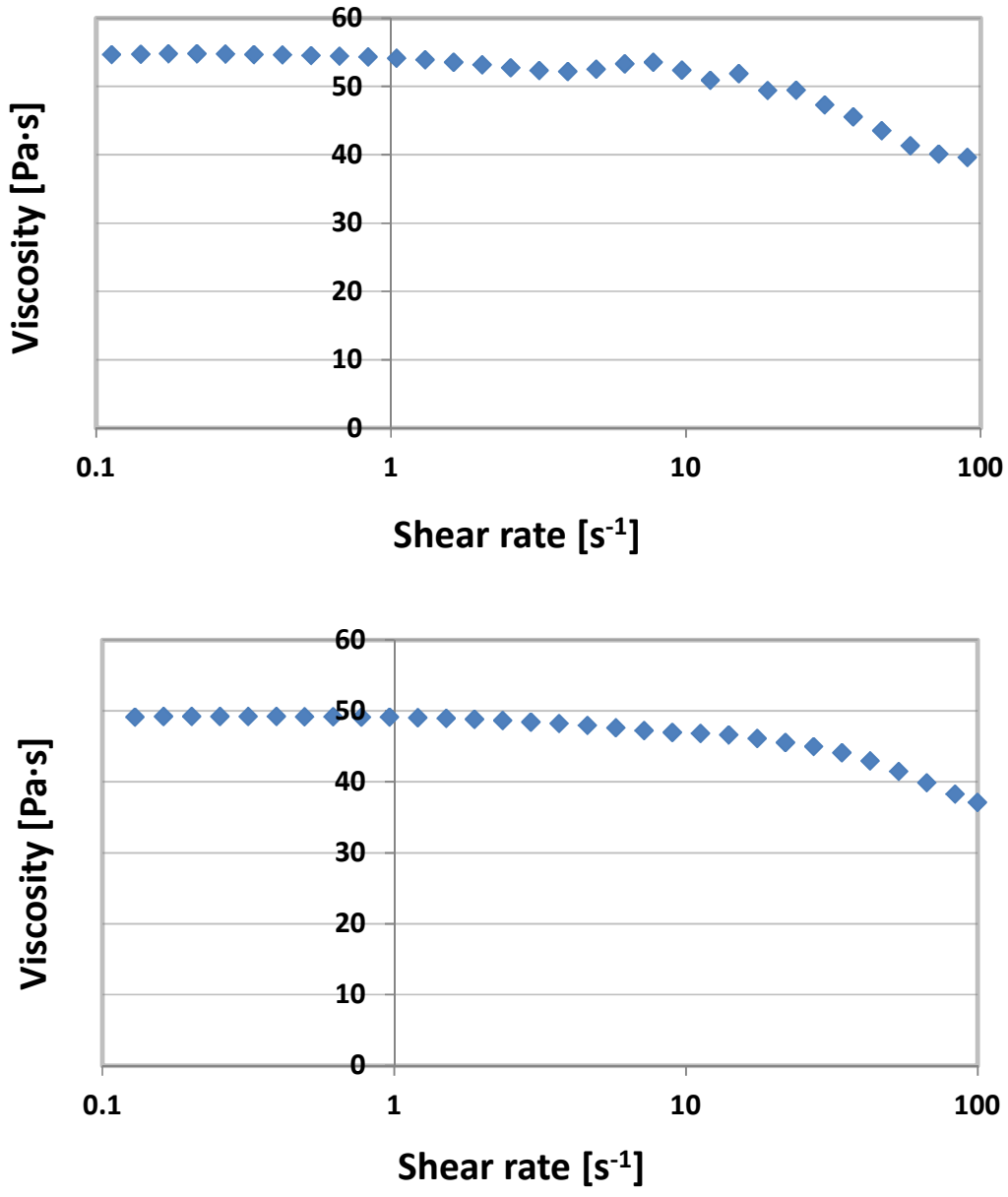

Figure 3. 16 Dynamic viscosity as a function of shear rate for the 60 Pa·s silicone oil (top) and the 60 Pa·s oil-Lipiodol formulation (bottom). All measurements were performed at 21°C.

For shear rates below 40 s^{-1}, the results showed that the addition of Lipiodol decreased the overall viscosity of the silicone oil by 5 Pa·s (from approximately 53 to 48 Pa·s) but did not alter its fluid characteristics as both formulations exhibited Newtonian

fluid behaviour (viscosity independence to shear rate). The results also showed that both oil formulations exhibited shear thinning behaviour at shear rates ranging from 40 to 100 s^{-1} with their viscosity reaching a lower limit of approximately 40 Pa·s.

Figure 3.17 presents the dynamic viscosity as a function of shear rate for the 10 Pa·s silicone oil formulation, which was prepared using 10 Pa·s silicone oil and 20% v/v Lipiodol. The data revealed that the presence of Lipiodol did not affect the viscosity of the silicone oil, which was maintained at 9.52 ± 0.08 Pa·s for shear rates ranging from 1 to 100 s^{-1}. The results also showed that the oil-Lipiodol formulation maintained the characteristics of the silicone oil and exhibited Newtonian fluid characteristics (viscosity independence to shear rate) at a temperature of 21 °C.

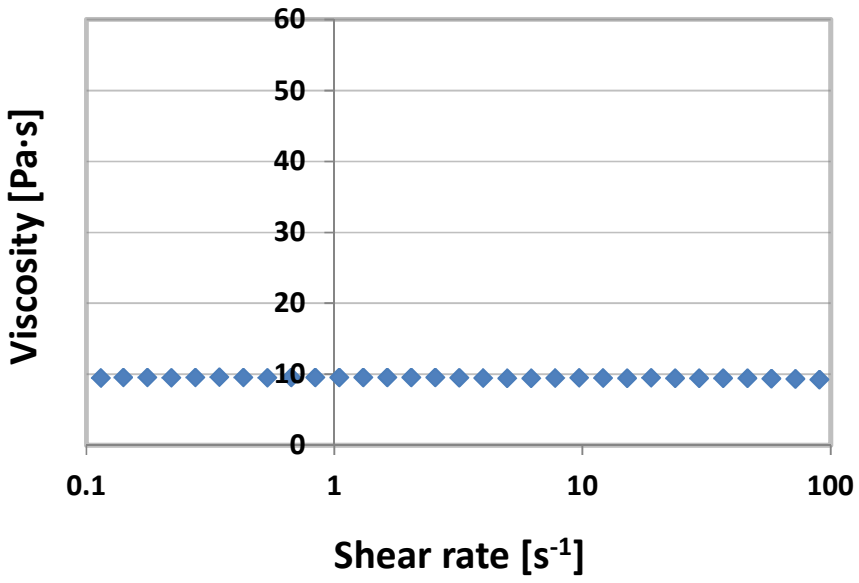

Figure 3. 17 Dynamic viscosity as a function of shear rate for the 10 Pa·s silicone oil-Lipiodol formulation. All measurements were performed at 21°C.

3.5 CEMENT POWDER IMAGING

Qualitative SEM analysis of the powder components (Figure 3.18) showed that Opacity+ (OC) and Osteopal V (OP) have similar as well as more uniform particle size and distribution (~19–69 and 18–55 µm, respectively) when compared to Parallax (PL) and Simplex P (SP), which have the largest and widest range of particle sizes (~11–105 and 7–83 µm, respectively). The non-circular particles in the images are the radiopacifiers, which appear to be large in OC and OP (both containing 45% w/w ZrO_2) and more granular in PL and SP (containing 30 and 10% w/w $BaSO_4$, respectively). Also, the angular-shaped particles observed in the OC powder are hydroxyapatite crystals.

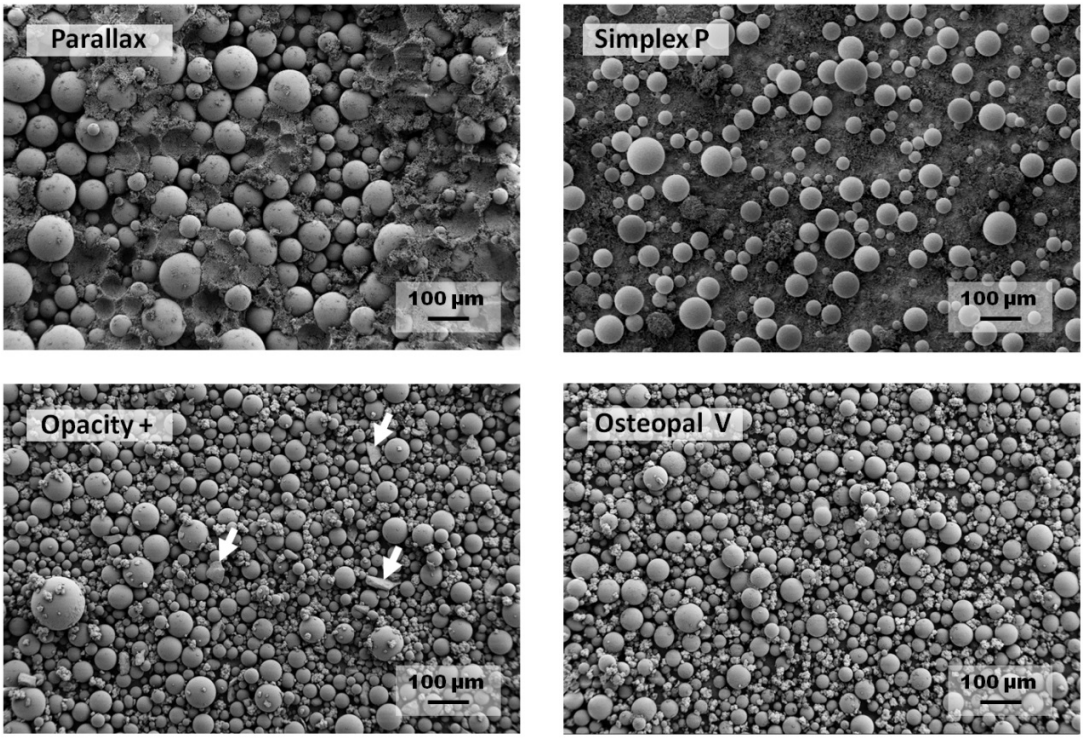

Figure 3. 18 SEM micrographs of the different powder components. The angular-shaped particles (white arrows) observed in the OC powder are hydroxyapatite crystals. The non-circular particles are the radiopacifiers, which appear to be large in OC and OP and more granular in PL and SP.

3.6 3D Bone Surrogate Injections

3.6.1 Needle Placement

The quantification of the needle tip placement within the 3D bone surrogates (Figure 3.19a) revealed that the average needle length (d) from the posterior wall was 23.0 ± 1.4 mm and the average needle angle (α) with respect to the posterior wall was 69.7 ± 2.3º. As the nominal CAD distance (d) is 25 mm and the nominal CAD angle (α) is 69.8º, the average error was 8% for the needle length (d) and 0.1% for the needle angle (α). Figure 3.19b shows the location of the needle tips (blue hollow circles) with respect to the fluoroscopy field of view. The distance between the fluoroscopy centroid (solid white circle) and the average location of the needle tips (solid red square) was 11.3 ± 2.8 mm.

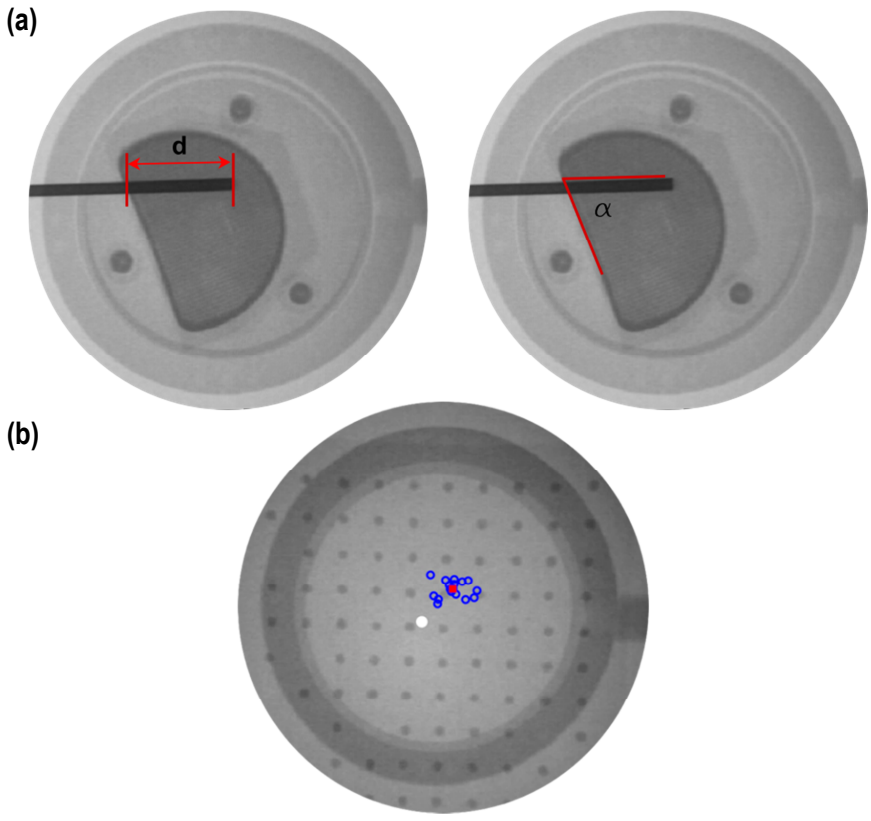

Figure 3. 19 (a) Measurements performed to quantify the error in the needle placement within the 3D surrogates. (b) Needle tip locations (blue hollow circles) with respect to the fluoroscopy field of view. The solid white circle represents the fluoroscopy centroid and the solid red square represents the average needle tip location.

3.6.2 Oil Injections

Flow Distribution

Figure 3.20 presents the resulting flow distribution after 5 mL of 10 and 60 Pa·s silicone oil (Si10 and Si60) were separately injected under a constant flow rate of 3 mL/min into each three-dimensional bone surrogate: osteoporosis (Osteo), multiple myeloma (MM) and metastasis (Lesion). The simulated flow distribution obtained numerically by R. P. Widmer for the Si60 oil is also included for comparison.

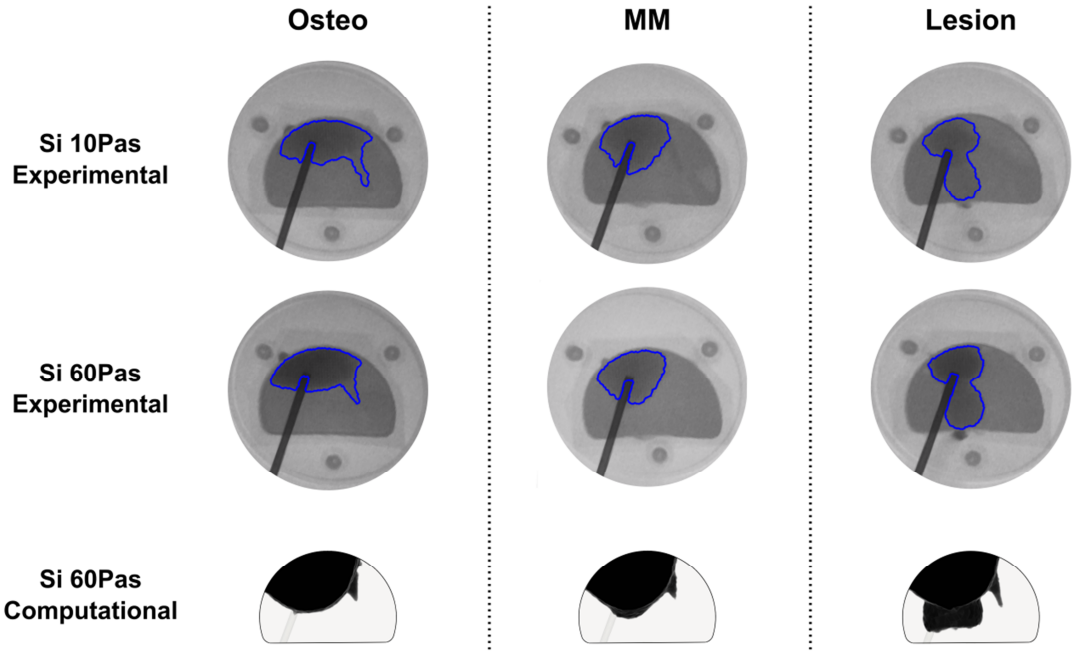

Figure 3. 20 Representative images of typical flow patterns after 5mL of 10 and 60 Pa·s silicone oil (Si10 and Si60) were separately injected into each 3D bone surrogate. The flow contours (blue) were obtained via image subtraction. The simulated flow distribution for Si60 is included for comparison.

Qualitative analysis showed that the experimental flow distribution in each surrogate was similar for both oils, independent of viscosity. Also, in the Osteo and MM surrogates there was a high tendency for anterior leakage only (neither oils reached the posterior wall), while in the Lesion surrogate there was a tendency for posterior leakage only (although both oils reached the anterior wall). The computer simulation predicted anterior leakage in all the bone surrogates, thus matching the experiments in

the Osteo and MM surrogates only. The posterior leakage observed experimentally in the Lesion surrogate was not predicted in the simulation. Figure 3.21 compares the experimental and computational flow evolution after 1, 3 and 5 mL of 60 Pa·s silicone oil was injected into each 3D bone surrogate.

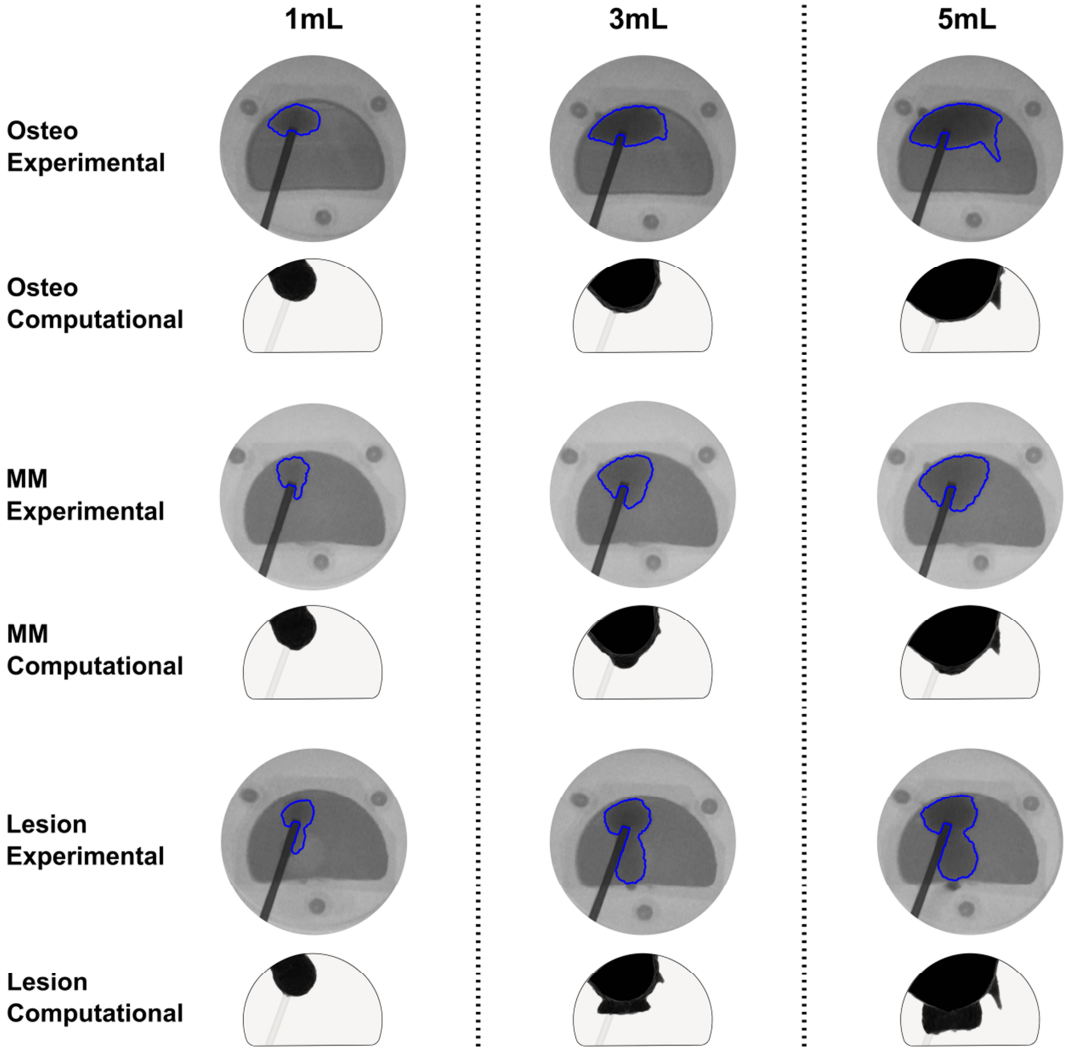

Figure 3. 21 Experimental and computational comparison between the typical flow evolution after 1, 3 and 5 mL of 60 Pa·s silicone oil was injected into each 3D bone surrogate.

In the Osteo surrogate, the experiments showed that the oils had a tendency to flow laterally along the path of the right needle insertion channel. This behaviour was not observed in the MM and Lesion surrogates due to the flow being preferentially along the lesions. The flow distribution obtained numerically via the computer simulation

was similar to that observed experimentally in the Osteo and MM surrogates, although in the simulation the flow extended further towards the posterior wall. Furthermore, in the MM surrogate, the simulation predicted lateral flow into the right needle insertion channel which was not observed experimentally. In the Lesion surrogate, the flow distribution obtained numerically did not match that observed experimentally since the simulated flow was preferentially horizontal and never reached the posterior wall.

Mean Spreading Distance

Figure 3.22 presents the mean spreading distance (MSD) as a function of time after 5 mL of Si10 and Si60 oils were separately injected into the Osteo, MM and Lesion surrogates. The MSD obtained numerically via the computer simulation for the Si60 oil is also included for comparison. The results showed that an increase in the oil viscosity from 10 to 60 Pa·s did not have a significant effect on the MSD. This agreed with the qualitative analysis which showed that the experimental flow distribution of both oils was similar in each surrogate (Figure 3.20).

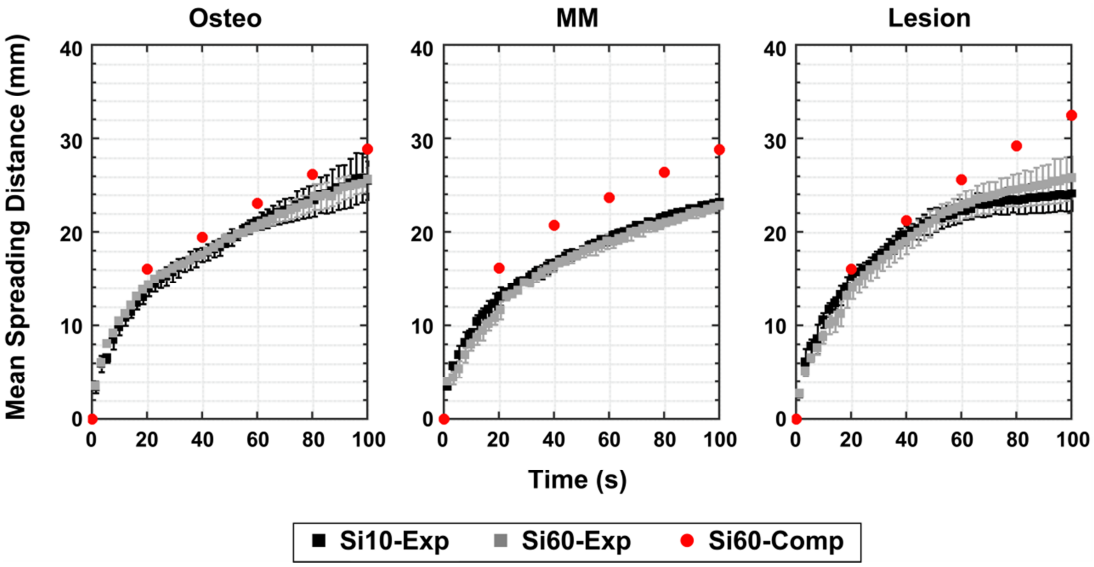

Figure 3. 22 The mean spreading distance as a function of time after 10 and 60 Pa·s silicone oil (Si10 and Si60) were separately injected into each 3D bone surrogate at a constant flow rate of 3 mL/min. The spreading distance obtained numerically for Si60 is included for comparison. The experimental data is presented as mean ± SD.

Relative to the Osteo surrogate, the presence of structural voids in the MM surrogate only, caused a significant ($p < 0.05$) decrease in the MSD (11.1%) from 25.7 to 22.9 mm after 5 mL of oil was injected, independent of viscosity. This decrease in MSD can also be observed qualitatively in the resulting contours describing the fluid shape (Figure 3.20). Following the injection of 5 mL of Si60, the MSD measured using the simulated flow distribution was higher than that measured experimentally. In the Osteo surrogate, the numerical MSD (28.9 mm) was 12.5% higher than the experimental (25.7 mm). In the MM and Lesion surrogates the difference between the numerical and experimental MSD was more pronounced. In the MM surrogate, the numerical MSD (28.8 mm) was 26.2% higher than the experimental (22.9 mm), and in the Lesion surrogate, the MSD obtained numerically (32.4 mm) was 25.2% higher than that measured experimentally (25.9 mm).

Leakage Time

Figure 3.23 presents the leakage time after the Si10 and Si60 oils were separately injected into the Osteo, MM and Lesion surrogates at a constant flow rate of 3 mL/min. The leakage time obtained numerically for the Si60 oil is also included for comparison. The results showed that increasing the starting viscosity from 10 to 60 Pa·s did not have a significant effect on the leakage time, independent of structure. However, introducing structural voids significantly increased the leakage time independent of the oil viscosity. Relative to the Osteo surrogate, the large void (Ø 19.0 mm) in the Lesion surrogate caused a more pronounced increase in the leakage time compared to the three small voids (Ø 6.0 mm each) in the MM surrogate. The leakage time for the Si10 and Si60 oils in the Osteo surrogate (uniform structure) was 21.6 ± 2.0 and 27.2 ± 1.7 s, respectively. In the MM surrogate, the leakage time for the Si10 and Si60 oils increased by 35.1 and 29.8%, respectively. In the Lesion surrogate, the leakage time of the Si10 oil doubled (21.9 s increase) while that of the Si60 oil increased by 77.8%.

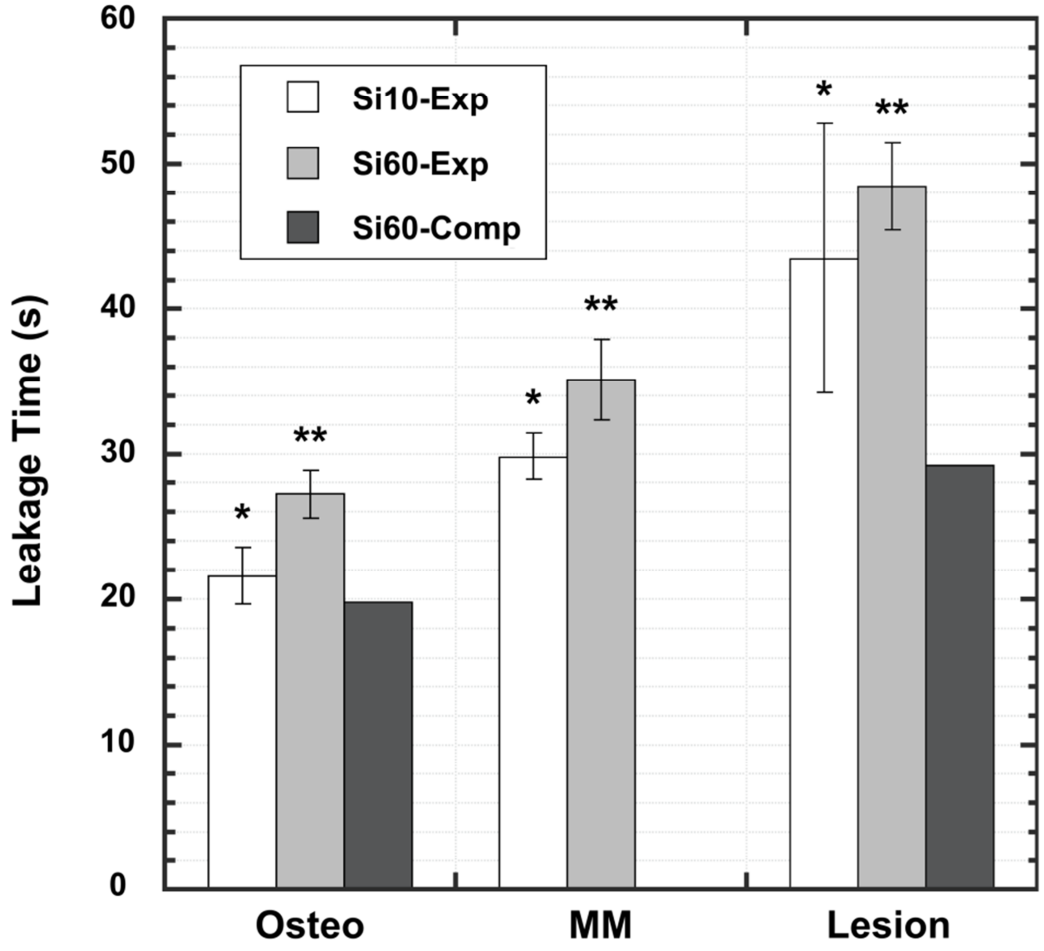

Figure 3. 23 The leakage time after 10 and 60 Pa·s silicone oil (Si10 and Si60) were separately injected into each 3D bone surrogate at a constant flow rate of 3 mL/min. The leakage time obtained numerically for Si60 is included for comparison. The experimental data is presented as mean ± SD. No significant differences were found between the oils in each surrogate type. The only significant differences ($p < 0.05$) were for each oil between the different surrogate types with Osteo being the control. These are labelled * and **.

Injection Pressure

Figure 3.24 presents the pressure required to inject the Si10 and Si60 oils into the Osteo, MM and Lesion surrogates as a function of time. The results showed that increasing the oil viscosity from 10 to 60 Pa·s had a significant ($p < 0.05$) increase on the injection pressure. The peak pressure required for injecting 5 mL of the Si10 and Si60 oils into the structure of each bone surrogate at 3 mL/min increased on average from 0.033 to 0.183 MPa. Furthermore, introducing structural voids did not have a significant effect on the peak injection pressure, independent of the oil viscosity.

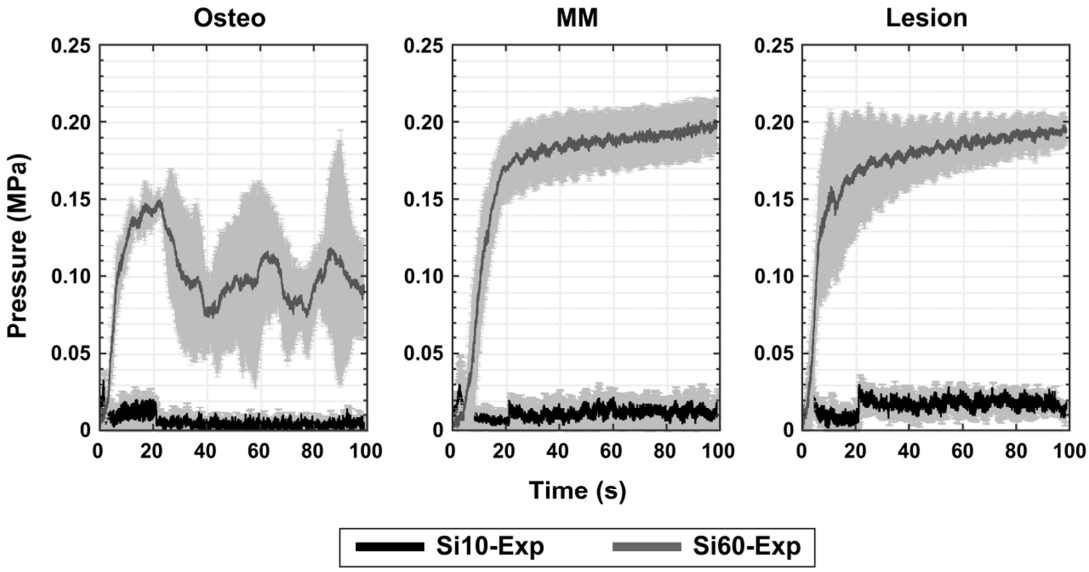

Figure 3. 24 The inlet pressure as a function of time for the 10 and 60 Pa·s silicone oil (Si10 and Si60) injected into each 3D bone surrogate at a constant flow rate of 3 mL/min. The experimental data is presented as mean ± SD.

3.6.3 Cement Injections

Flow Distribution

Figure 3.25 presents the resulting flow distribution after 5 mL of Simplex P bone cement (SP1:1, Table 2.7) was separately injected under a constant flow rate of 3 mL/min at 4 and 8 min (SP4 and SP8) after mixing into each three-dimensional bone surrogate: osteoporosis (Osteo), multiple myeloma (MM) and metastasis (Lesion). The simulated flow distribution obtained numerically by R. P. Widmer for the SP4 cement is also included for comparison.

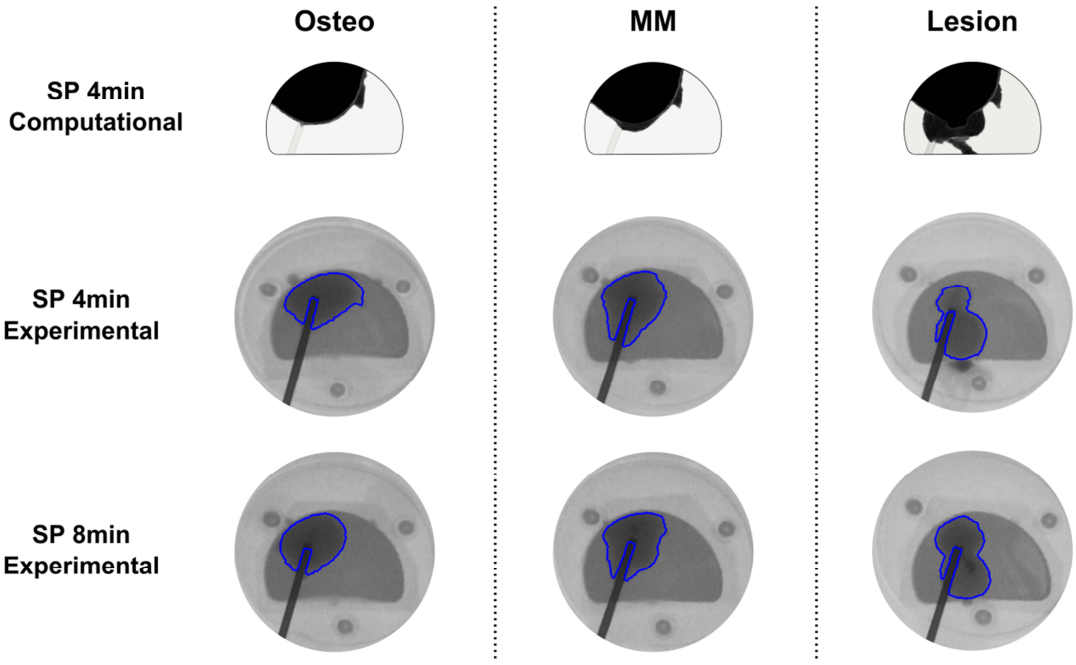

Figure 3. 25 Representative images of typical flow distribution after 5mL of Simplex P cement was separately injected 4 and 8 min after mixing (SP4 and SP8) into each 3D bone surrogate. The flow contours (blue) were obtained via image subtraction. The simulated flow distribution for SP4 is included for comparison.

In the Osteo surrogate, the cement injected at 4 min (SP4) had a tendency to flow laterally into the right needle insertion channel, which was kept open on the inside but closed off on the outer surface of the posterior wall. This behaviour was not observed in the MM and Lesion surrogates, independent of cement injection time, mainly due to the flow being preferentially along the lesions. Furthermore, qualitative analysis

showed that the experimental flow distribution in the MM surrogate was similar for both cements (SP4 and SP8). In the lesion surrogate, the SP4 cement never reached the anterior wall, whereas the SP8 cement reached the anterior wall and had a wider anterior fill. Figure 3.26 compares the experimental and computational flow evolution after 1, 3 and 5 mL of Simplex P cement was injected at 4 min after cement mixing (SP4) into each 3D bone surrogate.

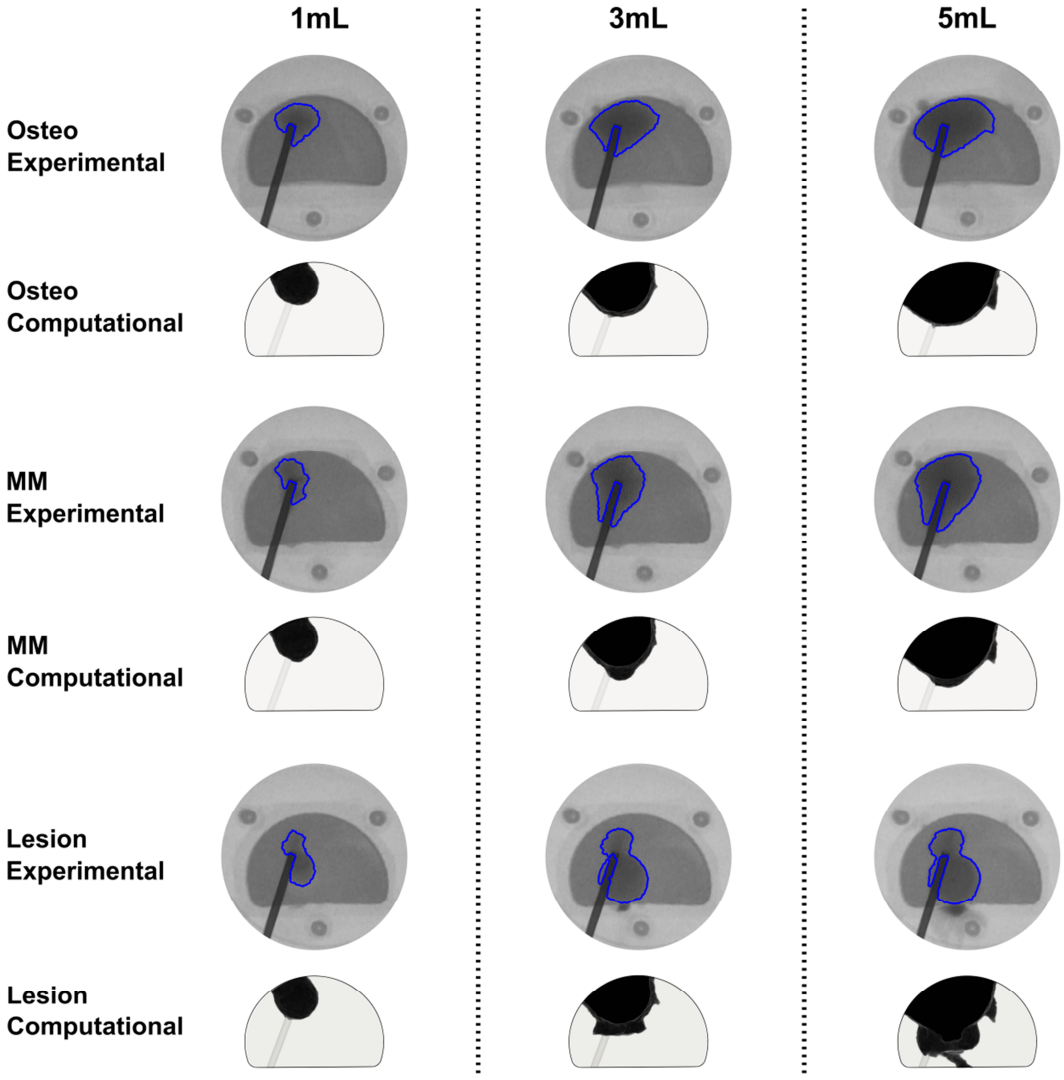

Figure 3. 26 Experimental and computational comparison between the typical flow evolution after 1, 3 and 5 mL of Simplex P cement injected at 4 min after mixing (SP4) into each 3D bone surrogate.

The flow distribution obtained numerically via the computer simulation was very similar to those observed experimentally in the Osteo surrogate. The simulated flow distribution was also similar to those observed experimentally in the MM surrogate; although, the simulation predicted lateral flow, while the experimental flow was preferentially along the lesions and extended more towards the posterior wall. In the Lesion surrogate, the flow distribution obtained numerically did not match that observed experimentally since the simulated flow was preferentially towards the anterior boundary and into the right needle insertion channel. Qualitative analysis of the experimental data showed that in the Osteo and MM surrogates there was a high tendency for anterior leakage only (the cements never reached the posterior wall), while in the Lesion surrogate there was a tendency for posterior leakage only (although SP8 cement reached the anterior wall). The computer simulation predicted anterior leakage in all the bone surrogates, thus matching the experiments in the Osteo and MM surrogates only. The posterior leakage observed experimentally in the Lesion surrogate was not predicted in the simulation, although the simulation predicted that the cement would reach the posterior wall.

Mean Spreading Distance

Figure 3.27 presents the mean spreading distance (MSD) as a function of time after 5 mL of SP4 and SP8 cements were separately injected into the 3D bone surrogates. The MSD obtained numerically via the computer simulation for the SP4 cement is also included for comparison. The experimental results showed that an increase in the injection time (i.e. cement viscosity) from 4 to 8 min after cement mixing did not have a significant effect on the MSD. This agreed with the qualitative analysis which showed that the experimental flow contours describing the shape of SP4 and SP8 were similar, mainly in the MM and Lesion surrogates (Figure 3.25). The results also showed that the presence of structural voids in the MM and Lesion surrogates did not have a significant effect on the MSD, independent of the injection time. After injecting 5 mL of SP4 cement, the MSD measured using the simulated flow distribution was significantly higher than that measured experimentally. In the Osteo surrogate, the numerical MSD (28.9 mm) was 22.7% higher than the experimental (23.5 mm), and in

the MM surrogate the numerical MSD (29.3 mm) was 16.3% higher than the experimental (25.2 mm). This is interesting especially when qualitatively the computational and experimental flow distributions were better matched in the Osteo surrogate. In the Lesion surrogate, the difference in the MSD obtained numerically (33.6 mm) and that measured experimentally (25.0 mm) was more pronounced (34.2%), which is not surprising especially when the simulated flow reached the anterior wall and was preferentially horizontal, while the experimental flow never reached the anterior wall and was along the lesion.

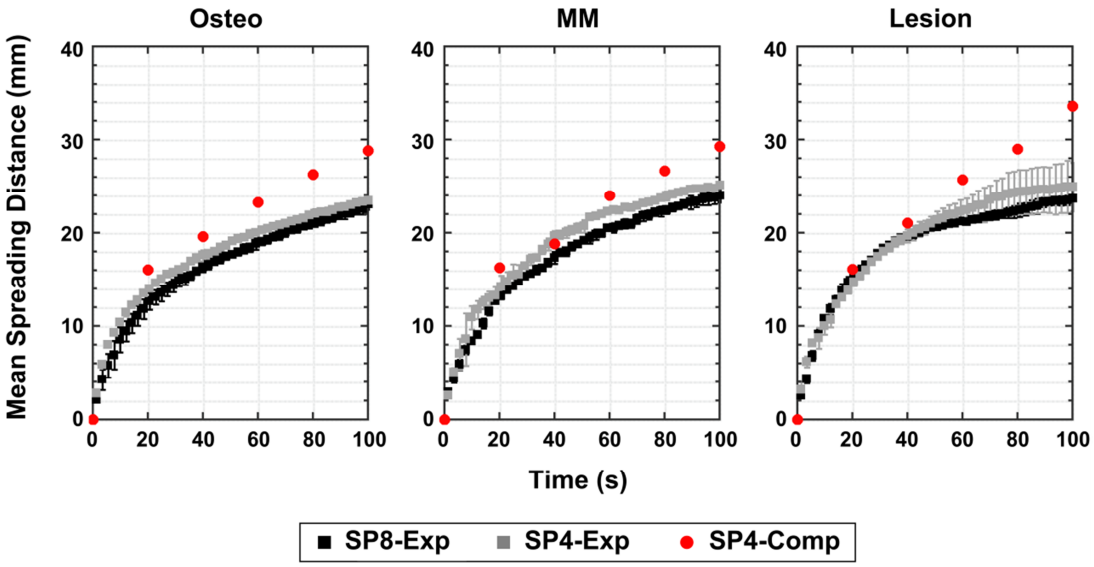

Figure 3. 27 The mean spreading distance as a function of time after Simplex P cement was separately injected at 4 and 8 min after mixing (SP4 and SP8) into each 3D bone surrogate at a constant flow rate of 3 mL/min. The spreading distance obtained numerically for SP4 is included for comparison. The experimental data is presented as mean ± SD.

Sphericity

Figure 3.28 (a) presents the sphericity after 5 mL of SP4 and SP8 cements were separately injected into the Osteo, MM and Lesion surrogates. The sphericity obtained numerically for the SP4 cement is also included for comparison. Figure 3.28 (b) provides a set of representative images for the resulting (experimental) cement bolus in each surrogate. In the Osteo and MM surrogates, the surperior surface of the cement bolus was flat indicating that the cement had reached the superior plate of the

specimen holder. In the Lesion surrogate however, it is evident that the cement flow was generally along the lesion in the inferior direction.

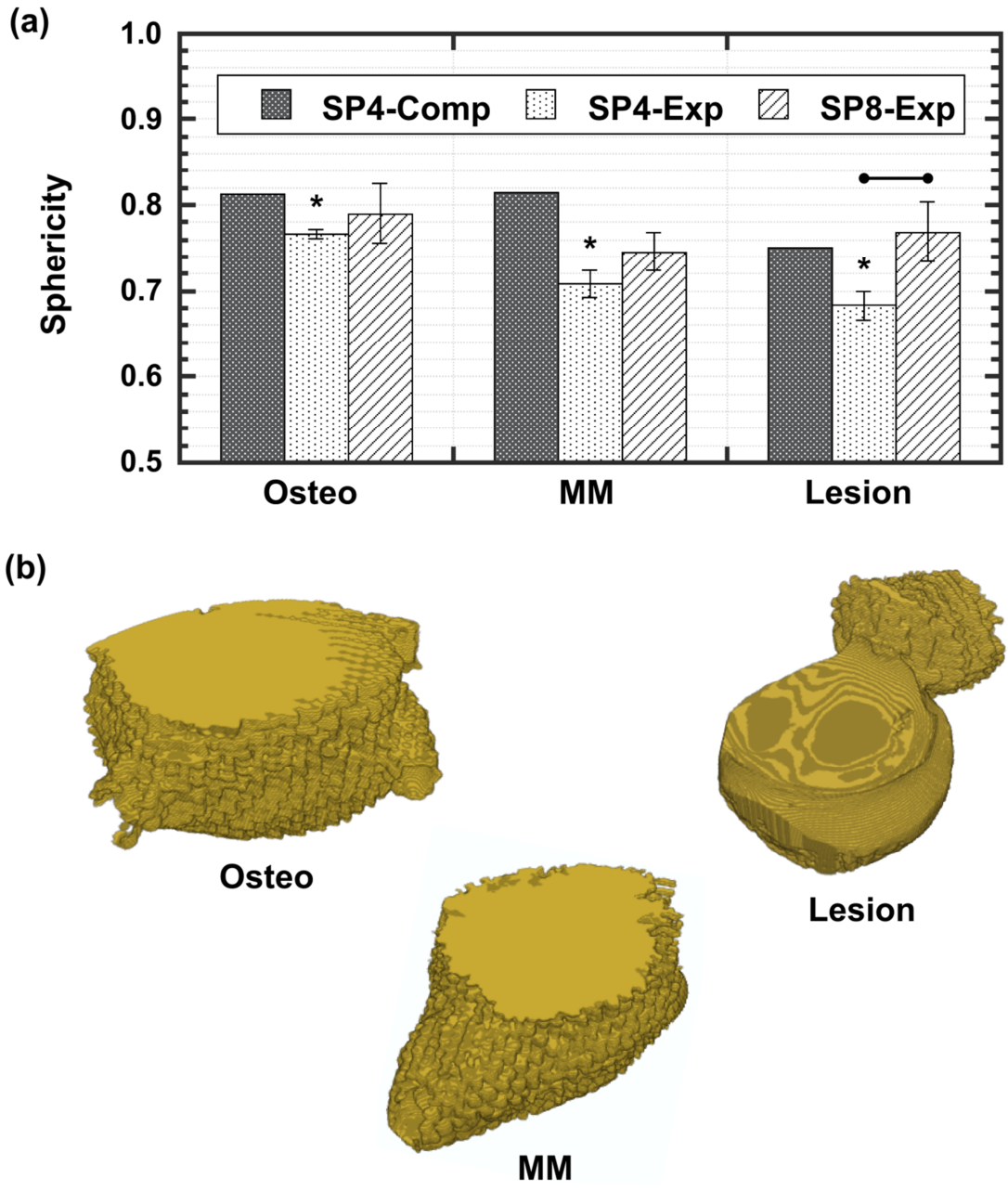

Figure 3. 28 (a) The sphericity after 5 mL of Simplex P cement was separately injected at 4 and 8 min after cement mixing (SP4 and SP8) into each 3D bone surrogate at a constant flow rate of 3 mL/min. The sphericity obtained numerically for SP4 is included for comparison. The experimental data is presented as mean ± SD and the signifcant differences ($p < 0.05$) are labelled * and ●——●. (b) Rrepresentative images of the SP4 cement bolus obtained from the experiments after 5 mL was injected into each 3D bone surrogate.

The analysis of the experimental data showed that increasing the injection time from 4 to 8 min after cement mixing significantly ($p < 0.05$) increased the sphericity in the Lesion surrogate only. The increase in sphericity was 12.6%, from 0.683 to 0.769 for SP4 and SP8, respectively. Furthermore, introducing structural voids significantly decreased the sphericity of the SP4 cement only, which was 0.767 ± 0.006, 0.708 ± 0.018 and 0.683 ± 0.018 in the Osteo, MM, and Lesion surrogates, respectively. Relative to the Osteo surrogate, the presence of the large void in the Lesion surrogate (Ø 19.0 mm) caused a more pronounced decrease (11.0%) in sphericity compared to the presence of three small voids (Ø 6.0 mm each) in the MM surrogate (7.7%). The sphericity obtained numerically via the computer simulation for the SP4 cement (0.812) was similar to that measured experimentally in the Osteo surrogate only (5.9% difference). In the MM and Lesion surrogates the sphericity obtained numerically was higher than that measured experimentally. In the MM surrogate, the numerical sphericity (0.813) was 14.9% higher than that measured experimentally, although the simulated flow distribution was qualitatively similar. In the Lesion surrogate, the difference in the sphericity obtained numerically (0.751) and that measured experimentally was less pronounced (10%), which is interesting especially when the simulated flow was preferentially horizontal while the experimental flow was along the lesion.

Leakage Time

Figure 3.29 presents the leakage time after the SP4 and SP8 cements were separately injected into the Osteo, MM and Lesion surrogates at a constant flow rate of 3 mL/min. The leakage time obtained numerically for the SP4 cement is also included for comparison. The experimental results showed that increasing the injection time from 4 to 8 min after cement mixing significantly ($p < 0.05$) increased the leakage time in the Osteo surrogate by 39.1% (from 28.4 to 39.5 s for SP4 and SP8, respectively) and in the MM surrogate by 49.4% (from 29.9 to 44.7 s for SP4 and SP8, respectively). The leakage time in the Lesion surrogate remained the same independent of the cement injection time (55.4 and 54.5 s for SP4 and SP8,

respectively). Relative to the Osteo surrogate (uniform structure) the structural void in the Lesion surrogate only caused a significant increase (95.3%) in the leakage time for the SP4 cement only. The leakage time obtained from the computer simulation was chosen to represent the time when any of the outlets (i.e. anterior or posterior) first became fully infiltrated by the cement (i.e. the time when the leakage likeliness first reached one). In the Osteo surrogate, the leakage time obtained numerically (25.2 s) was 11.2% lower than that measured experimentally. For the MM surrogate, the numerical leakage data could not be obtained as the leakage likeliness in the simulation never reached one. For the Lesion surrogate, the leakage time obtained numerically (30.8 s) was 44.3% lower than that measured experimentally, which is not surprising as the simulation predicted anterior leakage while the experiments showed a tendency for posterior leakage only.

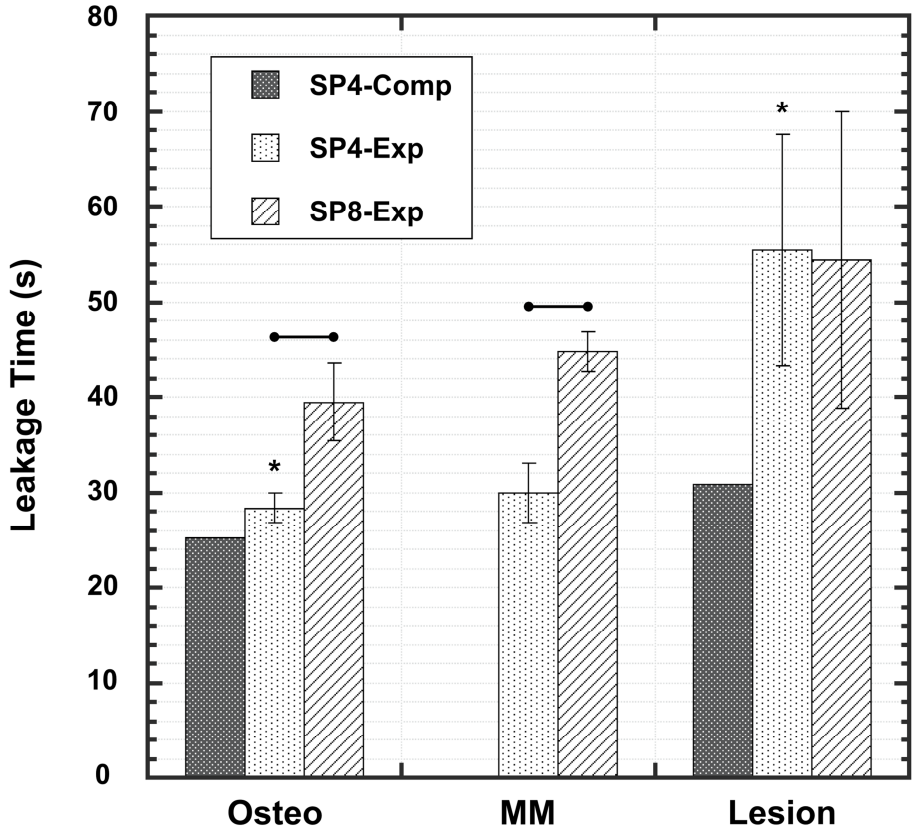

Figure 3. 29 The leakage time after Simplex P cement was separately injected at 4 and 8 min after mixing (SP4 and SP8) into each 3D bone surrogate at a constant flow rate of 3 mL/min. The leakage time obtained numerically for SP4 is included for comparison. The experimental data is presented as mean ± SD and the signifcant differences ($p < 0.05$) are labelled * and ●——●.

Injection Pressure

Figure 3.30 presents the pressure required to inject the SP4 and SP8 cements into the Osteo, MM and Lesion surrogates as a function of time. The results showed that increasing the injection time from 4 to 8 min after cement mixing significantly ($p < 0.05$) increased the peak injection pressure by 183.0% in the Osteo surrogate (from 0.143 to 0.404 MPa for SP4 and SP8, respectively), 54.2% in the MM surrogate (from 0.154 to 0.237 MPa) and 133.7% in the Lesion surrogate (from 0.101 to 0.235 MPa). Furthermore, the presence of structural voids generally decreased the peak injection pressure independent of the cement injection time. For the SP4 cement, the structural voids in the MM surrogate did not have a significant effect on the peak injection pressure which was similar to that recorded in the Osteo surrogate (7.6% difference). However, the structural void in the Lesion surrogate decreased the peak injection pressure by 29.5% relative to the Osteo surrogate. For the SP8 cement, the structural voids in the MM and Lesion surrogates decreased the peak injection pressure by 41.4% relative to the Osteo surrogate.

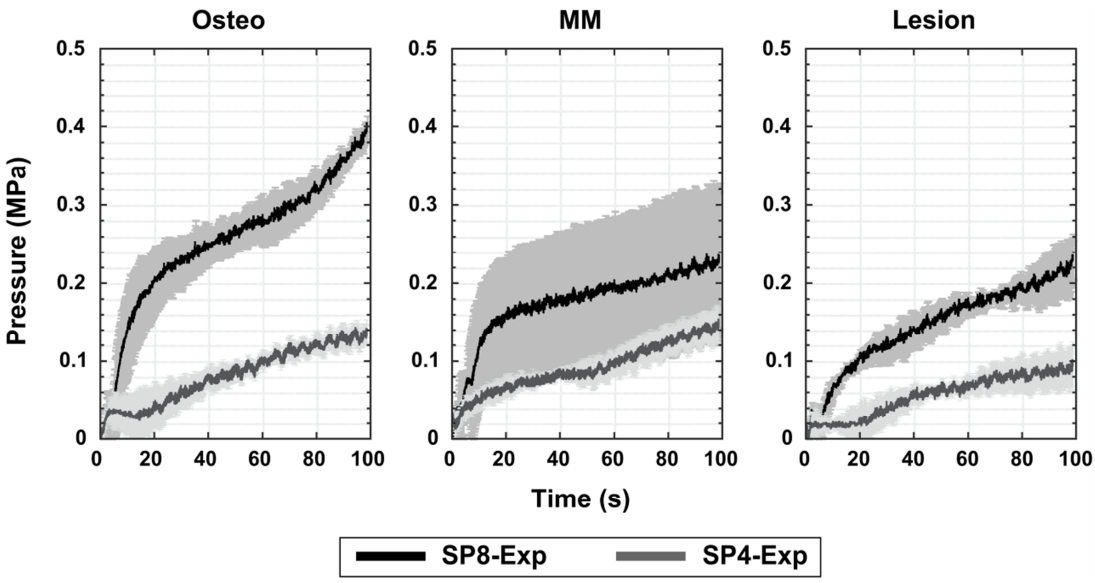

Figure 3. 30 The inlet pressure as a function of time after Simplex P cement was separately injected at 4 and 8 min after mixing (SP4 and SP8) into each 3D bone surrogate at a constant flow rate of 3 mL/min. The pressure obtained numerically for SP4 is included for comparison. The experimental data is presented as mean ± SD.

3.7 2D Flow Model Injections

3.7.1 Oil Injections

Figure 3.31 presents the resulting flow distribution when the oil reached the boundary of the 2D flow models. Table 3.3 summarizes the results of the multivariate general linear model (GLM) used to study the influence of the model structure (Osteo, Lesion and Fracture), the oil-marrow combination (Si10-M0.06, Si10-M0.4 and Si60-M0.4), and the injection flow rate (1 and 3 mL/min) on the peak pressure, the time to reach the boundary, the filled area, and the roundness.

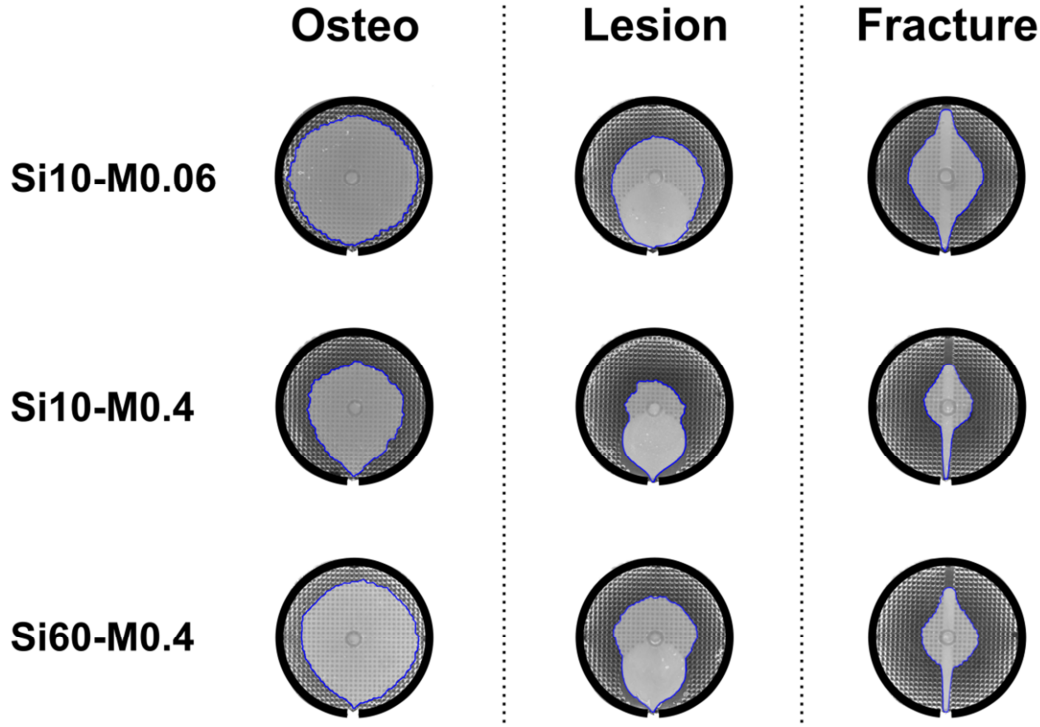

Figure 3. 31 Flow distribution when the silicone oils reached the boundary of the 2D flow models at constant flow rate of 1 mL/min. The flow contours (blue) were obtained via image subtraction.

The peak pressure significantly increased with an increase in the injection flow rate, independent of the structure and silicone oil viscosity (Figure 3.32). The oil-marrow combination significantly affected the peak pressure with Si10-M0.4 and Si60-M0.4 generally showing the lowest and highest recorded pressures, respectively. The structure significantly affected the peak pressure with the presence of fracture causing a more significant decrease compared to the presence of lesion.

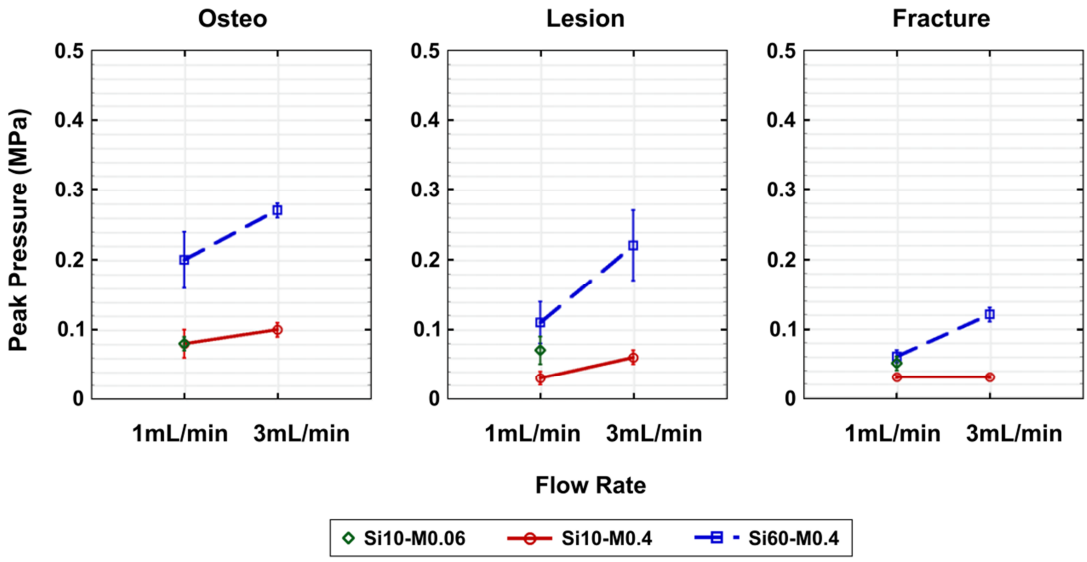

Figure 3. 32 The peak pressure required to deliver the silicone oils into the 2D flow models at two injection flow rates.

The increase in the injection flow rate significantly decreased the time it took the oil to reach the boundary, independent of the structure and oil viscosity (Figure 3.33). For the Si10-M0.4 oil-marrow combination, the oil had the fastest time to reach the boundary, while for the Si10-M0.06 and Si60-M0.4 combinations, the oils had a similar time to reach the boundary, independent of structure.

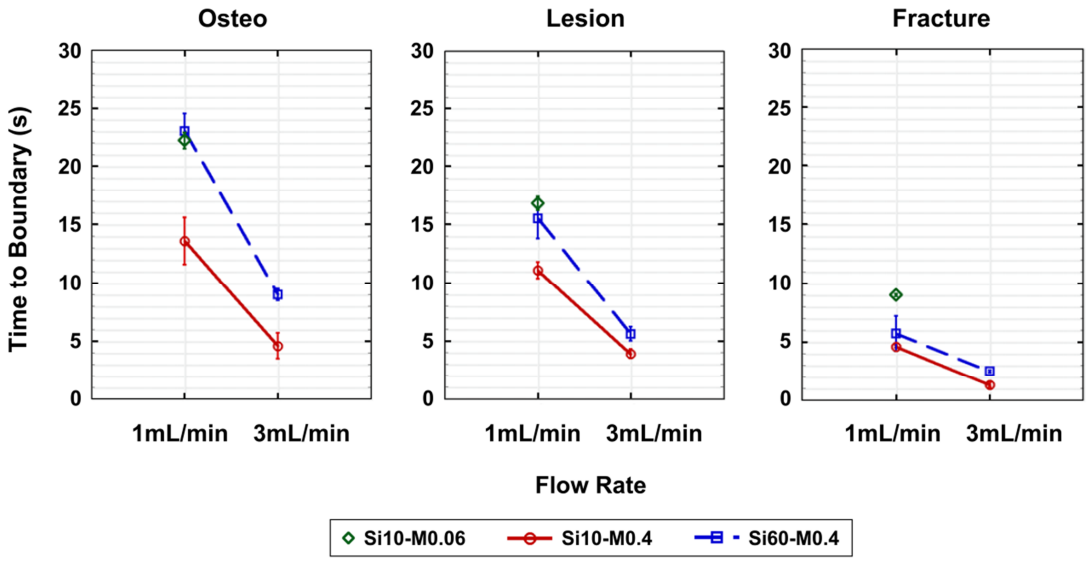

Figure 3. 33 The time it took the silicone oils to reach the boundary of the 2D flow models at two injection flow rates.

However, the structure had a significant effect on the time to reach the boundary with the presence of fracture causing a more significant decrease compared to the presence of lesion. The increase in the injection flow rate generally did not have a significant effect on the percent filled area, independent of the structure and oil viscosity (Figure 3.34). The oil-marrow combination significantly affected the percent filled area with the Si10-M0.4 and Si10-M0.06 generally showing the lowest and highest filled area, respectively. The structure also had a significant effect on the percent filled area with the presence of fracture causing a more significant decrease compared to the presence of lesion.

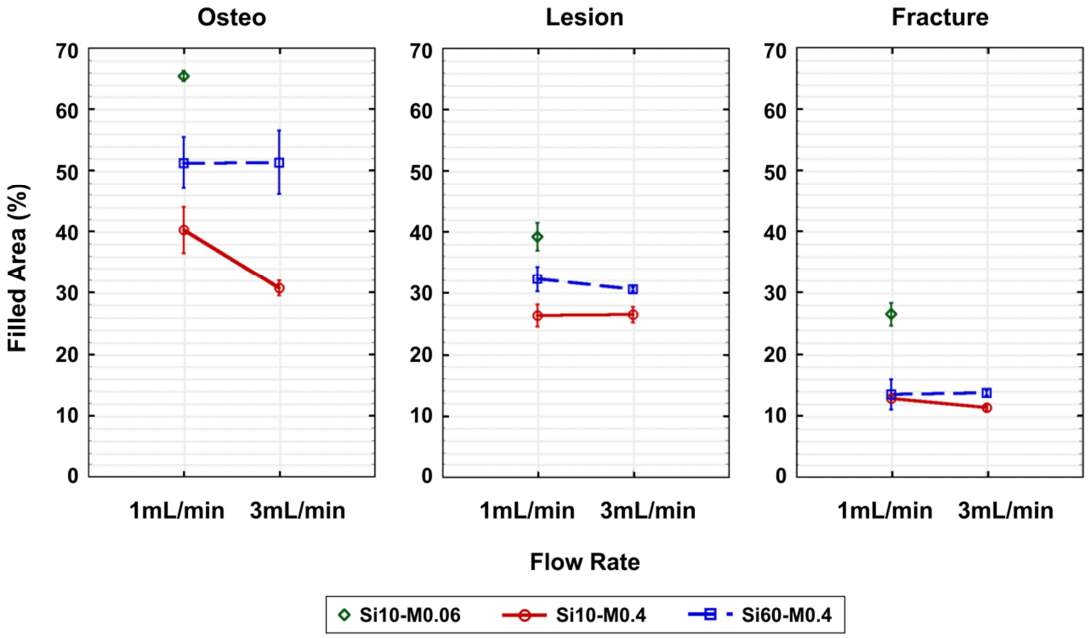

Figure 3. 34 The percent filled area when the silicone oils reach the boundary of the 2D flow models at two injection flow rates.

The injection flow rate did not have a significant effect on the roundness independent of the structure and oil viscosity (Figure 3.35). Similar to the filled area results, the oil-marrow combination significantly affected the roundness with the Si10-M0.4 and Si10-M0.06 generally showing the lowest and highest roundness values, respectively. The structure again had a significant effect on the roundess with the presence of fracture causing a more significant decrease compared to the presence of lesion.

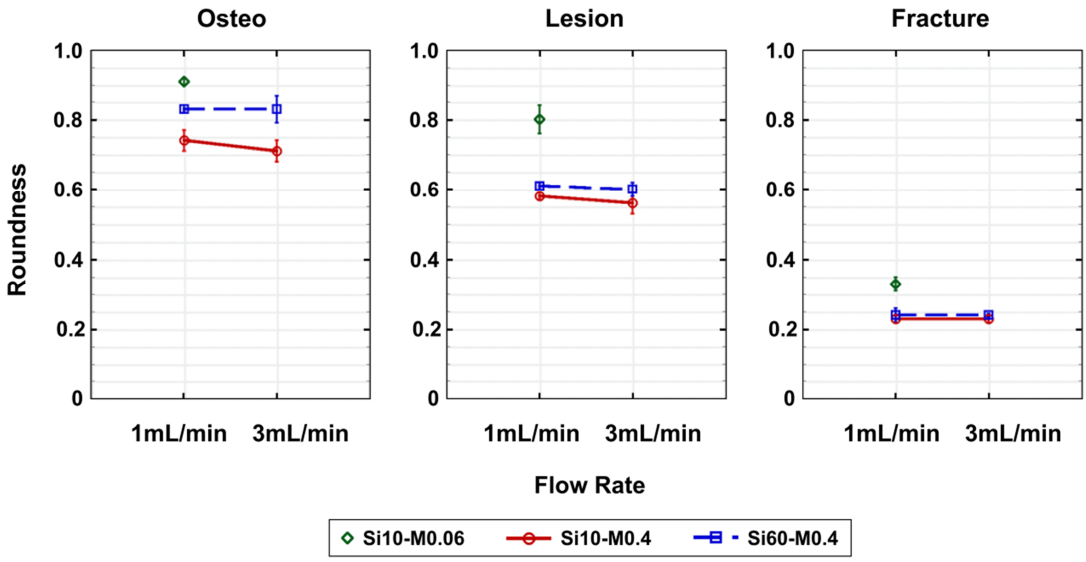

Figure 3. 35 The roundness of the flow contours when the silicone oils reach the boundary of the 2D flow models at two injection flow rates.

Table 3. 3 Parameter estimates from the GLM analysis. Only statistically significant factors and interactions are shown ($p<0.05$). The combination of the Osteo model, the Si60-M0.4 and the 3 mL/min flow rate correspond to the intercept. For any deviations from this combination, the corresponding parameter estimates are added to the intercept value.

Parameter Estimates	Filled Area (%)		Roundness		Time to boundary (s)		Peak Pressure (MPa)	
	B	Std. Error	B	Std. Error	B	Std. Error	B	Std. Error
Intercept	51.29	1.48	0.83	0.01	9.03	0.62	0.27	0.01
Fracture	-37.57	2.09	-0.58	0.02	-6.57	0.88	-0.16	0.02
Lesion	-20.84	2.09	-0.23	0.02	-3.47	0.88	-0.06	0.02
Si10-M0.06	14.19	2.09	0.08	0.02	-	-	-0.12	0.02
Si10-M0.4	-20.60	2.09	-0.12	0.02	-4.43	0.88	-0.17	0.02
FlowRate = 1.0 mL/min	-	-	-	-	14.00	0.88	-0.08	0.02
[Fracture] * [Si10-M0.06]	-	-	-	-	4.13	1.24	0.12	0.03
[Fracture] * [Si10-M0.4]	18.19	2.96	0.11	0.03	3.27	1.24	0.09	0.03
[Lesion] * [Si10-M0.06]	-7.21	2.96	0.11	0.03	-	-	0.08	0.03
[Lesion] * [Si10-M0.4]	16.53	2.96	0.08	0.03	2.80	1.24	-	-
[Fracture] * [FlowRate 1.0]	-	-	-	-	-10.73	1.24	-	-
[Lesion] * [FlowRate 1.0]	-	-	-	-	-4.07	1.24	-	-
[Si10-M0.4] * [FlowRate 1.0]	9.63	2.96	-	-	-5.03	1.24	0.06	0.03
[Fracture] * [Si10-M0.4] * [FlowRate 1.0]	-	-	-	-	5.10	1.75	-	-
[Lesion] * [Si10-M0.4] * [FlowRate 1.0]	-11.46	4.18	-	-	-	-	-	-

3.7.2 Cement Injections

Figure 3.36 presents the resulting flow distribution when the cement reached the boundary of the 2D flow models. All injections were performed under a constant flow rate of 3 mL/min.

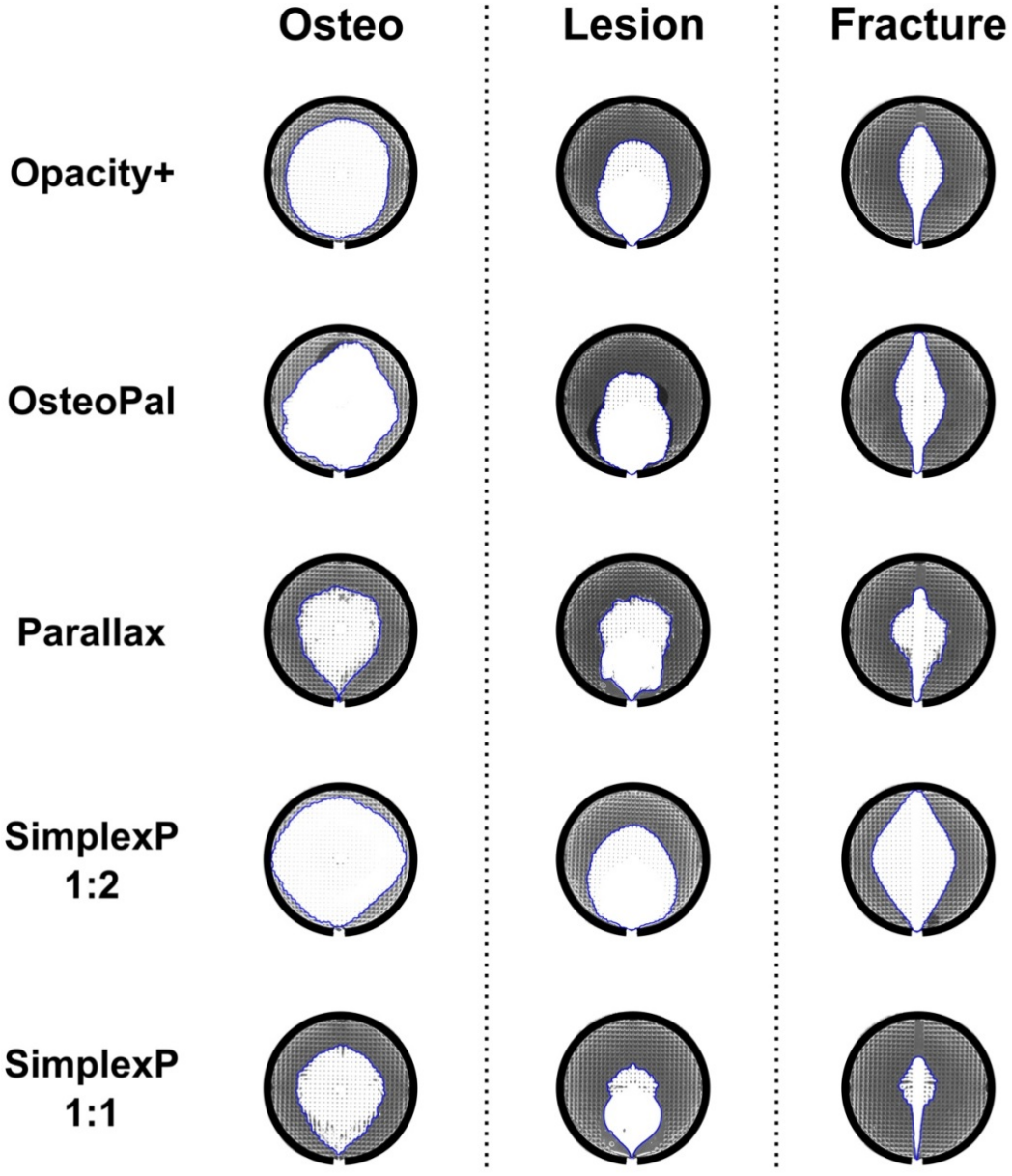

Figure 3. 36 Representative flow distribution for the various structures when the cements reached the boundary of the 2D flow models for the early injection time point of 4 min from the addition of the liquid to the powder. The flow contours (blue) were obtained via image subtraction.

Table 3.4 summarizes the results of the multivariate general linear model (GLM) used to study the influence of the structure (Osteo, Lesion and Fracture), the cement formulation (OC, OP, PL, SP1:2 and SP1:1), and the injection time point (4, 6 and 8 min) on the peak pressure, the time to reach the boundary, the filled area, and the roundness.

The peak pressure significantly increased with injection time and was generally independent of the model structure (Figure 3.37). The cement formulation significantly affected the peak pressure with SP1:1 and SP1:2 generally showing the lowest and highest recorded pressures, respectively. Furthermore, the injection pressure for OP significantly decreased in both lesion and fracture models, equally.

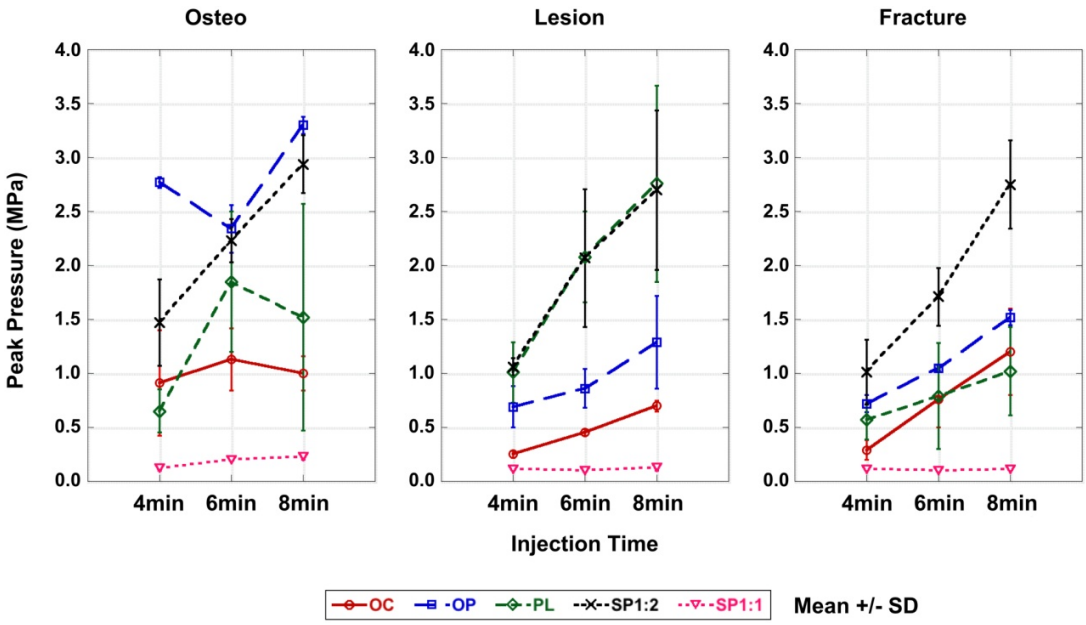

Figure 3. 37 The pressure required to deliver the cements at a constant flow rate of 3 mL/min into the 2D flow models for the various structures and injection time points after cement mixing.

The early injection time point (4 min) as well as the presence of lesion or fracture significantly decreased the time it took the cements to reach the boundary (Figure 3.38). PL and SP1:1 were the fastest cements to reach the boundary, however the behaviour of PL was improved in both lesion and fracture models. Relative to SP1:1, the time it took PL to reach the boundary significantly increased in the lesion and fracture models and became comparable to that of OC, OP and SP1:2.

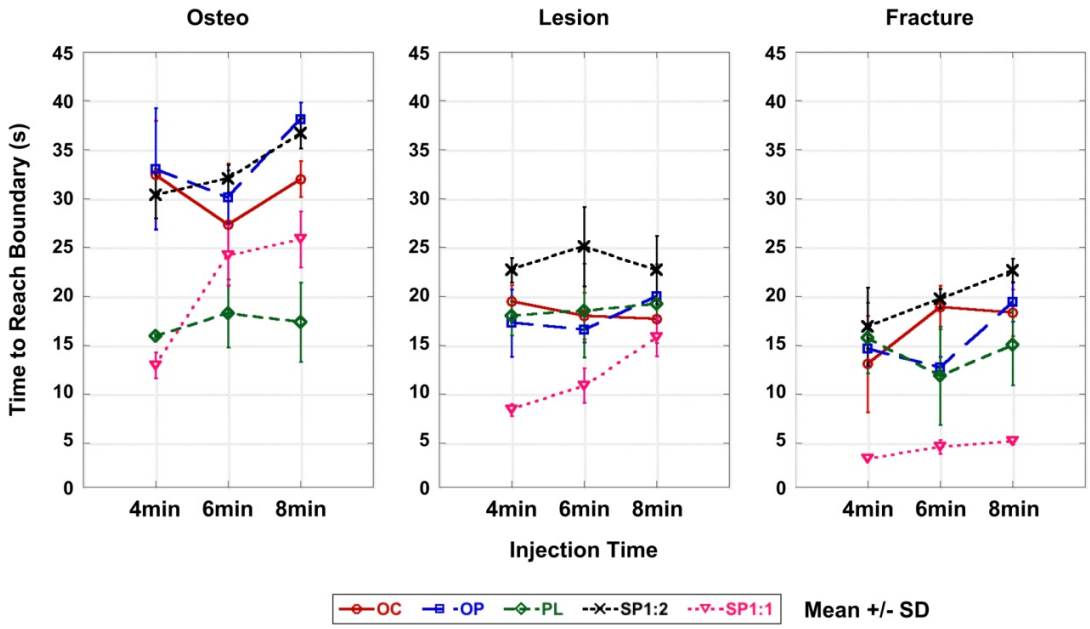

Figure 3. 38 The time it took the cements to reach the boundary of the 2D flow models for the various structures and injection time points after cement mixing.

The percent filled area was generally independent of the injection time, except for SP1:1 and OP which showed a significant decrease in filled area when injected at 4 min after cement mixing (Figure 3.39). The structure, however, significantly affected the filled area with the presence of fracture causing a more significant decrease compared to the presence of lesion. SP1:2 had the highest percent filled area for all structures, whereas PL had the lowest for the Osteo model and SP1:1 had the lowest for both lesion and fracture models. The behaviour of PL was improved in both lesion and fracture models (relative to SP1:1) as evident in the significant increase in its percent filled area, which became comparable to that of OC and OP.

The roundness significantly decreased in the presence of fracture only and was generally independent of the injection time (Figure 3.40). Similar to the filled area results, SP1:2 showed the highest roundness in all structures, whereas PL had the lowest in the Osteo model and SP1:1 had the lowest in both lesion and fracture models. Relative to SP1:1, the roundness for PL significantly increased in the lesion and fracture surrogates and became comparable to that of OC and OP.

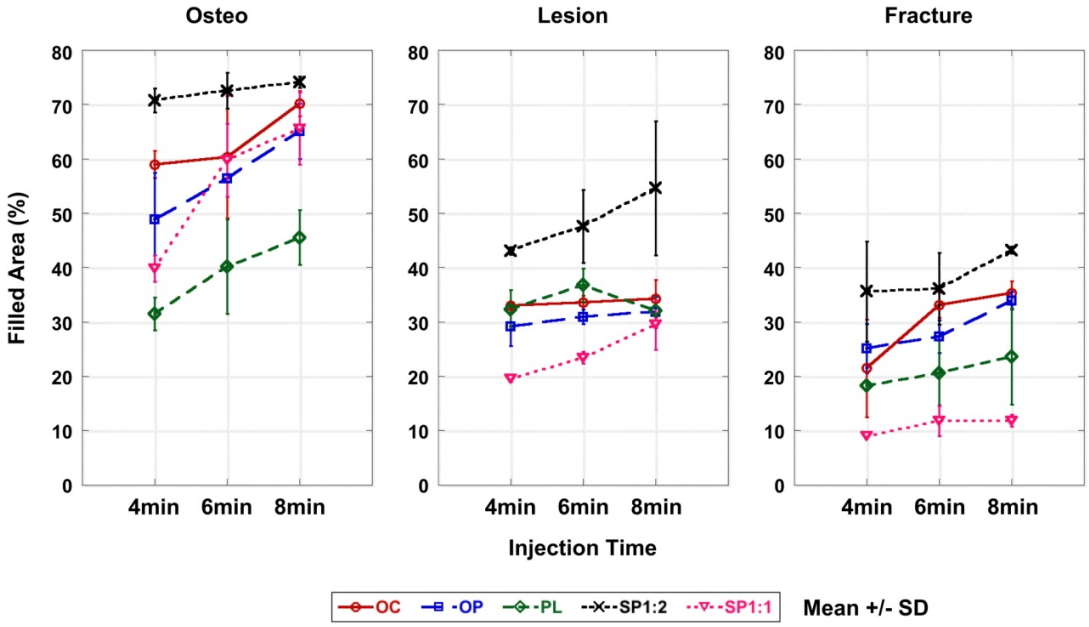

Figure 3. 39 The percent filled area when the cements reached the boundary of the 2D flow models for the various structures and injection time points after cement mixing.

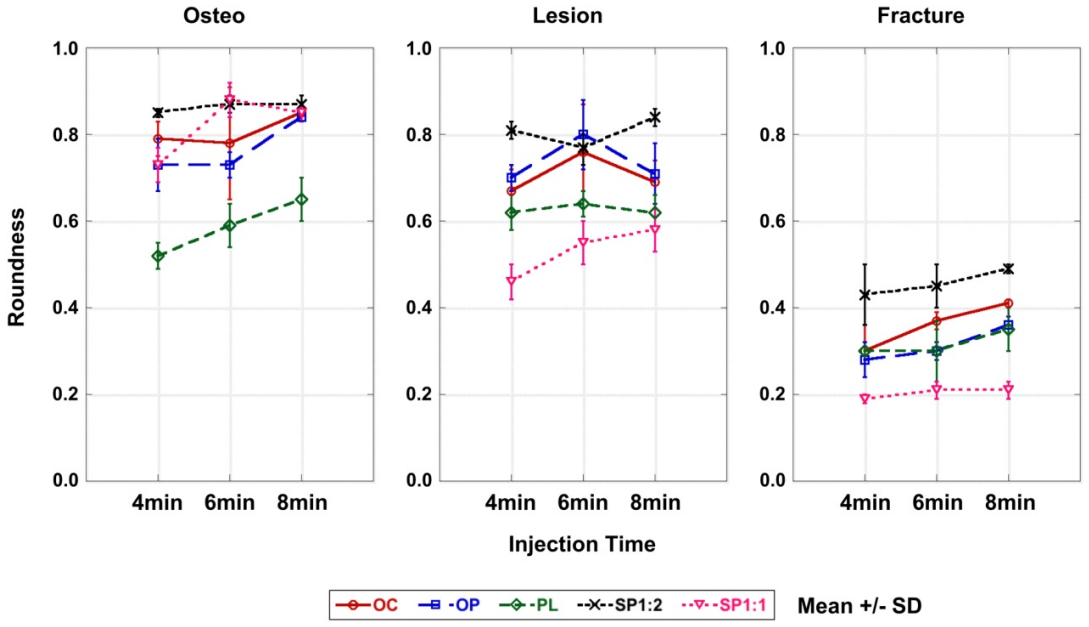

Figure 3. 40 The roundness of the flow contours when the cements reached the boundary of the flow models for the various structures and injection time points after cement mixing.

Table 3. 4 Parameter estimates from the GLM analysis. Only statistically significant factors and interactions are shown ($p<0.05$). The combination of the Osteo model, SP1:2 and injection time 8 min correspond to the intercept. For any deviations from this combination, the corresponding parameter estimates are added to the intercept value.

Parameter Estimates	Filled Area (%)		Roundness		Time to boundary (s)		Peak Pressure (MPa)	
	B	Std. Error	B	Std. Error	B	Std. Error	B	Std. Error
Intercept	74.10	3.14	0.87	0.03	36.70	1.89	2.94	0.22
Fracture	-30.90	4.44	-0.38	0.04	-14.03	2.67	-	-
Lesion	-19.50	4.44	-	-	-13.97	2.67	-	-
OC	-	-	-	-	-	-	-1.94	0.31
OP	-9.05	4.44	-	-	-	-	-	-
PL	-28.60	4.44	-0.22	0.04	-19.30	2.67	-1.42	0.31
SP1:1	-	-	-	-	-10.80	2.67	-2.71	0.31
4min	-	-	-	-	-6.27	2.67	-1.46	0.31
6min	-	-	-	-	-	-	-0.71	0.31
[Fracture] * [OP]	-	-	-	-	-	-	-1.59	0.44
[Fracture] * [PL]	-	-	-	-	11.70	3.78	-	-
[Fracture] * [SP1:1]	-22.90	6.28	0.26	0.06	-	-	-	-
[Lesion] * [OC]	-16.38	6.28	-0.13	0.06	-	-	-	-
[Lesion] * [OP]	-13.78	6.28	-	-	-	-	-1.78	0.44
[Lesion] * [PL]	-	-	-	-	15.83	3.78	1.48	0.44
[Lesion] * [SP1:1]	-16.64	6.28	-0.24	0.06	-	-	-	-
[OC] * [4min]	-	-	-	-	-	-	1.37	0.44
[OP] * [4min]	-12.83	6.28	-	-	-	-	0.93	0.44
[OP] * [6min]	-	-	-0.12	0.06	-	-	-	-
[PL] * [6min]	-	-	-	-	-	-	1.03	0.44
[SP1:1] * [4min]	-22.42	6.28	-	-	-	-	1.36	0.44
[Lesion] * [OC] * [4min]	18.05	8.88	-	-	-	-	-	-
[Lesion] * [OC] * [6min]	-	-	0.21	0.08	-	-	-	-
[Lesion] * [OP] * [4min]	21.76	8.88	-	-	-	-	-	-
[Lesion] * [OP] * [6min]	-	-	0.28	0.08	-	-	-	-
[Lesion] * [PL] * [4min]	22.42	8.88	-	-	-	-	-	-
[Lesion] * [PL] * [6min]	-	-	0.16	0.08	-	-	-	-
[Fracture] * [SP1:1] * [4min]	27.26	8.88	-	-	10.60	5.34	-	-
[Lesion] * [SP1:1] * [4min]	24.04	8.88	-	-	-	-	-	-

CHAPTER 4 Discussion

This chapter discusses the findings and significance of this project which focuses on the *in vitro* assessment of cement injection behaviour in cancellous bone. A novel methodology was developed to help study the influence of cement properties on injection behaviour and discern subtle differences in the flow behaviour of bone cement formulations. There has been substantial progress in fulfilling the aim of this project using a methodical approach defined by the study objectives (Table 4.1).

Table 4. 1 Summary of the study objectives and key findings.

Objective	Status	Key Findings
Develop and manufacture 3D bone surrogates.	Completed	3D bone surrogates were designed in a CAD software then manufactured using Projet 3D printer [a].
Develop and manufacture 2D bone surrogates.	Completed	2D bone surrogates were designed in a graphic suite then manufactured using flexography [b].
Perform morphology characterization.	Completed	- Structural variation in thickness and spacing was low (< 0.05 mm). - Morphology was similar to bone: • Porosity of 82.6 ± 1.1 % (3D) and 87.9 ± 2.0 % (2D). • Permeability of 43.1 ± 6.0 × 10^{-10} m^2.
Perform surface characterization.	Completed	Material wettability was comparable to bone with contact angles ranging from: - 49 to 77° (3D material). - 60 to 74° (2D material). - 60 to 75° (human cortical bone).
Develop methods to allow fluid injection under a controlled environment.	Completed	System was robust and repeatable: - Flow rate was kept constant at 3 mL/min. - Needle placement was consistent. - 1% error in measured vs. nominal volume.
Comparatively assess the flow behaviour of various formulations.	Completed	Subtle differences in the biomaterial flow properties can be discerned.

[a] Projet HD 3000, 3D Systems, South Carolina, USA.
[b] AFP-SH/DSH, Asahi Photoproducts Europe, Brussels, Belgium

The overall aim was to manufacture cost-effective, reproducible and pathologically specific bone surrogates with morphology and surface properties similar to bone. Biomaterial flow properties could then be ascertained following injections into the surrogates under a controlled environment. Bespoke methodology was developed to control the injection flow rate, measure the injection pressure, and allow visualization and quantitative analysis of the spreading distribution. This will help study cement-fluid interaction to better understand how rheological properties affect the cement flow within vertebral cancellous bone and ultimately provide a better prediction of the cement placement within the vertebral body, which has been identified as a critical parameter in the biomechanical behaviour post-augmentation.

4.1 Bone Surrogates

Researchers have tended to avoid the use of cadaveric tissues due to their inherent uniqueness and variability, which render the experiments irreproducible and make the scientific understanding of how the cement flows within cancellous bone difficult [166, 178]. Bone surrogates allow researchers to focus on the importance of geometry when the variability in the biological tissue is eliminated. Therefore, the relative importance of different geometrical or structural variations within the bone can be highlighted and evaluated through varying the structural geometry within the surrogates [200]. This allows for the pathological representation to remain fixed between investigations and the effects of subtle differences in the cement formulations to be assessed in a reproducible manner. Furthermore, bone surrogates have advantages in terms of health and safety, cost and limited ethical issues associated with their usage.

4.1.1 Surrogate Manufacturing

The 2D bone surrogates were manufactured using flexography, a technology used extensively within the print industry where a high degree of reproducibility is required. However, a suitable rapid prototyping (RP) technique had to be selected to allow manufacturing of the 3D bone surrogates and to ensure reliability of their

reproduction. There are several factors that influence the build resolution and the surface finish of an RP technique:

- The first factor is data preparation which includes errors caused by the STL file generation and the selection of the part build orientation. The STL file format represents the surface geometry of a three-dimensional CAD model using triangles to describe a polyhedral approximation of the boundary. Complex geometries introduce undesirable anomalies in the boundary surface, such as gaps or holes. These errors mostly occur in cylindrical geometries or curved surfaces. Since only two triangles are required to fully describe the boundary of a square, the unit cell of the proposed 3D bone surrogates was based on square beams. This reduces the overall number of triangles used to describe the surface geometry of the 3D models (i.e. file size) and minimizes such errors due to STL file generation. Also, the selection of the part build orientation is critical for minimizing the build time and the costs as well as achieving optimal build resolution.

- The second factor includes errors caused by process specific parameters during part building. When a thermal RP process is employed, such as in the SLS and the 3D printer techniques, the main source of error is material shrinkage which does not always occur uniformly as areas at high temperatures tend to shrink more than those at lower temperatures, and geometrical features such as thick walls tend to increase the shrinkage. However, to compensate for material shrinkage, a coefficient is calculated on test geometry and a scaling factor is applied to the STL file in all directions. Conversely, when a liquid based RP process such as the EnvisionTEC Perfactory is employed, the main source of error is warping caused by the phase change during the curing of the liquid resin. This is a major problem for all liquid based RP systems and means have been sought to optimize the curing process and reduce its effects.

- The third factor is part finishing or post-processing. This is the final step in any RP technique and mainly consists of cleaning and removing all excess material including the support material; however, this may also include applying a surface

treatment such as sanding, coating and/or spraying. Thus, the varying amount of material that has to be removed and the finishing technique applied are key determinants of the final surface finish and the extent loss of geometrical features degrading the build resolution [190-192].

The analysis of the benchmark results revealed that the Projet 3D Printer (Projet HD 3000, 3D Systems, South Carolina, USA) was the most suitable for manufacturing the proposed three-dimensional bone surrogates. The main challenge with the selected RP technique was removal of the support material without damaging the structure. However, this was resolved using an ultrasonic cleaner with an oil-soluble fluid (citrus greaser).

4.1.2 Surrogate Morphology

It is extremely important to control the surrogate morphology as bone cement precursors are heterogeneous, especially their powder component which varies in composition, size and molecular weight of the pre-polymerized polymer beads as well as the morphology of the radiopacifier particles. All these factors have a significant effect on the interaction between the liquid and the powder components during mixing and injection, resulting in different flow behaviour for different cement formulations. Previous bone surrogates used in experimental studies on cement flow [136, 166, 178, 180] have been made of open-porous aluminum foam with their porosity controlled to represent osteoporotic bone. However, the geometrical structure within a group of respective surrogates was irregular and uncontrolled. Thus, the surrogates were inherently unique. Achieving constant geometrical structure is crucial to reduce the variability, render the experiments reproducible and shift the focus onto understanding the influence of cement properties on the injection behaviour. This also allows for the injections to be performed at various time intervals after cement mixing into separate bone surrogates while assuming that the injections are being performed into the same structure.

The developed 2D and 3D bone surrogates within this study can be assumed constant in geometrical structure as the variability in their morphology was very low. The morphology analysis showed that the 3D osteoporosis (Osteo) bone surrogates had an overall strut thickness and pore spacing of 0.25 ± 0.04 and 0.89 ± 0.03 mm, respectively. The variability in the structure of the 2D Osteo flow models measured on their lateral profiles revealed that the overall edge-to-edge and valley-to-valley distances were 934 ± 3.2 and 1251 ± 0.5 µm, respectively (refer to Figure 2.14). The main disadvantage of the developed 2D and 3D bone surrogates is that they have a uniform structure and do not simulate the highly complex geometrical structures and architectural inhomogeneities of vertebral cancellous bone. The uniform structure in the 2D surrogates was chosen to reflect that of the 3D surrogates. However, the uniform structure in the 3D surrogates was chosen to simplify the representation of the bone morphology, facilitate the manufacturing process and ensure the reliable reproduction of the surrogates. When complex structures are involved, more support material is required during the manufacturing process. Thus, it is more difficult to remove the support material without damaging the actual structure, especially when regions within the structure (i.e. vertebral cancellous bone) are thin and not well connected.

Although the structure of the proposed bone surrogates was uniform, their porosity was comparable to that of vertebral cancellous bone. The porosity of the 2D Osteo models was 87.9 ± 2.0 % and that of the 3D Osteo surrogates obtained from the microCT data (100 - BV/TV) was 82.6 ± 1.1 %. Figure 4.1 compares the bone volume fraction (BV/TV) of the 3D Osteo surrogates to that reported in the literature [25, 31-34] for human osteoporotic vertebral cancellous bone. It is evident that the BV/TV of the 3D osteo surrogates was higher relative to that reported in all the studies included in the comparison. However, BV/TV is the percent material volume within the total volume of interest and is biased by the trabecular thickness and spacing. Thus, it is not surprising that BV/TV of the 3D Osteo surrogates was higher especially when the strut thickness of the surrogates was higher while the intercolumnar spacing of the surrogates was very similar.

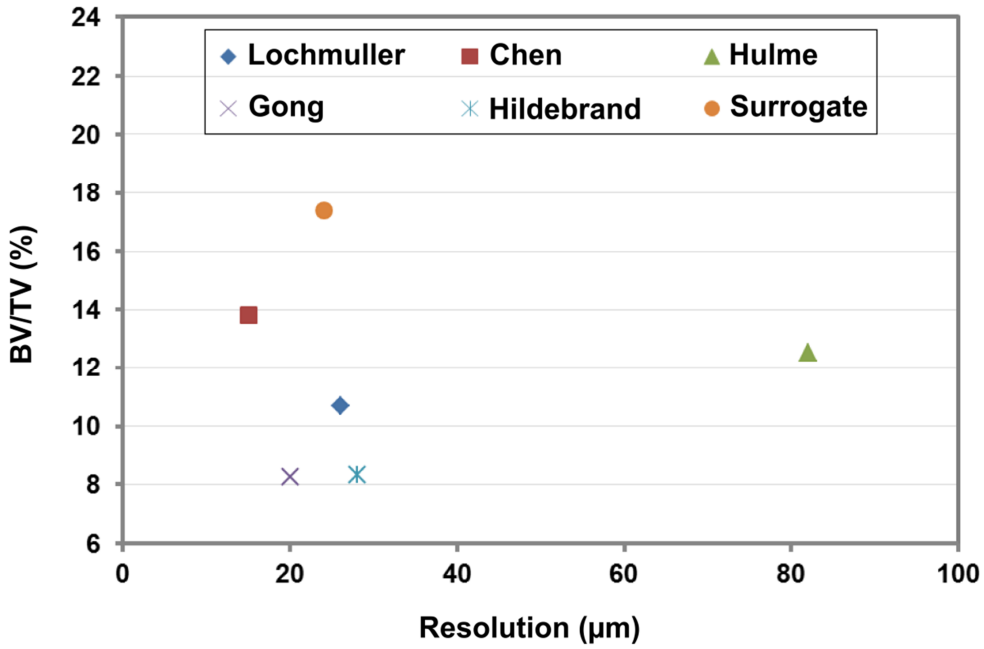

Figure 4. 1 Scatter plot showing the bone volume fraction of the 3D Osteo surrogate compared to that reported by Lochmuller et al. [31], Chen et al. [32], Hulme et al. [33], Gong et al. [34] and Hildebrand et al. [25] plotted against the microCT scan resolution used in each study.

Figure 4.2 compares the thickness (Tb.Th) and spacing (Tb.Sp) of the developed 3D Osteo bone surrogates to those reported for human osteoporotic vertebral cancellous bone. It is evident that the overall beam thickness (Tb.Th) of the 3D surrogates was comparable to that reported by Hulme et al. [33] but higher than that reported by Lochmuller et al. [31], Chen et al. [32], Gong et al. [34] and Hildebrand et al. [25]. Increasing the beam thickness of the 3D surrogates was necessary due to manufacturing limitations. However, the overall pore size (Tb.Sp) of the 3D surrogates was very similar to that reported in the aforementioned studies. Matching the pore size was important for assessing the cement flow behaviour. Small pores (0.8 mm) in the cancellous bone reduce the void volume available for cement flow, thus the cement's interstitial velocity increases to preserve the continuity with the entering superficial flow. This leads to an increase in the shear rate, which causes a decrease in the viscosity, as the cements are known to exhibit shear-thinning behaviour.

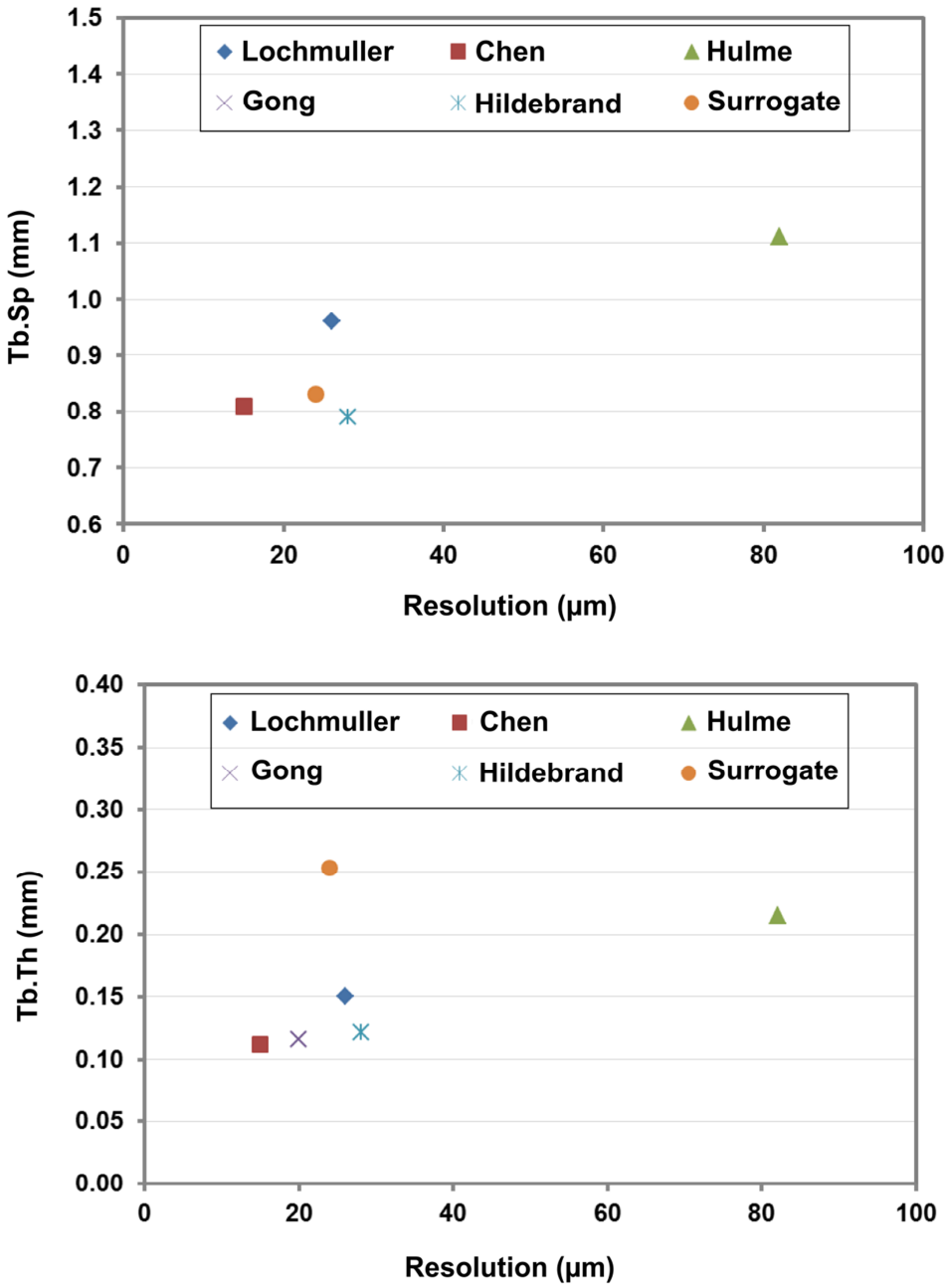

Figure 4. 2 Scatter plot showing the thickness (Tb.Th, bottom) and the spacing (Tb.Sp, top) of the 3D Osteo surrogate compared to those reported by Lochmuller et al. [31], Chen et al. [32], Hulme et al. [33], Gong et al. [34] and Hildebrand et al. [25] plotted against the microCT scan resolution used in each study. Gong et al. did not report any spacing data in their study thus Tb.Sp could not be included in the comparison.

It is important to note that the spatial resolution (82 µm) of the microCT scan used in the study by Hulme et al. [33] was significantly lower than the spatial resolution (24 µm) used in this thesis and the remainder four studies included in the comparison.

High spatial resolution is required for reliable measures of the morphometric indices. Kothari et al. [28] showed that morphometric indices, particularly the trabecular thickness (Tb.Th), have a strong dependency on spatial resolution and require a very high resolution to obtain reliable measures. Thus, it is important that the spatial resolution is high when measuring morphometric indices and similar when comparing these indices between different studies. Consequently, data from Hulme et al. [33] should be excluded from the comparison. Relative to the trabecular thickness (Tb.Th) reported by Lochmuller et al. [31], Chen et al. [32], Gong et al. [34] and Hildebrand et al. [25], Tb.Th reported by Hulme et al. [33] was higher mainly due to the low resolution of their microCT scan [28]. However, the BV/TV reported by Hulme et al. [33] was comparable to that reported in the aforementioned studies. This is not surprising especially when the trabecular separation (Tb.Sb) reported by Hulme et al. [33] was higher. Since Tb.Sp is not significantly affected by the scan resolution [28], the data suggests that the vertebral specimens measured by Hulme et al. [33] are highly osteoporotic, which is not properly reflected by their reported Tb.Th mainly due to the low resolution of their microCT scan.

A key advantage is that developed bone surrogates are reproducible and representative of a range of skeletal pathologies including osteoporotic bone (Osteo), metastatic infiltration (Lesion) and multiple myeloma (MM). To achieve the Lesion and MM surrogates, voids were incorporated into the Osteo structure (refer to Figure 2.1). This allowed studying how the presence of structural voids affects the flow behaviour of the cement formulations mainly from a geometrical perspective. The structural void (Ø = 19.0 mm) in the 2D and 3D Lesion surrogates occupied 11% of the total volume of the surrogate. The size of the void was based on data reported by Ahn et al. [183] and the location was chosen, breaching the posterior wall, to simulate a worst case scenario. The size and location of the voids in the 3D MM surrogates were based on in-house microCT scans of six human vertebrae from three donors whose cause of death was multiple myeloma. Three spherical voids, 6.0 mm in diameter each, were incorporated into the 3D MM structure and occupied 9% of the total volume of the surrogate.

Previous experimental studies on cement flow [136, 166, 178, 180] have used open-porous aluminum foam to represent osteoporotic bone. Although the porosity of the foam was well controlled, its geometric structure was inherently random. The proposed bone surrogates overcome the limitations of previous materials as their geometric structure is well controlled and can be tailored to mimic the morphology of specific bone conditions at different skeletal sites in the body. Another advantage is that the developed 2D and 3D bone surrogates have a boundary to simulate the vertebral shell which confines the flow and controls the intravertebral pressure, significantly affecting the filling pattern [185]. The boundary including the inlet and the flow exit points were kept constant for all the surrogates (refer to Figure 2.5 and Figure 2.13). The openings in the boundary simulate breaches through the cortex due to a fracture, a lesion and/or a blood vessel exchanging blood in and out of the vertebral body. This is important as such breaches create paths of least resistance providing means for leakage into the surrounding structures.

The surrogates also simulate the rheological environment within the vertebral body. The measured permeability of the 3D Osteo surrogate ($43.1 \pm 6.0 \times 10^{-10}$ m^2) was comparable to that reported by Nauman et al. [201] for human vertebral cancellous bone, which was $80.5 \pm 47.5 \times 10^{-10}$ and $35.9 \pm 19.0 \times 10^{-10}$ m^2 in the longitudinal and transverse directions, respectively. Furthermore, based on contact angle measurements, the surface wettability of the 2D and 3D surrogates matches that of bone. The range of contact angle measurements was 49 to77º for the Projet material used to manufacture the 3D bone surrogates, 60 to 74º for the photopolymer used to manufacture the 2D flow models and 60 to75º for cortical bone form a human femur. Also, the presence of the marrow substitute simulates the two-phase flow that occurs within the vertebral body. An aqueous solution of carboxymethyl cellulose (M_w ~250,000 - Sodium carboxymethyl cellulose, Sigma-Aldrich, MO, USA) 2.5% w/w was used as the bone marrow substitute with a nominal viscosity of 0.4 Pa·s which has been reported for red bovine marrow [156]. In previous studies, Bohner et al. [136] and Loeffel et al. [180] both used melted cow butter, whereas Baroud et al. [166] and Mohamed et al. [178] both used a water/gelatin solution. A true representation of the rheological properties of human red bone marrow present within the cancellous bone

channels is extremely important as such properties significantly affect the cement flow behaviour [136].

4.2 3D Flow Model Injections

Injections performed using the 3D bone surrogates aimed to test the influence of viscosity and structure on the flow behaviour. A novel methodological approach is presented to test how osteoporotic bone quality and the presence of lytic lesions due to metastatic infiltration and multiple myeloma affect the injection biomechanics from a geometrical perspective. Only two studies on cement flow in cancellous bone have examined the influence of structure on the spreading behaviour and the risk of leakage [136, 180]. These two studies have only focused on the effect of bone porosity and have not considered the effect of lytic lesions due to spinal metastasis and multiple myeloma. Furthermore, the results of these two studies are conflicting. Bohner et al. [136] presented a theoretical model (Equation 33) to assess the effect of several parameters on the risk of leakage and showed that increasing the matrix porosity (i.e. pore diameter) decreases the tendency of leakage. On the other hand, the experimental results reported by Loeffel et al. [180] showed that increasing the pore diamter of foam surrogates causes irregular flow patterns and therefore exhibits a higher risk of cement leakage. They recommend that the cement starting viscosity should be proportional to the degree of osteoporosis (i.e. higher pore diameter requires higher cement starting viscosity). In the current study, the 3D bone surrogates that mimic metastatic infiltration (Lesion) and multiple myeloma (MM) were achieved by introducing spherical voids into the surrogate representing osteoporotic bone quality (Osteo), which had a uniform structure. Thus, the Osteo surrogate can be used as a control to highlight and evaluate how the viscosity affects the injection biomechanics in the presence of structural voids.

4.2.1 Injection Parameters

Injection parameters such as the needle position, the needle gauge, the flow rate and the injected volume were kept constant for all the injections to shift the focus onto the influence of the structure and the time-dependent viscosity arising from cement composition. All the injections were performed at room temperature (21.5 ± 0.1ºC) using a unilateral approach. The needles were consistently placed through the left insertion channel while the entry point on the outside of the right insertion channel (i.e. outer surface of the posterior boundary) was closed off to prevent any fluid from escaping through the cortex (refer to Figure 2.18). The needle insertion channel incorporated into the 3D surrogates allowed consistent needle placement during injection. Based on the results, the mean needle depth (d) from the posterior wall in the posteroanterior direction was 23.0 ± 1.4 mm and the mean needle inclination (α) with respect to the posterior wall was 69.7 ± 2.3º (Figure 4.3).

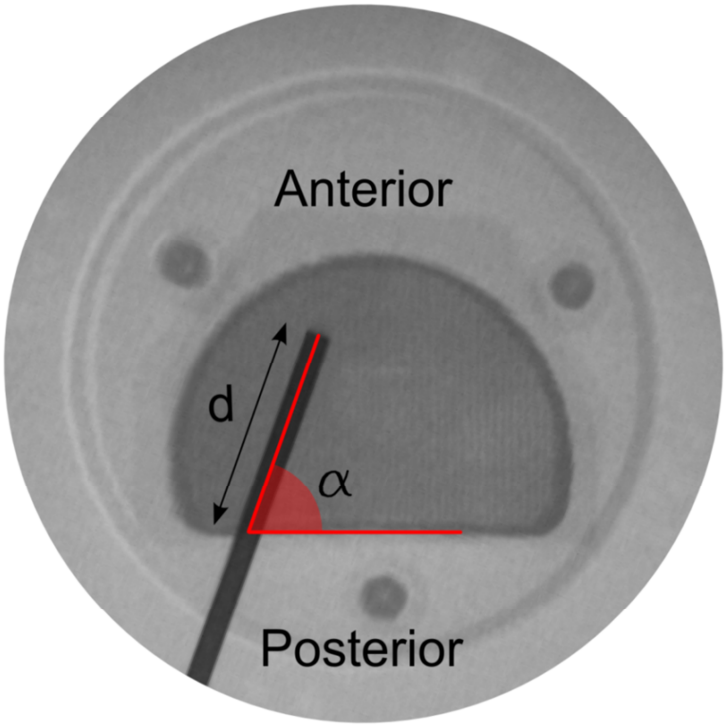

Figure 4. 3 Measurements performed to quantify the error in the needle placement within the 3D surrogates.

This shows that the error associated with the needle placement within the 3D bone surrogates was negligible. Achieving a constant needle placement is essential to minimize error and ensure that the flow inlet (i.e. needle tip) is in the same location for all the injections. The needle depth in the posteroanterior direction was chosen to allow cement deposition in the anterior third of the surrogates. This is the weight-bearing portion and generally the target site for cement deposition within the vertebral body during vertebral augmentation procedures [99]. Furthermore, the inclination of the needle insertion channel was chosen to mimic that of human thoracolumbar pedicles [21, 188]. The 12-gauge needles were chosen to represent the mean needle gauge used in the thoracolumbar spine. Typically, 13-gauge needles are used in the upper thoracic spine, whereas 11-gauge needles are used in the lower thoracic and lumbar spine [99].

In all the experiments performed using the 3D surrogates, the injection flow rate was kept constant at 3 mL/min and maintained for the duration of the injection. Figure 4.4 presents the measured displacement of the syringe plunger plotted against time.

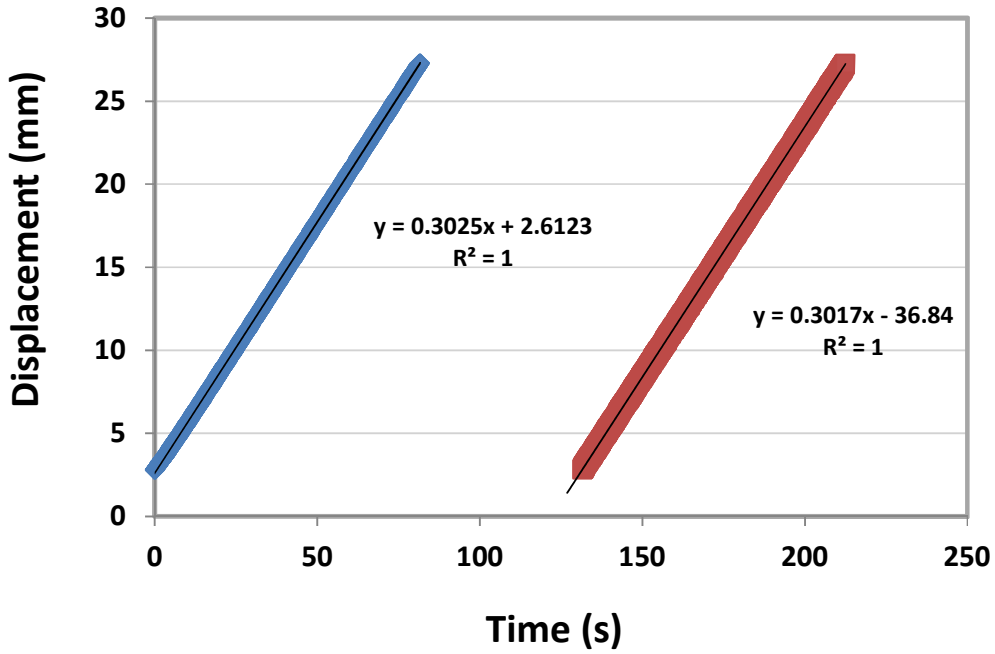

Figure 4. 4 Typical displacement of the syringe plunger plotted against time for Simplex P cement injected at 4 min (blue) and that in injected at 8 min (red).

An LVDT was used to determine the displacement of the syringe plunger and obtain a second, independent measure of flow rate. The mean slope for the measured displacement of the syringe plunger plotted against time was 0.302 ± 0.001 mm/s. Multiplying this slope by the cross-sectional area of the syringe (165.13 mm^2) confirms that the flow rate was constant at 2.99 ± 0.01 mL/min. The chosen flow rate was similar to that reported in previous cadaveric studies [202, 203] and falls within the range reported during clinical percutaneous vertebroplasty (PVP) which is 1.2 to 12.0 mL/min [204]. However, in clinical PVP intermittent injections are typically performed with pauses due to changing of syringes and/or changing of the needle position, which is often slightly retracted backwards due to excessive pressurization [204]. The continuous injection was necessary to simplify the injection parameters. However, due to the versatility of the proposed methodology, injecting the cement in multiple steps can be easily achieved and the effect will be addressed in future experiments. The injected volume of 5 mL was chosen to represent the volume of cement frequently injected into throracolumbar vertebrae during clinical PVP [123, 205-208]. Multiplying the total displacement of the syringe plunger by the cross-sectional area of the syringe confirmed that the injected volume was 4.95 ± 0.01 mL. This validates that the compliance of the system is negligible since there is only 1% error between the measured and the nominal injected volume.

4.2.2 Fluid Injections

The injections aimed to test the influence of viscosity and structure on the mean spreading distance, the sphericity, the leakage time and the injection pressure. Silicone oil with constant Newtonian viscosity of 10 and 60 Pa·s (independence to shear rate, refer to Figures 3.16 and 3.17) as well as Simplex P (SP1:1, Table 2.7) bone cement injected at 4 and 8 min after mixing (i.e. from the addition of the liquid to the powder) were injected into each 3D bone surrogate (Osteo, MM and Lesion) to assess the effect of viscosity and structure on the injection behaviour.

In the Osteo surrogate, the silicone oils and the Simplex P injected at 4 min (SP4) had a tendency to flow along the path of the right needle insertion channel, which was

kept open on the inside but closed off on the outer surface of the posterior wall. This channel creates a low resistance path (high permeability) simulating a blood vessel and/or a fracture plane within the vertebral body. The results suggest that when the viscosity is below 50 Pa·s, such as the case for both silicone oils (refer to Figures 3.16 and 3.17) and SP4 (based on data presented by Widmer et al. [198]), the injected fluid has a high tendency to follow low-resistance paths present within the structure. The results also suggest that there is a critical viscosity at which the injected fluid is less affected by such low-resistance paths as Simplex P injected at 8 min (SP8), which has a viscosity of approximately 70 Pa·s (based on data presented by Widmer et al. [198]), did not have a tendency to flow along the path of the right needle insertion channel. This agrees with the study by Loeffel et al. [180] who reported that increasing the cement starting viscosity from 50 to 100 Pa·s significantly increases the compactness of the cement, thus producing a more favorable flow pattern. In the MM and Lesion surrogates however, the flow was preferentially along the voids and did not follow the path of the right needle insertion channel, independent of viscosity and the injected fluid. This shows that the presence of structural voids, such as those incorporated into the current surrogates, has a dominating effect that dictates the tendency of the flow behaviour.

This study highlights the effect of structure on the flow behaviour. Independent of viscosity and the injected fluid, qualitative analysis showed that in the Osteo and MM surrogates there was a tendency for anterior leakage only, while in the Lesion surrogate there was a tendency for posterior leakage only. The injected fluid in the Osteo and MM surrogates never reached the posterior wall. This was expected in the Osteo surrogate especially when the structure was uniform and the target site for cement deposition was at the anterior third (refer to Figure 4.3). Moreover, the leakage patterns observed in this study were similar to those reported in cadaveric studies on cement leakage. Figure 4.5 compares the anterior leakage typically observed in a 3D Osteo surrogate to that reported by Lador et al. [209] who studied the points and pattern of cement extravasation in 23 human vertebrae with simulated compression fractures.

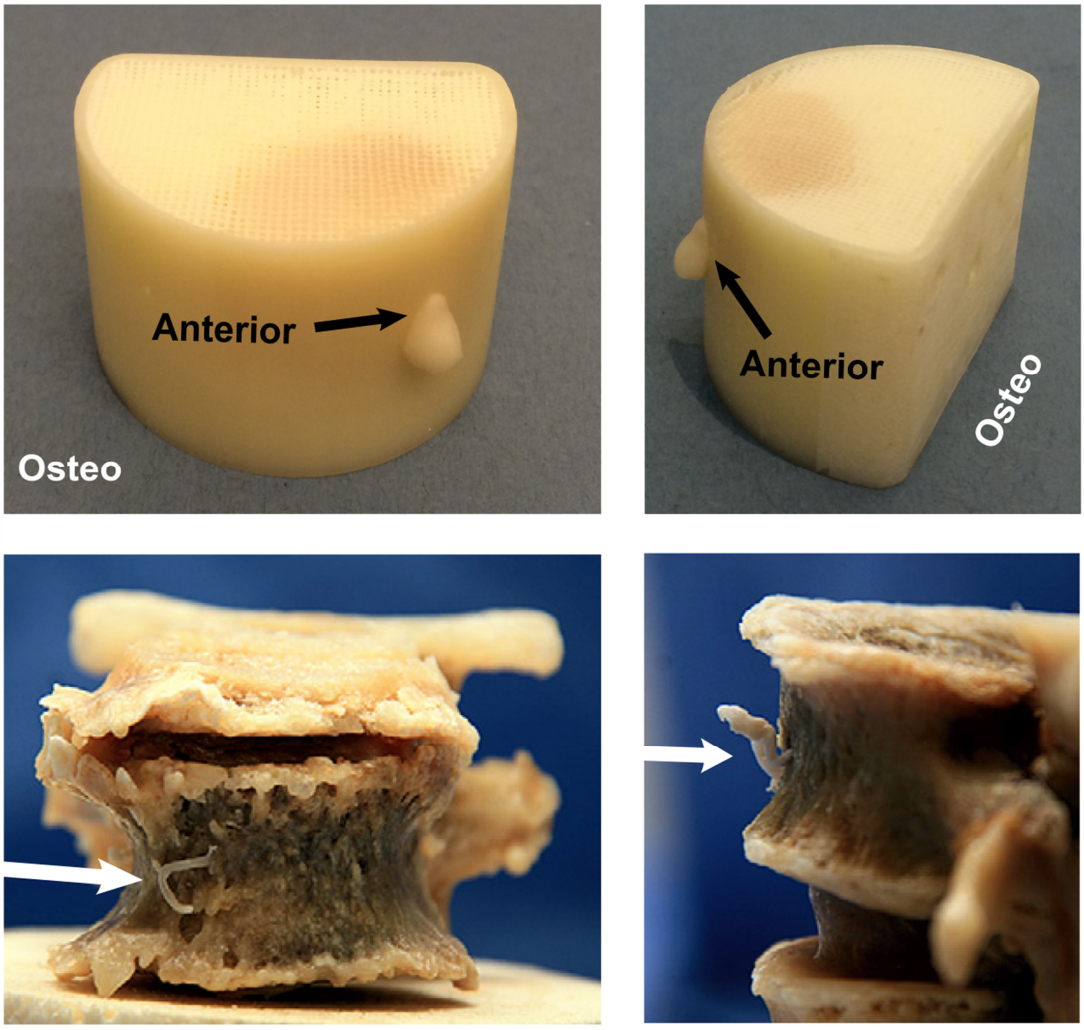

Figure 4. 5 Anterior leakage observed in the 3D Osteo surrogates (black arrows) compared to that reported by Lador et al. [209] (white arrows).

Lador et al. [209] showed that the most common type of leakage classified as severe was through small breaches in the cortex due to anterior blood vessels. This type of leakage occurred in 83% of the samples (19 out of 23), thus highlighting the importance of monitoring all vertebral walls for cement extravasation through breaches in the cortex to avoid complications and minimize possible life-threatening risks to the patients. This is important as leakage into the surrounding vasculature can reach remote areas of the body, such as the lungs, and cause pulmonary embolisms [210-212]. Figure 4.6 compares the posterior leakage typically observed in a 3D Lesion surrogate to that reported by Reidy et al. [203] who studied the cement filling pattern in seven osteoporotic human vertebrae with simulated lytic lesion occupying

approximately 15% of the vertebral body volume. Their results showed that the cement leakage through the posterior venous foramen of the vertebra into the spinal canal occurred in 86% of the samples (6 out of 7). This highlights the importance of monitoring cement extravasation through the posterior wall in patients with metastatic involvement to avoid complications such as nerve root or spinal cord compression [213].

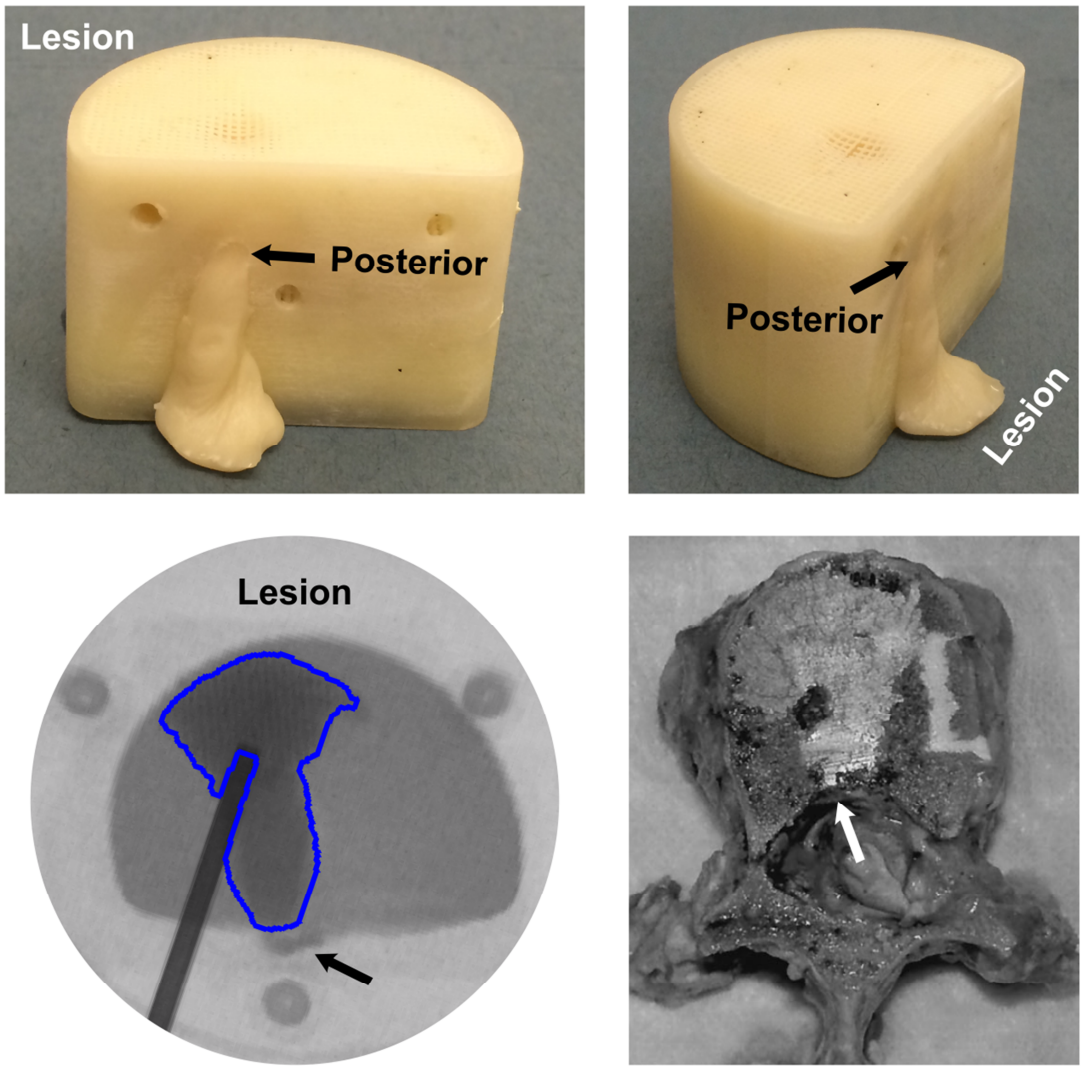

Figure 4. 6 Posterior leakage observed in the 3D Lesion surrogates (black arrows) compared to that reported by Reidy et al. [203] (white arrows).

As the needle placement was kept constant for all the surrogates, the structural voids in the MM surrogate were positioned so that the target site for cement

disposition was between the two anterior voids (refer to Figure 2.5) to simulate a surgeon's choice during clinical PVP [108]. This creates low-resistance paths in the anterior and posterior directions with the goal of filling the two anterior voids. In a clinical scenario, extreme caution would be taken when the cement reaches the posterior void and injections would be terminated if the cement approaches the posterior wall to avoid leakage into the spinal canal or the neural foramina [108]. This study shows that although in the MM surrogate there are three spherical voids collinear along the anteroposterior direction with one of the voids breaching the posterior wall, even low viscosity cements (for example SP4) injected between the two anterior voids do not reach the posterior wall. Care must be taken to prevent anterior leakage only. In the Lesion surrogate, the large spherical void (Ø 19.0 mm) was positioned so that the needle target site was at the anterior side of the void to simulate a surgeon's choice during clinical PVP and deposit the cement in the weight-bearing portion of the vertebral body [99]. The results suggest that at viscosities below 50 Pa·s (i.e. both oils and SP4), the injected fluid never reaches the anterior wall and is preferentially along the void. At higher viscosities however, the injected fluid (i.e. SP8) reaches the anterior wall and has a more favorable filling pattern (refer to Figure 3.25). It is interesting to note that the structural void in the Lesion surrogate generally increased the leakage time under the chosen injection parameters. This is not surprising especially when posterior leakage occurred and the target site for cement deposition was at the anterior third. Also, the void volume is large, thus the volume the injection has to fill is larger. Furthermore, increasing the fluid starting viscosity did not have a significant effect on the leakage time in the Lesion surrogate. However, increasing the cement injection time from 4 to 8 min after mixing (i.e. cement viscosity) significantly increased the leakage time in the Osteo and MM surrogates, thus decreasing the risk of leakage. This is consistent with the study by Baroud et al.[166] who also reported immediate leakage when the cement was injected at 5 min after cement mixing into foam material simulating human osteoporotic vertebral bone.

In this study, the sphericity could not be measured for the oil injections as the oils did not remain in the same position when the samples were microCT scanned post-injection but propagated downwards due to gravitational forces. For the cement

injections however, the sphericity was used to quantitatively describe the final shape of the cement bolus post-injection once the cement had set. A perfect sphere has a sphericity of one and the value approaches zero for randomly elongated geometries. Thus, the sphericity can be used to describe the uniformity of the cement distribution. We were able to show that increasing the cement starting viscosity in the Osteo and MM surrogates does not affect the uniformity of the cement distribution, as the sphericity remained the same. In the Lesion surrogates however, increasing the cement starting viscosity significantly ($p < 0.05$) increases the sphericity causing a more uniform filling pattern. Loeffel et al. [180] were the only group to study the influence of viscosity on the cement spreading pattern in human cadaveric vertebrae as well as foam material with similar morphological properties. They monitored the cement injection using uni-planar fluoroscopy and used circularity to quantitatively describe the final shape of the cement bolus post-injection by comparing the area (A_s) and the perimeter (P_s) of the resulting cement pattern (S) to the perimeter (P_c) of a circle with the same area as the cement contour $\left(\text{Circularity} = P_c/P_s = 2\sqrt{\pi A_s}/P_s\right)$. Their results showed that the measured circularity was similar in the cadaveric samples as well as the foam material, although in the cadaveric samples there was a rapid drop in circularity at the beginning of the injection possibly due to inhomogeneities in the trabecular structure of the human vertebra. Nonetheless, this suggests that bone surrogates can be used to achieve clinically relevant representation of cement filling patterns. Loeffel et al. [180] also found that increasing the cement viscosity from 50 to 100 Pa·s, resulted in significantly denser and more circular cement patterns (higher circularity). In the current study however, the silicone oil viscosity was increased from 10 to 50 Pa·s and that of the Simplex P injected at 4 and 8 min from mixing (SP4 and SP8, respectively) was increased from approximately 30 to 70 Pa·s (based on data presented by Widmer et al. [198]). Thus, all the viscosities tested were below 100 Pa·s, which may explain why there was no significant difference observed in the measured sphericity.

The mean spreading distance (MSD) was also measured in this study as the sphericity is a shape descriptor invariant of size. MSD can be used to quantitatively describe the flow behaviour where a decrease in MSD would signify a more localized

filling pattern. We were able to show that increasing the starting viscosity of the silicone oil and that of the Simplex P bone cement does not have a significant ($p < 0.05$) effect on the MSD, independent of structure. Loeffel et al. [180] reported that a minimal increase in the cement starting viscosity from 50 to 100 Pa·s significantly decreased the MSD. In the current study however, all the viscosities tested were below 100 Pa·s, which may explain why there was no significant difference observed in the MSD. The structure, on the other hand, had a significant effect on the MSD. Relative to the Osteo surrogate, the presence of structural voids in the MM surrogate only, caused a significant ($p < 0.05$) decrease in the MSD from 25.7 to 22.9 mm after 5 mL of silicone oil was injected, independent of viscosity. This shows that the three spherical voids, 6.0 mm in diameter each, present in the MM surrogate positively affect the flow behaviour causing a more localized filling pattern. This does not agree with the study by Loeffel et al. [180] who showed that increasing the average pore diameter from 1.2 to 2.3 mm significantly increases the MSD, thus negatively affecting the compactness of the spreading distribution.

As expected, the injection pressure measured in this study significantly ($P < 0.05$) increased with an increase in the cement injection time (4 vs. 8 min from mixing) and the oil starting viscosity. This is consistent with the study by Kerbs et al. [204] who also reported significantly ($P < 0.001$) higher *in vivo* cement injection pressure during the later phase of the cement polymerization (7 vs. 11 min from mixing). Furthermore, the presence of structural voids generally decreased the peak injection pressure independent of the cement injection time. The void in the Lesion surrogate caused a more pronounced decrease, especially for low viscosity cements such as SP4. As the cement viscosity increased (i.e. SP8) the decrease in the peak injection pressure was similar in the Lesion and MM surrogates. This is not consistent with the study by Reidy et al. [203] who reported no significant difference in the force required to inject bone cement into osteoporotic human vertebrae with and without simulated lytic lesion occupying approximately 15% of the vertebral body volume. However, in the study by Reidy et al. [203], the lesion was filled with soft tumour tissue. It is important to note that the overall hydraulic permeability of the vertebra is mainly a function of the cortical shell, the porosity and the rheological proprieties of the “fluid”

phases (tumour and/or marrow) present within the trabecular network. From a geometrical perspective only, the presence of lytic lesion (structural void) increases the porosity thus the overall hydraulic permeability of the vertebra, which decreases the peak injection pressure as evident in the results of this thesis. On the other hand, soft tumour tissue (with higher viscosity relative to bone marrow) present within the lesion decreases the overall hydraulic permeability of the vertebra. This may explain why there was no significant difference in the force reported by Reidy et al. [203] which was required to inject bone cement into osteoporotic human vertebrae with and without simulated lytic lesion. Further experiments are required to elucidate the effects of soft tumour tissue on the injection biomechanics.

In the oil injections, introducing structural voids did not have a significant effect on the peak injection pressure, independent of the oil viscosity. This suggests that the increase in the overall hydraulic permeability of the surrogates due to the presence of structural voids has a less significant effect on the oils which exhibit Newtonian fluid behaviour relative to the cements which are a suspension of particles. Furthermore, it is important to note that the reported pressure is the pressure (ΔP_s) required to inject the fluid into the structure of the bone surrogates. When the pressure (ΔP_n) required to inject the fluid through the needle is in included, the total pressure ($\Delta P_t = \Delta P_s + \Delta P_n$) becomes independent of the structure (Figure 4.7). This is mainly due to the pressure required to inject the fluid (oil or cement) through the 12-gauge needle dominating over that required to distribute the fluid into the structure. This finding highlights the role of syringe tip diameter and needle gauge in controlling the pressure required to deliver the cement into porous structures such as cancellous bone, although the choice of needle gauge is mainly dictated by the vertebral level being augmented. Figure 4.7 also shows that increasing the fluid starting viscosity significantly increases the total pressure independent of structure.

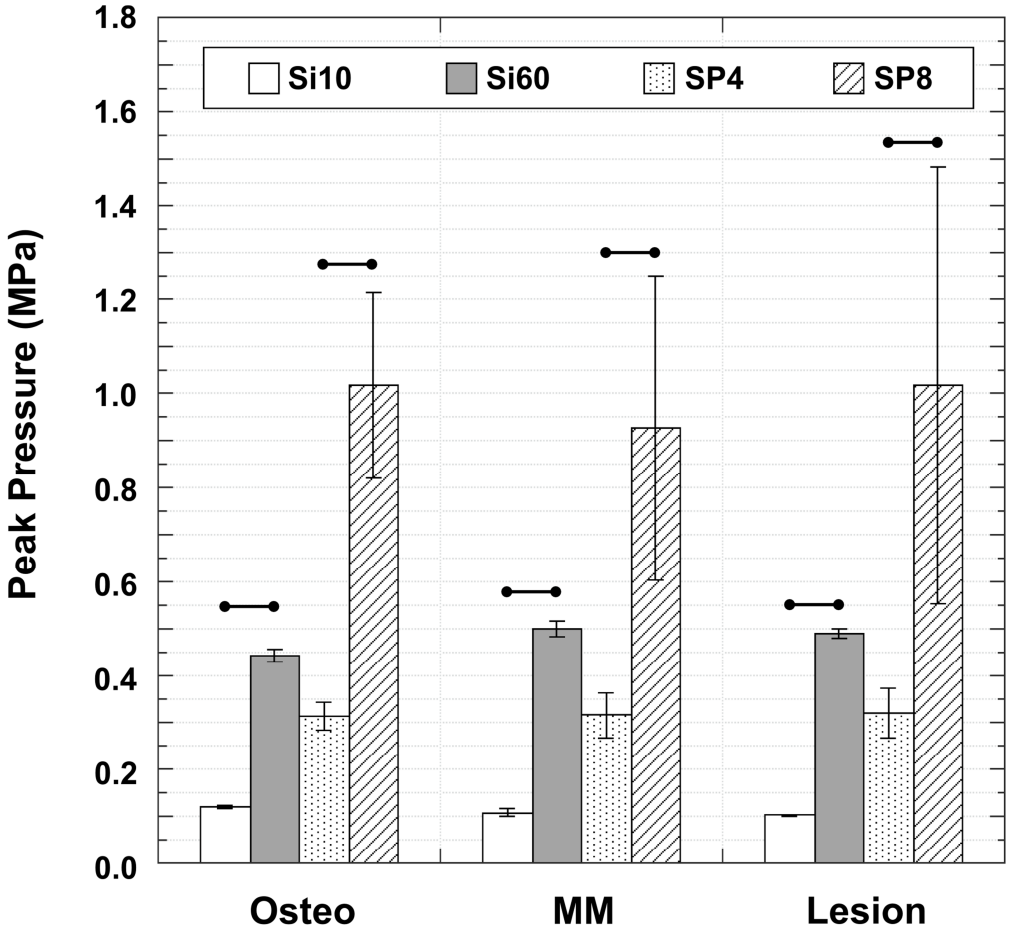

Figure 4. 7 The peak pressure at the syringe plunger required to inject the silicone oils (Si10 and Si 60) as well as the Simplex P bone cements (SP4 and SP8) through the needle and into the structure of the bone surrogates. The data is presented as mean ± SD and the signifcant differences ($p < 0.05$) are labelled with a bar (●——●).

4.2.3 Experimental vs. Computational

This section discusses the results of the experimental-computational cross-validation study comparing the data obtained from the experiments performed in this thesis to that obtained from the computer simulation developed by R. P. Widmer. The advantage of the experimental methodology presented is that it provides a clinically relevant representation of cement flow patterns and a tool for validating computational simulations. The design of the experimental set-up facilitates the modeling aspect of the computer simulation. The injection parameters (i.e. needle gauge, needle placement, flow rate, injected volume) were well controlled and kept constant for all

the injections. The boundary including the openings and the needle insertion channels (Figure 2.2) were kept constant for all the bone surrogates. Furthermore, the structure of the surrogates was uniform to reduce the variability in the morphology (i.e. thickness and spacing) and the structural geometry, thus achieving a near constant intrinsic permeability coefficient, particularly in the Osteo surrogate. It is important to control the structural properties as these dictate the permeability tensor and in combination with the applied pressure gradient the flow in the porous medium. The experimental-computational cross-validation demonstrates that the computational model developed (by R. P. Widmer) to simulate the flow of two immiscible fluids through porous media agrees with the experimental data in the Osteo and MM surrogates. The difference between the experimental data and the simulations was more pronounced in the Lesion surrogate, as the experimental flow was preferentially along the void towards the posterior wall, while the simulated flow was preferentially horizontal and towards the anterior wall.

The computer simulation is based on the assumption that the flow process of two immiscible fluids is mainly governed by the structural properties of the porous medium and the rheological properties of the fluids present within the porous medium. Thus, the accuracy of the simulation depends inherently on (i) how the permeability coefficients are determined and (ii) how the viscosities of the two fluids are measured. In the current simulation, the coefficients of the permeability were estimated using the Kozeny equation [214], which is given by:

$$k^s = c\,\frac{\beta^3}{{S_v}^2} \qquad (37)$$

where β (m^3/m^3) is the porosity of the surrogates, S_v is the specific surface of the surrogates (m^{-1}) and c is a correlation constant called the Kozeny constant. The Kozeny equation is based on hydraulic radius theories that assume the porous medium to be *hydraulically equivalent* to a bed of thin tubes. Such theories are a consequence of the observation that the permeability has the dimensions of length squared. Thus, the equations are designed to estimate this length, which is termed the *hydraulic radius*. The premises of hydraulic radius theories include: (i) fluid motion is similar to

motion through a batch of capillaries, (ii) pores are distributed randomly (iii) pores are not isolated, (iv) pore-size is reasonably uniform and (v) the porous medium has a low porosity. These assumptions hold well in the Osteo surrogate and may explain the strong agreement between the simulations and the experimental data, which is reflected in the low discrepancy in the flow distribution, the spreading distance and the sphericity measured experimentally and those obtained numerically via the computer simulation. The presence of the large structural void in the Lesion surrogate violates assumptions (iv) and (v) as the pore size is not uniform due to the presence of the large void (11% of surrogate volume) and the porous medium has a 100% porosity (i.e. infinite permeability) inside the void. Thus, the equations hold on average and may explain the weaker agreement between the simulations and the experimental data in the Lesion surrogate.

A further source of error for this discrepancy in the Lesion surrogate may be due to the difference between the experimental needle tip position and the nominal position of the inlet (i.e. needle tip) in the CAD model which was adopted in the simulation. The distance between the posterior wall and the needle tip measured experimentally on the superior view of the fluoroscopy projection (Figure 4.3) was on average 2 mm shorter (i.e. closer to the posterior wall) compared to nominal position of the inlet in the simulations. This could have a significant effect on the flow behavior and may explain the difference between the simulated and the experimental flow patterns (i.e. the experimental flow being preferentially along the void towards the posterior wall, while the simulated flow being preferentially horizontal towards the anterior wall). Additional experiments are needed to clarify the effect of needle tip position (i.e. injection inlet) on the flow behaviour, especially in the presence of a large structural void. It is important to note that there was also strong agreement between the simulations and the experimental data in the MM surrogate even in the presence of the three small voids (9% of surrogate volume). This suggests that the assumptions and consequently the equations hold and the effect of such voids on the estimation of the permeability coefficients may be negligible.

In the current simulation, the viscosities of the fluid phases were governed using a power law, which adjusts the viscosity of each fluid phase depending on the time and the shearing rate. Although the viscosities of all the fluids tested in this study (i.e. the Simplex P bone cement, the silicone oil and the marrow substitute) were measured experimentally and well characterized with respect to time and shear rate, the accuracy of the simulation is inherently dependent on how the shear rate is determined. In this simulation, the shear rate was computed from the Darcy flux (Equation 36), which is the apparent velocity vector that represents the average fluid velocity in the porous medium. Thus, the shear rate is approximated at the macroscopic length scale and may differ by orders of magnitudes from the effective pore-scale deformation rates. Furthermore, the simulation neglects other factors that may affect the rheology of the fluids such as the fluid temperature or the yield stresses. More importantly, the simulation expresses Darcy's law in the form of one single constitutive equation in terms of the mixture of the two fluid phases and does not take into account the potential effect of the fluid-fluid interface induced by the surface tension. However, this study shows that the computer simulation developed by R. P. Widmer is an effective tool that can be used to predict the cement placement in cancellous bone, which has been identified as a critical parameter in the biomechanical behaviour of the construct post-augmentation.

4.3 2D Flow Model Injections

4.3.1 Cement Injections

The cement injections performed into the developed 2D flow models aimed to study the influence of the structure (Osteo, Lesion and Fracture), the cement formulation (OC, OP, PL, SP1:2 and SP1:1), and the injection time point (4, 6 and 8 min) on the peak pressure, the time to reach the boundary, the filled area, and the roundness. The goal was to validate the proposed methodology in discerning differences between the tested cement formulations and to highlight the influence of the cement composition on the spreading behaviour. We were able to show that varying the liquid-to-powder (L/P) ratio drastically alters the cement injection behaviour as evident in all the

measured parameters for SP1:1 compared to SP1:2. The results also showed that OP and OC have similar injection behaviour, which is not surprising as these two cement formulations have very similar composition and particle size (Table 2.7, Figure 3.18). Furthermore, we were able to show that the injection behaviour of certain cement formulations, such as PL, improves in the presence of lesion or fracture, thus suggesting the notion of pathology specific cements. It is important to note that the rheological properties play a crucial role in the cement flow behaviour during injection and within a porous structure such as cancellous bone. Although many factors influence the injection biomechanics, the cement viscosity has been identified as a key determinant of the cement flow behaviour [136, 165, 166]. There are two processes that contribute to the rise in viscosity as a function of time: swelling of the polymer particles in the monomer and polymerization of the monomer itself. This implies that the rate of viscosity rise is affected by various factors including particle size (surface area), shape, and distribution as well as the composition of the polymer particles and molecular weight distribution of the polymer components [140].

The peak injection pressure recorded in this study was comparable to that reported during clinical PVP and showed a similar increase with injection time [204]. However, our results showed that the peak pressure was independent of structure (refer to Figure 3.37). This may be due to the pressure required to inject the cement through the inlet (Ø2.4 mm) dominating over that required to distribute the cement into the structure. Filled area and roundness were used to quantitatively describe the resulting flow contours. Both indicators were needed as roundness is a shape descriptor invariant of size. Mean spreading distance and circularity have been previously used [180], however we found that areal measurements (compared to point measurements) reduced the error associated with irregular shapes, while roundness was most sensitive to elongation, with a high value for roundness signifying a more circular pattern, which is an indication of uniform spreading. Contrary to data reported by Loeffel et al. [180], our results showed that increasing the elapsed time from mixing, thus cement viscosity, generally did not have a significant effect on both indicators, especially roundness. This may be due to the cements used in our study having a high starting viscosity at the early injection time point of 4 min compared to the range reported by

Loeffel et al. (50 to 100 Pa·s). The filled area significantly decreased when SP1:1 was injected at 4 min after cement mixing, however this cement formulation has a viscosity in the range reported by Loeffel et al. (based on data presented by Widmer et al. [198]). Our results showed that the presence of a fracture significantly decreases the filled area compared to the presence of lesion and is more likely to cause irregular flow patterns, emphasizing the influence of structure on the cement spreading. In this study, there was a high leakage rate at the early injection time point (4 min) independent of structure and cement formulation, which is consistent with the study performed by Baroud et al.[166] who also reported immediate leakage when the cement was injected at 5 min after cement mixing. This suggests that there is a critical injection point at which the risk of leakage can be significantly reduced. Our results also emphasized the influence of structure on the time to reach the boundary and showed that the presence of lesion or fracture increases the risk of leakage.

The parameters measured in this study can be translated into parameters of interest to help in the design of new injectable biomaterials. Peak injection pressure can be used as an indication for the ease of injectability. Our results showed that, as expected, the injectability seems to increase with L/P ratio as the recorded pressure was lowest for SP1:1, which has the highest L/P ratio (Table 2.7). The pressure was generally highest for SP1:2 and PL indicating that the injectability was lowest for these two cement formulations, which differ from OP and OC in terms of powder composition, wider range of particle sizes, and radiopacifier composition and concentration. A relatively high amount of small-sized polymer beads has been found to increase the polymerization rate, while a high amount of large-sized beads prolongs the onset of curing [150, 215]. Our results suggest that the injectability was lower for cements containing $BaSO_4$; these also had a lower filler concentration (19 and 29.4% w/w for SP1:2 and PL, respectively) than those containing ZrO_2 (both OC and OP contained 45% w/w). Hernández et al. [216] showed that a PMMA cement with 10% w/w $BaSO_4$ has a similar viscosity-time curve but a much earlier onset of viscosity rise compared to the same cement with no radiopacifier. Their results also showed that the same PMMA cement with 10% w/w bismuth salicylate as the radiopacifier had a significantly lower viscosity and much longer onset of viscosity rise compared to the

cement with 10% w/w $BaSO_4$. This highlights the effect of varying the radiopacifier composition on the viscosity of the cement, thus the injection behaviour of that cement suspension. However, further research is needed to elucidate the effect of varying the concentration of the radiopacifier on the injection behaviour of the cement. Our results also suggest that the injectability seems to decrease with an increase in the DMPT concentration. OC and OP have very similar powder composition and particle size, however the injectability was lower for OP, which has a DMPT concentration twice higher compared to OC (Table 2.7). This is consistent with the study performed by Pascual et al. [217] who reported that the cement setting time was lowered as the DMPT and BPO concentrations increased. The roundness and time to reach the boundary can be used to predict the uniformity of the cement spreading and the risk of leakage. High values for these parameters indicate a more uniform spreading pattern and a reduced risk of leakage. Due to boundary we are imposing (i.e. flow exit point, fracture plane and lesion), a high filled area would also signify that the cement is less affected by the structure. A low viscosity cement (such as SP1:1) would have a low filled area as it will follow the path of least resistance and reach the boundary quicker. Based on our results, cement formulations with a high L/P ratio (such as SP1:1) should be avoided in the presence of a large lytic lesion or fracture.

An important limitation of this study is that the flow rate was kept constant at 3 mL/min and the effect of varying flow rates was not considered. This is significant as acrylic cements are known to exhibit shear thinning behaviour. A second limitation is that the models only allow fluid flow in one plane and do not simulate a three-dimensional flow, which occurs in the vertebral body. However, these models represent an alternative simulated environment to quickly and effectively study the flow behaviour of different bone cement formulations without the use of ex-vivo models.

4.3.2 Oil Injections

The oil injections performed into the developed 2D flow models aimed to study the influence of the structure (Osteo, Lesion and Fracture), the oil-marrow combination (Si10-M0.06, Si10-M0.4 and Si60-M0.4), and the injection flow rate (1 and 3 mL/min) on the peak pressure, the time to reach the boundary, the filled area, and the roundness. Silicone oil of constant Newtonian viscosity (independence to shear rate i.e. flow rate) was chosen to reduce the complexity and shift the focus onto understanding the influence of the oil-marrow viscosity ratio and the flow rate on the injection behaviour.

The injections showed that the structure had a significant effect on all the measured parameters with the presence of fracture causing a more significant decrease compared to the presence of lesion. This suggests that at low viscosities (10 and 60 Pa·s) the presence of fracture in the structure causes lower injection pressure, higher risk of leakage and more irregular filling patterns compared to the presence of lesion. It is important to note that for the cement injections the peak pressure was independent of structure. A possible explanation is that the cement is a suspension of particles thus requires a significantly higher pressure to inject through the inlet (Ø2.4 mm) compared to that required to inject the oil, which behaves as a Newtonian fluid. Furthermore, the oil viscosity is relatively low, thus the pressure required to distribute the oil into the structure is significant and not dominated by that required to inject it through the inlet.

This study also showed that the oil-marrow combination has a significant effect on all the measured parameters. The Si10-M0.4 and Si60-M0.4 oil-marrow combination generally showed the lowest and highest recorded pressures, respectively. This shows that the pressure increases as a function of the oil viscosity and is less affected by the viscosity of the marrow substitute. The Si10-M0.4 and Si10-M0.06 oil-marrow combinations had the lowest and highest viscosity ratios, respectively. Furthermore, the viscosity ratio of the Si60-M0.4 (150) was closer to that of the Si10-M0.06 (167). The results suggest that the filled area and roundness increase with the oil-to-marrow viscosity ratio independent of structure since Si10-M0.4 and Si10-M0.06 had the

lowest and highest values, respectively. An increase in the oil-to-marrow viscosity ratio also caused a significant increase in the time to reach the boundary, thus decreasing the risk of leakage. The oil in the Si10-M0.4 oil-marrow combination was the fastest to reach the boundary, while the oils in the Si10-M0.06 and Si60-M0.4 oil-marrow combinations both had an equal and slower time to reach the boundary, independent of structure. This agrees with the study by Bohner et al. [136] who also showed that the risk of leakage increases with an increase in the marrow viscosity (i.e. decrease in the cement-to-marrow viscosity ratio). This confirms that the marrow viscosity has a significant effect on the flow behaviour and must be taken into consideration when assessing injectable biomaterials in cancellous bone.

This study also showed that an increase in the injection flow rate from 1 to 3 mL/min significantly increased the peak pressure independent of structure and silicone oil viscosity. This is consistent with Darcy's law (Equations 19) which shows that the flow rate is directly proportional to the injection pressure. The increase in the injection flow rate significantly decreased the time it took the oil to reach the boundary thus increasing the risk of leakage, independent of the structure and the oil viscosity. This does not agree with the study by Bohner et al. [136] who presented a theoretical model of cement flow in cancellous bone with a special focus on the characterization of cement leakage. Their theoretical model (Equation 33) predicts that the risk of leakage is not a function of flow rate. However, they recommend injecting the cement at a slow flow rate as the cements are known to exhibit shear thinning behaviour. Thus, at high flow rates the cements experience higher shear rates which would cause their viscosity to decrease and the risk of leakage to increase. Furthermore, the increase in the injection flow rate generally did not have a significant effect on the percent filled area and the roundness, independent of the structure and oil viscosity. This agrees with the study by Loeffel et al. [180] who also showed that the injection flow rate did not have a significant effect on the mean spreading distance and circularity which were used in their study to quantify the resulting flow contours.

4.4 3D vs. 2D Surrogates

The 2D flow models were developed to represent the cross-section of the 3D surrogates. However, this was mainly implemented in the Osteo and Lesion surrogates only. Thus, the discussion is focused on results related to these two surrogates and the differences among the results were assessed using Kruskal-Wallis one-way analysis of variance by ranks. Also, the association between the measured 2D and 3D parameters was assessed using the Spearman's rank correlation coefficient (r_s). In all cases, a nominal significance level of $\alpha = 0.05$ was used. All statistical analyses were performed using designated software (R v. 3.0.1, R Foundation for Statistical Computing, Vienna, Austria).

The flow rate in all the 2D and 3D bone surrogates was well controlled and kept constant at 3 mL/min, and the same load cell was used to measure the injection pressure. The injection inlet in the 2D models (Ø = 2.4 mm) was comparable to the inner diameter of the 12-gauge needles (Ø = 2.1 mm) used to perform the injections into the 3D surrogates. Furthermore, the porosity of the 2D Osteo model (87.9 ± 2.0 %) was comparable to that of the 3D Osteo surrogate (82.6 ± 1.1 %), while the large circular void in the 2D Lesion model had the same diameter (Ø = 19.0 mm) as the spherical void in the 3D Lesion surrogate. The analysis of the results revealed that the peak pressure required to inject the Silicone oil and the Simplex P bone cement into the structure of the 3D Osteo and Lesion surrogates was not significantly different ($p = 0.112$) from that measured during the injections performed using the 2D flow models. However, the total pressure measured during the injections performed using the 3D surrogates, which includes the pressure required to inject the fluid through the needle, was significantly higher ($p < 0.05$) compared to that measured during the injections performed using the 2D models. This is not surprising especially when the 2D injection pressure does not account for the pressure drop along the 4 inch needle, which was shown in this study to have a significant effect on the peak injection pressure. Thus, the pressure drop along the needle should be separately calculated and added to the injection pressure measured using the 2D flow models to achieve more accurate and clinically relevant estimations of the injection pressure.

In all the surrogates the time to reach the boundary was measured to provide an indication for the risk of leakage. Quantitative analysis of the data showed that the leakage time measured in the 3D surrogates was significantly higher ($p < 0.05$) than that measured during injections performed using the 2D flow models. This is not surprising especially when the 2D models only allow fluid flow in one plane. However, a correlation was found between the leakage time measured during injections performed using the 2D models and that measured during injections performed using the 3D surrogates ($r_s = 0.77$, $p = 0.10$). Furthermore, relative to the 2D Osteo model the presence of the large structural void in the 2D Lesion model significantly decreased the leakage time, while in the 3D surrogates the opposite was observed. However, this is mainly due to the type of leakage observed in the 3D surrogates (i.e. anterior leakage in the Osteo surrogate vs. posterior leakage in the Lesion surrogate). Figure 4.5 illustrates the superior view of the 2D and 3D bone surrogates showing the positions of the inlets and outlets (i.e. openings in the boundary) in each surrogate.

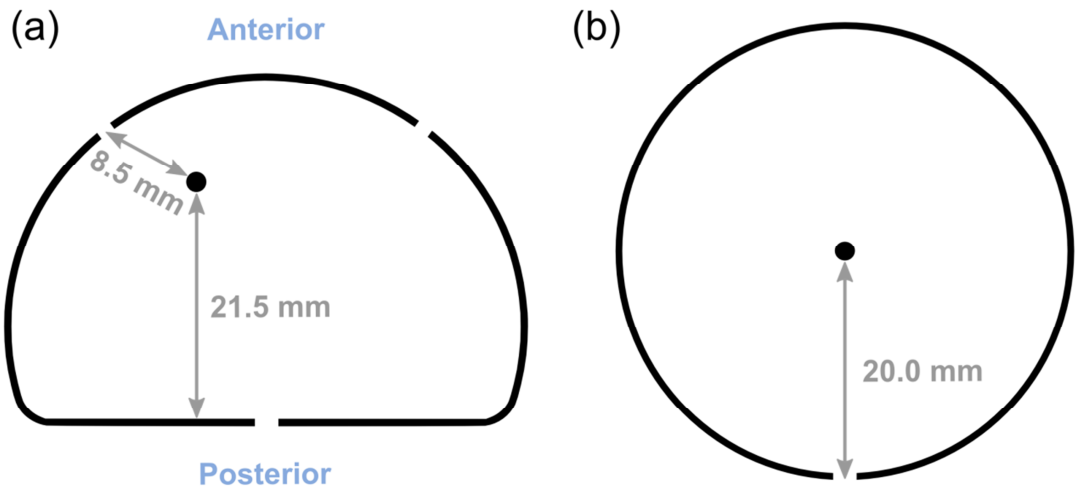

Figure 4. 8 Schematic representation showing the positions of the inlets (black dot) and outlets (breaches in the boundary) on the superior view of (a) the 3D surrogate and (b) the 2D flow model.

It is evident that in the 3D surrogates the distance between the inlet and the left anterior outlet (8.5 mm) is shorter compared to the distance between the inlet and the posterior outlet (21.5 mm). Thus, it is reasonable for the leakage time to increase in the 3D Lesion surrogate, especially when the flow was preferentially along the void in

the posterior direction. Further experiments are needed to clarify the correlation between the 2D and 3D surrogates with respect to the measured leakage time. It is also necessary to adjust the boundary of the 2D models to better match that of the 3D surrogates.

The roundness and the sphericity were used to quantify the resulting cement (SP4 and SP8) spreading patterns in the 2D and 3D bone surrogates, respectively. Roundness is commonly used in the 2D shape characterization of particles [199], while sphericity is its equivalence in the 3D image analysis of objects [197]. Both indicators provide a measure of compactness and approach zero for increasingly elongated contours. Thus, these indicators can be used as a measure of predictability providing an indication for the uniformity of the cement spreading pattern. The analysis of the data revealed that there was no significant difference ($p = 0.70$) between the roundness measured using the resulting cement flow contours in the 2D Osteo model compared to the sphericity measured using the final shape of the cement bolus in the 3D Osteo surrogate. However, the sphericity measured using the 3D Lesion surrogate was significantly higher ($p < 0.05$) than the roundness measured using the 2D Lesion model. Although there was significant difference between the two indicators in the Lesion surrogates, a strong correlation was observed between the roundness measured using the resulting flow contours in the 2D Lesion model compared to the sphericity measured using the final shape of the cement bolus in the 3D Lesion surrogate ($r_s = 0.89$, $p = 0.03$).

The 3D surrogates provide a clinically relevant representation of *in vivo* cement flow patterns, while the 2D flow models only allow fluid flow in one plane and do not simulate the three-dimensional flow that occurs in the vertebral body. However, the use of 2D flow models has a key advantage over three-dimensional surrogates in terms of monitoring the cement spreading during the injection, which is performed using a camera instead of a fluoroscope. This simplifies the experimental set-up and avoids exposure to x-rays. Furthermore, the 2D flow models represent an alternative simulated environment to quickly and effectively study the flow behaviour of different bone cement formulations without the use of ex-vivo model. The injections performed

using the 2D flow models point to the suitability of this methodology in discerning differences between the tested cement formulations. Table 4.2 summarizes the pros and cons for assessing cement injection behaviour in cancellous bone using the developed bone surrogates.

Table 4. 2 The pros and cons of using the developed 2D and 3D bone surrogates for assessing cement injection behaviour in cancellous bone.

2D Flow Models	3D Bone Surrogates
+ Alternative simulated environment + Fast, robust and repeatable + Cost-effective + Injection parameters well controlled + Simplified set-up using a camera to monitor the flow distribution + Effective in discerning biomaterial flow properties	+ Clinically relevant representation + Fast, robust and repeatable + Cost-effective + Pathologically representative + Injection parameters well controlled + Versatile set-up and easily adaptable + Effective in discerning biomaterial flow properties
- Fluid flow in one plane only - Fixed injection inlet	- Fluoroscopy required to monitor flow distribution - CT scan required to measure the final shape of cement bolus

The bone surrogates developed in this thesis are cost-effective, reproducible and pathologically representative with morphology and surface properties similar to bone. They overcome limitations of previous bone surrogates as their geometrical structure is constant and can be tailored to mimic the morphology of specific bone conditions at different skeletal sites. This is crucial to reduce the variability, render the experiments reproducible and shift the focus onto understanding the influence of cement properties on the injection behaviour. This also allows for the pathological representation to remain fixed between investigations and the effects of subtle differences in the cement formulations to be assessed in a reproducible manner following injections into the surrogates under a controlled environment.

CHAPTER 5 Conclusions and Future Work

The rheological properties play a crucial role in the cement flow behaviour during injection and within a porous structure such as cancellous bone. However, many factors influence the injection biomechanics making the scientific understanding of cement flow and cement placement within the vertebral body particularly challenging. This thesis presents a novel methodology to help study the influence of cement properties on injection behaviour. The developed methodology provides a tool for discerning subtle differences in bone cement formulations and allows comprehensive assessment of cement flow behaviour in a fast, robust and reproducible manner. This has been achieved using a methodical approach defined by the study objectives:

Objective 1: Development and manufacturing of reproducible and pathologically representative 2D and 3D bone surrogates

Objective 2: Assessment of bone surrogate morphology and surface properties.

Objective 3: Development of methods for allowing controlled injections into the 2D and 3D bone surrogates.

Objective 4: Comprehensive assessment of bone cements via *in vitro* experiments.

5.1 Conclusions

Novel 2D and 3D bone surrogates were developed to represent osteoporosis and other skeletal pathologies including spinal metastasis and multiple myeloma. These surrogates overcome limitations of previous materials as their geometrical structure was well controlled. Thus, the pathological representation could remain fixed between investigations and the effects of subtle differences in the flow behaviour of the cement formulations could be assessed in a reproducible manner. Controlling the surrogate environment was extremely important as bone cement precursors are heterogeneous, especially their powder component which varies in composition, size and molecular weight of the pre-polymerized polymer beads as well as the morphology of the

radiopacifier particles. All these factors have a significant effect on the interaction between the liquid and the powder components during mixing and injection, resulting in different flow behaviour for different cement formulations.

The 2D flow models were manufactured using flexography (AFP-SH/DSH, Asahi Photoproducts Europe, Brussels, Belgium), while the 3D bone surrogates were manufactured using Projet 3D Printer (Projet HD 3000, 3D Systems, South Carolina, USA). The morphology analysis revealed that the variability in the 2D and 3D bone surrogates was very low, indicating that the geometrical structure of the surrogates was constant. Achieving bone surrogates with constant geometrical structure was crucial to reduce the variability, render the experiments reproducible and shift the focus onto understanding the influence of cement properties on the injection behaviour. The morphology analysis also revealed that the overall pore size of the surrogates was very similar to that reported for human osteoporotic vertebral cancellous bone, indicating that the surrogates were pathologically representative. A further advantage is that the 2D and 3D surrogates had a boundary to simulate the vertebral shell which confines the flow and controls the intravertebral pressure, significantly affecting the filling pattern. The boundary including the flow inlet (i.e. needle placement for 3D surrogates) and the flow exit points were kept constant for all the surrogates. The openings in the boundary simulated breaches through the cortex due to a fracture, a lesion and/or a vessel exchanging blood in and out of the vertebral body. Furthermore, the surrogates simulated the rheological environment within the vertebral body. Based on contact angle measurements, the surface wettability of the 2D and 3D bone surrogates matched that of bone. Also, the presence of the marrow substitute simulated the two-phase flow that occurs within the vertebral body.

Bespoke methodology was developed to control the injection volume and flow rate, measure the injection pressure, and allow visualization and quantitative analysis of the spreading distribution. Two experimental testing rigs were designed to control the displacement of the syringe plunger and achieve a constant injection volume and flow rate. One testing rig uses a syringe pump to control the injections into the 3D surrogates, while the other uses a materials testing machine to control the injections

into the 2D flow models. The rig with the syringe pump can also be used to control injections into the 2D flow models. Furthermore, both testing rigs were designed so that the same load cell could be instrumented and used to measure the injection pressure. For the 3D bone surrogates, a fluoroscope was used to monitor the flow distribution. However, the 2D flow models have a key advantage over the currently developed and previously used 3D bone surrogates in terms of monitoring the flow distribution during the injection, which was performed using a camera instead of a fluoroscope. This simplifies the experimental set-up and avoids exposure to x-rays.

Silicone oil of constant Newtonian viscosity (10 and 50 Pa·s) and Simplex P bone cement (SP1:1 at 4 and 8 min after mixing) were separately injected into each 3D bone surrogate to assess how viscosity and structure such as osteoporotic bone quality (Osteo) and the presence of structural voids due to multiple myeloma (MM) and metastatic infiltration (Lesion) affect the injection behaviour. The study showed that:

- Low viscosity fluids (below 50 Pa·s) have a high tendency to follow low-resistance paths present within the Osteo structure.
- Fluid flow is preferentially along the structural voids in the MM and Lesion surrogates, independent of viscosity and the injected fluid.
- Care must be taken to prevent posterior leakage in the Lesion surrogate and anterior leakage in the Osteo and MM surrogates. Even 5 mL of low viscosity cement injected between the two anterior voids in the MM surrogate does not reach the posterior wall.
- Increasing the fluid starting viscosity in the Osteo and MM surrogates does not have a significant effect on the uniformity of the spreading distribution; however, it significantly decreases the risk of leakage.
- Increasing the fluid starting viscosity in the Lesion surrogate does not have a significant effect on the leakage risk; however, it significantly increases the sphericity causing a more uniform filling pattern.
- Increasing the fluid starting viscosity significantly increases the injection pressure; however, it does not have a significant effect on the mean spreading distance (MSD), independent of structure.

- The presence of structural voids in the MM surrogate only, causes a significant decrease (relative to the Osteo surrogate) in the MSD indicating a more localized filling pattern.
- The presence of structural voids generally decreases the peak injection pressure independent of the cement injection time.

The cement injections performed into the developed 2D flow models validated the proposed methodology in discerning differences between the tested cement formulations (OC, OP, PL, SP1:2 and SP1:1) and highlighted the influence of the structure (Osteo, Lesion and Fracture) and the cement viscosity (injections at 4, 6 and 8 min) on the spreading behaviour. The injections showed that:

- Varying the liquid-to-powder (L/P) ratio drastically alters the cement injection behaviour. Cement formulations with a high L/P ratio, such as SP1:1, cause irregular filling patterns and have a high risk of leakage, thus should be avoided in the presence of a large lytic lesion or fracture.
- Cement formulations with similar composition and particle size, such as OP and OC, have very similar injection behaviour.
- The injection behaviour of certain cement formulations, such as PL, improves in the presence of lesion or fracture, suggesting the notion of pathology specific bone cements.
- Early injections (4min from mixing) significantly increase the risk of leakage independent of structure and cement formulation, suggesting there is a critical injection point at which the risk of leakage can be significantly reduced.
- Later injections (6 and 8 min from mixing) generally do not have a significant effect on the roundness and the filled area, independent of structure and cement formulation (except SP1:1).
- The presence of structural voids significantly increases the risk of leakage; however, the presence of a fracture significantly decreases the filled area compared to the presence of lesion and is more likely to cause irregular flow patterns.

The oil injections performed into the developed 2D flow models aimed to study the influence of the structure (Osteon, Lesion and Fracture), the oil-marrow combination (Si10-M0.06, Si10-M0.4 and Si60-M0.4), and the injection flow rate (1 and 3 mL/min) on the injection behaviour. The injections showed that:

- The presence of fracture in the structure causes lower injection pressure, higher risk of leakage and more irregular filling patterns compared to the presence of lesion.
- The injection pressure increases as a function of the oil viscosity and is less affected by the viscosity of the marrow substitute, independent of structure.
- Increasing the oil-to-marrow viscosity ratio significantly decreases the risk of leakage and causes more uniform filling patterns, independent of structure.
- Increasing the injection flow rate does not have a significant effect on the percent filled area and the uniformity of the spreading distribution; however, it significantly increases the peak pressure and the risk of leakage, independent of the structure and silicone oil viscosity.

The presented methodology provides a novel tool for quick, robust differentiation in the injection behaviour of various biomaterial formulations through controlling the surrogate morphology, controlling the injection parameters, measuring the injection pressure, and allowing the visualization and quantitative analysis of the spreading distribution. The advantage of the experimental methodology presented is that it provides a clinically relevant representation of cement flow patterns and a tool for validating computational simulations. As there are no standardized methods for assessing cement injection behaviour in cancellous bone, the proposed methodology may be beneficial for cement manufacturers to help test novel cement formulations. The advantage is that the structure and the injection parameters are well controlled and kept constant. Thus, the pathological representation can remain fixed between investigations and the effects of subtle differences in the cement formulations can be assessed in a reproducible manner. This also allows studying how cement formulations behave in various pathological representations providing an indication for their suitability, which may help in the development of pathology specific cements.

A further benefit is that the developed methodology can be used as a training tool for surgeons to help minimize their learning curve. This also helps surgeons better understand how cement viscosity (i.e. injection time from mixing) and injection parameters (i.e. injection flow rate, injection volume, needle placement and needle gauge) affect the injection behaviour in different pathological representations.

5.2 Future Work

All the developed bone surrogates were filled with bone marrow substitute formulated using an aqueous solution of carboxymethyl cellulose 2.5% w/w to reach a nominal viscosity of 0.4 Pa·s which has been reported for red bovine marrow [156]. A true representation of the rheological properties of red bone marrow is extremely important as such properties significantly affect the cement flow behaviour [136]. Although there has been data in the literature that describes the rheological properties of human yellow bone marrow [157, 159], there is still a need to test the rheological properties of human red bone marrow which is found within the bony channels of the vertebral body. Furthermore, the developed surrogates did not simulate the soft tumour tissue present within lytic lesions caused by metastatic infiltration and multiple myeloma. This study only focused on how lesions in the structure affect the injection behaviour from a geometrical perspective. Therefore, it is still necessary to study how the presence of soft tumor tissue within the lesion affects the injection behaviour.

In the current study, all the injection parameters were well controlled and kept constant for the duration of the injection. It would be interesting to investigate how changes in the size and position of the injection inlet (i.e. needle size and placement for 3D surrogates) affect the injection behaviour, particularly in the Lesion surrogates. Furthermore, the developed methodology allowed injections into the surrogates under a continuous, constant flow rate. However, the effect of varying flow rates (ramping up) and intermittent injections typically performed in a clinical setting should be addressed in future experiments. It is also interesting to compare injections performed into the surrogates using the developed methodology to that manually performed by an experienced surgeon.

The use of 2D flow models has a key advantage over three-dimensional surrogates in terms of monitoring the cement spreading during the injection, which is performed using a camera instead of a fluoroscope. This simplifies the experimental set-up and avoids exposure to x-rays. It would be interesting to develop a portable, compact testing rig using a syringe pump to control injections into the 2D flow models and a camera to monitor the flow distribution. Data acquisition and analysis could also be automated to provide indication for the flow rate and the injection pressure as well as the quantitative description of the flow behaviour including the risk of leakage (time to reach the boundary), the percent filled area and the uniformity of the spreading pattern (roundness). This compact testing rig can be used as a demonstration tool for medical students or as a training tool for surgeons to better understand the influence of cement properties, cement viscosity and porous structures on the injection behaviour.

A future modification to the experiment set-up should include a temperature controlled environment as this has been shown to affect the cement viscosity rise, thus the injection behaviour. This can be achieved by instrumenting a temperature controlled heating plate into the specimen holder of the 2D flow models. A further approach is to fill the surrogates with bone marrow substitute which has been heated to body temperature (37 °C) before performing the cement injections. It is also interesting to compare the injection behaviour under the developed methodology which controls the injection flow rate (displacement control) to methodology designed to control the injection pressure (force control).

References

1. Melton, L.J., 3rd, *Epidemiology of spinal osteoporosis.* Spine (Phila Pa 1976), 1997. **22**(24 Suppl): p. 2S-11S.
2. Chrischilles, E., T. Shireman, and R. Wallace, *Costs and health effects of osteoporotic fractures.* Bone, 1994. **15**(4): p. 377-86.
3. Ray, N.F., et al., *Medical expenditures for the treatment of osteoporotic fractures in the United States in 1995: report from the National Osteoporosis Foundation.* J Bone Miner Res, 1997. **12**(1): p. 24-35.
4. Burge, R., et al., *Incidence and Economic Burden of Osteoporosis-Related Fractures in the United States, 2005–2025.* Journal of Bone and Mineral Research, 2007. **22**(3): p. 465-475.
5. Riggs, B.L. and L.J. Melton, 3rd, *The worldwide problem of osteoporosis: insights afforded by epidemiology.* Bone, 1995. **17**(5 Suppl): p. 505S-511S.
6. EPOS, *Incidence of vertebral fracture in europe: results from the European Prospective Osteoporosis Study (EPOS).* J Bone Miner Res, 2002. **17**(4): p. 716-24.
7. Ortiz, O. and J.M. Mathis, *Vertebral body reconstruction: techniques and tools.* Neuroimaging Clin N Am, 2010. **20**(2): p. 145-58.
8. Mathis, J.M. and W. Wong, *Percutaneous vertebroplasty: technical considerations.* J Vasc Interv Radiol, 2003. **14**(8): p. 953-60.
9. Lewis, G., *Percutaneous vertebroplasty and kyphoplasty for the stand-alone augmentation of osteoporosis-induced vertebral compression fractures: present status and future directions.* J Biomed Mater Res B Appl Biomater, 2006. **81**(2): p. 371-86.
10. Nussbaum, D.A., P. Gailloud, and K. Murphy, *A review of complications associated with vertebroplasty and kyphoplasty as reported to the Food and Drug Administration medical device related web site.* J Vasc Interv Radiol, 2004. **15**(11): p. 1185-92.
11. Leake, C.B., et al., *Trends of inpatient spine augmentation: 2001-2008.* AJNR Am J Neuroradiol, 2011. **32**(8): p. 1464-8.
12. Long, S.S., W.B. Morrison, and L. Parker, *Vertebroplasty and Kyphoplasty in the United States: Provider Distribution and Guidance Method, 2001-2010.* American Journal of Roentgenology, 2012. **199**(6): p. 1358-1364.
13. Laredo, J.D. and B. Hamze, *Complications of percutaneous vertebroplasty and their prevention.* Skeletal Radiol, 2004. **33**(9): p. 493-505.
14. Childers, J.C., Jr., *Cardiovascular collapse and death during vertebroplasty.* Radiology, 2003. **228**(3): p. 902; author reply 902-3.
15. Lee, B.J., S.R. Lee, and T.Y. Yoo, *Paraplegia as a complication of percutaneous vertebroplasty with polymethylmethacrylate: a case report.* Spine (Phila Pa 1976), 2002. **27**(19): p. E419-22.
16. Jang, J.S., S.H. Lee, and S.K. Jung, *Pulmonary embolism of polymethylmethacrylate after percutaneous vertebroplasty: a report of three cases.* Spine (Phila Pa 1976), 2002. **27**(19): p. E416-8.

17. Ratliff, J., T. Nguyen, and J. Heiss, *Root and spinal cord compression from methylmethacrylate vertebroplasty.* Spine (Phila Pa 1976), 2001. **26**(13): p. E300-2.
18. Harrington, K.D., *Major neurological complications following percutaneous vertebroplasty with polymethylmethacrylate : a case report.* J Bone Joint Surg Am, 2001. **83-A**(7): p. 1070-3.
19. Padovani, B., et al., *Pulmonary embolism caused by acrylic cement: a rare complication of percutaneous vertebroplasty.* AJNR Am J Neuroradiol, 1999. **20**(3): p. 375-7.
20. Schnuerer, A.P. and J. Gallego, *Basic Anatomy and Pathology of the Spine*. 2nd ed. 2003.
21. Panjabi, M.M., et al., *Thoracic human vertebrae. Quantitative three-dimensional anatomy.* Spine (Phila Pa 1976), 1991. **16**(8): p. 888-901.
22. Odgaard, A., *Quantification of Cancellous Bone Architecture*, in *Bone Mechanics Handbook*, S.C. Cowin, Editor. 2001, CRC Press: Boca Raton, FL. p. 1-17.
23. Webste, S.S.J., *Integrated Bone Tissue Physiology: Anatomy and Physiology*, in *Bone Mechanics Handbook*, S.C. Cowin, Editor. 2011, CRC Press: Boca Raton, FL. p. 1-55.
24. Borah, B., et al., *Three-dimensional microimaging (MRmicroI and microCT), finite element modeling, and rapid prototyping provide unique insights into bone architecture in osteoporosis.* Anat Rec, 2001. **265**(2): p. 101-10.
25. Hildebrand, T., et al., *Direct three-dimensional morphometric analysis of human cancellous bone: microstructural data from spine, femur, iliac crest, and calcaneus.* J Bone Miner Res, 1999. **14**(7): p. 1167-74.
26. Odgaard, A., *Three-dimensional methods for quantification of cancellous bone architecture.* Bone, 1997. **20**(4): p. 315-28.
27. Feldkamp, L.A., et al., *The direct examination of three-dimensional bone architecture in vitro by computed tomography.* J Bone Miner Res, 1989. **4**(1): p. 3-11.
28. Kothari, M., et al., *Impact of Spatial Resolution on the Prediction of Trabecular Architecture Parameters.* Bone, 1998. **22**(5): p. 437-443.
29. Muller, R., *Hierarchical microimaging of bone structure and function.* Nat Rev Rheumatol, 2009. **5**(7): p. 373-81.
30. Ridler, T.W. and S. Calvard, *Picture Thresholding Using an Iterative Selection Method.* Systems, Man and Cybernetics, IEEE Transactions on, 1978. **8**(8): p. 630-632.
31. Lochmuller, E.M., et al., *Does thoracic or lumbar spine bone architecture predict vertebral failure strength more accurately than density?* Osteoporos Int, 2008. **19**(4): p. 537-45.
32. Chen, H., et al., *Regional variations of vertebral trabecular bone microstructure with age and gender.* Osteoporos Int, 2008. **19**(10): p. 1473-83.
33. Hulme, P.A., S.K. Boyd, and S.J. Ferguson, *Regional variation in vertebral bone morphology and its contribution to vertebral fracture strength.* Bone, 2007. **41**(6): p. 946-57.

34. Gong, H., et al., *Regional variations in microstructural properties of vertebral trabeculae with structural groups.* Spine (Phila Pa 1976), 2006. **31**(1): p. 24-32.
35. Gong, H., et al., *Regional variations in microstructural properties of vertebral trabeculae with aging.* J Bone Miner Metab, 2005. **23**(2): p. 174-80.
36. Groen, R.J., et al., *Anatomical and pathological considerations in percutaneous vertebroplasty and kyphoplasty: a reappraisal of the vertebral venous system.* Spine (Phila Pa 1976), 2004. **29**(13): p. 1465-71.
37. Batson, O.V., *The Function of the Vertebral Veins and Their Role in the Spread of Metastases.* Ann Surg, 1940. **112**(1): p. 138-49.
38. Ibukuro, K., et al., *Topographic anatomy of the vertebral venous system in the thoracic inlet.* AJR Am J Roentgenol, 2001. **176**(4): p. 1059-65.
39. Crock, H.V., H. Yoshizawa, and S.K. Kame, *Observations on the venous drainage of the human vertebral body.* J Bone Joint Surg Br, 1973. **55**(3): p. 528-33.
40. Airaksinen, O., et al., *Chapter 4. European guidelines for the management of chronic nonspecific low back pain.* Eur Spine J, 2006. **15 Suppl 2**: p. S192-300.
41. Panjabi, M.M. and A.A. White, 3rd, *Basic biomechanics of the spine.* Neurosurgery, 1980. **7**(1): p. 76-93.
42. Panjabi, M.M., *Clinical spinal instability and low back pain.* J Electromyogr Kinesiol, 2003. **13**(4): p. 371-9.
43. Nachemson, A.L., *Advances in low-back pain.* Clin Orthop Relat Res, 1985. **200**(200): p. 266-78.
44. Pope, M.H. and M. Panjabi, *Biomechanical definitions of spinal instability.* Spine (Phila Pa 1976), 1985. **10**(3): p. 255-6.
45. Panjabi, M.M., *The stabilizing system of the spine. Part I. Function, dysfunction, adaptation, and enhancement.* J Spinal Disord, 1992. **5**(4): p. 383-9; discussion 397.
46. Panjabi, M.M., *The stabilizing system of the spine. Part II. Neutral zone and instability hypothesis.* J Spinal Disord, 1992. **5**(4): p. 390-6; discussion 397.
47. *Consensus development conference: diagnosis, prophylaxis, and treatment of osteoporosis.* Am J Med, 1993. **94**(6): p. 646-50.
48. McDonnell, P., P.E. McHugh, and D. O'Mahoney, *Vertebral osteoporosis and trabecular bone quality.* Ann Biomed Eng, 2007. **35**(2): p. 170-89.
49. Parfitt, A.M., et al., *Relationships between surface, volume, and thickness of iliac trabecular bone in aging and in osteoporosis. Implications for the microanatomic and cellular mechanisms of bone loss.* J Clin Invest, 1983. **72**(4): p. 1396-409.
50. Melton, L.J., 3rd, et al., *Perspective. How many women have osteoporosis?* J Bone Miner Res, 1992. **7**(9): p. 1005-10.
51. Benito, M., et al., *Deterioration of trabecular architecture in hypogonadal men.* J Clin Endocrinol Metab, 2003. **88**(4): p. 1497-502.
52. Nguyen, T.V., et al., *Risk factors for osteoporotic fractures in elderly men.* Am J Epidemiol, 1996. **144**(3): p. 255-63.
53. Parfitt, A.M., *Misconceptions (2): turnover is always higher in cancellous than in cortical bone.* Bone, 2002. **30**(6): p. 807-9.

54. Burr, D.B., et al., *Bone remodeling in response to in vivo fatigue microdamage.* J Biomech, 1985. **18**(3): p. 189-200.
55. Frost, H.M., *Skeletal structural adaptations to mechanical usage (SATMU): 2. Redefining Wolff's law: the remodeling problem.* Anat Rec, 1990. **226**(4): p. 414-22.
56. McNamara, L.M., et al., *Strength of cancellous bone trabecular tissue from normal, ovariectomized and drug-treated rats over the course of ageing.* Bone, 2006. **39**(2): p. 392-400.
57. Schaffler, M.B., *Role of bone turnover in microdamage.* Osteoporos Int, 2003. **14 Suppl 5**: p. S73-7; discussion S77-80.
58. Turner, C.H., V. Anne, and R.M. Pidaparti, *A uniform strain criterion for trabecular bone adaptation: do continuum-level strain gradients drive adaptation?* J Biomech, 1997. **30**(6): p. 555-63.
59. van der Meulen, M.C., et al., *Cancellous bone adaptation to in vivo loading in a rabbit model.* Bone, 2006. **38**(6): p. 871-7.
60. Thomsen, J.S., E.N. Ebbesen, and L.I. Mosekilde, *Age-related differences between thinning of horizontal and vertical trabeculae in human lumbar bone as assessed by a new computerized method.* Bone, 2002. **31**(1): p. 136-42.
61. Bouxsein, M.L., *Bone quality: where do we go from here?* Osteoporos Int, 2003. **14 Suppl 5**: p. S118-27.
62. Kanis, J.A., et al., *A reference standard for the description of osteoporosis.* Bone, 2008. **42**(3): p. 467-75.
63. Cummings, S.R., D. Bates, and D.M. Black, *Clinical use of bone densitometry: scientific review.* JAMA, 2002. **288**(15): p. 1889-97.
64. Marshall, D., O. Johnell, and H. Wedel, *Meta-analysis of how well measures of bone mineral density predict occurrence of osteoporotic fractures.* BMJ, 1996. **312**(7041): p. 1254-9.
65. Genant, H.K., et al., *Noninvasive assessment of bone mineral and structure: state of the art.* J Bone Miner Res, 1996. **11**(6): p. 707-30.
66. Gluer, C.C., *Quantitative ultrasound techniques for the assessment of osteoporosis: expert agreement on current status. The International Quantitative Ultrasound Consensus Group.* J Bone Miner Res, 1997. **12**(8): p. 1280-8.
67. Kanis, J.A. and C.C. Gluer, *An update on the diagnosis and assessment of osteoporosis with densitometry. Committee of Scientific Advisors, International Osteoporosis Foundation.* Osteoporos Int, 2000. **11**(3): p. 192-202.
68. Mazess, R., et al., *Performance evaluation of a dual-energy x-ray bone densitometer.* Calcif Tissue Int, 1989. **44**(3): p. 228-32.
69. Kanis, J.A., et al., *The diagnosis of osteoporosis.* J Bone Miner Res, 1994. **9**(8): p. 1137-41.
70. Wehrli, F.W., et al., *Quantitative magnetic resonance imaging in the calcaneus and femur of women with varying degrees of osteopenia and vertebral deformity status.* J Bone Miner Res, 2002. **17**(12): p. 2265-73.
71. Garnero, P., *Markers of bone turnover for the prediction of fracture risk.* Osteoporos Int, 2000. **11 Suppl 6**: p. S55-65.

72. Sundaresan, N., et al., *Tumors of the osseous spine.* J Neurooncol, 2004. **69**(1-3): p. 273-90.
73. Kenan, S. and J. Mechanick, *Skeletal Metastases.* , in *Holland-Frei Cancer Medicine.* , P.R. Kufe DW, Weichselbaum RR, et al., Editor. 2003, BC Decker: Hamilton (ON).
74. Wong, D.A., V.L. Fornasier, and I. MacNab, *Spinal metastases: the obvious, the occult, and the impostors.* Spine (Phila Pa 1976), 1990. **15**(1): p. 1-4.
75. Bilsky, M.H. and S. Azeem, *Multiple Myeloma: Primary Bone Tumor with Systemic Manifestations.* Neurosurgery Clinics of North America, 2008. **19**(1): p. 31-40.
76. Constans, J.P., et al., *Spinal metastases with neurological manifestations. Review of 600 cases.* J Neurosurg, 1983. **59**(1): p. 111-8.
77. Sundaresan, N., et al., *Treatment of neoplastic spinal cord compression: results of a prospective study.* Neurosurgery, 1991. **29**(5): p. 645-50.
78. Roodman, G.D., *Mechanisms of bone metastasis.* N Engl J Med, 2004. **350**(16): p. 1655-64.
79. Sciubba, D.M. and Z.L. Gokaslan, *Diagnosis and management of metastatic spine disease.* Surg Oncol, 2006. **15**(3): p. 141-51.
80. Sciubba, D.M., et al., *Diagnosis and management of metastatic spine disease. A review.* J Neurosurg Spine, 2010. **13**(1): p. 94-108.
81. Tomita, K., et al., *Surgical strategy for spinal metastases.* Spine (Phila Pa 1976), 2001. **26**(3): p. 298-306.
82. Habermann, E.T. and R.A. Lopez, *Metastatic disease of bone and treatment of pathological fractures.* Orthop Clin North Am, 1989. **20**(3): p. 469-86.
83. Nelson, J.B., et al., *Identification of endothelin-1 in the pathophysiology of metastatic adenocarcinoma of the prostate.* Nat Med, 1995. **1**(9): p. 944-9.
84. Galasko, C.S., *Mechanisms of lytic and blastic metastatic disease of bone.* Clin Orthop Relat Res, 1982(169): p. 20-7.
85. Taube, T., et al., *Histomorphometric evidence for osteoclast-mediated bone resorption in metastatic breast cancer.* Bone, 1994. **15**(2): p. 161-6.
86. Bataille, R., D. Chappard, and M. Basle, *Excessive bone resorption in human plasmacytomas: direct induction by tumour cells in vivo.* Br J Haematol, 1995. **90**(3): p. 721-4.
87. Taube, T., et al., *Abnormal bone remodelling in patients with myelomatosis and normal biochemical indices of bone resorption.* Eur J Haematol, 1992. **49**(4): p. 192-8.
88. Denis, F., *The three column spine and its significance in the classification of acute thoracolumbar spinal injuries.* Spine (Phila Pa 1976), 1983. **8**(8): p. 817-31.
89. Fourney, D.R. and Z.L. Gokaslan, *Spinal instability and deformity due to neoplastic conditions.* Neurosurg Focus, 2003. **14**(1): p. e8.
90. Fourney, D.R., et al., *Percutaneous vertebroplasty and kyphoplasty for painful vertebral body fractures in cancer patients.* J Neurosurg, 2003. **98**(1 Suppl): p. 21-30.
91. Izzo, R., et al., *Biomechanics of the spine. Part II: spinal instability.* Eur J Radiol, 2013. **82**(1): p. 127-38.

92. Currey, J.D., *Bone strength: what are we trying to measure?* Calcif Tissue Int, 2001. **68**(4): p. 205-10.
93. Myers, E.R. and S.E. Wilson, *Biomechanics of osteoporosis and vertebral fracture.* Spine (Phila Pa 1976), 1997. **22**(24 Suppl): p. 25S-31S.
94. Cooper, C., T. O'Neill, and A. Silman, *The epidemiology of vertebral fractures. European Vertebral Osteoporosis Study Group.* Bone, 1993. **14 Suppl 1**: p. S89-97.
95. Grigoryan, M., et al., *Recognizing and reporting osteoporotic vertebral fractures.* Eur Spine J, 2003. **12 Suppl 2**: p. S104-12.
96. Genant, H.K., et al., *Vertebral fracture assessment using a semiquantitative technique.* J Bone Miner Res, 1993. **8**(9): p. 1137-48.
97. Genant, H.K., et al., *Comparison of semiquantitative visual and quantitative morphometric assessment of prevalent and incident vertebral fractures in osteoporosis The Study of Osteoporotic Fractures Research Group.* J Bone Miner Res, 1996. **11**(7): p. 984-96.
98. Genant, H.K. and M. Jergas, *Assessment of prevalent and incident vertebral fractures in osteoporosis research.* Osteoporos Int, 2003. **14 Suppl 3**: p. S43-55.
99. Eckel, T.S. and W. Olan, *Vertebroplasty and vertebral augmentation techniques.* Tech Vasc Interv Radiol, 2009. **12**(1): p. 44-50.
100. Mendel, E., et al., *Percutaneous techniques in the treatment of spine tumors: what are the diagnostic and therapeutic indications and outcomes?* Spine (Phila Pa 1976), 2009. **34**(22 Suppl): p. S93-100.
101. Binning, M.J., et al., *Minimally invasive treatments for metastatic tumors of the spine.* Neurosurg Clin N Am, 2004. **15**(4): p. 459-65.
102. Mathis, J.M., et al., *Percutaneous vertebroplasty: a developing standard of care for vertebral compression fractures.* AJNR Am J Neuroradiol, 2001. **22**(2): p. 373-81.
103. Galibert, P., et al., *[Preliminary note on the treatment of vertebral angioma by percutaneous acrylic vertebroplasty]*. Neurochirurgie, 1987. **33**(2): p. 166-8.
104. Jensen, M.E., et al., *Percutaneous polymethylmethacrylate vertebroplasty in the treatment of osteoporotic vertebral body compression fractures: technical aspects.* AJNR Am J Neuroradiol, 1997. **18**(10): p. 1897-904.
105. Cortet, B., et al., *Percutaneous vertebroplasty in the treatment of osteoporotic vertebral compression fractures: an open prospective study.* J Rheumatol, 1999. **26**(10): p. 2222-8.
106. Gaughen, J.R., Jr., et al., *Relevance of antecedent venography in percutaneous vertebroplasty for the treatment of osteoporotic compression fractures.* AJNR Am J Neuroradiol, 2002. **23**(4): p. 594-600.
107. Weill, A., et al., *Spinal metastases: indications for and results of percutaneous injection of acrylic surgical cement.* Radiology, 1996. **199**(1): p. 241-7.
108. Cotten, A., et al., *Percutaneous vertebroplasty for osteolytic metastases and myeloma: effects of the percentage of lesion filling and the leakage of methyl methacrylate at clinical follow-up.* Radiology, 1996. **200**(2): p. 525-30.
109. Vasconcelos, C., et al., *Transient arterial hypotension induced by polymethylmethacrylate injection during percutaneous vertebroplasty.* J Vasc Interv Radiol, 2001. **12**(8): p. 1001-2.

110. Cyteval, C., et al., *Acute osteoporotic vertebral collapse: open study on percutaneous injection of acrylic surgical cement in 20 patients.* AJR Am J Roentgenol, 1999. **173**(6): p. 1685-90.
111. Scroop, R., J. Eskridge, and G.W. Britz, *Paradoxical cerebral arterial embolization of cement during intraoperative vertebroplasty: case report.* AJNR Am J Neuroradiol, 2002. **23**(5): p. 868-70.
112. Deramond, H., et al., *Percutaneous vertebroplasty with polymethylmethacrylate. Technique, indications, and results.* Radiol Clin North Am, 1998. **36**(3): p. 533-46.
113. Peh, W.C., L.A. Gilula, and D.D. Peck, *Percutaneous vertebroplasty for severe osteoporotic vertebral body compression fractures.* Radiology, 2002. **223**(1): p. 121-6.
114. Alvarez, L., et al., *Percutaneous vertebroplasty: functional improvement in patients with osteoporotic compression fractures.* Spine (Phila Pa 1976), 2006. **31**(10): p. 1113-8.
115. Anselmetti, G.C., et al., *Pain relief following percutaneous vertebroplasty: results of a series of 283 consecutive patients treated in a single institution.* Cardiovasc Intervent Radiol, 2007. **30**(3): p. 441-7.
116. Legroux-Gerot, I., et al., *Long-term follow-up of vertebral osteoporotic fractures treated by percutaneous vertebroplasty.* Clin Rheumatol, 2004. **23**(4): p. 310-7.
117. McGraw, J.K., et al., *Prospective evaluation of pain relief in 100 patients undergoing percutaneous vertebroplasty: results and follow-up.* J Vasc Interv Radiol, 2002. **13**(9 Pt 1): p. 883-6.
118. Zoarski, G.H., et al., *Percutaneous vertebroplasty for osteoporotic compression fractures: quantitative prospective evaluation of long-term outcomes.* J Vasc Interv Radiol, 2002. **13**(2 Pt 1): p. 139-48.
119. Buchbinder, R., et al., *A randomized trial of vertebroplasty for painful osteoporotic vertebral fractures.* N Engl J Med, 2009. **361**(6): p. 557-68.
120. Kallmes, D.F., et al., *A randomized trial of vertebroplasty for osteoporotic spinal fractures.* N Engl J Med, 2009. **361**(6): p. 569-79.
121. Clark, W., S. Lyon, and J. Burnes, *Trials of Vertebroplasty for Vertebral Fractures.* New England Journal of Medicine, 2009. **361**(21): p. 2097-2100.
122. Klazen, C.A., et al., *Vertebroplasty versus conservative treatment in acute osteoporotic vertebral compression fractures (Vertos II): an open-label randomised trial.* Lancet, 2010. **376**(9746): p. 1085-92.
123. Anselmetti, G.C., et al., *Percutaneous vertebroplasty and bone cement leakage: clinical experience with a new high-viscosity bone cement and delivery system for vertebral augmentation in benign and malignant compression fractures.* Cardiovasc Intervent Radiol, 2008. **31**(5): p. 937-47.
124. Cahana, A., et al., *Percutaneous vertebroplasty in octogenarians: results and follow-up.* Pain Pract, 2005. **5**(4): p. 316-23.
125. Cheung, G., et al., *Percutaneous vertebroplasty in patients with intractable pain from osteoporotic or metastatic fractures: A prospective study using quality-of-life assessment.* Can Assoc Radiol J, 2006. **57**(1): p. 13-21.
126. Ramos, L., et al., *Medium-term results of percutaneous vertebroplasty in multiple myeloma.* Eur J Haematol, 2006. **77**(1): p. 7-13.

127. Dudeney, S., et al., *Kyphoplasty in the treatment of osteolytic vertebral compression fractures as a result of multiple myeloma.* J Clin Oncol, 2002. **20**(9): p. 2382-7.
128. Gerszten, P.C., et al., *Combination kyphoplasty and spinal radiosurgery: a new treatment paradigm for pathological fractures.* J Neurosurg Spine, 2005. **3**(4): p. 296-301.
129. Khanna, A.J., et al., *Functional outcomes of kyphoplasty for the treatment of osteoporotic and osteolytic vertebral compression fractures.* Osteoporos Int, 2006. **17**(6): p. 817-26.
130. Lane, J.M., et al., *Kyphoplasty enhances function and structural alignment in multiple myeloma.* Clin Orthop Relat Res, 2004(426): p. 49-53.
131. Pflugmacher, R., et al., *Percutaneous balloon kyphoplasty in the treatment of pathological vertebral body fracture and deformity in multiple myeloma: a one-year follow-up.* Acta Radiol, 2006. **47**(4): p. 369-76.
132. Pflugmacher, R., et al., *Balloon kyphoplasty in the treatment of metastatic disease of the spine: a 2-year prospective evaluation.* Eur Spine J, 2008. **17**(8): p. 1042-8.
133. Pearson, J.R.A. and P.M.J. Tardy, *Models for flow of non-Newtonian and complex fluids through porous media.* Journal of Non-Newtonian Fluid Mechanics, 2002. **102**(2): p. 447-473.
134. Pinder, G.F. and W.G. Gray, *Essentials of Multiphase Flow and Transport in Porous Media.* 2008: John Wiley & Sons, Inc.. .
135. Widmer, R.P. and S.J. Ferguson, *A mixed boundary representation to simulate the displacement of a biofluid by a biomaterial in porous media.* J Biomech Eng, 2011. **133**(5): p. 051007.
136. Bohner, M., et al., *Theoretical and experimental model to describe the injection of a polymethylmethacrylate cement into a porous structure.* Biomaterials, 2003. **24**(16): p. 2721-30.
137. Widmer Soyka, R.P., et al., *Numerical description and experimental validation of a rheology model for non-Newtonian fluid flow in cancellous bone.* J Mech Behav Biomed Mater, 2013. **6161**(13): p. 00214-2.
138. Krause, W.R., J. Miller, and P. Ng, *The viscosity of acrylic bone cements.* J Biomed Mater Res, 1982. **16**(3): p. 219-43.
139. Nzihou, A., et al., *A rheological, thermal and mechanical study of bone cementâ€"from a suspension to a solid biomaterial.* Powder Technology, 1998. **99**(1): p. 60-69.
140. Farrar, D.F. and J. Rose, *Rheological properties of PMMA bone cements during curing.* Biomaterials, 2001. **22**(22): p. 3005-13.
141. Dunne, N.J. and J.F. Orr, *Influence of mixing techniques on the physical properties of acrylic bone cement.* Biomaterials, 2001. **22**(13): p. 1819-26.
142. Dunne, N.J. and J.F. Orr, *Flow characteristics of curing polymethyl methacrylate bone cement.* Proc Inst Mech Eng H, 1998. **212**(3): p. 199-207.
143. Li, C., J. Mason, and D. Yakimicki, *Thermal characterization of PMMA-based bone cement curing.* J Mater Sci Mater Med, 2004. **15**(1): p. 85-9.
144. Baleani, M., L. Cristofolini, and A. Toni, *Temperature and ageing condition effects on the characterization of acrylic bone cement.* Proc Inst Mech Eng H, 2001. **215**(1): p. 113-8.

145. Akashi, A., et al., *The relationship between water absorption characteristics and the mechanical strength of resin-modified glass-ionomer cements in long-term water storage.* Biomaterials, 1999. **20**(17): p. 1573-8.
146. Harper, E.J., et al., *Influence of sterilization upon a range of properties of experimental bone cements.* J Mater Sci Mater Med, 1997. **8**(12): p. 849-53.
147. Nottrott, M., A.O. Molster, and N.R. Gjerdet, *Time dependent mechanical properties of bone cement. An in vitro study over one year.* J Biomed Mater Res B Appl Biomater, 2007. **83**(2): p. 416-21.
148. Lewis, G., S. Janna, and A. Bhattaram, *Influence of the method of blending an antibiotic powder with an acrylic bone cement powder on physical, mechanical, and thermal properties of the cured cement.* Biomaterials, 2005. **26**(20): p. 4317-25.
149. He, S., et al., *Effect of choice of surgical gloves on dough time measurements of acrylic bone cement.* Biomaterials, 2003. **24**(2): p. 235-7.
150. Lewis, G. and M. Carroll, *Rheological properties of acrylic bone cement during curing and the role of the size of the powder particles.* J Biomed Mater Res, 2002. **63**(2): p. 191-9.
151. Lewis, G., *Injectable bone cements for use in vertebroplasty and kyphoplasty: State-of-the-art review.* Journal of Biomedical Materials Research Part B: Applied Biomaterials, 2006. **76B**(2): p. 456-468.
152. San Millan Ruiz, D., et al., *Pathology findings with acrylic implants.* Bone, 1999. **25**(2 Suppl): p. 85S-90S.
153. Baroud, G., E. Cayer, and M. Bohner, *Rheological characterization of concentrated aqueous Î²-tricalcium phosphate suspensions: The effect of liquid-to-powder ratio, milling time, and additives.* Acta Biomaterialia, 2005. **1**(3): p. 357-363.
154. Lieberman, I.H., D. Togawa, and M.M. Kayanja, *Vertebroplasty and kyphoplasty: filler materials.* The Spine Journal, 2005. **5**(6, Supplement): p. S305-S316.
155. Dickerson, D.A., E.A. Sander, and E.A. Nauman, *Modeling the mechanical consequences of vibratory loading in the vertebral body: microscale effects.* Biomech Model Mechanobiol, 2008. **7**(3): p. 191-202.
156. Bryant, J.D., et al., *Rheology of bovine bone marrow.* Proc Inst Mech Eng H, 1989. **203**(2): p. 71-5.
157. Davis, B.L. and S.S. Praveen, *Nonlinear Versus Linear Behavior of Calcaneal Bone Marrow at Different Shear Rates*, in *American Society of Biomechanics Annual Meeting*2006: Blacksburg, VA.
158. Gurkan, U.A. and O. Akkus. *An implantable magnetoelastic sensor system for wireless physiological sensing of viscosity*. in *ASME Summer Bioengineering*. 2007. New York.
159. Zhong, Z. and O. Akkus, *Effects of age and shear rate on the rheological properties of human yellow bone marrow.* Biorheology, 2011. **48**(2): p. 89-97.
160. Eguchi, Y. and T. Karino, *Measurement of rheologic property of blood by a falling-ball blood viscometer.* Ann Biomed Eng, 2008. **36**(4): p. 545-53.
161. Gurkan, U.A. and O. Akkus, *The mechanical environment of bone marrow: a review.* Ann Biomed Eng, 2008. **36**(12): p. 1978-91.

162. Tavassoli, M. and J.M. Yoffey, *Bone Marrow, Structure and Function*. 1983, New York: A.R. Liss.
163. Huggins, C. and B.H. Blocksom, *Changes in outlying bone marrow accompanying a local increase of temperature within physiological limits.* J Exp Med, 1936. **64**(2): p. 253-74.
164. Huggins, C. and W.J. Noonan, *An increase in reticulo-endothelial cells in outlying bone marrow consequent upon a local increase in temperature.* J Exp Med, 1936. **64**(2): p. 275-80.
165. Baroud, G., et al., *Injection biomechanics of bone cements used in vertebroplasty.* Biomed Mater Eng, 2004. **14**(4): p. 487-504.
166. Baroud, G., M. Crookshank, and M. Bohner, *High-viscosity cement significantly enhances uniformity of cement filling in vertebroplasty: an experimental model and study on cement leakage.* Spine (Phila Pa 1976), 2006. **31**(22): p. 2562-8.
167. Liebschner, M.A., W.S. Rosenberg, and T.M. Keaveny, *Effects of bone cement volume and distribution on vertebral stiffness after vertebroplasty.* Spine (Phila Pa 1976), 2001. **26**(14): p. 1547-54.
168. Tschirhart, C.E., S.E. Roth, and C.M. Whyne, *Biomechanical assessment of stability in the metastatic spine following percutaneous vertebroplasty: effects of cement distribution patterns and volume.* Journal of Biomechanics, 2005. **38**(8): p. 1582-1590.
169. Whitaker, S., *Flow in porous media II: The governing equations for immiscible, two-phase flow.* Transport in Porous Media, 1986. **1**(2): p. 105-125.
170. Darcy, H., *Les fontaines publiques de la ville de Dijon*. Vol. Vol. 647. 1856, Dalmont, Paris.
171. Baroud, G., et al., *Constitutive Model and Parameter Identification for the Cement Infiltration of Osteoporotic Bone*, in *Tenth Annual Symposium on Computational Methods in Orthopaedic Biomechanics*2002: Dallas.
172. Baroud, G., et al., *Experimental and theoretical investigation of directional permeability of human vertebral cancellous bone for cement infiltration.* J Biomech, 2004. **37**(2): p. 189-96.
173. Baroud, G., et al., *How to determine the permeability for cement infiltration of osteoporotic cancellous bone.* Med Eng Phys, 2003. **25**(4): p. 283-8.
174. Teo, J.C.M., et al., *Correlation of cancellous bone microarchitectural parameters from microCT to CT number and bone mechanical properties.* Materials Science and Engineering: C, 2007. **27**(2): p. 333-339.
175. Baroud, G. and F.B. Yahia, *A finite element rheological model for polymethylmethacrylate flow: analysis of the cement delivery in vertebroplasty.* Proc Inst Mech Eng H, 2004. **218**(5): p. 331-8.
176. Lian, Z., C.K. Chui, and S.H. Teoh, *A biomechanical model for real-time simulation of PMMA injection with haptics.* Comput Biol Med, 2008. **38**(3): p. 304-12.
177. Teo, J., S.C. Wang, and S.H. Teoh, *Preliminary study on biomechanics of vertebroplasty: a computational fluid dynamics and solid mechanics combined approach.* Spine (Phila Pa 1976), 2007. **32**(12): p. 1320-8.

178. Mohamed, R., et al., *Cement filling control and bone marrow removal in vertebral body augmentation by unipedicular aspiration technique: an experimental study using leakage model.* Spine (Phila Pa 1976), 2010. **35**(3): p. 353-60.
179. Habib, M., et al., *Cement leakage and filling pattern study of low viscous vertebroplastic versus high viscous confidence cement.* The International Society for the Advancement of Spine Surgery, 2010. **4**: p. 26-33.
180. Loeffel, M., et al., *Vertebroplasty: experimental characterization of polymethylmethacrylate bone cement spreading as a function of viscosity, bone porosity, and flow rate.* Spine (Phila Pa 1976), 2008. **33**(12): p. 1352-9.
181. Mosekilde, L., *Age-related changes in vertebral trabecular bone architecture--assessed by a new method.* Bone, 1988. **9**(4): p. 247-50.
182. Tschirhart, C.E., A. Nagpurkar, and C.M. Whyne, *Effects of tumor location, shape and surface serration on burst fracture risk in the metastatic spine.* J Biomech, 2004. **37**(5): p. 653-60.
183. Ahn, H., et al., *Stability of the metastatic spine pre and post vertebroplasty.* J Spinal Disord Tech, 2006. **19**(3): p. 178-82.
184. Takasu, M., et al., *Multiple myeloma: microstructural analysis of lumbar trabecular bones in patients without visible bone lesions--preliminary results.* Radiology, 2011. **260**(2): p. 472-9.
185. Baroud, G., et al., *Effect of vertebral shell on injection pressure and intravertebral pressure in vertebroplasty.* Spine (Phila Pa 1976), 2004. **30**(1): p. 68-74.
186. Zhou, S.H., et al., *Geometrical dimensions of the lower lumbar vertebrae--analysis of data from digitised CT images.* Eur Spine J, 2000. **9**(3): p. 242-8.
187. Sander, E.A., et al., *Examination of continuum and micro-structural properties of human vertebral cancellous bone using combined cellular solid models.* Biomech Model Mechanobiol, 2003. **2**(2): p. 97-107.
188. Panjabi, M.M., et al., *Human lumbar vertebrae. Quantitative three-dimensional anatomy.* Spine (Phila Pa 1976), 1992. **17**(3): p. 299-306.
189. Schneider, C.A., W.S. Rasband, and K.W. Eliceiri, *NIH Image to ImageJ: 25 years of image analysis.* Nat Meth, 2012. **9**(7): p. 671-675.
190. Noorani, R., *Rapid Prototyping: Principles and Applications*. 2006, Hoboken, NJ: John Wiley & Sons, Inc.
191. Pham, D.T. and S.S. Dimov, *Rapid Manufacturing: The Technologies and Applications of Rapid Prototyping and Rapid Tooling*. 2001, Wiltshire, UK: The Cromwell Press Limited.
192. Wong, Y.S., et al., *Rapid prototyping and manufacturing (RP&M) benchmarking*, in *Software Solutions for Rapid Prototyping*, I. Gibson, Editor. 2002, The Cromwell Press Limited: Wiltshire, UK. p. 57-92.
193. O'Mahony, C., et al., *Characterization of micromechanical structures using white-light interferometry.* Measurement Science and Technology, 2003. **14**(10): p. 1807-14.
194. Quan, C., et al., *Study on the use of white light interferometry for multifiber-end surface profile measurement.* Optical Engineering, 2006. **45**(5): p. 055603-9.

195. Hughes, S.W., *Archimedes revisited: a faster, better, cheaper method of accurately measuring the volume of small objects.* Physcis Education, 2005. **40**(5).
196. Widmer, R.P. and S.J. Ferguson, *On the interrelationship of permeability and structural parameters of vertebral trabecular bone: a parametric computational study.* Comput Methods Biomech Biomed Engin, 2012. **16**(8): p. 908-22.
197. Lin, C.L. and J.D. Miller, *3D characterization and analysis of particle shape using X-ray microtomography (XMT).* Powder Technology, 2005. **154**(1): p. 61-69.
198. Widmer Soyka, R.P., et al., *Numerical description and experimental validation of a rheology model for non-Newtonian fluid flow in cancellous bone.* J Mech Behav Biomed Mater, 2013. **27**: p. 43-53.
199. Hentschel, M.L. and N.W. Page, *Selection of Descriptors for Particle Shape Characterization.* Particle & Particle Systems Characterization, 2003. **20**(1): p. 25-38.
200. Lohfeld, S., V. Barron, and P.E. McHugh, *Biomodels of bone: a review.* Ann Biomed Eng, 2005. **33**(10): p. 1295-311.
201. Nauman, E.A., K.E. Fong, and T.M. Keaveny, *Dependence of intertrabecular permeability on flow direction and anatomic site.* Ann Biomed Eng, 1999. **27**(4): p. 517-24.
202. Ahn, H., et al., *The effect of pre-vertebroplasty tumor ablation using laser-induced thermotherapy on biomechanical stability and cement fill in the metastatic spine.* Eur Spine J, 2007. **16**(8): p. 1171-8.
203. Reidy, D., et al., *A biomechanical analysis of intravertebral pressures during vertebroplasty of cadaveric spines with and without simulated metastases.* Spine (Phila Pa 1976), 2003. **28**(14): p. 1534-9.
204. Krebs, J., et al., *Clinical measurements of cement injection pressure during vertebroplasty.* Spine (Phila Pa 1976), 2005. **30**(5): p. E118-22.
205. Barragan-Campos, H.M., et al., *Percutaneous vertebroplasty for spinal metastases: complications.* Radiology, 2006. **238**(1): p. 354-62.
206. Calmels, V., et al., *Osteoblastic and mixed spinal metastases: evaluation of the analgesic efficacy of percutaneous vertebroplasty.* AJNR Am J Neuroradiol, 2007. **28**(3): p. 570-4.
207. Tseng, Y.Y., et al., *Percutaneous polymethylmethacrylate vertebroplasty in the treatment of pain induced by metastatic spine tumor.* Surg Neurol, 2008. **70 Suppl 1**: p. S1:78-83; discussion S1:83-4.
208. Yang, Z., et al., *Treatment of metastatic spinal tumors by percutaneous vertebroplasty versus percutaneous vertebroplasty combined with interstitial implantation of 125I seeds.* Acta Radiol, 2009. **50**(10): p. 1142-8.
209. Lador, R., et al., *A pictorial classification atlas of cement extravasation with vertebral augmentation.* Spine J, 2010. **10**(12): p. 1118-27.
210. Gosev, I., et al., *Right ventricular perforation and pulmonary embolism with polymethylmethacrylate cement after percutaneous kyphoplasty.* Circulation, 2013. **127**(11): p. 1251-3.

211. Habib, N., et al., *Cement pulmonary embolism after percutaneous vertebroplasty and kyphoplasty: an overview*. Heart Lung, 2012. **41**(5): p. 509-11.
212. Tourtier, J.-P. and S. Cottez, *Pulmonary Cement Embolism after Vertebroplasty.* New England Journal of Medicine, 2012. **366**(3): p. 258-258.
213. Sidhu, G.S., et al., *Neurological deficit due to cement extravasation following a vertebral augmentation procedure.* J Neurosurg Spine, 2013. **19**(1): p. 61-70.
214. Arramon, Y.P. and E. Nauman, *The Intrinsic Permeability of Cancellous Bone*, in *Bone Mechanics Handbook*, S.C. Cowin, Editor. 2001, CRC Press: Boca Raton, FL. p. 1–17.
215. Hernández, L., M. Gurruchaga, and I. Goñi, *Influence of powder particle size distribution on complex viscosity and other properties of acrylic bone cement for vertebroplasty and kyphoplasty.* Journal of Biomedical Materials Research Part B: Applied Biomaterials, 2006. **77B**(1): p. 98-103.
216. Hernández, L., et al., *Preparation of acrylic bone cements for vertebroplasty with bismuth salicylate as radiopaque agent.* Biomaterials, 2006. **27**(1): p. 100-107.
217. Pascual, B., et al., *New aspects of the effect of size and size distribution on the setting parameters and mechanical properties of acrylic bone cements.* Biomaterials, 1996. **17**(5): p. 509-516.

Appendix A

Technical drawing of the benchmark part.

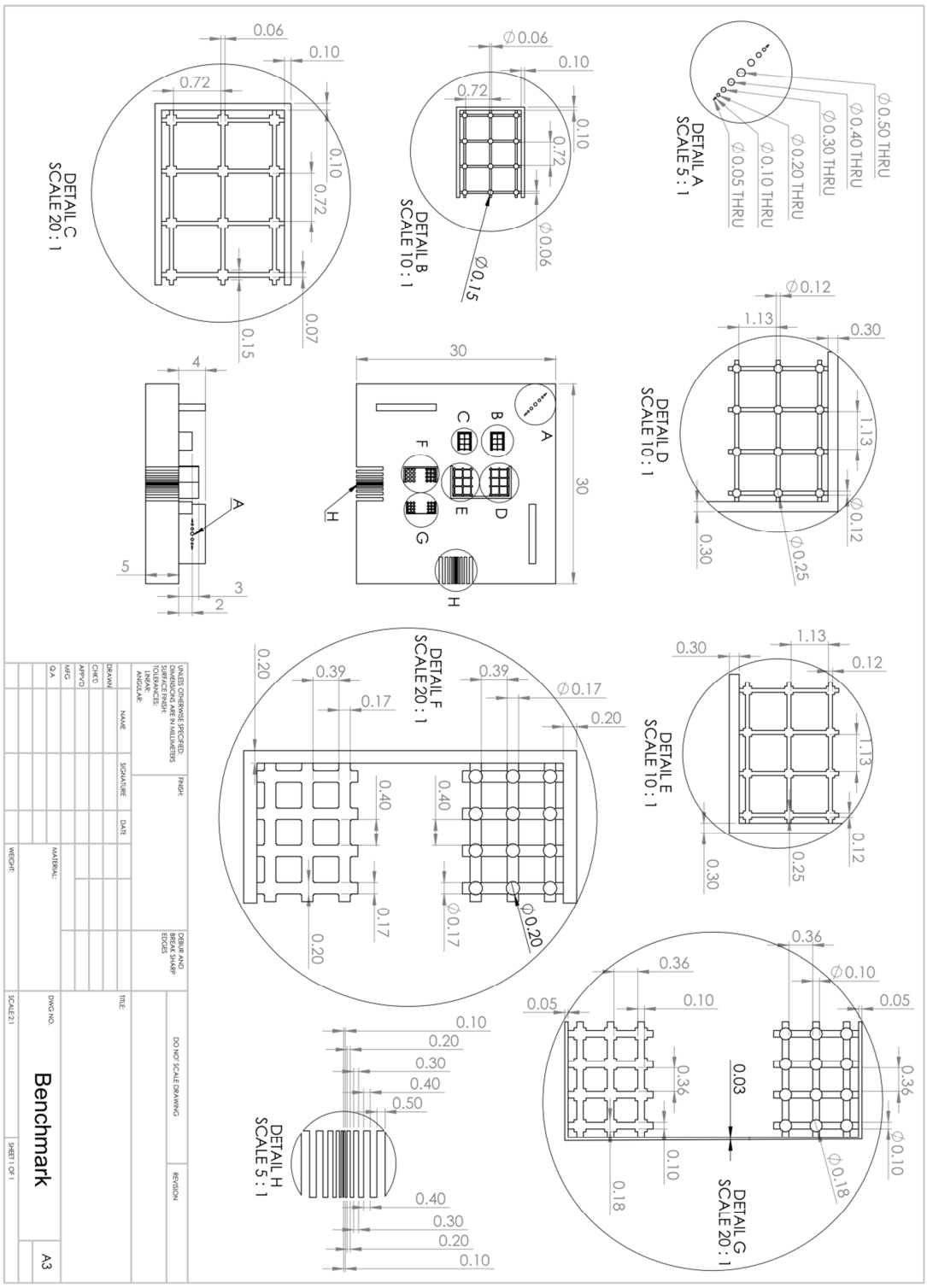
DETAIL A
SCALE 5 : 1
∅0.50 THRU
∅0.40 THRU
∅0.30 THRU
∅0.20 THRU
∅0.10 THRU
∅0.05 THRU
DETAIL B
SCALE 10 : 1
∅0.06
0.10
0.72
∅0.15
DETAIL C
SCALE 20 : 1
0.06
0.10
0.72
0.07
0.15
DETAIL D
SCALE 10 : 1
∅0.12
1.13
0.30
∅0.25
30
A
B
C
D
E
F
G
H
4
5
3
2
DETAIL E
SCALE 10 : 1
DETAIL F
SCALE 20 : 1
0.20
0.39
0.17
∅0.17
0.40
∅0.20
DETAIL G
SCALE 20 : 1
0.36
∅0.10
0.05
0.03
∅0.18
DETAIL H
SCALE 5 : 1
0.10
0.20
0.30
0.40
0.50
UNLESS OTHERWISE SPECIFIED:
DIMENSIONS ARE IN MILLIMETERS
SURFACE FINISH:
TOLERANCES:
LINEAR:
ANGULAR:
FINISH:
BREAK AND
REMOVE SHARP
EDGES
NAME
SIGNATURE
DATE
DRAWN
CHK'D
APPV'D
MFG
Q.A
MATERIAL:
WEIGHT:
TITLE:
DWG NO.
Benchmark
A3
SCALE:2:1
SHEET 1 OF 1
DO NOT SCALE DRAWING
REVISION

Appendix B

Calibration curves for:

i. the LVDT used to measure the displacement of the syringe plunger.
ii. the load cell used to measure the force on the syringe plunger.

(i)

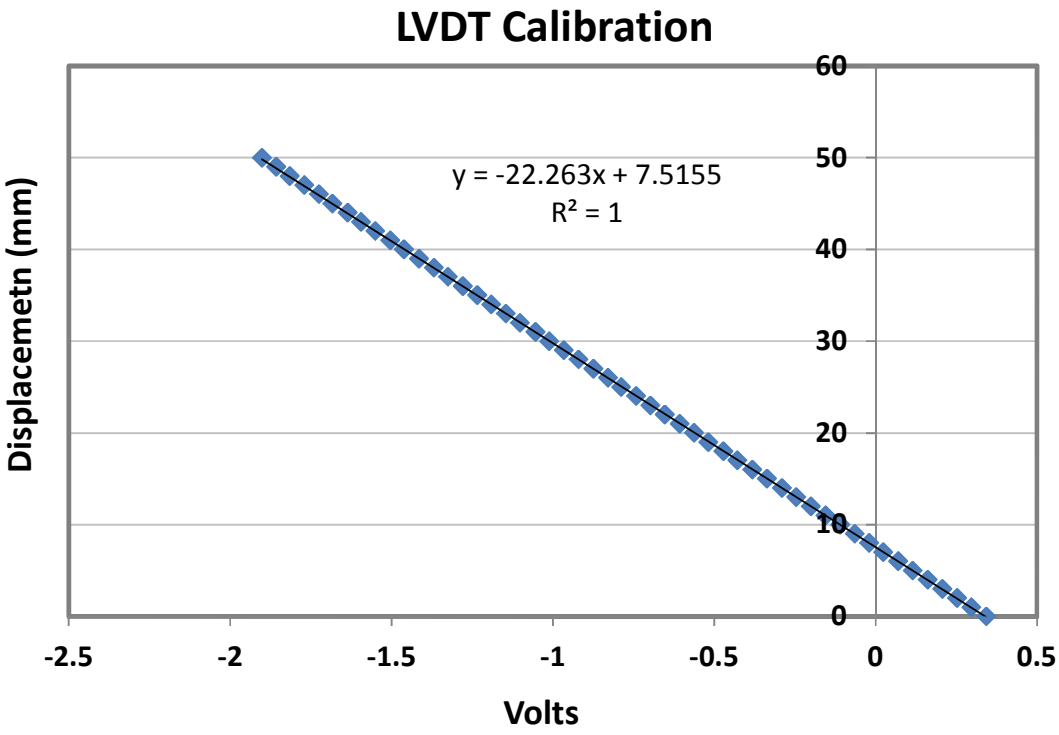
LVDT Calibration
y = -22.263x + 7.5155
R² = 1
Displacemetn (mm)
60
50
40
30
20
10
0
-2.5
-2
-1.5
-1
-0.5
0
0.5
Volts

(ii)

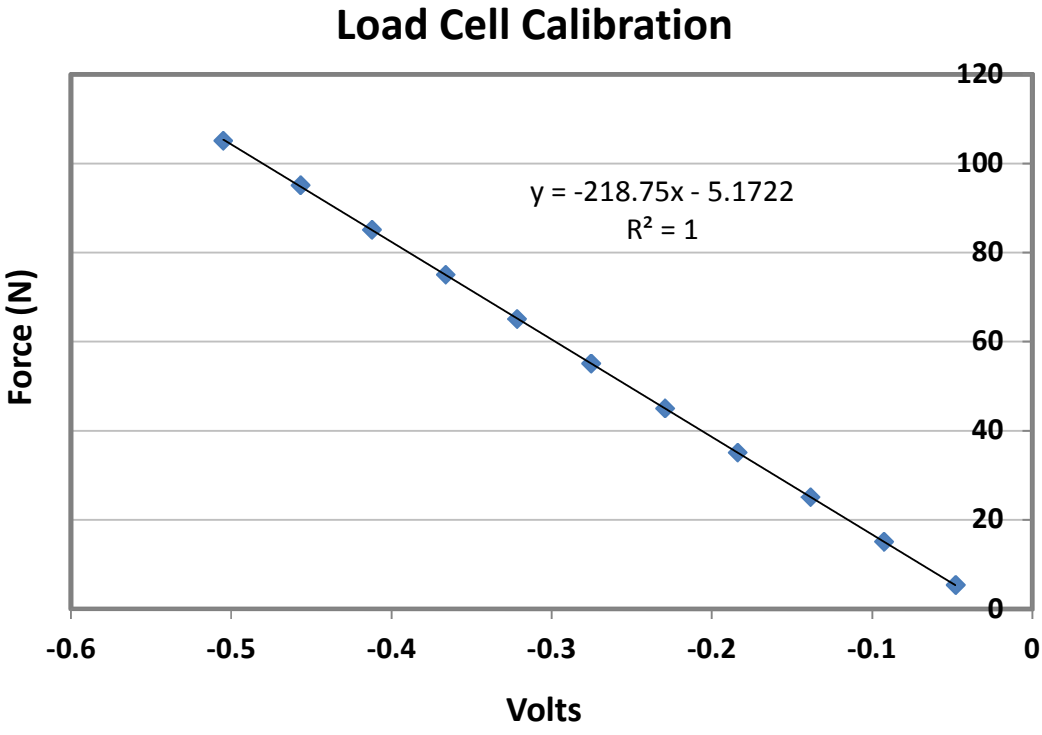
Load Cell Calibration
y = -218.75x - 5.1722
R² = 1
Force (N)
120
100
80
60
40
20
0
-0.6
-0.5
-0.4
-0.3
-0.2
-0.1
0
Volts

Appendix C

LabVIEW codes developed to:

i. control the syringe pump through serial communication.
ii. acquire the load cell and LVDT data during injections into the 3D surrogates.
iii. acquire the video and load cell dat during injections into the 2D flow models.

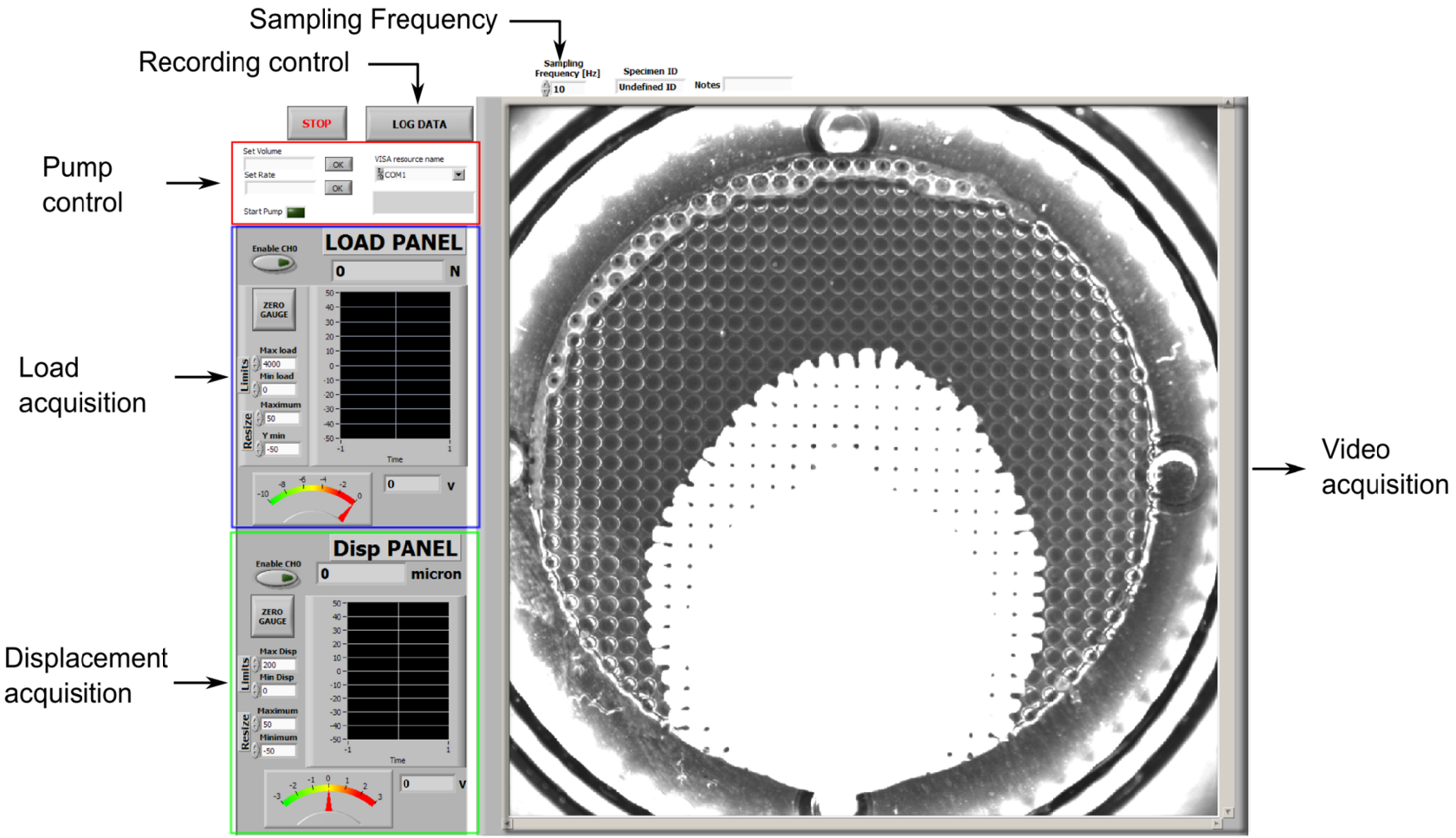

Front Panel of the developed LabVIEW code

(i)

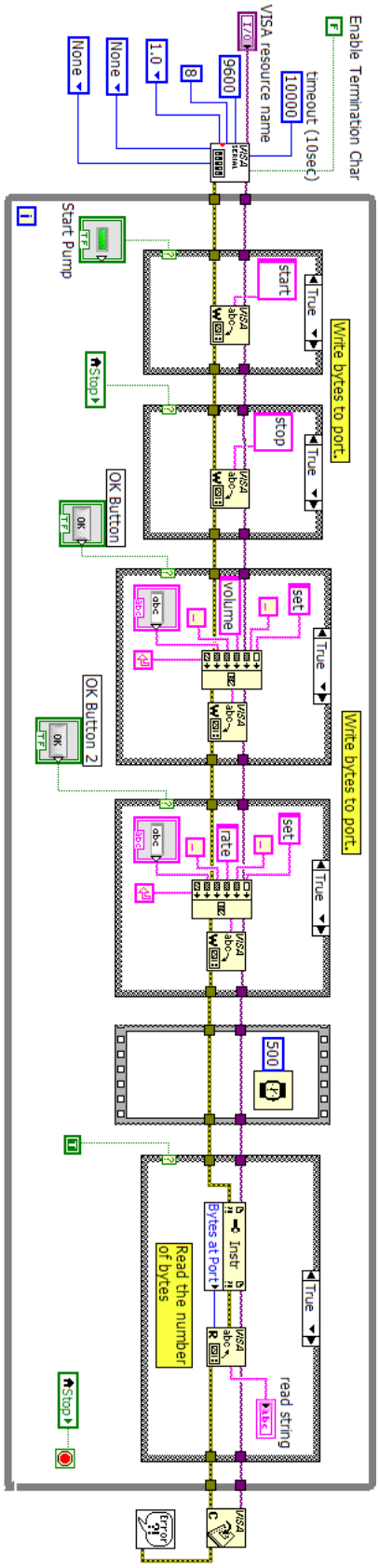
Enable Termination Char
VISA resource name
timeout (10sec)
10000
9600
8
1.0
None
None
Start Pump
start
True
Write bytes to port.
Stop
stop
True
OK Button
volume
set
True
OK Button 2
Write bytes to port.
rate
set
True
500
Read the number of bytes
Bytes at Port
Instr
True
read string
Stop
error

(ii)

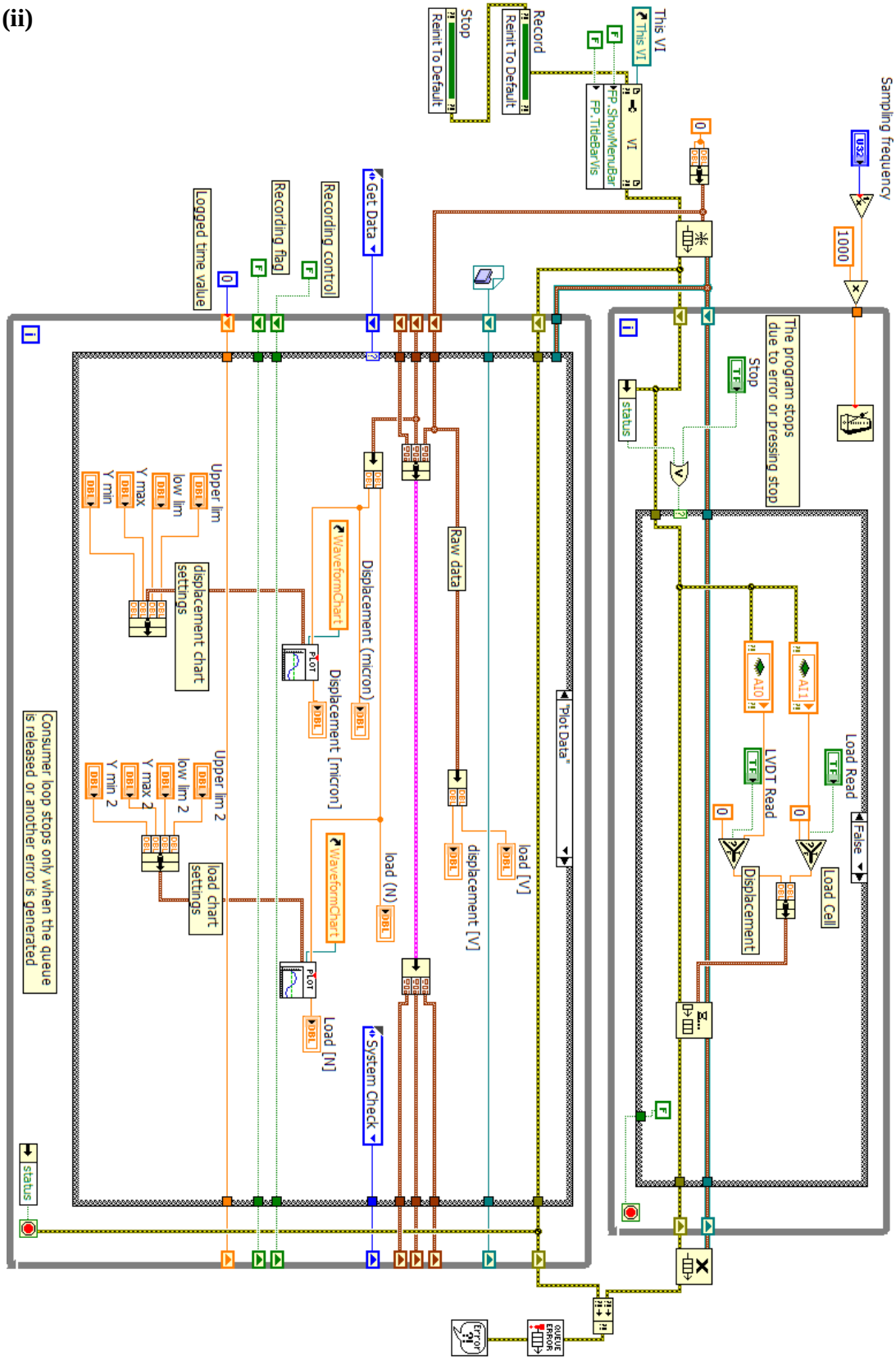
Sampling frequency
1000
This VI
FP.ShowMenuBar
FP.TitleBarVis
Record
Reinit To Default
Stop
Reinit To Default
The program stops due to error or pressing stop
Stop
status
AI0
AI1
LVDT Read
Load Read
False
Displacement
Load Cell
Get Data
Logged time value
Recording flag
Recording control
Raw data
Plot Data
load [V]
displacement [V]
load (N)
Displacement (micron)
WaveformChart
Displacement [micron]
Load [N]
Upper lim
low lim
Y max
Y min
displacement chart settings
Upper lim 2
low lim 2
Y max 2
Y min 2
load chart settings
System Check
Consumer loop stops only when the queue is released or another error is generated
status
Error
QUEUE ERROR

(iii)

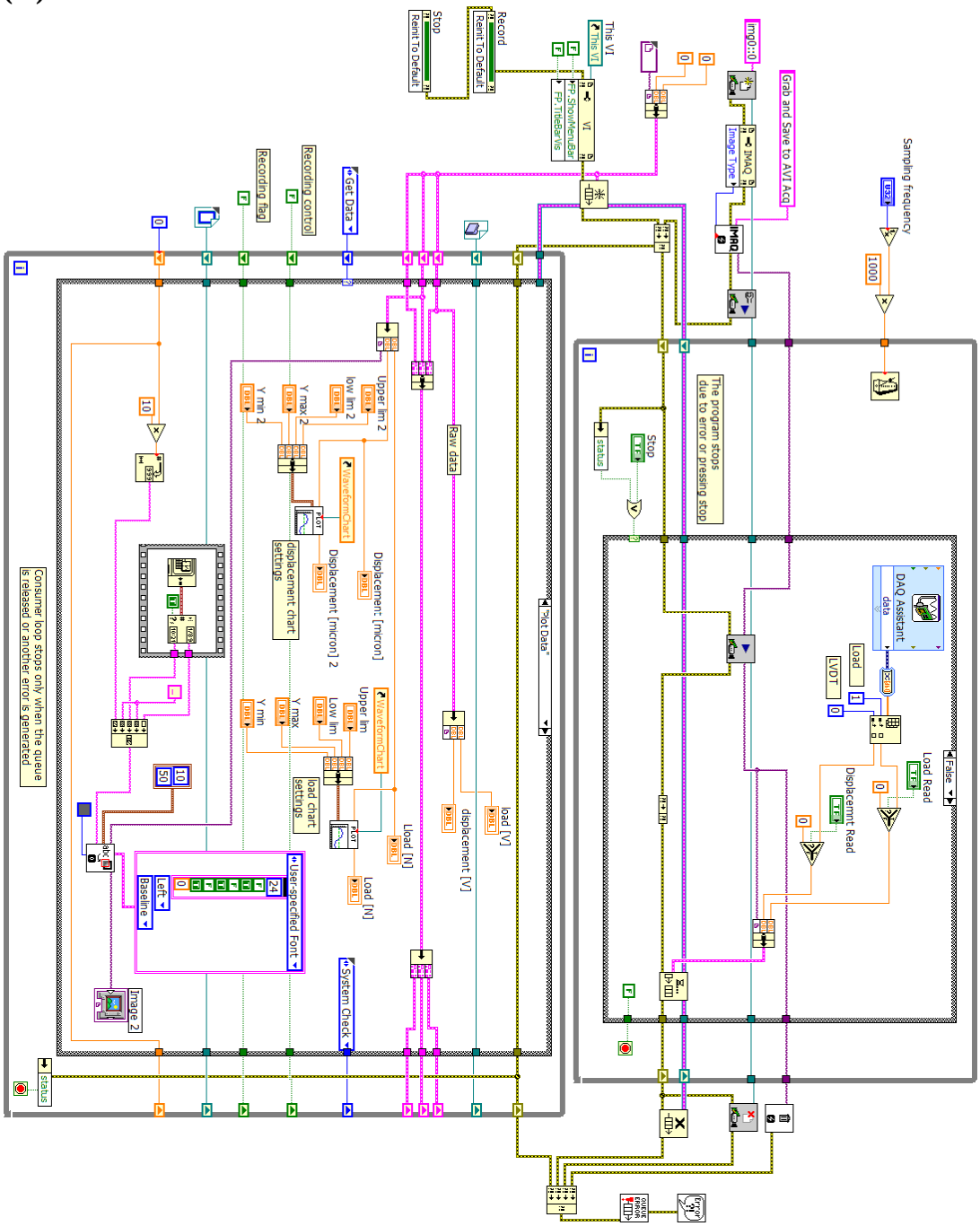
Stop
Record
This VI
img0::0
Grab and Save to AVI Acq
Sampling frequency
1000
Recording flag
Recording control
Get Data
Raw data
Upper lim 2
low lim 2
Y max 2
Y min 2
WaveformChart
displacement chart
Displacement [micron]
Displacement [micron] 2
Upper lim
Low lim
load chart
load [V]
displacement [V]
Load [N]
PlotData
Consumer loop stops only when the queue is released or another error is generated
The program stops due to error or pressing stop
status
Stop
DAQ Assistant
data
Load
LVDT
Load Read
Displacemnt Read
False
Left
Baseline
User-specified Font
System Check
Image 2

Appendix D

Matlab scripts developed to:

i. allow automated segmentation of the flow distribution.
ii. correct the inherent pincushion distortion in the fluoroscopy image.

(i)

```
% Open video file
path = '\\fengstore2\store5\SpineFX\Antony\3D_experiments\Osteo\SP\'
name = 'Osteo_SP1to1_r4.avi'
obj =  mmreader([path name])

% read the frame number which corresponds to the time just before the
% injected fluid is observed in the specimen
% convert to greyscale, initialize the counter i and the time
F= read (obj, 285);
GF=rgb2gray(F);
i=1;
time=1;

% read specific frame numbers corresponding to the duration of the
injection
% at predefined increments in this case 50 frames (note sampling
frequency is % set at 25 Hz). Frames are read every 2 seconds for the
duration of the      % injection
for n=310:50:2610
L= read(obj,n);
GL=rgb2gray(L);
HS=GF-GL;

% threshold / convert to logical
LHS=false(size(HS,1), size(HS,2));
for m=1:size(HS,1)
for n=1:size(HS,2)
if HS(m,n)>=4
LHS(m,n)=1;
else
LHS(m,n)=0;
end
end
end


% create image with a filled circle and use it for masking in order
% to remove boundary noise
t = 0:pi/20:2*pi;
R0 = 70; x0 = 402; y0 = 307;
xi = R0*cos(t)+x0;
yi = R0*sin(t)+y0;
roimask = poly2mask(xi,yi, size(LHS,1), size(LHS,2));

% multiply mask to image
MS=LHS.*roimask;

% remove unconnected regions
se = strel('disk',2); NS=imopen(MS,se);

% fill holes in the segmented region
se = strel('disk',3); SS=imclose(NS,se);
```

```
% further removing of noise
se = strel('disk',4); SSS=imopen(SS,se);

% Show the raw image and overlay the contour of the segmented image
figure
imshow(L)
hold on
bound=bwboundaries(SSS);
for k = 1:numel(bound)
    plot(bound{k}(:,2), bound{k}(:,1), 'b', 'Linewidth', 2);
end

% Export the images
filename = sprintf('4min_r4_%d.png', i);
saveas(gcf, filename, 'png')

% Measure the properties of the segmented (filled) area using image
% analysis
Stats=regionprops(SSS,'Area','Perimeter','Eccentricity','MajorAxisLen
gth','MinorAxisLength','Orientation', 'Centroid');
disp(['Area ' num2str(Stats.Area) ' px ' ]);
disp(['Perimeter ' num2str(Stats.Perimeter) ' px ' ]);
disp(['Eccentricity ' num2str(Stats.Eccentricity) ' px ' ]);
disp(['MajorAxis ' num2str(Stats.MajorAxisLength) ' px ' ]);
disp(['MinorAxis ' num2str(Stats.MinorAxisLength) ' px ' ]);

% Save the image analysis data into a matrix
Results(i,:)=[time, Stats.Area, Stats.Perimeter, Stats.Eccentricity,
Stats.MajorAxisLength, Stats.MinorAxisLength, Stats.Orientation,
Stats.Centroid];

% Export the binary image which shows only the filled area
SI=imcomplement(SSS);
imwrite(SI,['SSS',num2str(i),'.tif']);

% Increment the counter i and the time
% End the for loop
i=i+1;
time=time+2;
end

% Export the image analysis data into an excel sheet
Labels={'Time', 'Area', 'Perimeter', 'Eccentricity', 'MajorAxis',
'MinorAxis','Orientation', 'Centroid'};
xlswrite('4min_r41.xls', Labels, 1, 'B1');
xlswrite('4min_r41.xls', Results, 1, 'B2');
```

(ii)

```
% Open video file, read specific frame number and show grayscale
% image
obj =  mmreader('Calib107cm456.avi')
II= read (obj, 115);
I=rgb2gray(II);
imshow(I);

% Apply a linear transformation matrix to compress the image by 40 px
% along the vertical direction
I4 = imresize(I, [536 720]);

% Apply a radial distortion correction using the matlab function
% lensdistort
I5 = lensdistort(I4, 0.05, 'interpolation'  , 'nearest', 'padmethod'
, 'symmetric', 'ftype', 4);

% Apply an edge detection function to outline the bead projections
IE= EDGE(I5,'canny', 0.05);

% Apply a mask to obtain the region of interest
t = 0:pi/20:2*pi;
R0 = 100; x0 = 395; y0 = 280;
xi = R0*cos(t)+x0;
yi = R0*sin(t)+y0;
roimask = poly2mask(xi,yi, size(IE,1), size(IE,2));
MS=IE.*roimask;

% Fill the bead outlines
LI=imclose(MS, strel ('disk', 2));
NS=imfill(LI,'holes');

% Remove noise
SS=imopen(NS,strel ('disk', 4));

% Show the corrected image and overlay the bead outlines
figure
imshow(I5)
hold on
bound=bwboundaries(SS);
for k = 1:numel(bound)
    plot(bound{k}(:,2), bound{k}(:,1), 'b', 'Linewidth', 2);
end

% Export the binary image which shows only the filled beads
imwrite(SS,['SS_corrected.tif']);
```

Appendix E

Conference Publications

List of conference presentations:

1. A Bou Francis, N Kapur, RM Hall, Novel 2D bone surrogate models for assessing cement injection behaviour in vertebroplasty, GRIBOI, Boston, USA, April, 2013.

2. A Bou Francis, N Kapur, RM Hall, Novel methodology for assessing cement injection behavior in vertebroplasty, EUROSPINE, Liverpool, UK, October, 2013.

3. A Bou Francis, N Kapur, RM Hall, Novel methodology for assessing cement injection behaviour in vertebroplasty, CORS, Venice, Italy, October, 2013. (Best Oral Presentation Award)

4. A Bou Francis, A López, C Persson, RM Hall, N Kapur, Assessing cement injection behavior in vertebroplasty: An in-vitro study using flow models, WCB, Boston, USA, July, 2014.

Appendix F

Journal Publication